

CR-184101

Final Report On
(NAS8-37764)

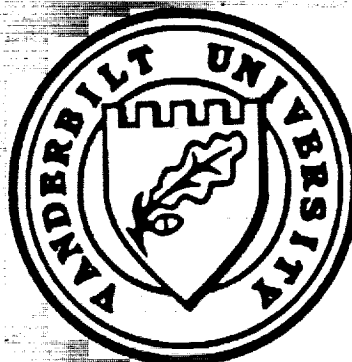
ANALYSIS OF ROLLING CONTACT SPALL LIFE
IN 440C STEEL BEARING RIMS

Prepared for

George C. Marshall Space Flight Center
Alabama, 35812

by

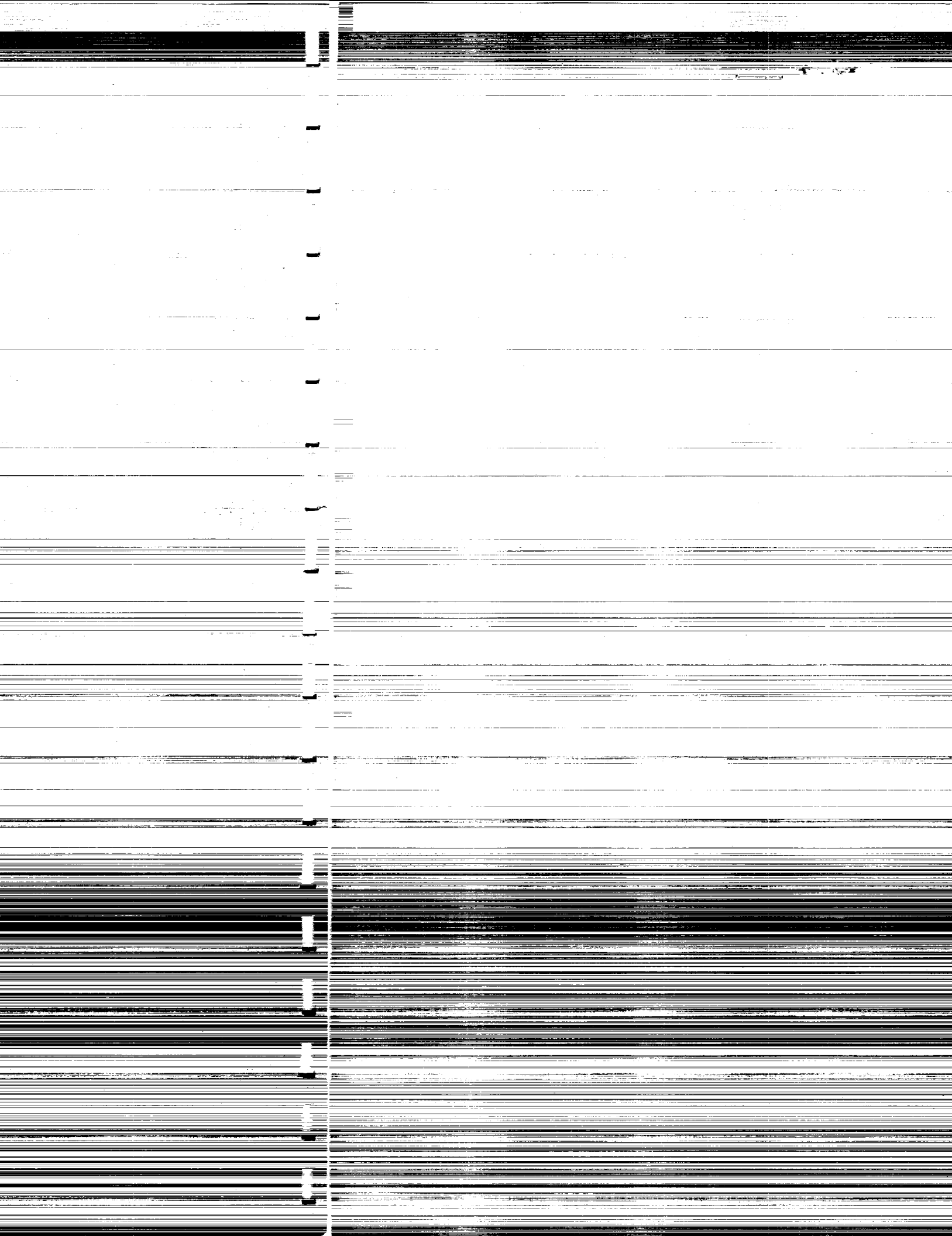
P.C. Bastias, V. Bhargava, A.P. Bower, J. Du, V. Gupta,
G.T. Hahn, S.M. Kulkarni, A.M. Kumar, X. Leng, and C.A. Rubin



CENTER FOR MATERIALS TRIBOLOGY
P.O. Box 1593, Station B
Vanderbilt University
Nashville, TN 37235

January 23, 1991

273



AFFILIATIONS

- 1) P.C. Bastias, J. Du, V. Gupta, G.T. Hahn, X. Leng, and C. A. Rubin are with Vanderbilt University, Nashville, TN.
- 2) A.P. Bower is with Cambridge University, U.K.
- 3) V. Bhargava is with General Electric Corporate Research Laboratory, Schenectady, N.Y.
- 4) S.M. Kulkarni is with TRW Safety Systems/Mesa, Mesa, AZ.
- 5) A.M. Kumar is with Washington State University, Pullman, WA.

TABLE OF CONTENTS

	<u>Page</u>
. ABSTRACT.....	iii
.. LIST OF FIGURES.....	iv
... LIST OF TABLES.....	xxii
1. INTRODUCTION.....	1
1.1 Background.....	1
1.2 Summary.....	2
2. CYCLIC STRESS-STRAIN PROPERTIES.....	5
2.1 Background.....	5
2.2 Experimental Procedures.....	9
2.3 Cyclic Stress-Strain Properties of 440C Steel...	11
2.4 Cyclic stress-Strain Properties of 7075-T6 Aluminum.....	17
2.5 Discussion and Conclusions.....	17
3. FINITE ELEMENT ANALYSES.....	28
3.1 Background.....	28
3.2 Analytical Procedures.....	31
3.3 Three-Dimensional Rolling Contact of Bearing Steel.....	40
3.4 Three-Dimensional Rolling Contact of Hardened Aluminum.....	67
3.5 Two-Dimensional Rolling-Plus-Sliding with Heat Generation.....	82
3.6 Conclusions.....	94
4. EVALUATION OF THE FRACTURE MECHANICS DRIVING FORCE FOR SPALL GROWTH.....	96
4.1 Background.....	96
4.2 Contributions to the Spall Growth Driving Force.....	96
4.3 Evaluation of the Mode I and Mode II Driving Force for Two-Dimensional, Surface Breaking Cracks with Fluid in the Crack Cavity.....	99
4.4 Comparisons of the Contributions to the Driving Force for Surface Breaking Cracks.....	101
4.5 Evaluation of the Threshold Crack Sizes.....	133
4.6 Conclusions.....	137
5. ROLLING CONTACT FAILURE.....	138
5.1 Background.....	138
5.2 Experimental Materials and Procedures.....	138

5.3	Retained Austenite.....	171
5.4	Nucleation Vs. Growth.....	171
5.5	Surface Roughness.....	181
5.6	Replication and Metallographic Studies of Spalls in 440C Steel.....	181
5.7	Rolling Contact of Hardened Aluminum.....	185
5.8	Conclusions.....	186
6.	GENERAL DISCUSSION.....	188
6.1	Finite Element Calculations of Contact Plasticity.....	188
6.2	Spall Nucleation.....	189
6.3	Growth and Spalling.....	190
6.4	Conclusions.....	191
7.	CONCLUSIONS.....	196
8.	ACKNOWLEDGEMENTS.....	199
	REFERENCES.....	200
APPENDIX 1.	3-DIMENSIONAL DISPLACEMENT BOUNDARY CONDITIONS.....	210
APPENDIX 2.	BOUNDARY CONDITIONS FOR 2-DIMENSIONAL ROLLING-PLUS-SLIDING CONTACT WITH FRICTIONAL HEATING.....	218
APPENDIX 3.	STRESS-STRAIN CONTOURS FOR 3- DIMENSIONAL ROLLING CONTACT OF HARDENED ALUMINUM.....	230



Report Documentation Page

1. Report No.	2. Government Accession No.	3. Recipient's Catalog No.
4. Title and Subtitle ANALYSIS OF ROLLING CONTACT SPALL LIFE IN 440C BEARING RIMS - FINAL REPORT		5. Report Date January 23, 1991
		6. Performing Organization Code None
7. Author(s) Pedro C. Bastias, Vivek Bhargava, Allan P. Bower, Jianqun Du, Vikas Gupta, George T. Hahn, Sanjeev M. Kulkarni, Arun M. Kumar, Xiaogang Leng, and Carol A. Rubin		8. Performing Organization Report No.
		10. Work Unit No.
9. Performing Organization Name and Address Vanderbilt University, Center for Materials Tribology P.O. Box 1593 - Station B Nashville, TN 37235		11. Contract or Grant No. NAS8-37764
		13. Type of Report and Period Covered Final Report
12. Sponsoring Agency Name and Address National Aeronautics and Space Administration Marshall Space Flight Center Huntsville, AL 35812		14. Sponsoring Agency Code
15. Supplementary Notes Project Monitor, Steve Gentz, NASA Marshall Space Flight Center		
16. Abstract This report describes the results of a 2-year study of the mechanism of spall failure in the HPOTP bearings. The objective was to build a foundation for detailed analyses of the contact life in terms of: (i) cyclic plasticity, (ii) contact mechanics, (iii) spall nucleation and (iv) spall growth. Since the laboratory rolling contact testing is carried out in the 3-ball/rod contact fatigue testing machine, the analysis of the contacts and contact lives produced in this machine received attention. The results from the experimentally observed growth lives are compared with calculated predictions derived from the fracture mechanics calculations.		
17. Key Words (Suggested by Author(s)) Spalling; Fatigue; Failure Mechanisms; Stress Intensity Factors; HPOTP Bearings		18. Distribution Statement Unclassified - Unlimited
19. Security Classif. (of this report) Unclassified	20. Security Classif. (of this page) Unclassified	21. No. of pages 249
		22. Price N.A.

PREPARATION OF THE REPORT DOCUMENTATION PAGE

The last page of a report facing the third cover is the Report Documentation Page, RDP. Information presented on this page is used in announcing and cataloging reports as well as preparing the cover and title page. Thus it is important that the information be correct. Instructions for filling in each block of the form are as follows:

Block 1. Report No. NASA report series number, if preassigned.

Block 2. Government Accession No. Leave blank.

Block 3. Recipient's Catalog No. Reserved for use by each report recipient.

Block 4. Title and Subtitle. Typed in caps and lower case with dash or period separating subtitle from title.

Block 5. Report Date. Approximate month and year the report will be published.

Block 6. Performing Organization Code. Leave blank.

Block 7. Author(s). Provide full names exactly as they are to appear on the title page. If applicable, the word editor should follow a name.

Block 8. Performing Organization Report No. NASA installation report control number and, if desired, the non-NASA performing organization report control number.

Block 9. Performing Organization Name and Address. Provide affiliation (NASA program office, NASA installation, or contractor name) of authors.

Block 10. Work Unit No. Provide Research and Technology Objectives and Plans (RTOP) number.

Block 11. Contract or Grant No. Provide when applicable.

Block 12. Sponsoring Agency Name and Address. National Aeronautics and Space Administration, Washington, D.C. 20546-0001. If contractor report, add NASA installation or HQ program office.

Block 13. Type of Report and Period Covered. NASA formal report series; for Contractor Report also list type (interim, final) and period covered when applicable.

Block 14. Sponsoring Agency Code. Leave blank.

Block 15. Supplementary Notes. Information not included elsewhere: affiliation of authors if additional space is re-

quired for block 9, notice of work sponsored by another agency, monitor of contract, information about supplements (film, data tapes, etc.), meeting site and date for presented papers, journal to which an article has been submitted, note of a report made from a thesis, appendix by author other than shown in block 7.

Block 16. Abstract. The abstract should be informative rather than descriptive and should state the objectives of the investigation, the methods employed (e.g., simulation, experiment, or remote sensing), the results obtained, and the conclusions reached.

Block 17. Key Words. Identifying words or phrases to be used in cataloging the report.

Block 18. Distribution Statement. Indicate whether report is available to public or not. If not to be controlled, use "Unclassified-Unlimited." If controlled availability is required, list the category approved on the Document Availability Authorization Form (see NHB 2200.2, Form FF427). Also specify subject category (see "Table of Contents" in a current issue of STAR), in which report is to be distributed.

Block 19. Security Classification (of this report). Self-explanatory.

Block 20. Security Classification (of this page). Self-explanatory.

Block 21. No. of Pages. Count front matter pages beginning with iii, text pages including internal blank pages, and the RDP, but not the title page or the back of the title page.

Block 22. Price Code. If block 18 shows "Unclassified-Unlimited," provide the NTIS price code (see "NTIS Price Schedules" in a current issue of STAR) and at the bottom of the form add either "For sale by the National Technical Information Service, Springfield, VA 22161-2171" or "For sale by the Superintendent of Documents, U.S. Government Printing Office, Washington, DC 20402-0001," whichever is appropriate.

ABSTRACT

This report describes the results of a 2-year study of the mechanism of spall failure in the HPOTP bearings. The objective was build a foundation for detailed analyses of the contact life in terms of; (i) cyclic plasticity, (ii) contact mechanics, (iii) spall nucleation and (iv) spall growth. Since the laboratory rolling contact testing is carried out in the 3-ball-rod contact fatigue testing machine, the analysiss of the contacts and contact lives produced in this machine received attention.

The analysis of previous cyclic stress-strain hysteresis loop measurements of 440C steel was refined to account for the plasticity of the fillet regions. In addition, the hysteresis loop shapess of the hardened 7075 aluminum alloy were measured. In both cases the elastic-linear-kinematic-hardening-plastic (ELKP) loop parameters were evaluated. Elasto-plastic, finite element analyses of the repeated, 3-dimensional, frictionless, rolling contact produced in the 3-ball-rod testing machine at Hertzian pressures of $p_0 = 2.4, 4.0$ and 5.4 GPa (for 440C steel) and 1.25 GPa (for hardened aluminum) were carried out using the appropriate ELKP-loop parameters. These calculations were also extended for 440C steel properties to 3-dimensional rolling-plus-sliding and to the 2-dimensional (line contact) thermal-mechanical coupled rolling-plus-sliding with frictional heating. The results of calculations are compared with observations of aluminum rods subjected to contact under these conditions.

Rolling contact tests of the 440C steel and the hardened aluminum were performed in the 3-ball-rod testing machine with smooth and roughened balls. Efforts were made to evaluate the effects of retained austenite. A series of tests were performed on the 440C samples with small $\approx 100 \mu\text{m}$ indentations in the running track which make it possible to locate and follow the progress of spall nucleation and growth. The results define the spall nucleation- and spall growth-component of the contact life of the 440C steel over a range of the contact pressures. They also provide evidence for a threshold pressure for crack growth. In addition, the 3-dimensional features of the spall were studied by a novel replicating technique and metallographic sections of the spalls.

The contributions to the fracture mechanics crack growth driving force for surface breaking cracks arising from the Hertzian stresses, surface irregularities, fluid in the crack cavity, centrifugal stresses and thermal stresses are reviewed and the results of 2- and 3-dimensional analyses are compiled and compared. New calculations for the Bower model of a 2-dimensional surface breaking crack with fluid pressure in the crack cavity are pressented. A numerical expression for the Mode I crack driving force for a 3-dimensional crack with fluid in the crack cavity is used to calculate the spall growth component of the contact life. These calculations are compared with and are in reasonable agreement with the measurements of spall growth.

LIST OF FIGURES

<u>Figure</u>		<u>Page</u>
2.1	Shear stress-shear strain hysteresis loops: (a) the loop for idealized, isotropic, elastic-perfectly-plastic (EPP) behavior, and (b) the loops displayed by 440C steel after N=15 and N=250 stress cycles. While the EPP-loop is drawn so that its 0.035%-offset, shear yield strength corresponds with that of the N=15 loop of the 440C steel, it is clear that the EPP loop does not come close to representing the cyclic stress strain behavior of the steel.....	6
2.2	Schematic of the bilinear, 3-parameter, elastic-linear-kinematic-hardening-plastic (ELKP) representation of the hysteresis loop: (a) conventional form employed for 440C steel and (b) special form employed for 7075-T6 aluminum to accommodate the differences in the elastic modulus in tension and compression. The 3 ELKP-parameters are: (for tension-compression) the elastic modulus, E, the kinematic yield strength, σ_k , and the plastic modulus (G, k_k , and M_s for torsion). The relations between these parameters and more conventional parameters are given in Table 2.1.....	7
2.3	Axial fatigue test specimen used to measure 7075-T6 hysteresis loops. All dimensions are in meters.....	10
2.4	Variation of the non-reversibility of the 440C steel hysteresis loop produced by a mean shear stress, $\tau_m = 200$ MPa, with number of cycles.....	12
2.5	Variation of the kinematic yield strength of 440C steel with number of cycles.....	13
2.6	Variation of the plastic modulus of 440C steel with number of cycles.....	14
2.7	Variation of the loop area (per cycle plastic work) with the plastic strain range. The loop areas calculated from the ELKP-parameters: $U' = 2 \cdot \epsilon^p \cdot \sigma_k$, are close to the	

	actual values.....	15
2.8	Examples of the axial stress-strain hysteresis loops displayed by 7075-T6 aluminum for constant plastic strain range, $\epsilon^P = 0.001$, by the $N = 20$ and $N = 780$ cycles.....	18
2.9	Examples of the axial stress-strain hysteresis loops displayed by 7075-T6 aluminum for constant plastic strain range cycles, $\Delta\epsilon^P = 0.0025$ and a mean stress, $\sigma_m = -100$ MPa by the $N = 30$ and $N = 330$ cycles.....	19
2.10	Variation of the kinematic yield strength of 7075-T6 with number of cycles for different values of the constant plastic strain range. The $\Delta\epsilon^P = 0.00025$ strain range test was carried out with a mean stress, $\sigma_m = -100$ MPa.....	20
2.11	Variation of the plastic modulus of 7075-T6 with number of cycles for different values of the constant plastic strain range. The $\Delta\epsilon^P = 0.00025$ strain range test was carried out with a mean stress, $\sigma_m = -100$ MPa.....	21
2.12	Variation of the stress amplitude of 7075-T6 with number of cycles for different values of the constant plastic strain range. The $\Delta\epsilon^P = 0.00025$ strain range test was carried out with a mean stress, $\sigma_m = -100$ MPa.....	22
2.13	Variation of the kinematic yield strength, stress amplitude and plastic modulus of 7075-T6 with the plastic strain range. The value of σ_k for zero strain range was obtained by a linear extrapolation. Note that the half equivalent strain range corresponds with the conventional strain range.....	23
2.14	Variation of the conventional cyclic strength properties of 7075-T6 (measured from zero stress) with the plastic strain range. values quoted for a strain range of $\Delta\epsilon^P = 0.00025$ were obtained with a mean stress, $\sigma_m = -100$ MPa, which produces different conventional strength values during the forward and reverse part of the cycle. Note that the half equivalent strain range corresponds with the conventional strain range.....	24

2.15	Comparison of the loop areas by the ELKP-parameters, with the actual loop areas recorded for 7075-T6.....	25
3.2.1	Finite element mesh used for the 3-dimensional calculations; the size of the elliptical contact patch and the axis (with their nomenclature) are also indicated in the figure.....	32
3.2.2	Finite element mesh used for the 2-dimensional calculations which accounted for rolling-plus-sliding, with the resulting heat generation.....	38
3.3.1	Contour distribution of equivalent (Mises) stresses on the surface of the mesh (viewed along the z-axis), for high, medium and low pressures. The size of the contact is indicated in the figure. The schematic drawing shows the viewed slice. The values are expressed in N/m^2 (Pascals).....	41
3.3.2	Contour distribution of equivalent (Mises) stresses on the side of the mesh (viewed along the x-axis), for high, medium and low pressures. The size of the contact is indicated in the figure. The schematic drawing shows the viewed slice. The values are expressed in N/m^2 (Pascals).....	43
3.3.3	Contour distribution of equivalent (Mises) stresses on a set of elements at the center of the mesh (viewed along the y-axis), for high, medium and low pressures. The size of the contact is indicated in the figure. The schematic drawing shows the observed slice. The values are expressed in N/m^2 (Pascals).....	44
3.3.4	Contour distribution of direct, σ_{zz} , stresses viewed along the z-axis (top surface), for high, medium and low pressures. The size of the contact is indicated in the figure. The schematic drawing shows the observed slice. The values are expressed in N/m^2 (Pascals).....	45
3.3.5	Distribution of shear stresses, σ_{xy} , viewed along the z-axis. The figure indicates the size of the contact as well as the values for the contours. The stresses are indicated in N/m^2 (Pascal). The schematic drawing shows	

	the portion of the mesh under observation.....	46
3.3.6	Distribution of circumferential, σ_{yy} , direct stresses under the surface. The pressure distribution has been translated halfway through one pass. The schematic drawing indicates the slice of material under observation. The values for the contours are in units of N/m^2 (Pascals).....	47
3.3.7	Antisymmetric distribution of shear stress, σ_{yz} , viewed along the -x direction. The schematic drawing shows the portion of the mesh under observation. The stresses are in units of N/m^2 (Pascals).....	49
3.3.8	Distribution of normal, σ_{xx} , stresses viewed along the -y direction. The contours are shown for the material at the center of the mesh directly under the contact, as indicated in the schematic drawing. The stresses are in units of N/m^2 (Pascals).....	50
3.3.9	Contour distribution of shear stresses, σ_{xz} , under the surface and immediately below the contact, at the center of the mesh. The schematic drawing shows the portion of material under consideration. The contours show the stresses in units of N/m^2 (Pascals).....	51
3.3.10	Distribution of iso-contours for the equivalent plastic strains, viewed along the z-direction. The dimension of the contacts are indicated in the figure. The schematic shows the slice of material under observation.....	52
3.3.11	Distribution of equivalent plastic strains under the surface, viewed along the -x direction. The schematic drawing shows the slice of mesh under consideration.....	53
3.3.12	Distribution of equivalent plastic strains under the surface, viewed along the -y direction for a slice of material located at the center of the mesh as indicated in the schematic drawing.....	54
3.3.13	Contour distribution of the amount of energy dissipated as irrecoverable plastic work per unit volume, viewed along the x-direction. The contours are in units of $N.m$ (Joules).....	56

3.3.14	Contour distribution of energy dissipated by plastic work, viewed along the z-direction on the slice of material indicated in the schematic drawing. The contours are in units of N.m (Joules).....	57
3.3.15	Distribution of residual direct stresses at the center of the mesh in the axial direction (normalized with respect to the kinematic shear yield strength) as a function of the depth (normalized with respect to the semi-major contact width). Results for the three different loadings are indicated in the Fig.....	58
3.3.16	Distribution of residual direct stresses at the center of the mesh in the circumferential direction (normalized with respect to the kinematic shear yield strength) as a function of the depth (normalized with respect to the semi-major contact width). Results for the three different loadings are indicated in the Fig.....	59
3.3.17	Distribution of residual direct stresses at the center of the mesh in the radial direction (normalized with respect to the kinematic shear yield strength) as a function of the depth (normalized with respect to the semi-major contact width). Results for the three different loadings are indicated in the Fig.....	60
3.3.18	Iso-contours of the half equivalent plastic strain range for pure rolling with high loading ($p_0/k \approx 9$). The contours are for a slice of material located at the center of the mesh, as shown on the schematics. Strain values are shown magnified $\times 10^3$	62
3.3.19	Iso-contours of the half equivalent plastic strain range for pure rolling with medium loading ($p_0/k \approx 6$). The contours are for a slice of material located at the center of the mesh, as shown on the schematics. Strain values are shown magnified $\times 10^3$	63
3.3.20	Iso-contours of the half equivalent plastic strain range for pure rolling with low loading ($p_0/k \approx 4$). The contours are for a slice of material located at the center of the mesh, as shown on the schematics. Strain	

	values are shown magnified $\times 10^3$	64
3.3.21	Iso-contours of the half equivalent plastic strain range for rolling plus sliding with high loading ($p_0/k \approx 9$). The contours are for a slice of material located at the center of the mesh, as shown on the schematics. Strain values are shown magnified $\times 10^3$	65
3.3.22	Comparison of the variation in the half plastic strain range with depth, for the three different loads under pure rolling, and the high load under rolling plus sliding (these values are taken at the same locations as Figs. 3.3.18-21).....	66
3.4.1	Contours of von Mises equivalent stress on two different sections of the mesh (the sections are schematically indicated by the side of each figure). The numbers on the individual contours represent different equivalent values of the contours.....	68
3.4.2	Equivalent plastic strain contours representing the plastic strain history as the pressure ellipsoid completes one translation.....	69
3.4.3	Variation of the half-equivalent plastic strain range, plastic strain range, $\epsilon_p/2$, with normalized depth, for the first and second contacts.....	70
3.4.4	Contours of the out-of-plane (or axial) residual stress, σ_x^r . The stress values are tensile close to the rolling surface (as indicated by the contour levels 7 through 11).....	71
3.4.5	Contours of the circumferential residual stress, σ_y^r . The stress values are tensile close to the rolling surface (as indicated by the contour levels 9 through 11).....	72
3.4.6	Variation of the out-of-plane (or axial) residual stress, σ_x^r , with normalized depth. The values of σ_x^r are obtained from integration points located near the middle of the mesh, where the effects of the boundary are not significant.....	73
3.4.7	Variation of the circumferential residual	

	stress, σ_y^r , with normalized depth. The values of σ_y^r are obtained from integration points located near the middle of the mesh, where the effects of the boundary are not significant.....	74
3.4.8	In-plane shear stress-shear strain history experienced by a point in the model at a relative depth: $z = 0.4 w$. This is also the location of the maximum continuing plastic strain, ϵ^P	75
3.4.9	Comparison of plastic strain contours obtained from finite element calculations and the microstructural changes produced by rolling: (a) after 10^3 contacts, and (b) after 2.3×10^6 contacts. The microstructure and the adjoining contours are shown on the same scale.....	77
3.4.10	Comparison of half-equivalent plastic strain range distribution obtained from finite element calculations and the microstructural changes produced by rolling on a section parallel to the rolling direction.....	78
3.4.11	Distribution of sub-surface cracks with depth below the surface. The variation of the equivalent plastic strain amplitude, $\Delta\epsilon^P/2$, is indicated by dashed lines.....	79
3.4.12	Distribution of sub-surface crack length with depth below the surface. The variation of the axial (σ_x) and circumferential (σ_y) residual stresses are indicated by the dashed lines.....	80
3.4.13	Schematic diagram of spall formation in 7075 T6 aluminum.....	81
3.5.1	Normalized residual stresses as a function of the normalized depth, y/w . Mechanic unloading followed by cooling to the ambient temperature.....	84
3.5.2	Circumferential residual stresses for thermo-mechanical (open symbols) and pure mechanical loading (filled symbols).....	85
3.5.3	Axial residual stresses for thermo-mechanical (open symbols) and pure mechanical loading (filled symbols), for a point located at the center of the mesh.....	86

3.5.4	Residual equivalent plastic strain contours.....	87
3.5.5	Residual equivalent plastic strain variation with depth for a point located at the center of the mesh.....	88
3.5.6	Deformed residual configuration of the mesh after cooling to room temperature. Magnification factor x590.....	89
3.5.7	Distribution of surface temperature halfway through the pass, for different passes.....	90
3.5.8	Temperature contours half way through the third pass.....	91
3.5.9	Hysteresis loop, shear stress versus shear strain, for the second pass.....	92
3.5.10	Hysteresis loop, shear stress versus shear strain, for the third pass.....	93
4.1	Geometry and nomenclature used for the surface breaking crack problem which was solved using the Bowers (1989) analytical solution. The load was translated from left to right. The traction q_0 is considered positive when its direction coincides with the rolling direction.....	100
4.2	Variation of the normalized, Mode II stress intensity factor versus the normalized distance between the contact and the crack mouth for dry contact, a relative crack length, $a/w = 1$, crack inclinations $\theta = -20^\circ$ and -30° , the traction ratio, $q_0/p_0 = 0.01$, and crack face friction, $\mu^C = 0$	102
4.3	Variation of the normalized, Mode II stress intensity factor versus the normalized distance between the contact and the crack mouth for dry contact, a relative crack length, $a/w = 1$, crack inclinations $\theta = -20^\circ$ and -30° , the traction ratio, $q_0/p_0 = 0.01$, and crack face friction, $\mu^C = 0.2$	103
4.4	Variation of the normalized Mode II crack tip driving force versus the normalized crack tip depth for dry contact, crack inclinations, θ $= -20^\circ$ and -30° , the traction ratio, $q_0/p_0 =$ 0.01 , and crack face friction, $\mu^C = 0.2$	104

4.5	Variation of the normalized Mode II crack tip driving force versus the normalized crack tip depth for dry contact, crack inclinations, $\theta = -20^\circ$ and -30° , the traction ratio, $q_0/p_0 = 0.05$ and crack face friction, $\mu^C = 0.2$	105
4.6	Variation of the normalized Mode II crack tip driving force versus the normalized crack tip depth for dry contact, crack inclinations, $\theta = -20^\circ$ and -30° , the traction ratio, $q_0/p_0 = 0.1$ and crack face friction, $\mu^C = 0.2$	106
4.7	Variation of the normalized Mode II crack tip driving force versus the normalized crack tip depth for dry contact, crack inclinations, $\theta = -20^\circ$ and -30° , the traction ratio, $q_0/p_0 = -0.01$ and crack face friction, $\mu^C = 0$	107
4.8	Variation of the normalized Mode II crack tip driving force versus the normalized crack tip depth for dry contact, crack inclinations, $\theta = -20^\circ$ and -30° , the traction ratio, $q_0/p_0 = -0.05$ and crack face friction, $\mu^C = 0$	108
4.9	Variation of the normalized Mode II crack tip driving force versus the normalized crack tip depth for dry contact, crack inclinations, $\theta = -20^\circ$ and -30° , the traction ratio, $q_0/p_0 = -0.1$ and crack face friction, $\mu^C = 0$	109
4.10	Variation of the normalized Mode II crack tip driving force versus the normalized crack tip depth for dry contact, crack inclinations, $\theta = -20^\circ$ and -30° , the traction ratio, $q_0/p_0 = 0.1$ and crack face friction, $\mu^C = 0.2$	110
4.11	Variation of the normalized Mode II crack tip driving force versus the normalized crack tip depth for dry contact, crack inclinations, $\theta = -20^\circ$ and -30° , the traction ratio, $q_0/p_0 = -0.05$ and crack face friction, $\mu^C = 0.2$	111
4.12	Variation of the normalized Mode II crack tip driving force versus the normalized crack tip depth for dry contact, crack inclinations, $\theta = -20^\circ$ and -30° , the traction ratio, $q_0/p_0 = -0.1$ and crack face friction, $\mu^C = 0.2$	112
4.13	Variation of the normalized, Mode I and Mode II stress intensity factor versus the normalized distance between the contact and	

	the crack mouth for lubricated contact, a relative crack length, $a/w = 0.5$, crack inclinations $\theta = -30^\circ$, the traction ratio, $q_0/p_0 = 0.1$, and crack face friction, $\mu^C = 0$	113
4.14	Variation of the normalized, Mode I and Mode II stress intensity factor versus the normalized distance between the contact and the crack mouth for lubricated contact, a relative crack length, $a/w = 0.5$, crack inclinations $\theta = -30^\circ$, the traction ratio, $q_0/p_0 = 0.1$, and crack face friction, $\mu^C = 0.2$	114
4.15	Variation of the normalized Mode II crack tip driving force versus the normalized crack tip depth for lubricated contact, crack inclinations, $\theta = -20^\circ$ and -30° , the traction ratio, $q_0/p_0 = 0.01$ and crack face friction, $\mu^C = 0$	115
4.16	Variation of the normalized Mode II crack tip driving force versus the normalized crack tip depth for lubricated contact, crack inclinations, $\theta = -20^\circ$ and -30° , the traction ratio, $q_0/p_0 = 0.05$ and crack face friction, $\mu^C = 0$	116
4.17	Variation of the normalized Mode II crack tip driving force versus the normalized crack tip depth for lubricated contact, crack inclinations, $\theta = -20^\circ$ and -30° , the traction ratio, $q_0/p_0 = 0.1$ and crack face friction, $\mu^C = 0$	117
4.18	Variation of the normalized Mode II crack tip driving force versus the normalized crack tip depth for lubricated contact, crack inclinations, $\theta = -20^\circ$ and -30° , the traction ratio, $q_0/p_0 = 0.01$ and crack face friction, $\mu^C = 0.2$	118
4.19	Variation of the normalized Mode II crack tip driving force versus the normalized crack tip depth for lubricated contact, crack inclinations, $\theta = -20^\circ$ and -30° , the traction ratio, $q_0/p_0 = 0.05$ and crack face friction, $\mu^C = 0.2$	119
4.20	Variation of the normalized Mode II crack tip driving force versus the normalized crack tip depth for lubricated contact, crack inclinations, $\theta = -20^\circ$ and -30° , the traction ratio, $q_0/p_0 = 0.1$ and crack face friction, $\mu^C = 0.2$	120

4.21	Variation of the normalized Mode I crack tip driving force versus the normalized crack tip depth for lubricated contact, crack inclinations, $\theta = -20^\circ$ and -30° . The Mode I values are independent of the traction ratio and the crack face friction.....	121
4.22	Variation of the normalized, Mode I and Mode II stress intensity factor versus the normalized distance between the contact and the crack mouth for lubricated contact, a relative crack length, $a/w = 0.5$, crack inclinations $\theta = -20^\circ$, the traction ratio, $q_0/p_0 = -0.1$, and crack face friction, $\mu^C = 0$	122
4.23	Variation of the normalized, Mode I and Mode II stress intensity factor versus the normalized distance between the contact and the crack mouth for lubricated contact, a relative crack length, $a/w = 0.5$, crack inclinations $\theta = -30^\circ$, the traction ratio, $q_0/p_0 = -0.1$, and crack face friction, $\mu^C = 0.2$	123
4.24	Variation of the normalized, Mode I and Mode II stress intensity factor versus the normalized distance between the contact and the crack mouth for lubricated contact, a relative crack length, $a/w = 0.5$, crack inclinations $\theta = -30^\circ$, the traction ratio, $q_0/p_0 = -0.1$, and crack face friction, $\mu^C = 0$	124
4.25	Variation of the normalized, Mode I and Mode II stress intensity factor versus the normalized distance between the contact and the crack mouth for lubricated contact, a relative crack length, $a/w = 0.5$, crack inclinations $\theta = -30^\circ$, the traction ratio, $q_0/p_0 = -0.1$, and crack face friction, $\mu^C = 0.2$	125
4.26	Variation of the normalized Mode II crack tip driving force versus the normalized crack tip depth for lubricated contact, crack inclinations, $\theta = -20^\circ$ and -30° , the traction ratio, $q_0/p_0 = -0.01$ and crack face friction, $\mu^C = 0$	126
4.27	Variation of the normalized Mode II crack tip driving force versus the normalized crack tip	

	depth for lubricated contact, crack inclina- tions, $\theta = -20^\circ$ and -30° , the traction ratio, $q_0/p_0 = -0.05$ and crack face friction, $\mu^C =$ 0.....127
4.28	Variation of the normalized Mode II crack tip driving force versus the normalized crack tip depth for lubricated contact, crack inclina- tions, $\theta = -20^\circ$ and -30° , the traction ratio, $q_0/p_0 = -0.1$ and crack face friction, $\mu^C = 0$128
4.29	Variation of the normalized Mode II crack tip driving force versus the normalized crack tip depth for lubricated contact, crack inclina- tions, $\theta = -20^\circ$ and -30° , the traction ratio, $q_0/p_0 = -0.01$ and crack face friction, $\mu^C =$ 0.2.....129
4.30	Variation of the normalized Mode II crack tip driving force versus the normalized crack tip depth for lubricated contact, crack inclina- tions, $\theta = -20^\circ$ and -30° , the traction ratio, $q_0/p_0 = -0.05$ and crack face friction, $\mu^C =$ 0.2.....130
4.31	Variation of the normalized Mode II crack tip driving force versus the normalized crack tip depth for lubricated contact, crack inclina- tions, $\theta = -20^\circ$ and -30° , the traction ratio, $q_0/p_0 = -0.1$ and crack face friction, $\mu^C =$ 0.2.....131
4.32	Normalized, Mode I and Mode II stress intensity factor ranges reported by different investigators for different sources of the cyclic crack growth driving force and for different relative crack lengths. Details can be found in Table 4.1. The following abbreviations are used: 2D - 2-dimensional, 3D - 3-dimensional, D - dry, L - lubricated, C - centrifugal stress and T - thermal stress.....134
4.33	Curves describing the conditions at the threshold for cyclic crack growth for either a Hertzian contact pressure, $p_0 = 2.4$ GPa and a $\Delta K_{THRESH} = 2$ MPa or $p_0 = 3.6$ GPa and a $\Delta K_{THRESH} = 3$ MPa. These are overlayed on data points representing the normalized, Mode I and Mode II stress intensity factor ranges reported for different sources of the cyclic crack growth driving force in 4.32. The

	coincidence defines the conditions for the onset of crack growth in each case. The following abbreviations are used: 2D - 2-dimensional, 3D - 3-dimensional, D - dry, L-lubricated, C - centrifugal stress and T - thermal stress.....	135
4.34	Curves describing the conditions at the threshold for cyclic crack growth for a Hertzian contact pressure, $p_0 = 2.4$ GPa and a $\Delta K_{THRESH} = 5$ MPa. These are overlaid on data points representing the normalized, Mode I and Mode II stress intensity factor ranges reported for different sources of the cyclic crack growth driving force in Figure 4.32. The coincidence defines the conditions for the onset of crack growth in each case. The following abbreviations are used: 2D - 2-dimensional, 3D - 3-dimensional, D - dry, L-lubricated, C - centrifugal stress and T - thermal stress.....	136
5.1	Test specimen design according to Glover (1982), all the dimensions are in inches.....	139
5.2	Surface roughness of 440C RCF test sample. (a) Shows the profilometer trace, with a peak-to-valley value of $56.75 \mu\text{in}$, (b) shows an analysis of the profile (notice the surface finish of $6.5 \mu\text{in}$), and (c) the roundness analysis indicates a good value, i.e. $50\text{-}60 \mu\text{in}$	142
5.3.a	Surface roughness analysis of a 52100 RCF ball. The ball has been grit (sand) blasted to a surface finish of $4.18 \mu\text{in}$, for a peak-to-valley of $97.63 \mu\text{in}$	143
5.3.b	Surface roughness analysis of a 52100 RCF ball. The ball has been lapped to a surface finish of $0.34 \mu\text{in}$, for a peak-to-valley of $6.34 \mu\text{in}$	144
5.4	Weibull plot for the RCF test results presented in Tables 5.3 and 5.4, peak pressure, $p_0 = 5.4$ GPa. Case 1 (circles) represents the statistical analysis of the results of the Test Series 1 and 4 from Tables 5.2. Case 2 (triangles) gives the results of the study of the influence of retained austenite on the fatigue life, i.e. Test Series 3 from Table 5.2.....	147

5.5	Weibull plot for the RCF test results presented in Tables 5.6.a (circles) and 5.6.b (triangles), peak pressure, $p_0=3.3$ GPa. The upper and lower 75% confidence limits are indicated in the figure.....	151
5.6	Weibull plot for the RCF test results presented in Tables 5.8.a (circles) and 5.8.b (triangles), peak pressure, $p_0=4.0$ GPa. The upper and lower 75% confidence limits are indicated in the figure.....	154
5.7.a	Weibull plot for the RCF test results presented in Tables 5.10.a (circle) and 5.10.b (triangles), peak pressure, $p_0=5.45$ GPa. The upper and lower 75% confidence limits are indicated in the figure.....	157
5.7.b	Weibull plot for the RCF test results presented in Tables 5.11 (circle) and 5.12 (triangles), peak pressure, $p_0=5.41$ GPa. The upper and lower 75% confidence limits are indicated in the figure.....	160
5.8	Spall and gold coated replica of a spall in sample A7, track L5. Viewed at 300X in both cases.....	161
5.9	Traces of the spall's surface obtained with the Dektak Surface Profilometer. The scales are indicated in the figure, as well as the relative position of the traces in the spall.....	162
5.10	3-Dimensional digitized view of spall A7-L5 created under a pressure of $p_0=5.45$ GPa. The digitized 3-dimensional view results from the traces obtained with a surface profilometer on the surface of the plastic replica. The rolling direction is indicated in the figure. The projection on a plane perpendicular to the radial direction shows the height iso-contours in the spall.....	164
5.11	Schematic representation of a spall indicating the nomenclature used in Table 5.13, angles are measured with respect to the surface of the sample.....	166
5.12.a	Radial view of spall A1-L1 at 50X, and 80X view of a circumferential cut of the same spall. This sample was tested at a peak	

pressure of $p_0=5.45$ GPa. The position where the cut was made is indicated on the top view of the spall. The rolling direction is also indicated, i.e. R.D. A micropit can be observed at the tip of the V-shaped spall. Rough balls were used for this test.....167

- 5.12.b Radial view of spall A1-L2 at 50X, and 80X view of a circumferential cut of the same spall. This sample was tested at a peak pressure of $p_0=5.45$ GPa. A $120\text{ }\mu\text{m}$ hardness impression can be observed near the tip of the spall. The position where the cut was made is indicated on the top view of the spall. The rolling direction is also indicated, i.e. R.D. Rough balls were used for this test.....168
- 5.12.c Radial view of spall A3-L1 at 50X, and 80X view of a circumferential cut of the same spall. This sample was tested at a peak pressure of $p_0=5.45$ GPa. A $120\text{ }\mu\text{m}$ hardness impression can be observed near the tip of the spall. The position where the cut was made is indicated on the top view of the spall. The rolling direction is also indicated, i.e. R.D. Rough balls were used for this test.....169
- 5.12.d Radial view of spall A7-L7 at 50X, and 80X view of a circumferential cut of the same spall. This sample was tested at a peak pressure of $p_0=5.45$ GPa. The position where the cut was made is indicated on the top view of the spall. The rolling direction is also indicated, i.e. R.D. Rough balls were used used for this test.....170
- 5.13.a Radial view of spall A3-L3 at 50X, the axial cut is shown at 80X. This experiment was run under a peak pressure of $p_0=5.45$ GPa, with rough balls. The position where the cut was made is indicated on the top view of the spall. The rolling direction is also indicated, i.e. R.D. A micro pit can be seen near the tip of the spall.....172
- 5.13.b Radial view of spall A7-L5 at 50X, the axial cut is shown at 80X. This experiment was run under a peak pressure of $p_0=5.45$ GPa, with rough balls. The position where the cut was

- made is indicated on the top view of the spall. The rolling direction is also indicated, i.e. R.D.....173
- 5.13.c Radial view of spall A7-L4 at 50X, the axial cut is shown at 80X. This experiment was run under a peak pressure of $p_0=5.45$ GPa, with rough balls. The position where the cut was made is indicated on the top view of the spall. The rolling direction is also indicated, i.e. R.D.....174
- 5.13.d Radial view of spall A7-L8 at 50X, the axial cut is shown at 80X. This experiment was run under a peak pressure of $p_0=5.45$ GPa, with rough balls. The position where the cut was made is indicated on the top view of the spall. The rolling direction is also indicated, i.e. R.D.....175
- 5.14 Fatigue lives versus contact stress level for 440C RCF test samples. Note: these are the nucleation and growth lives for unindented samples. The lives for dented samples are approximately equal to the growth part because nucleation is very short. The keys for the figure are indicated in the graph.....176
- 5.15 Cyclic lives and shakedown pressures for near-surface (C,D) and subsurface rolling contact failures (A,B) in steel 52100 after Lorosch (1987). Results labeled (C) are for 100 μm surface indents.....177
- 5.16.a Examples of early stages of spall formation near the hardness indent. The photomicrograph was taken after 4 hours of run time (approx. 2.1 million stress cycles). The rolling direction is indicated, i.e. R.D. The boxed region shown in (a) is magnified further in (b)...178
- 5.16.b The location shown in Figure 5.16a is shown here after 6 hours run time (approx. 3.1 million stress cycles). The rolling direction is indicated, i.e. R.D. The boxed region shown in (a) is magnified further in (b).....179
- 5.16.c Fully formed spall near the location shown in the previous two figures, after 10.3 hours (approx. 5.3 million stress cycles). The rolling direction is indicated, i.e. R.D. The boxed region shown in (a) is magnified

	further in (b).....	180
5.17	Effects of a small, 120 μm dent (A) in the raceway of a bearing steel RCF sample subjected to rolling contact at $p_o/k=8.9$. The rolling direction is also indicated, i.e. R.D. (a) dent [A] before test, (b) crack nucleus [B] is visible on surface after $N = 0.62 \times 10^6$ contacts, (c) $N = 1.3 \times 10^6$ contacts, and (d) spall [C] forms after $N = 1.5 \times 10^6$ contacts.....	182
5.18	Backscattered electron image of the specimen running surface (A6-L2), after (a) 0.26×10^6 cycles, (b) 2.73×10^6 cycles, and (c) lower magnification secondary electron micrograph of the spall formed after 2.73×10^6 cycles. The boxed area shown in (c) is the location chosen for the micrograph in (a) and (b). The rolling direction is indicated, i.e. R.D.....	183
5.19	Micrograph of the running surface of the 52100 RCF test balls showing two nearby microspalls linked together.....	184
6.1	Resistance curves for different bearing steels, after Bamberger et al. (1982). Additional information is presented in Table 6.1.....	193
6.2	Fatigue Life (number of stress cycles to failure) versus the Contact Stress (peak Hertzian pressure) for bearing steel 440C. The figure indicates the experimentally obtained growth lives obtained for tests run with rough and smooth balls. The band represents the upper and lower limits for the total number of cycles calculated using the results from Section 4.4, and the data from Figure 6.1 and Table 6.1.....	195
A.1.1	A concentrated vertical force, P, and a tangential force, T, acting on the surface of a half space.....	214
A.2.1	The thermal load, $q(x)$, translating across the surface of the half-space at a velocity, V.....	220
A.2.2	A concentrated vertical force, P_V , acting on the surface of a half-plane.....	223

A.2.3	A concentrated horizontal force, P_H , acting on the surface of a half-plane.....	227
A.3.1	Axial stress (σ_x) contours when the load is in the center of the mesh.....	232
A.3.2	Circumferential stress (σ_y) contours when the load is in the center of the mesh.....	233
A.3.3	Radial stress (σ_z) contours when the load is in the center of the mesh.....	234
A.3.4	Shear stress (σ_{xy}) contours when the load is in the center of the mesh.....	235
A.3.5	Shear stress (σ_{yz}) contours when the load is in the center of the mesh.....	236
A.3.6	Shear stress (σ_{xz}) contours when the load is in the center of the mesh.....	237
A.3.7	Axial residual stress (σ^r_x) contours.....	238
A.3.8	Circumferential residual stress (σ^r_y) contours.....	239
A.3.9	Radial residual stress (σ^r_z) contours.....	240
A.3.10	Residual shear stress (σ^r_{yz}) contours.....	241
A.3.11	Residual shear stress (σ^r_{xz}) contours.....	242
A.3.12	Axial residual plastic strain (ϵ^{pr}_x) contours.....	243
A.3.13	Circumferential residual plastic strain (ϵ^{pr}_y) contours.....	244
A.3.14	Radial residual plastic strain (ϵ^{pr}_z) contours.....	245
A.3.15	Residual shear plastic strain (γ^{pr}_{xy}) contours.....	246
A.3.15	Residual shear plastic strain (γ^{pr}_{xz}) contours....	247

LIST OF TABLES

<u>Table</u>		<u>Page</u>
2.1	Relationship Between the ELKP Loop Parameters: E , σ_k , M , and the Conventional Properties of the Loop.....	8
2.2	Near-end-of-life values of the hysteresis loop parameters for 440C steel.....	16
2.3	Near-end-of-life values of the hysteresis loop parameters for 7075-T6 Aluminum.....	18
3.2.1	Material Parameter for 3D model.....	34
3.2.2	Loading and Geometry for 3D model.....	35
3.2.3	Computational Requirements.....	37
3.2.4	Thermo-physical properties for 2D calculations plus contact loading and geometry.....	39
3.3.1	Direct residual stresses.....	61
4.1	Summary of fracture mechanics ΔK driving force calculations for surface breaking cracks subjected to rolling contact.....	132
5.1	Composition of 440C and 52100.....	141
5.2	Result of Rolling Tests.....	145
5.3	Two-Parameter Weibull Estimate for Case 1....	146
5.4	Two-Parameter Weibull Estimate for Case 2....	146
5.5.a	Rolling experiments without hardness impression ($p_0 = 3300$ MPa).....	149
5.5.b	Rolling experiments with hardness impression ($p_0 = 3300$ MPa).....	149
5.6.a	Weibull parameters for rolling test without hardness impression ($p_0 = 3300$ MPa).....	150
5.6.b	Weibull parameters for rolling test with hardness impression ($p_0 = 3300$ MPa).....	150
5.7.a	Rolling experiments without hardness	

	impression ($p_0 = 4000$ MPa).....	152
5.7.b	Rolling experiment with hardness impression ($p_0 = 4000$ MPa).....	152
5.8.a	Weibull parameters for rolling test without hardness impression ($p_0 = 4000$ MPa).....	153
5.8.b	Weibull parameters for rolling test with hardness impression ($p_0 = 4000$ MPa).....	153
5.9.a	Rolling experiment without hardness impression ($p_0 = 5450$ MPa).....	155
5.9.b	Rolling experiment with hardness impression ($p_0 = 5450$ MPa).....	155
5.10.a	Weibull parameters for rolling test without hardness impression ($p_0 = 5450$ MPa).....	156
5.10.b	Weibull parameters for rolling test with hardness impression ($p_0 = 5450$ MPa).....	156
5.11	Rolling test results without hardness impression and smooth balls ($p_0=5410$ MPa)....	159
5.12	Rolling test results with hardness impression and smooth balls ($p_0=5410$ MPa)....	159
5.13	Spalls Geometry.....	165
6.1	Heat Treatments and Fracture Toughness Data for Bearing Steels, after Bamberger et al. (1982).....	194

1. INTRODUCTION

1.1 Background

Spall failures limit the life and performance of the HPOTP bearings in the space shuttle main engines. While the general features of spalling are known, detailed quantitative analyses of the contact life in terms of contact geometry, loading and basic material properties have not been developed. As a consequence, efforts to improve life proceed by trial and error and are closely tied to uncertain and time consuming laboratory testing--uncertain because the laboratory tests do not reproduce the service conditions.

The analysis of contact life is complicated by the existence of 2 distinct failure modes that result from 2 sources of contact plasticity (Hahn and Rubin, 1990):

- Subsurface Originated Spall Failure. This is caused by the translating, Hertzian pressure pulse which produces peak amounts of cyclic plasticity and damage in an annular layer at a depth, $z \approx 0.5 w$ ($2w$ is the contact width) below the surface.

- Near-Surface Originated Spall Failure. This is produced by the cyclic plasticity and damage produced just below the running track at depths, $z \approx 1 \mu\text{m}$ to $50 \mu\text{m}$, caused by several sources: (i) stationary pressure spikes produced by surface irregularities, asperities, debris dents, etc, (ii) tractions arising from the sliding of the contact with friction, and (iii) thermal stresses from frictional heating.

The distinction is important because both the nature of the cyclic deformation and damage leading to spall nucleation, and the mechanism of growth of the spall are different for the 2 modes. Both the observations of spalls in the HPOTP bearings (Bhat and Dolan, 1982) and the results of this study support the view that the failures of the 440C steel bearings are of the near-surface mode.

Work aimed at improving the performance of the HPOTP bearings can benefit from an analysis of the near-surface spall failure mode composed of the following elements:

- (i) Cyclic Plasticity. The definition of the continuing, near-surface cyclic plasticity. This is governed by the shape of the cyclic stress-strain hysteresis loop of the steel. While the 440C loop shapes were measured in a previous NASA-supported study (Kumar et al., 1987), subsequent work revealed that the analysis of the measurements requires improvement. The connections between the material microstructure and the stress-strain properties must be clarified.

(ii) Contact Mechanics. The definition of the cyclic plasticity must also draw on the mechanics of contact. This can be treated using elasto-plastic finite element methods. In the previous work (Kumar et al., 1987) the present authors have devised finite element analyses of 2-dimensional (line contact) rolling-plus-sliding, and rolling-plus-sliding with heat generation (Kulkarni et al., 1991). These methods need to be extended to the 3-dimensional contact, refined and critically tested.

(iii) Crack Nucleation. The rates with which the continuing cyclic plasticity lead to the accumulation of damage and crack nucleation must be formulated. The work to accomplish this is in its early stages (Keer et al., 1986) and can benefit from experimental determinations of the nucleation component of the contact life and the factors that influence it.

(iv) Spall Growth. The rate of spall growth must be evaluated. This is governed by the fracture mechanics driving force and the steel's Mode I, II and III, da/dN - ΔK characteristics. The cracks produced by the near-surface mode become surface breaking at an early stage of their life. As a result, the driving force is amplified by the pressure of lubricant fluid forced in the crack cavity (Bower, 1988). In the absence of lubricant, thermal stresses arising from frictional heating enhance the crack driving force (Goshima and Keer, 1990). The analysis of the growth life calls for calculations of the driving force for small surface-breaking cracks containing fluid pressure as well as measurements of relevant da/dN - K properties of the material. Finally, there is a pressing need for measurements of the spall growth component of the contact life that can be used to test the reliability of the fracture mechanics method.

1.2 Summary

This report describes the results of a 2-year follow-on to an earlier NASA-supported study on the mechanism of spall failure in the HPOTP bearings (Kumar et al., 1987). The objective was to build a foundation for detailed analyses of the contact life along the lines described above. Since much of the laboratory rolling contact testing is carried out in the 3-ball-rod contact fatigue testing machine, the analysis of the contacts and contact lives produced in this machine received attention.

The following tasks were undertaken:

(i) Cyclic Plasticity. The analysis of the previous cyclic, stress-strain hysteresis loop measurements of 440C steel was refined to account for the contribution of plasticity in the fillet regions. In addition, the stress-strain hysteresis loop shape of the hardened 7075 Al alloy was measured and the elastic-

linear-kinematic-hardening plastic- (ELKP-) loop parameters were evaluated. These studies are described in Sections 2.3 and 2.4. The results are incorporated in 3-dimensional, elastoplastic, finite element analyses of the 3-ball-rod testing machine contact conditions described in Section 3.

(ii) Elasto-Plastic Finite Element Analyses. Elastoplastic, finite element analyses of the 3-dimensional rolling produced in the Federal Mogul/Bowers/NTN, 3-ball-rod testing machine at several contact pressures were carried out using both the 440C steel and 7075 aluminum ELKP loop parameters (see Sections 3.3 and 3.4). The calculations are compared in Section 3.4 with experimental observations on aluminum rods (tested in the 3-ball-rod testing machine) that characterize the size and shape of the 3-dimensional contact cyclic plastic zone and the propensity for subsurface crack nucleation and growth. In addition, the finite element calculations were extended to 3-dimensional rolling-plus-sliding (Section 3.3) and to the 2-dimensional (line contact) thermal-mechanical coupled problem for 440C steel, ELKP loop properties (Section 3.5).

(iii) Fracture Mechanics Analyses of Surface Breaking Cracks. Contributions to the crack growth driving force from the Hertzian stresses, surface irregularities, fluid in the crack cavity, centrifugal stresses and thermal stress are reviewed and the results of different 2-dimensional and 3-dimensional analyses compiled and compared in Section 4.4. New calculations for the Bower model of a 2-dimensional surface breaking crack with fluid in the crack cavity were carried out and are presented in Section 4.3. The implications of the driving force values with respect to the threshold crack size were examined (Section 4.5).

(iv) Retained Austenite. Efforts were made to evaluate the effects of retained austenite in 440 C steel on the contact life and these are described in Section 5.3.

(v) Measurements of the Nucleation and Growth Lives. The separate contributions of nucleation and growth components of the contact lives of 440C steel rods tested in the 3-ball-rod testing machine were measured. These experiments also reveal effects of surface roughness and a threshold crack size for spall growth. This is presented in Sections 5.4 and 5.5.

(vi) Characterization of the 3-Dimensional Spall. A novel replication technique was developed to find the three dimensional features of the spalls, this technique is reported in Section 5.6. This section also reports the results of metallographic investigation of the main geometric features of the spall.

(vii) Evaluation of the Fracture Mechanics Driving Force for Spall Growth. Calculations were performed to determine the

Mode II crack driving force under different conditions, as reported in Section 4.3. These results were compared with other works which accounted for thermal loading and three dimensional effects, and are reported in Section 4.4. The critical, i.e. threshold, crack sizes were evaluated in light of the above mentioned results in Section 4.5.

(viii) Analysis of the growth life. An attempt is made to compare the experimentally observed lives with those predicted based upon the results drawn in (vii). The conclusions are reported in Section 4.6.

2. CYCLIC STRESS-STRAIN PROPERTIES

2.1 Background

The continuing cyclic plasticity, which accompanies rolling contact when the Hertzian contact pressure exceeds the shakedown limit, damages the material and may ultimately lead to spall nucleation (Hahn and Rubin, 1990). The plasticity may also assist the process of cyclic crack growth (Bastias, 1990). Both the value of the shakedown pressure and the amounts and distribution of cyclic plasticity that occurs above shakedown depend on the material's resistance to plasticity (Merwin and Johnson, 1963, Bhargava et al., 1985, 1990, Hahn et al., 1987, Hahn and Rubin 1990). For the case of repeated contacts which produce essentially fully reversed cyclic plasticity, the resistance is given by the shape of the stress-strain hysteresis loop (Hahn et al., 1990). The constitutive relations that describe the loop shape must be incorporated into the finite element models of contact described in Section 3.

In the past, it has been common practice to treat the cyclic plasticity as isotropic and elastic-perfectly-plastic (EPP). The loop produced by this highly idealized behavior, shown schematically in Figure 2.1a, can be described by 2 parameters: the elastic modulus, E , and the shear yield strength, k . Figure 2.1b illustrates that the loop shapes of 440C steel and other bearing steels are not approximated by EPP-behavior. The real loops display rapid strain hardening and kinematic behavior (Hahn et al., 1990). To improve the analyses, the authors have devised a bilinear, 3-parameter elastic-linear-kinematic-hardening-plastic (ELKP) representation of the loop illustrated in Figure 2.2a (Hahn et al., 1987, Hahn et al., 1990). The loop parameters: the elastic modulus, G , the kinematic shear yield strength, k_k , and the plastic modulus, M_s , are defined in Figure 2.2a. The relations between these parameters and the conventional parameters defined in Figure 2.2a, including the stress amplitude, σ_a , and the energy dissipated (loop area), U' , are given in Table 2.1.

In an earlier report (Kumar et al., 1987) the authors described the results of cyclic torsion tests performed on hardened 440C steel which were used to evaluate the ELKP parameters. These analyses assumed that the contribution of the fillet region could be neglected. Subsequent work showed this to be a poor approximation and a method for accounting for the plasticity of the fillet was devised (Hahn et al., 1990). This method has been employed here to analyze the measurements reported earlier so as to provide more reliable values of the parameters for 440C steel.

In addition, cyclic torsion tests were performed on hardened 7075 aluminum, to establish the ELKP-parameters for finite

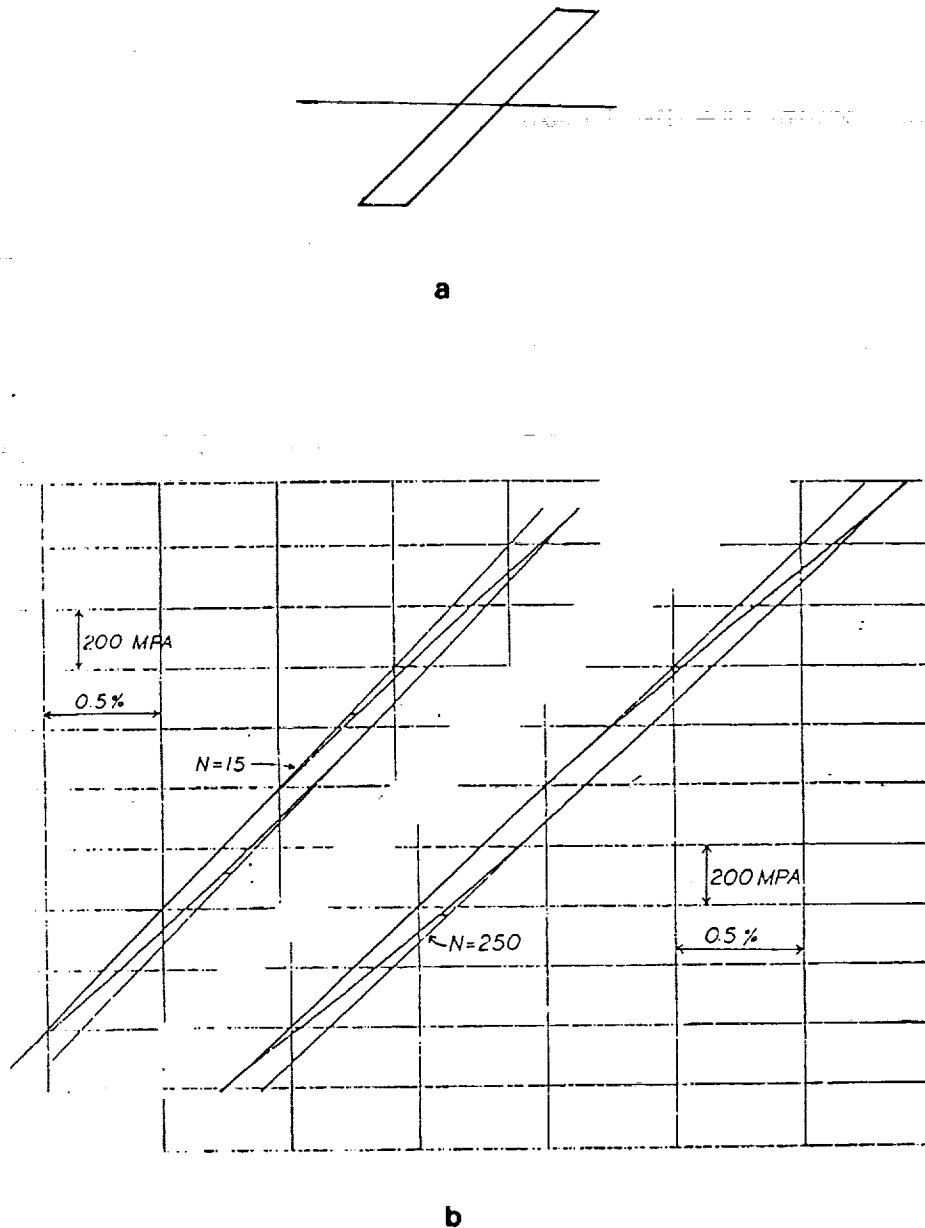


Figure 2.1

Shear stress-shear strain hysteresis loops: (a) the loop for idealized, isotropic, elastic-perfectly-plastic (EPP) behavior, and (b) the loops displayed by 440C steel after $N=15$ and $N=250$ stress cycles. While the EPP-loop is drawn so that its 0.035%-offset, shear yield strength corresponds with that of the $N=15$ loop of the 440C steel, it is clear that the EPP loop does not come close to representing the cyclic stress-strain behavior of the steel.

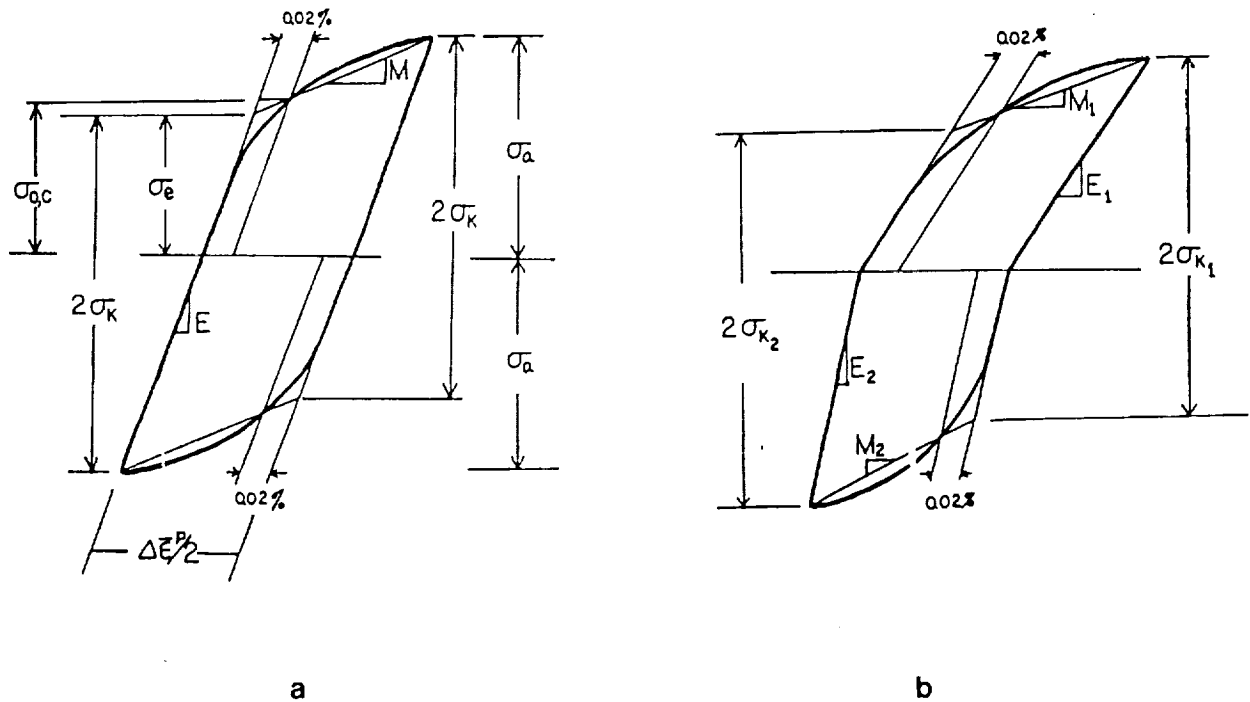


Figure 2.2

Schematic of the bilinear, 3-parameter, elastic-linear-kinematic-hardening-plastic (ELKP) representation of the hysteresis loop: (a) conventional form employed for 440C steel and (b) special form employed for 7075-T6 aluminum to accommodate the differences in the elastic modulus in tension and compression. The 3 ELKP-parameters are: (for tension-compression) the elastic modulus, E , the kinematic yield strength, σ_K , and the plastic modulus (G , k_K , and M_S for torsion). The relations between these parameters and more conventional parameters are given in Table 2.1.

Table 2.1 Relationship Between the ELKP Loop Parameters:
E, σ_k , M, and the Conventional Properties of the
Loop.

$$\sigma_e = \sigma_k - [E M / (E - M)] \Delta\epsilon^P/2 \pm \sigma_m$$

$$\sigma_{O,C}(0.02\%) = \sigma_k - [E M / (E - M)] (\Delta\epsilon^P/2 - 0.0002) \pm \sigma_m$$

$$\sigma_a = \sigma_k + [E M / (E - M)] \Delta\epsilon^P/2$$

$$U' = 2 \sigma_k \epsilon^P$$

E	-	Young's Modulus
M	-	Kinematic Hardening Modulus
σ_k	-	Kinematic yield strength
σ_e	-	Cyclic elastic limit (measured from zero stress)
$\sigma_{OC}(0.02\%)$	-	Cyclic, 0.02% offset yield strength (measured from zero stress)
σ_a	-	Stress amplitude
σ_m	-	Mean stress
$\Delta\epsilon^P/2$	-	Plastic strain amplitude
U'	-	Per cycle plastic work or loop area

element analyses of rolling contact for this material for reasons mentioned in Sections 3.4.

2.2 Experimental Procedures

The Cyclic torsion tests were carried out on hollow cylindrical 440C using the procedures described in a previous report (Kumar et al., 1987). The cyclic torsion tests were plastic strain amplitude controlled. The torque-rotation loop was recorded, converted into a shear stress-shear strain hysteresis loop, the ELKP-parameters: the kinematic shear yield strength, k_k , the plastic modulus, M_s , described, and the equivalent tensile values, σ_k and M , were evaluated (Hahn et al., 1990). Unlike the analysis employed in the previous report (Kumar et al., 1987) the procedure accounted for the plastic contribution of the filler regions, which is significant (Hahn et al., 1990).

The studies performed on the hardened 7075-T6¹ aluminum alloy were carried out in uniaxial, push-pull fatigue. The test bar is illustrated in Figure 2.3. The average hardness of the as-heat treated samples was HRB-87 (HK-170). The test pieces for the 3-ball-rod testing machine, referred to in Section 3.4, were machined from the same stock and heat treated in the same way. The shapes of the cyclic stress-strain hysteresis loops obtained under conditions of constant strain amplitude were measured at room temperature at a frequency of $f=0.75$ Hz with a servohydraulic testing machine by manually adjusting the stress amplitude. The axial strain was measured with an extensometer attached to the gage section and the hysteresis loops were periodically recorded and analyzed with a high speed data acquisition system programmed to evaluate the ELKP-parameters, σ_k and M . The details of the procedure are similar to the one used to analyze the axial torsion tests mentioned above (Hahn et al., 1990).

In the case of the 7075-T6 aluminum, the slope of the elastic portions of the loop on the tensile side, $E = 68.6$ GPa, is significantly lower than the slope on the compression side of the loop, $E = 71.5$ GPa, as shown schematically in Figure 2.2b. These values do not change with number of stress cycles. When the difference in the values of the slopes was recognized and accounted for, as in Figure 2.2b, the values of σ_k and M for the tensile and compressive portions of the cycle were in close agreement. To simplify the treatment of the constitutive relation, the averages of the values of E , σ_k and M obtained from the tensile and compression part of the cycle are quoted and were inserted in the finite element analyses reported in Section

¹ Composition and heat treatment of the 7075 aluminum alloy: Zn-5.6, Mg-2.5, Cu-1.6 and Cr-0.23; the alloy was solution treated at 870°F, spray quenched in water and aged at 250°F for 24 hours.

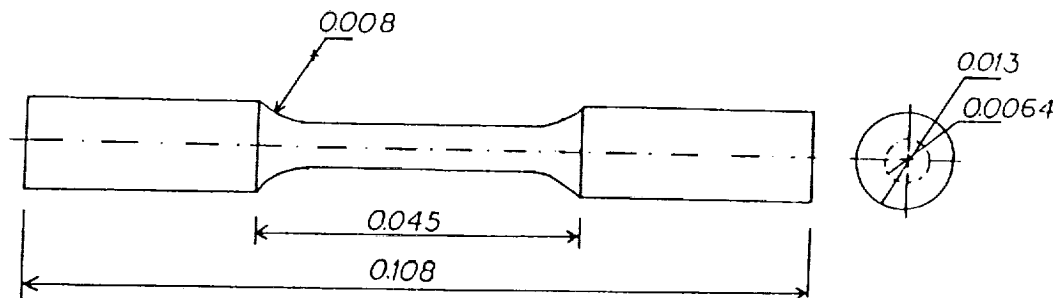


Figure 2.3 Axial fatigue test specimen used to measure 7075-T6 hysteresis loops. All dimensions are in meters.

3.4. The difference between the tension and compression modulus observed here is similar to that quoted in the ASM Metals Handbook (Vol.2, 9th Edition, 1979). The origin of the difference is not known to the authors. It is possible that a large number of the small, 5 μm diameter particles, in the alloy may rupture during the tensile portion of the first few stress cycles producing small cracks that reduce the stiffness in tension but not in compression.

2.3 Cyclic Stress-Strain Properties of 440C Steel

Results of the hysteresis loop measurements are summarized in Figures 2.1b, 2.4-2.7 and in Table 2.2. Examples of the hysteresis loops displayed by 440C steel samples are reproduced in Figure 2.1b. The 0.035% shear strain offset (equivalent to an 0.02% tensile strain offset) is marked by the short horizontal tick in Figure 2.1b. The application of a mean stress produces a not-fully reversed loop -- more plasticity in one direction than in the other. However, the non-reversibility² diminishes with increasing number of cycles and effectively disappears after $N \sim 10^3$ cycles as shown in Figure 2.4. This is viewed as evidence that the cyclic behavior closely approaches kinematic behavior after $N \geq 10^3$ cycles. The systematic decrease of the conventional cyclic yield strength, σ_{0C} , with increasing plastic strain amplitude, and the negative value of this quantity at the largest strain amplitude, are also incompatible with isotropic behavior and consistent with kinematic behavior.

The variation of the kinematic yield strength, σ_k , with numbers of cycles is shown in Figure 2.5. All of the samples display noticeable cyclic hardening -- increases in σ_k with number of cycles -- during their relatively short lives: $300 < N < 600$, and are still hardening after $N = 600$ cycles. The near-end-of-life values³ reported in Table 2.2 represent a lower bound estimate of the kinematic yield strength appropriate for large numbers of cycles, e.g. $N = 10^6$ to 10^9 . These σ_k -values are about 15% lower than the values reported earlier which were obtained neglecting the plasticity in the fillet regions. The values of the plastic modulus, M , in Figure 2.6 show virtually no dependence on the number of cycles. These values are about 2% smaller than those reported earlier.

² Non-reversibility is defined as: $NR = 1 - \epsilon_{P_f} / \epsilon_{P_r}$, where ϵ_{P_f} is the plastic strain increment in the forward direction and ϵ_{P_r} is the increment in the reverse direction. Non-reversibility is associated with isotropic cyclic behavior and is absent for kinematic cyclic behavior. The decay of the non-reversibility is symptomatic of the approach to kinematic behavior.

³ Values for the largest number of stress cycles that appear unaffected by the nucleation and growth of a crack.

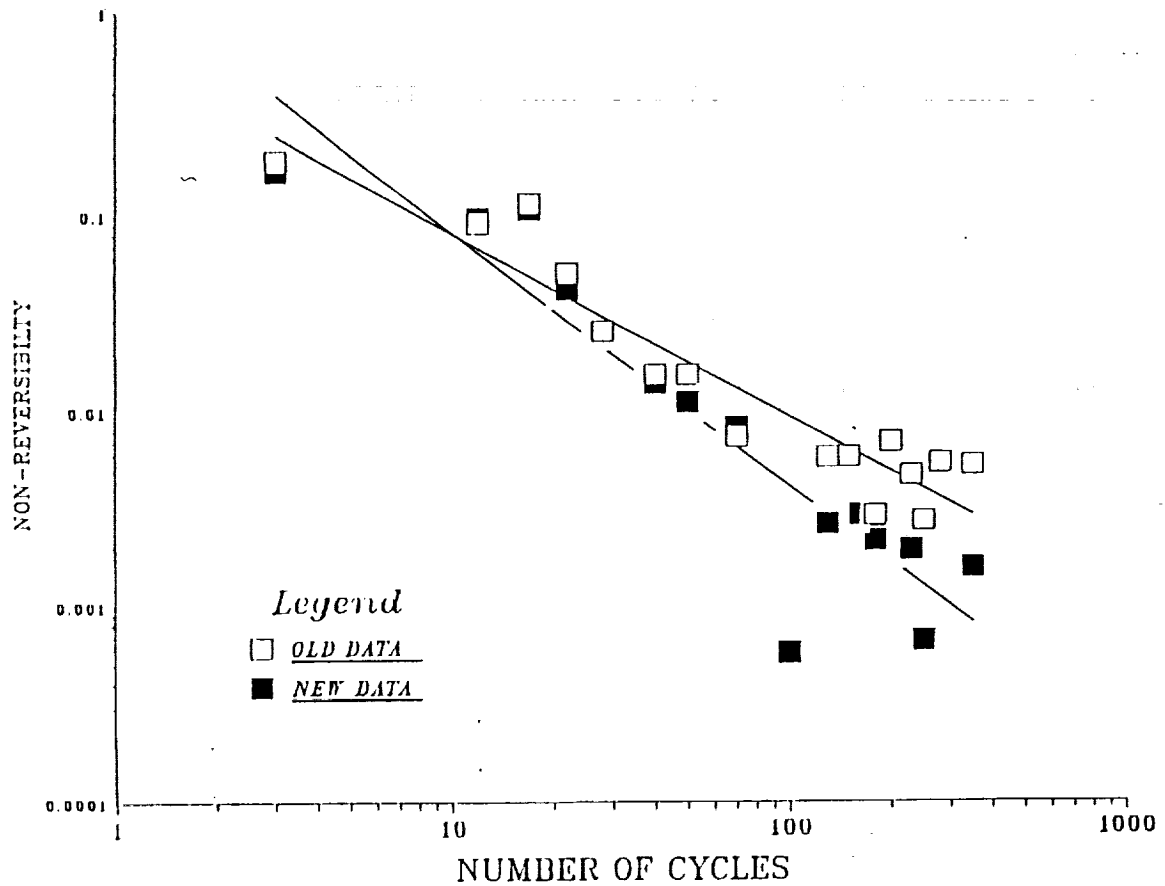


Figure 2.4

Variation of the non-reversibility of the 440C steel hysteresis loop produced by a mean shear stress, $\tau_m = 200$ MPa, with number of cycles.

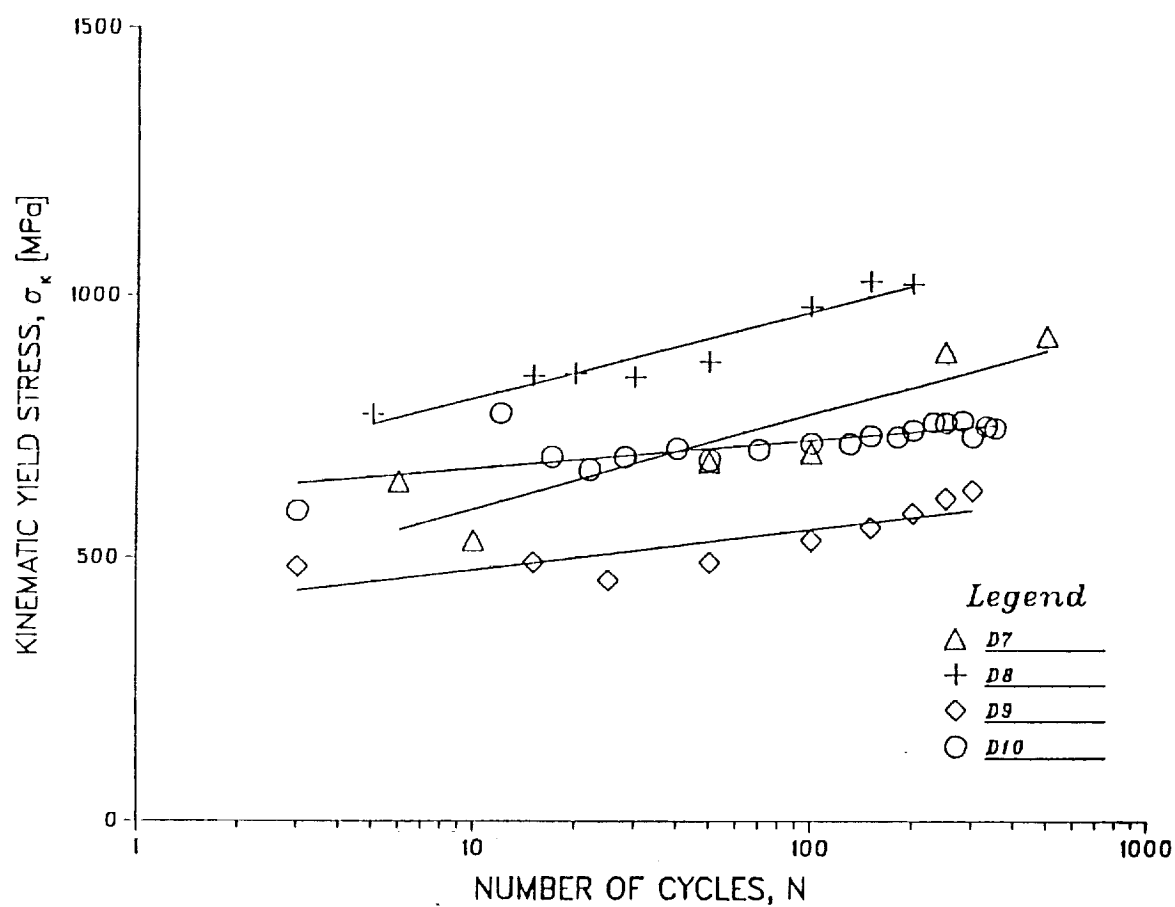


Figure 2.5

Variation of the kinematic yield strength of 440C steel with number of cycles.

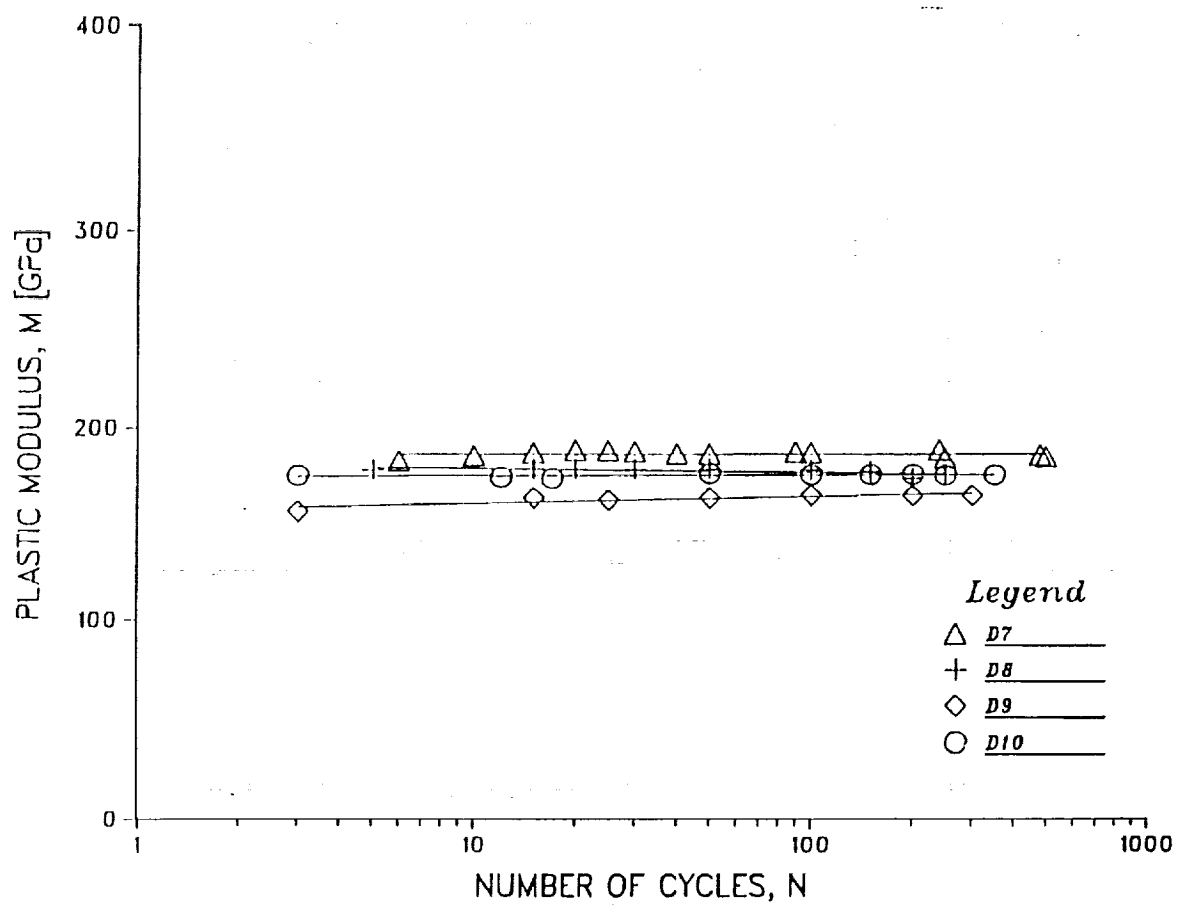


Figure 2.6 Variation of the plastic modulus of 440C steel with number of cycles.

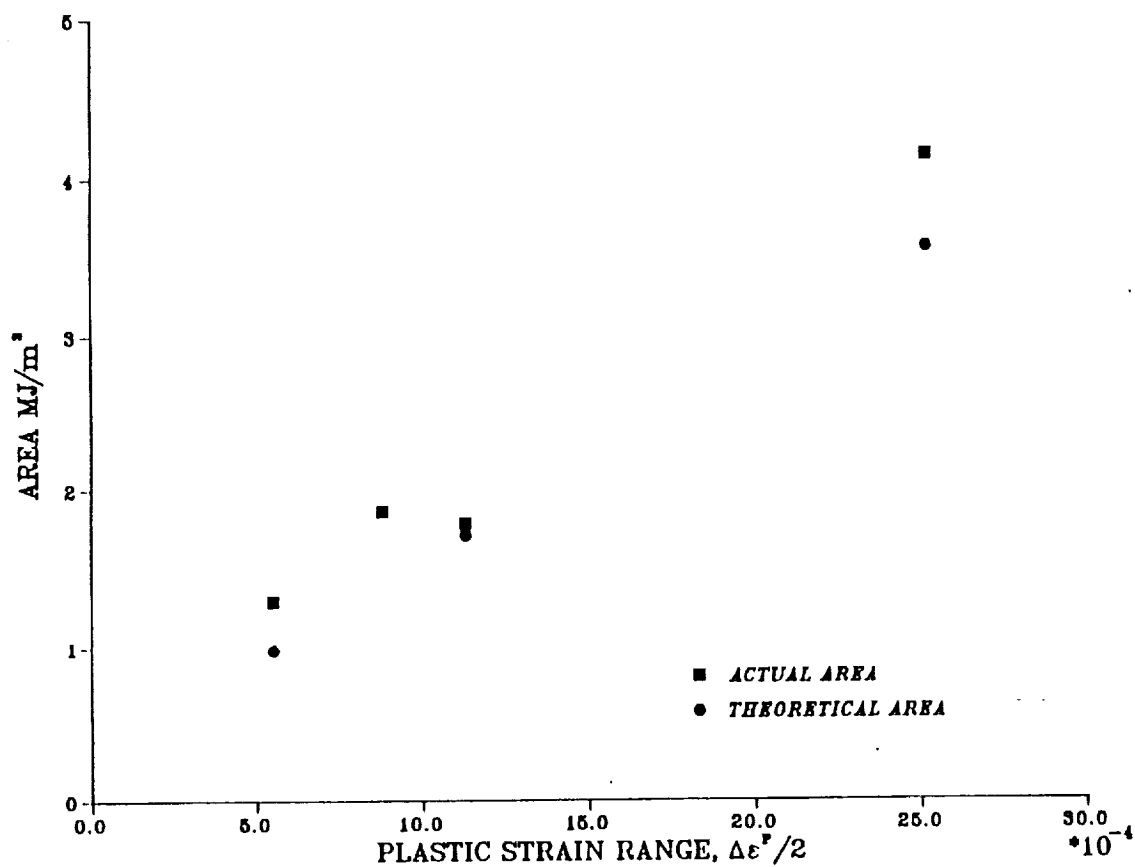


Figure 2.7

Variation of the loop area (per cycle plastic work) with the plastic strain range. The loop areas calculated from the ELKP-parameters: $U' = 2 \cdot \epsilon^p \cdot \sigma_k$, are close to the actual values.

Table 2.2 Near-end-of-life values of the hysteresis loop parameters for 440-C steel.

Specimen ID	ϵ^p	τ_m (MPa)	N_F	N	σ_k (MPa)	σ_{oc} (MPa)	σ_a (MPa)	M (GPa)
D7	0.0005	0	608	500	926.0	978.9	1671.7	193.5
D8	0.001	0	284	250	1063.7	715.5	1736.3	182.3
D9	0.002	0	305	300	719.9	-297.2	1736.9	167.7
D10	0.001	200	351	350	746.0	225.1	+923.0 -642.7	180.6
Average					864.0			181.0

ϵ^p - Plastic strain amplitude
 τ_m - Shear mean stress
 N_F - Number of cycles to failure
N - Number of cycles at near-end-of-life beyond which the loop parameters are affected by the growing crack.
 σ_k - Kinematic yield strength
 σ_{oc} - Cyclic, 0.02% offset yield strength (measured from zero stress)
 σ_a - Stress amplitude
M - Plastic modulus

The area of the hysteresis loop corresponds with the plastic work, the bulk of which is converted to heat. Figure 2.7 shows that the area of the bilinear, ELKP-loop ($U' = 2 \cdot \epsilon^P \cdot \sigma_k$) is a good approximation of the actual loop area for small strain amplitudes. The variation of the cyclic life with strain amplitude can be approximated by the relation: $N=A(\epsilon^P/2)^m$ where $A = 7.94$ and $m = -0.5$.

2.4 Cyclic Stress-Strain Properties of 7075-T6 Aluminum

Results of the hysteresis loop measurements for the hardened aluminum alloy are summarized in Figures 2.8 - 2.15 and in Table 2.3. Examples of the hysteresis loops are shown in Figure 2.9. The horizontal ticks mark the 0.02% plastic strain offset. Figure 2.9 illustrates that the loop shape changes little in the range $20 < N < 780$ stress cycles. Figure 2.10 illustrates the loop shapes produced by cycling with a mean stress $\sigma_M = -100$ MPa. Initially, the mean stress produces a non-fully reversed loop. As is the case with the 440C steel, the non-reversibility, NR, decays with increasing number of cycles. The loop is essentially fully reversed after $N = 330$ strain cycles. This, and the observations that the ELKP parameters are insensitive to mean stress (see Table 2.3) while the conventional parameters show a dependence, are consistent with kinematic behavior. Figures 2.11 and 2.12 show that none of the loop parameters, conventional and ELKP, are sensitive to strain amplitude in this case.

The kinematic yield strength, plastic modulus and stress amplitude change very little with increasing number of stress cycles as shown in Figures 2.13 - 2.15. In the absence of significant cyclic hardening, the near-end-of-life values listed in Table 2.3 appear to be useful estimates of the ELKP-parameters appropriate for large numbers of stress cycles. Figure 2.16 shows that the ELKP-parameters provide a reasonable description of the loop area.

2.5 Discussion and Conclusions

The ELKP-parameters derived from the hysteresis loops of the 440C steel are very similar to those previously found for hardened 1070 and 52100 bearing steel (Hahn et al., 1990). For this reason, the previous average values, modified slightly to account for a strain rate effect: $\sigma_k = 1050$ MPa and $M = 188$ GPa which are reasonable approximations for all three materials, have been used in the finite element calculations of rolling contact described in Section 3.

The hysteresis loop measurements performed on the 7075-T6 aluminum reveal that while the resistance of this material to cyclic plasticity is 1/3 to 1/2 of that displayed by 440C steel, the cyclic plastic behavior is kinematic, and analogous to the cyclic behavior of 440C. The use of aluminum as a model material

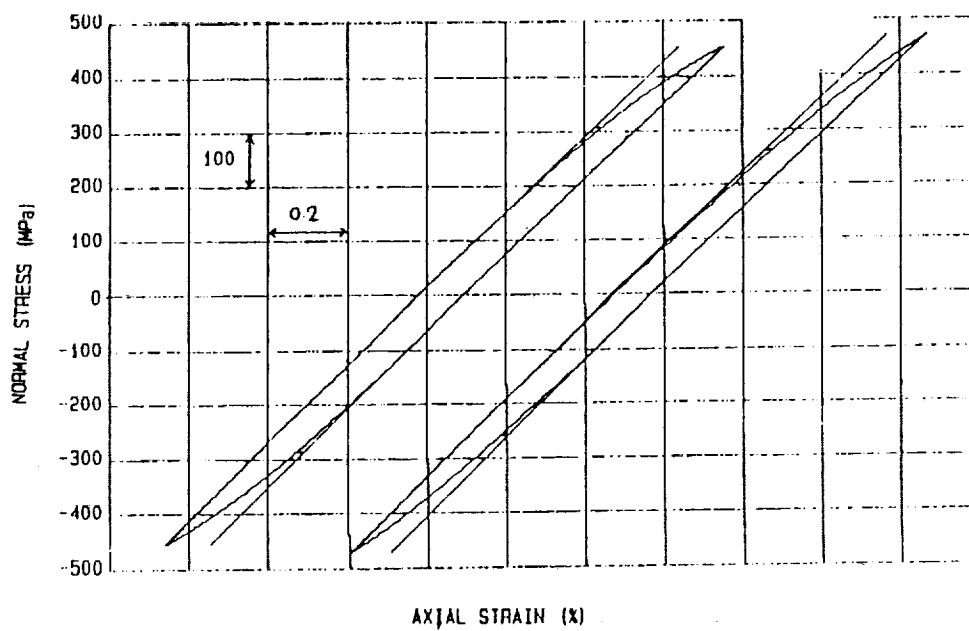


Figure 2.8

Examples of the axial stress-strain hysteresis loops displayed by 7075-T6 aluminum for constant plastic strain range, $\Delta\epsilon^P = 0.001$, by the $N = 20$ and $N = 780$ cycles .

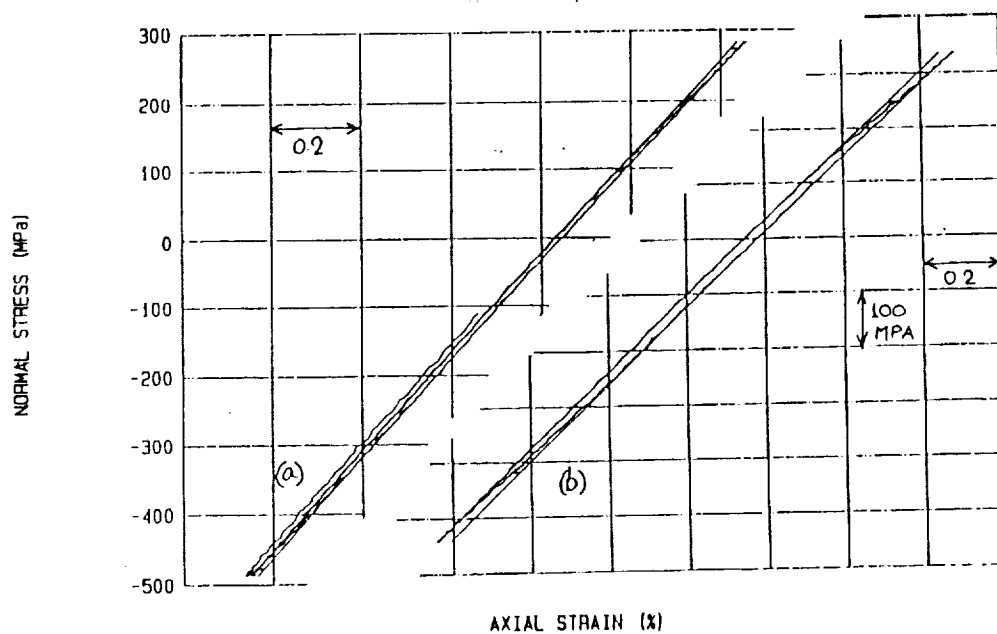


Figure 2.9

Examples of the axial stress-strain hysteresis loops displayed by 7075-T6 aluminum for constant plastic strain range cycles, $\Delta\epsilon^P = 0.0025$ and a mean stress, $\sigma_m = -100$ MPa by the $N = 30$ and $N = 330$ cycles.

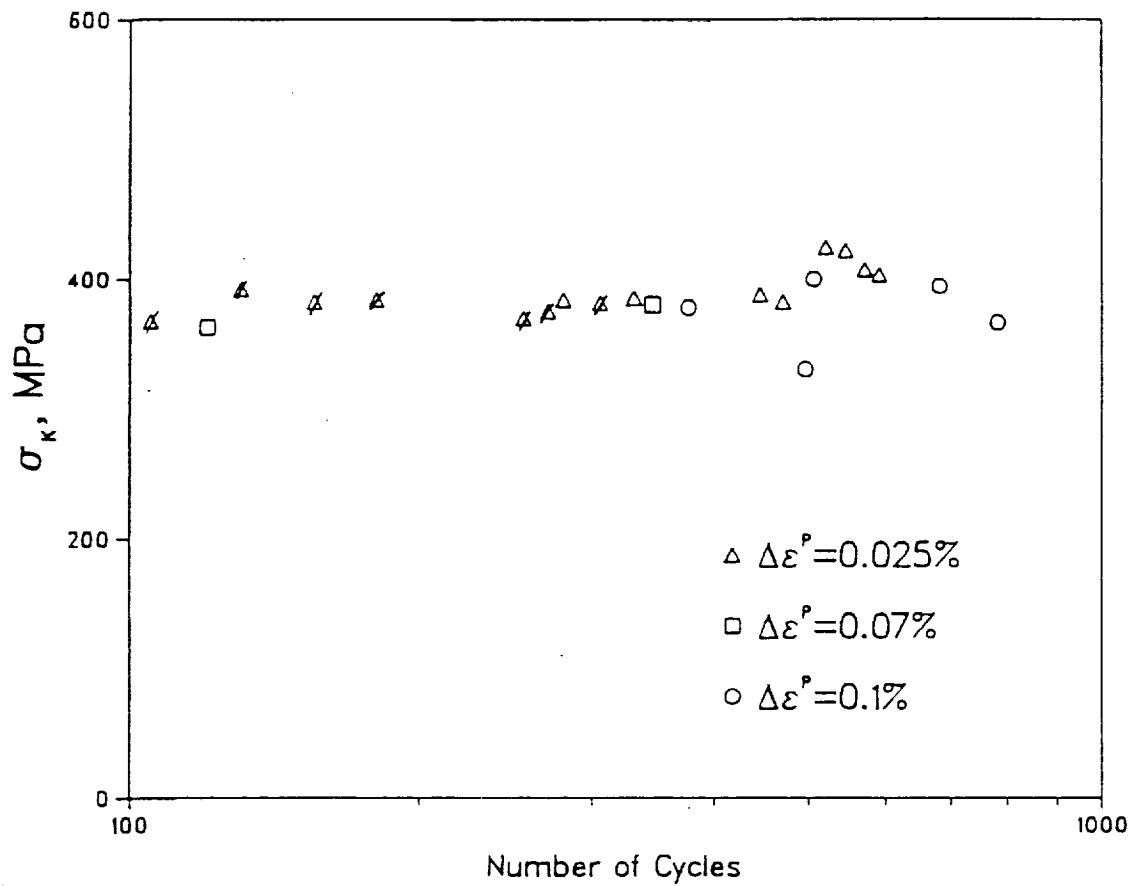


Figure 2.10

Variation of the kinematic yield strength of 7075-T6 with number of cycles for different values of the constant plastic strain range. The $\Delta \epsilon^P = 0.00025$ strain range test was carried out with a mean stress, $\sigma_m = -100$ MPa.

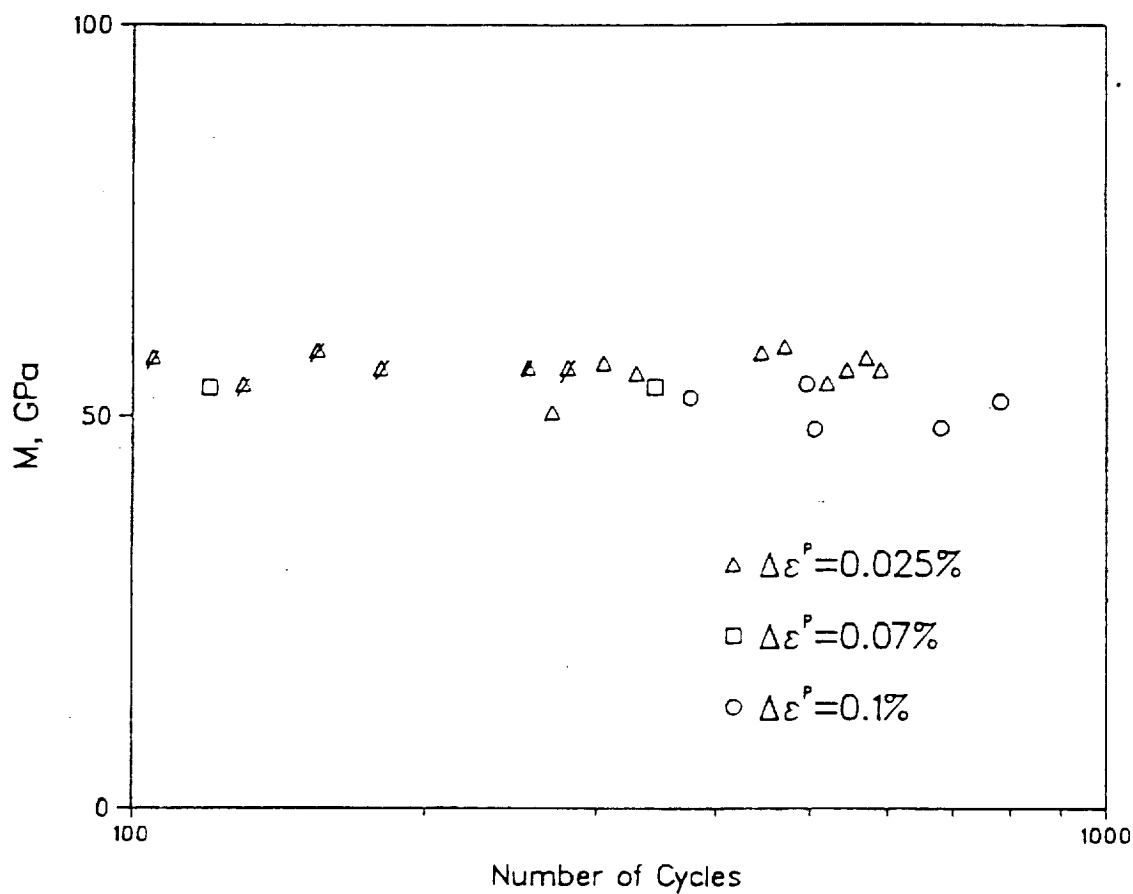


Figure 2.11

Variation of the plastic modulus of 7075-T6 with number of cycles for different values of the constant plastic strain range. The $\Delta \epsilon^P = 0.00025$ strain range test was carried out with a mean stress, $\sigma_m = -100$ MPa.

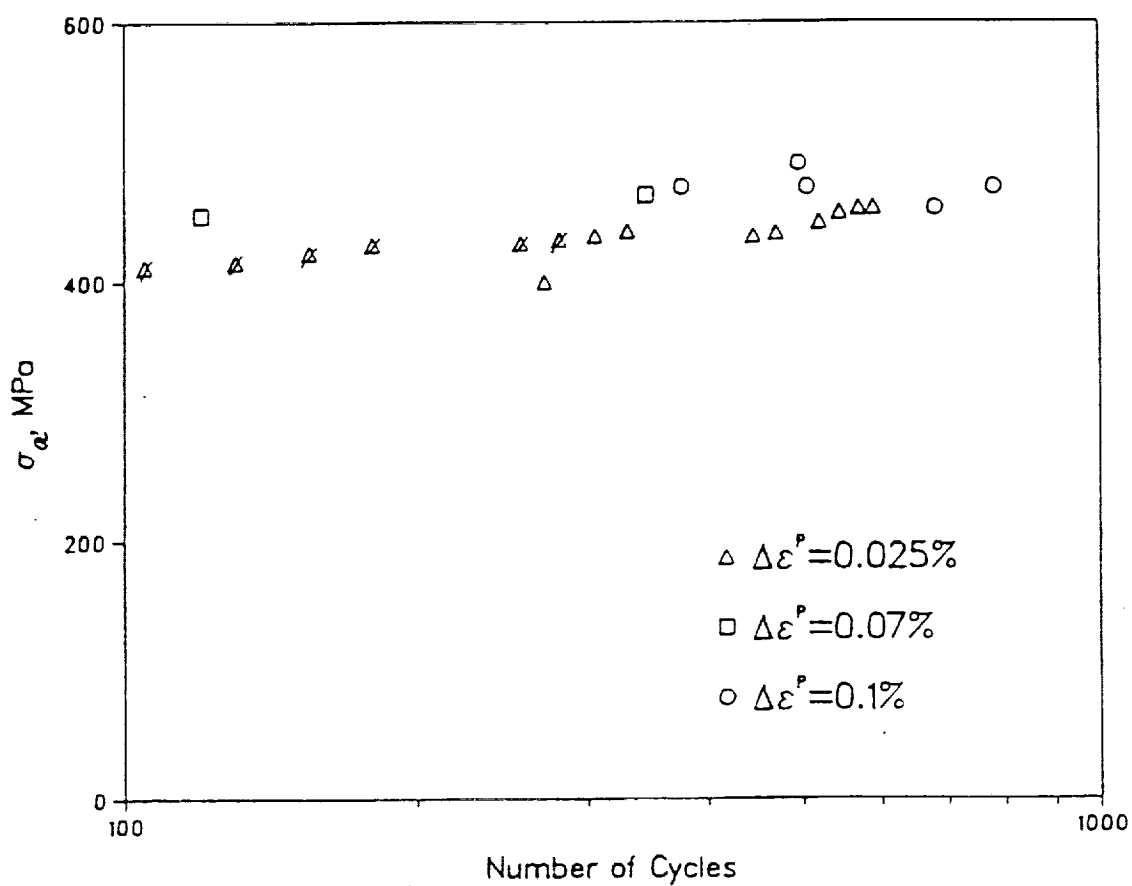


Figure 2.12 Variation of the stress amplitude of 7075-T6 with number of cycles for different values of the constant plastic strain range. The $\Delta \epsilon^P = 0.00025$ strain range test was carried out with a mean stress, $\sigma_m = -100$ MPa.

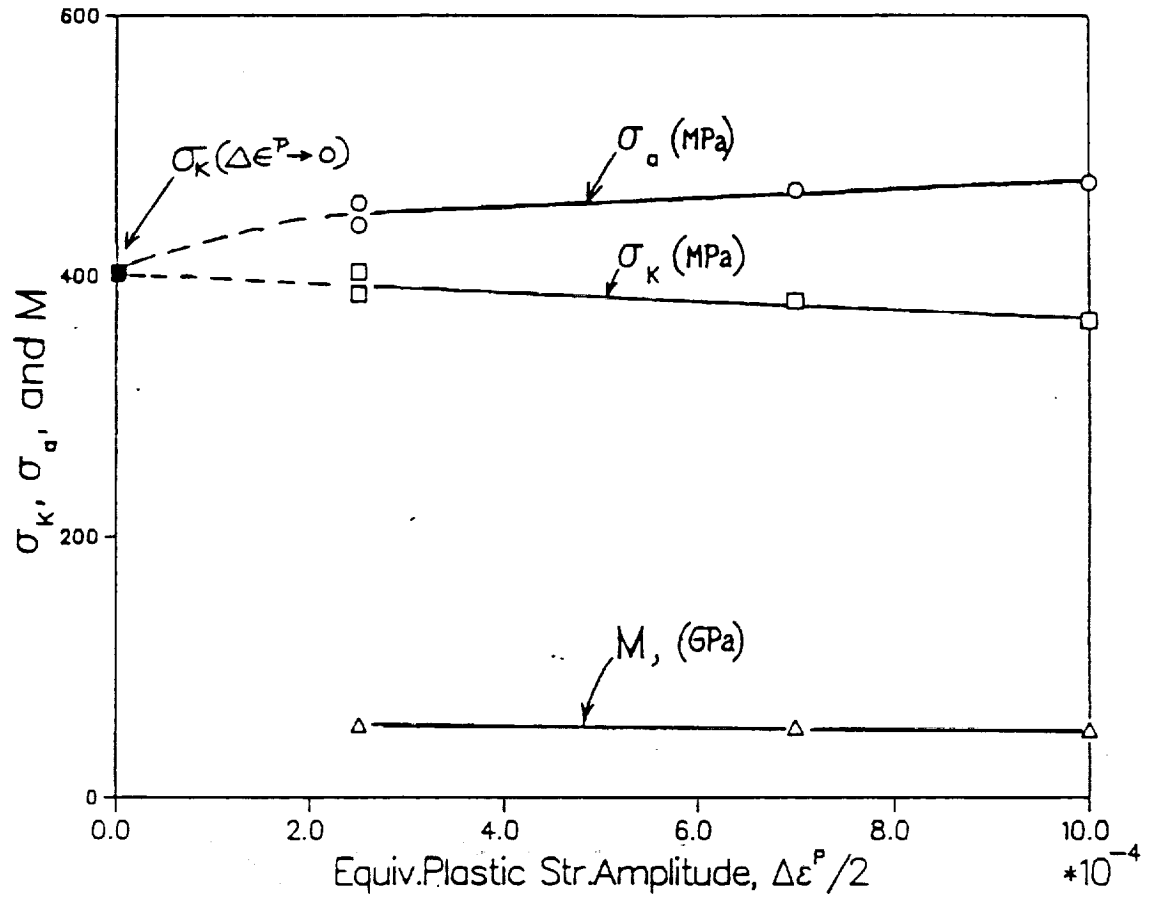


Figure 2.13

Variation of the kinematic yield strength, stress amplitude and plastic modulus of 7075-T6 with the plastic strain range. The value of σ_k for zero strain range was obtained by a linear extrapolation. Note that the half equivalent strain range corresponds with the conventional strain range.

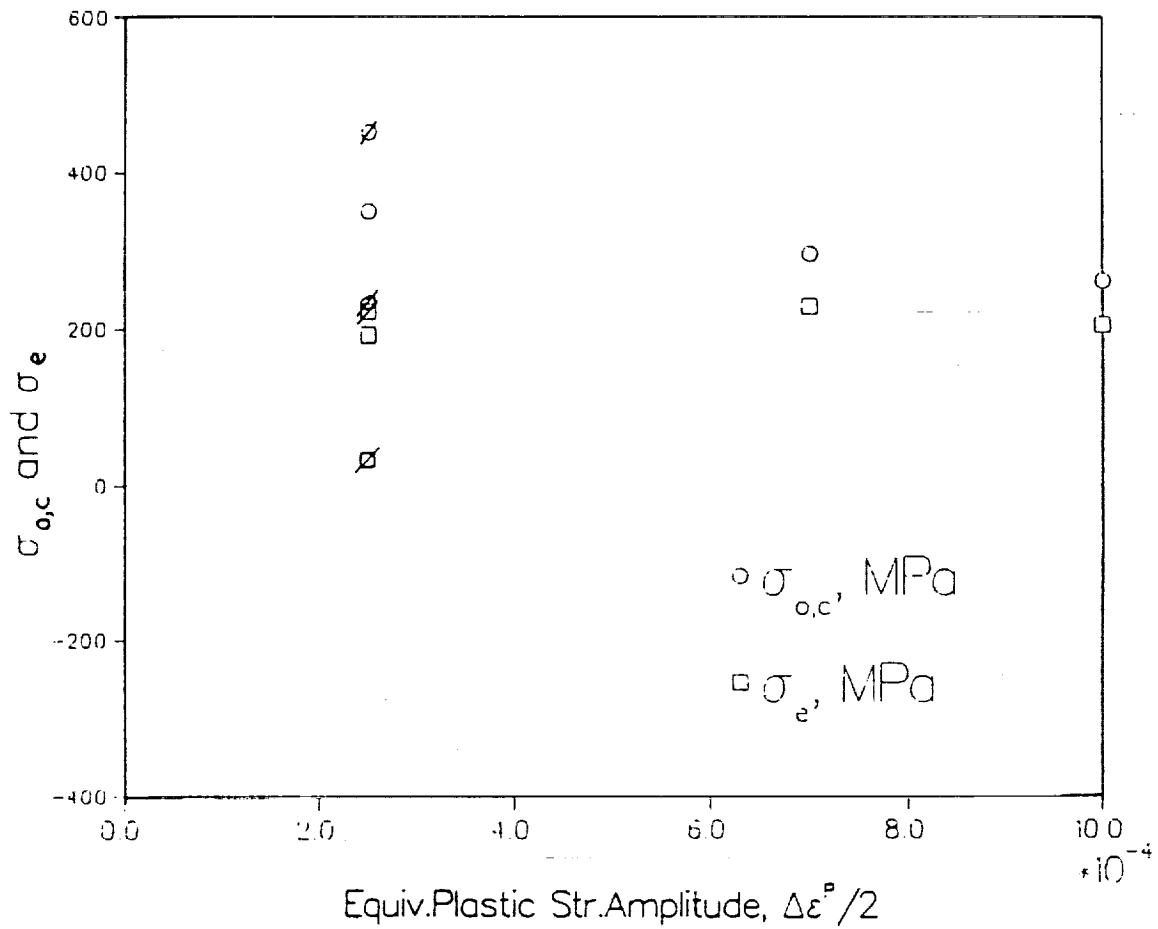


Figure 2.14

Variation of the conventional cyclic strength properties of 7075-T6 (measured from zero stress) with the plastic strain range. Values quoted for a strain range of $\Delta\epsilon^p = 0.00025$ were obtained with a mean stress, $\sigma_m = -100$ MPa, which produces different conventional strength values during the forward and reverse part of the cycle. Note that the half equivalent strain range corresponds with the conventional strain range.

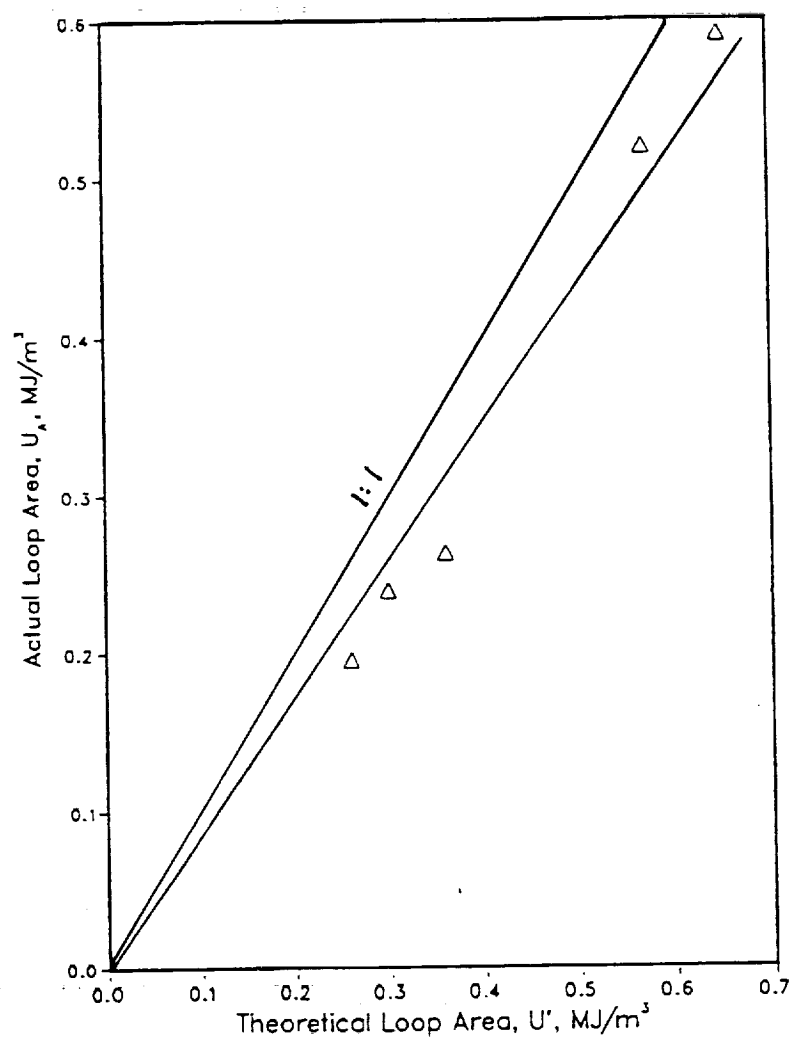


Figure 2.15

Comparison of the loop areas by the ELKP-parameters, with the actual loop areas recorded for 7075-T6.

Table 2.3 Near-end-of-life values of the hysteresis
loop parameters for 7075-T6 Aluminum

Test No	ϵ_P (%)	σ_m (MPa)	N	σ_k (MPa)	σ_e (MPa)	$\sigma_{O,C}$ (MPa)	σ_a (MPa)	M (GPa)	U' (MJ/m ³)	U_A (MJ/m ³)	Samp. ID
1	0.025	0	590	403	192	350	456	55.9	0.30	0.24	a1
2	0.025	-100	330	382	+222 +34	+451 +216	439	55.7	0.26	0.20	a6
3	0.070	0	345	381	228	295	466	53.9	0.54	0.48	a2
4	0.100	0	780	364	205	261	472	52.0	0.74	0.69	a3

$\sigma_k(\text{average}) = 382 \text{ MPa}$

$M(\text{average}) = 54.4 \text{ GPa}$

ϵ_P	-	Strain amplitude
σ_m	-	Shear mean stress
N	-	Cycle number corresponding to the last data set before failure.
σ_k	-	Kinematic yield strength
σ_e	-	Cyclic elastic limit (measured from zero stress)
σ_{OC}	-	Cyclic, 0.02% offset yield strength (measured from zero stress)
σ_a	-	Stress amplitude
M	-	Plastic modulus
U'	-	Loop area calculated from ELKP-parameters
U_A	-	Actual area of recorded loop

offers several new opportunities which are explored in Section 3. For one thing, the cyclic plasticity generated in hardened aluminum can be revealed metallographically, and this offers a way of testing elastoplastic finite element analyses of rolling contact. Secondly, the subsurface contact failure proceeds in as little as $N \sim 10^6$ contacts in hardened aluminum even at relatively modest relative contact pressures. These may provide opportunities for studying the effects of residual stresses and material variables on the process and for testing fracture mechanics analyses of spall growth.

3. FINITE ELEMENT ANALYSES

3.1 Background

This section describes finite element calculations of the plasticity and residual stresses produced by repeated contact in the 3-ball-rod rolling contact fatigue testing machine. The machine is used in this study (see Sections 5.2) and by other investigators to evaluate material resistance to rolling contact failure. Detailed analyses of the test results and their interpretation must take into account the two distinct failure origins described in Section 1.1, as well as the cyclic plasticity present at those places.

Service contact failures can be of either the subsurface or near-surface type. However, the work described in Section 5 shows that the failure of 440C steel obtained with the 3-ball-rod tester with standard roughened balls and ground rods are of the near-surface type. Consequently, the calculations in this section are not directly applicable to the test results. The calculations would be relevant for tests performed with the 3-ball-rod machine with lapped balls and rods that produce subsurface failures.

Three dimensional, elastoplastic calculations of repeated contact are complex and, until recently, relatively little progress has been made. A brief summary of work in this field follows.

A review by Johnson (1986) examines the possible mechanisms of failure and predicts the nature of the residual stress state. Ponter et al. (1985) apply the kinematical shakedown theorem to investigate the mode of deformation for rolling and sliding point contacts. The authors calculate optimal upper bounds for both the elastic and plastic shakedown limits for varying coefficients of friction and shapes of the loaded ellipse. Bower et al. (1986) used the above mentioned theorem to closely look at the conditions under which cumulative deformation occurs in the corner of a railhead, assuming elastic-perfectly plastic behavior. The study was further extended to a work-hardening quarter space. Hills and Sackfield (1984) studied the yield and shakedown states in the contact of generally curved bodies, with and without friction. Hills and Sackfield (1983a, 1983b, 1986) have done additional work treating the point contact problem mathematically.

Kalker (1979) has developed a computer code for treating elastic 3-dimensional rolling contact with dry friction. Kannel and Tevaarwek (1984) presented a computer model for evaluating the subsurface stresses incurred during rolling-sliding contacts. Hardy et al. (1971) developed a finite element model of a rigid sphere indenting (not rolling on) an elastic-perfectly plastic

half-space. Equations were obtained by Hamilton and Goodman (1966) for the complete stress field due to a circular contact region carrying a 'hemispherical' Hertzian normal pressure and a proportionally distributed shearing traction. Chiu and Hartnett (1983) have presented a numerical method of solution for three-dimensional Hertzian contact problems involving layered solids. Hills and Ashelby (1982) have analyzed the residual stresses and their influence on the contact load bearing capacity for 3-dimensional rolling. Rydholm and Fredriksson (1981) devised a finite element model for analyzing shakedown problems in 3-dimensional rolling contacts for elastic-perfectly plastic and kinematic hardening material responses. Martin and Hay (1972) developed a 3-dimensional finite element model to analyze the yielding of a rail material, the subsequent development of residual stresses, and plastic flow due to a moving load. Line contact of two cylinders or of a cylinder and a half-space, with plane strain deformation, has also been studied in detail by Bhargava et al. (1985a, 1985b, 1986), Merwin and Johnson (1963) and Johnson and Jefferies (1963).

Ghonem and Kamath (1984) and Bhargava et al. (1986) have demonstrated that the cyclic stress strain properties of rail steel approach elastic-linear-kinematic-hardening plastic (ELKP) behavior after $10^3 < N < 10^4$ cycles. Kinematic behavior can be expected to produce significantly different continuing plastic deformation and residual stresses. This was confirmed by Bhargava et al. (1988a) in a 2-dimensional elasto-plastic finite element study, where it was found that the residual stresses were 50%, and the cyclic strains were an order of magnitude smaller, for ELKP than for EPP calculations at comparable relative peak pressures. McDowell and Moyar (1986) used a Mroz type kinematic hardening rule (which has been proven to be reliable for non-proportional loading) to perform an approximate numerical calculation for 2-dimensional rolling-sliding contact, incorporating rail steel properties. The experimental work by Bower and Cheesewright (1988) and calculations by Bhargava et al. (1988b) reinforce the view that the rail-wheel contact must be treated as a 3-dimensional problem.

Repeated contact loading for highly stressed mechanical components is accompanied by small amounts of continuing plasticity. The plastic deformation produces net shape changes, residual stresses, and may lead to the nucleation and growth of cracks. The effect of contact loads have been experimentally studied by Groom (1983) and Bower and Cheesewright (1988). Though there exist a number of treatments of the 3-dimensional problem of rolling contact, the information obtained is limited. Most of the analyses employ elastic (Johns and Davies (1976), Hellier et al. (1986)), or elastic-perfectly plastic (Martin and Hay (1972), Johns and Davies (1976), Keer et al. (1986), Orkisz et al. (1986)) material behavior. Some of them evaluate the shakedown limits and provide peak values of certain normal

residual stresses. However, there is very little information on residual stresses, strains and plastic strain range distributions in the half space, especially in the vicinity of the contact. Only two of the studies deal with the stress-strain history (Ponter et al. (1985), Bower et al. (1986)).

Previous analyses have required arbitrary simplifying assumptions; for example, in theoretical studies certain stresses were neglected, and in finite element studies the boundaries were assumed to be rigid. For three-dimensional contact, all six components of residual stress are possible, and they are functions of the position of the material point with respect to the load. In addition, out-of-plane plasticity is expected in 3-dimensional contact. Overall, the cyclic stress-strain variation is much more complex than in a 2-dimensional configuration.

A physically more accurate treatment of the 3-dimensional frictionless rolling contact problem has been presented by Kulkarni et al. (1988, 1990a, 1990b, 1990c), by means of a finite element calculation. This model addresses the elastic displacement of the boundaries and incorporates the experimentally observed elastic-kinematic-hardening-plastic constitutive behavior. This model is used for the present calculations and is described below. Du et al. (1990) have extended Kulkarni's model to account for the presence of surface shear tractions. Initial calculations are introduced and compared to those resulting for the pure rolling case. These methods are adapted here to the 3-ball-rod tester contact geometry.

The mechanisms of elasto-plastic rolling-plus-sliding contact with friction, in the absence of heating, has been examined by Johnson and Jefferies (1963) and Ham et al. (1988). In reality, the heating that accompanies friction will introduce thermal stresses and locally alter the elastic and plastic properties of the material. Existing literature predominantly deals with a) surface limited analyses: Barber (1971a, 1972, 1973a, 1976, 1980a, 1980b, 1982), Comninou and Dundurs (1979), Comninou et al. (1981), Hills and Barber (1986), Korovchinski (1965), Mikic (1974), Panek and Dundurs (1979), and b) the contact of rough surfaces, including flash temperatures (the localized transient temperatures due to asperity contact): Archard (1959), Blok (1937, 1963), Holm (1948), Kuhlman-Wilsdorf (1985), Nagaraj et al. (1979), Winer and Cheng (1980) and Zumgahr (1987).

Many studies have examined the competing processes of: a) frictional heating at the contact interface and the resulting thermal expansion with b) heat transfer and wear. The unstable increases in the contact stress, known as thermoelastic instability (TEI) have been investigated by: Barber (1967, 1968, 1969, 1971b, 1973b), Burton et al. (1973), Dow (1972), Dow and Burton (1972, 1973), Dow and Stockwell (1977) and Johnson et al.

(1988). The manifestation of TEI as scuffing has been studied by Durkee (1978), Durkee and Cheng (1979), and Sovak and Cheng (1982). Except for Newman (1986), who has developed an elasto-plastic finite element model to study the stress field in welded plates, all the investigations discussing the subsurface effects of thermomechanical contact are elastic: Kennedy and Karpe (1982), Ling and Mow (1965), Mow and Cheng (1967) and Tseng and Burton (1982).

Premature failure due to overheating of HPOTP bearings used in the Space Shuttle Main Engine (Maurer and Pallini (1985), Bhat and Dolan (1983)), confirms the need for an elasto-plastic thermo-mechanical finite element model to simulate frictional rolling contact more realistically. A preliminary step in that direction was taken by Kulkarni et al. (1988) with the introduction of a stationary thermo-mechanical analysis of a conductive half plane with a convective surface subjected to the combination of mechanical pressure and different thermal loads (representing the heat generated due to friction). Although the mechanical effect of the surface tractions and the cyclic nature of the applied loads was not considered, the study established the existence of varying levels of residual tensions proportional to the attending temperature gradients. The work describes a transient, translating, elasto-plastic, thermo-mechanical finite element model of a 2-dimensional frictional rolling contact. The temperature variations, stress-plastic strains distributions and deformations are calculated for specific contact conditions. Additional work, now in progress, includes modelling of the three-dimensional 3-ball-rod pure rolling contact experiments, and three-dimensional rolling-plus-sliding studies.

The present work reports the results of several finite element studies. Three-dimensional elasto-plastic finite element models have been developed to study frictionless rolling and rolling-sliding contact on a 3-ball-rod contact fatigue tester configuration. These analyses have been performed for an AISI 440C steel and a 7075-T6 aluminum alloy. In addition, a two-dimensional finite element mesh was developed to simulate rolling-plus-sliding contact with heat generation. Descriptions of the models and results of the analyses are presented below.

3.2 Analytical Procedures

Frictionless rolling of a sphere on a semi-infinite body is simulated by translating a semi-ellipsoid pressure distribution over one face of a three dimensional finite element mesh. The finite element model is intended to reproduce the loading conditions prevailing on the 3-ball-rod experimental set up described by Glover (1982). A finite sized mesh, Figure 3.2.1, is used to represent a semi-infinite body by applying the appropriate elastic displacements on the other faces of the 3-dimensional mesh. For this purpose the semi-ellipsoidal pressure

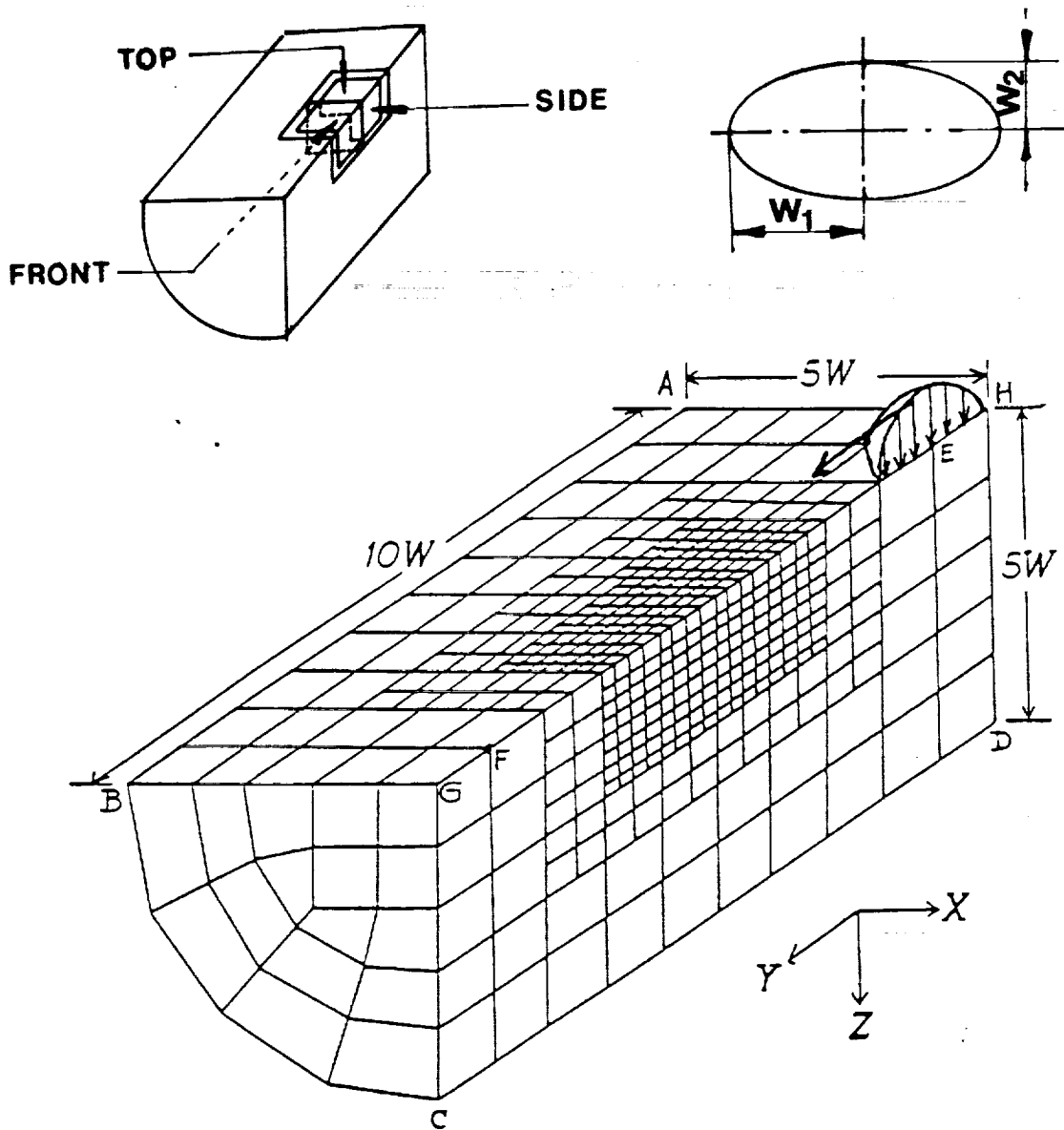


Figure 3.2.1 Finite element mesh used for the 3-dimensional calculations, the size of the elliptical contact patch and the axis (with their nomenclature) are also indicated in the figure.

distribution is discretized into numerous concentrated forces directed along the z-axis.

Rolling-plus-sliding is represented by adding to the above mentioned pressure a distribution of shear tractions resulting from considering uniform slip at the contact. The shear tractions are obtained by first determining the "consistent nodal forces" resulting from the application of the semi-elliptical pressure distribution. These forces are the reaction forces which would arise at the nodes on the top surface, were these constrained to move along the z-direction. These nodal reactions are then multiplied by a constant friction coefficient and applied along the y-direction.

The displacements of the boundary nodes are then calculated for each of these concentrated forces along the y- and z-directions using the appropriate solution to the Boussinesq's problem, and then superimposing the solutions for many loads (the relevant equations used for these calculations are presented in Appendix 1). Kulkarni et al. (1990a) have tested the accuracy of the model against a closed form analytical solution for the purely elastic indentation of a 3-dimensional space; there is excellent agreement between the results. The same authors have shown that the presence of the 'elastic' boundaries does not affect the distribution of residual stresses.

Because of the symmetry of the pressure distribution about the rolling direction, the 3-dimensional mesh has the shape of a quadrant of a circle extended in the second dimension. The present study, in the most general case, pertains to two mechanical components in a three dimensional rolling situation, and hence the x-axis will be referred to as the axial direction, the y-axis, or the direction of translation of the load, as the circumferential direction, and the z-axis as the radial direction. The mesh is finer at the center, and coarser towards the 'elastic' boundaries. The mesh is $10w_1$ long in the circumferential direction, and extends $5w_1$ along the radial and axial directions, where w_1 is the dimension of the semi-major contact patch.

The mesh is made of 8-noded linear brick elements closer to the boundaries, and more refined 20- and 27-noded quadratic brick elements toward the center. There is a total of 1392 elements and 4649 nodes. The elasto-plastic material properties for steel AISI 440C and aluminum alloy 7075-T6, as well as the different loading schemes used in the calculations, are shown in Table 3.2.1. Table 3.2.2 shows the different loading conditions and geometries studied for the present report.

Three loading levels were analyzed for the pure rolling case on steel, they will be hereafter referred to as high, medium and low pressures. For the rolling plus sliding study on steel, only

Table 3.2.1 Material Parameter for 3-dimensional model

Parameter	AISI 440C	Al. 7075-T6
Young's Modulus (GPa)	207.0	70.0
Poisson's Ratio	0.3	0.3
Kinematic Yield Strength (MPa)	1050.0	382.0
Hardening Modulus (GPa)	188.0	56.43
Kinematic Shear Yield Strength (MPa)	606.0	220.55

Table 3.2.2 Loading and Geometry for 3-dimensional model

a) Pure rolling - Aluminum

<u>Load</u> (N)	<u>Peak Pressure</u> (MPa)	p_o/k_k^4	<u>Semi Contact Width</u>	
			<u>Major</u> w_1 (m)	<u>Minor</u> w_2 (m)
47.8	1250.0	5.7	1.79×10^{-4}	1.02×10^{-4}
Geometry of ball		R1 = 0.0127 m R2 = 0.0127 m		
Geometry of sample		R1' = 0.004787 m R2' = ∞		

b) Pure rolling - Steel

<u>Load</u> (N)	<u>Peak Pressure</u> (MPa)	p_o/k_k^1	<u>Semi Contact Width</u>	
			<u>Major</u> w_1 (m)	<u>Minor</u> w_2 (m)
1083.5	5412.0	8.93	4.0889×10^{-4}	2.3073×10^{-4}
438.1	3999.0	6.59	3.0237×10^{-4}	1.7062×10^{-4}
96.7	2413.0	3.98	1.8276×10^{-4}	1.0312×10^{-4}

c) Rolling-plus-Sliding - Steel

1083.5	5412.0	8.93	4.0889×10^{-4}	2.3073×10^{-4}
Ratio of tangential to normal force = 0.1				
Geometry of ball		R1 = 0.0127 m R2 = 0.0127 m		
Geometry of sample		R1' = 0.0048 m R2' = ∞		

⁴ p_o/k_k = Ratio of Hertzian Peak Pressure to Kinematic Shear Yield Strength.

the high pressure condition was analyzed. The ratio of the shear traction to the normal force was assumed to be equal to 0.1. Only one load level was analyzed in the case of the aluminum alloy.

The following assumptions are made for the analyses: a) the contact area, which is calculated from the elastic material properties and the geometry of the bodies, does not change after the semi-infinite body begins to deform plastically, and b) the applied pressure distribution remains Hertzian throughout the analysis. The Hertzian pressure is applied at one end of the mesh and incrementally translated through a distance of $8w_1$ to the other end of the mesh. The translational increments vary according to the position of the load on the mesh. The first increment, w_1 , is followed by two increments of $0.5w_1$, sixteen increments of $0.25w_1$, two increments of $0.5w_1$ and finally one increment of w_1 before the mesh is unloaded. This loading sequence defines a single contact cycle.

The non-linear finite element package ABAQUS (1989) was used for the calculations. Table 3.2.3 shows the various computational facilities and the required CPU times for each of the studies.

The finite element mesh used for rolling-plus-sliding with heat generation is similar to the one used by Kulkarni et al. (1990a) and is shown in Figure 3.2.2. It is a 2-dimensional mesh consisting of 285 elements and 919 nodes. Eight noded isoparametric plane strain elements are used. These elements are biquadratic for displacements and linear for temperature variation. The mesh extends for $24w$ in the circumferential (x) direction and for $12w$ in the radial (y) direction. The mesh is graded; very fine in the vicinity of the global origin and coarser away from it. The thermo physical properties used in the calculations are indicated in Table 3.2.4.

Boundary conditions⁵ are applied to make the mesh simulate a semi-infinite half plane and to model appropriate thermal behavior. Side AB is the free surface; to simulate frictional rolling contact, a thermo-mechanical load is repeatedly translated across AB. The mechanical load is the combination of a normal Hertzian pressure distribution, and a tangential surface traction component. The tangential tractions are related to the normal pressures through the friction coefficient. The thermal loads are coupled to the mechanical loads (tangential tractions) by the velocity term. Side AB loses heat by convection; the film coefficient is indicated in Table 3.2.4.

The non-surface boundaries are displaced elastically to make

⁵ The derivation of the appropriate boundary conditions is presented in Appendix 2.

Table 3.2.3 Computational Requirements

Case	Computer	CPU (hrs)
3-dimensional rolling Steel	Cray Y-MP ⁶	0.5
3-dimensional rolling Aluminum	Cray X-MP ⁶	1.5
3-dimensional rolling+ sliding Steel	Vax 3500 workstation ⁷	84.0

⁶San Diego Supercomputer Center.

⁷The rolling sliding calculations are in the development stage; they will be implemented on the Cray Y-MP.

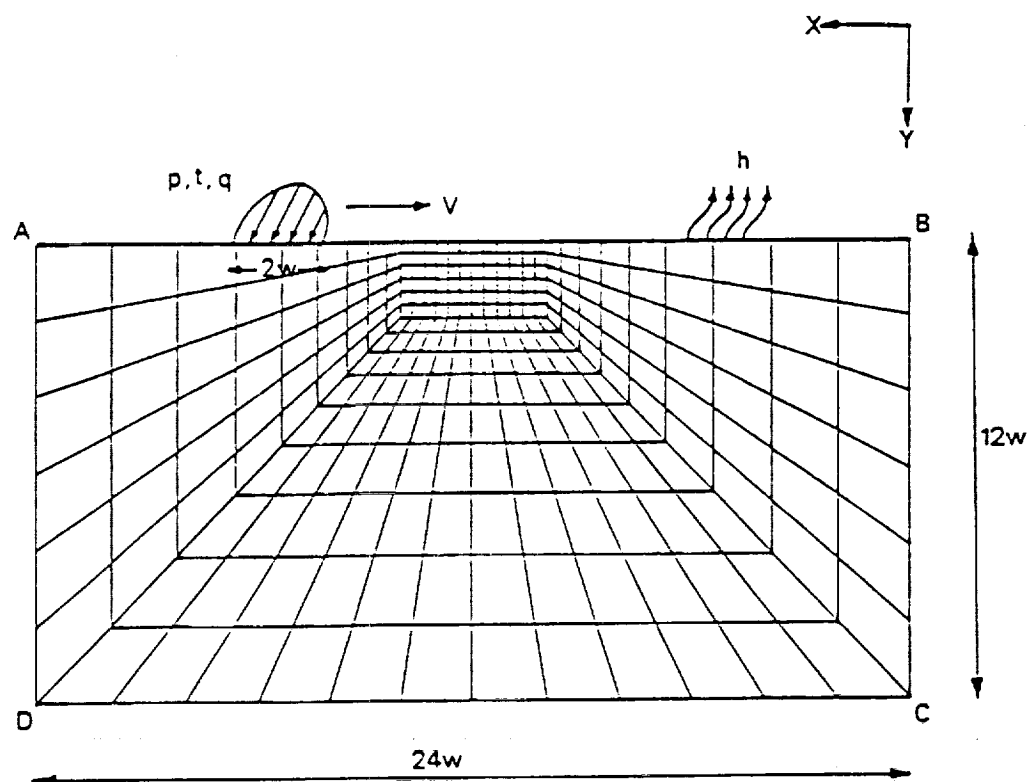


Figure 3.2.2 Finite element mesh used for the 2-dimensional calculations which accounted for rolling-plus-sliding, with the resulting heat generation.

Table 3.2.4 Thermo physical properties for 2-dimensional
calculations plus contact loading and geometry

Parameter	Value
Young's Modulus	207.0 GPa
Poisson's Ratio	0.3
Kinematic Yield Strength	1050.0 MPa
Hardening Modulus	188.0 GPa
Kinematic Shear Yield Strength	606.0 MPa
Peak Hertzian pressure	3.031 GPa
Half contact width	0.5×10^{-3} m
Mass density	7850.0 kg/m ³
Specific heat	550.0 J/kg °C
Friction coefficient	0.2
Thermal expansion coefficient	1.2×10^{-5} m/m °C
Film coefficient	150.0 W/m ² °C
Thermal conductivity	60.0 W/m °C

the mesh behave as a semi-infinite half space. The non-uniform mechanical loads, p and t , are discretized into several concentrated forces, each acting on an infinitesimal area.

Elastic displacements due to each of these forces are calculated at the non-surface boundary nodes using the equations derived in Appendix 1, and the principle of superposition is applied. For the nodes along the bottom surface, DC, both X- and Y-displacements are prescribed while for those on the sides AD and BC, only displacements in the X-direction are calculated using the elastic solution. The following assumptions have been made: (1) temperature independent mechanical and thermo-physical properties, (2) arbitrary heat transfer coefficient h , (3) no heat generation due to inelastic straining, (4) the bearing material is assumed to be a continuum (metallurgical transformations accompanying the high temperatures are not considered).

3.3 Three Dimensional Rolling Contact of Bearing Steel

Results are presented for the loaded state in the form of iso-contours. Given the complicated three dimensional nature of the problem, views along all three orthogonal axes are presented, i.e. the top view (along the z-axis), the front view (along the y-axis), and the side view (along the x-axis). The residual state values are presented for a set of elements located at the center of the mesh as a function of the depth. The stress-plastic strain histories in the half space are also introduced. The stresses are normalized with respect to k_k , the strains with respect to k_k/G and the depth with respect to w_1 .

As mentioned earlier, three different load levels were used for the pure rolling analyses. The alternating or translating component of the stresses acting upon the half-space, is shown in the form of stress contours for the three pressure distributions (high, medium and low) as well as for the three possible views (top, front and side), for the case when the pressure is half way through the second contact. The schematic drawings included with the figures indicate the plane where the stresses are viewed. All figures are shown for the second pass, however results for the first pass were almost identical.

Figure 3.3.1 shows the distribution of equivalent Mises stresses for high, medium and low pressure⁸ viewed from the top face of the model, i.e. along the z-axis. In this figure, as well as all other figures representing the loaded model (i.e. all

⁸ For the top and side views the contour plots represent the high, medium and low pressures, from top to bottom. For the front view the high, medium and low pressure plots are arranged from left to right respectively.

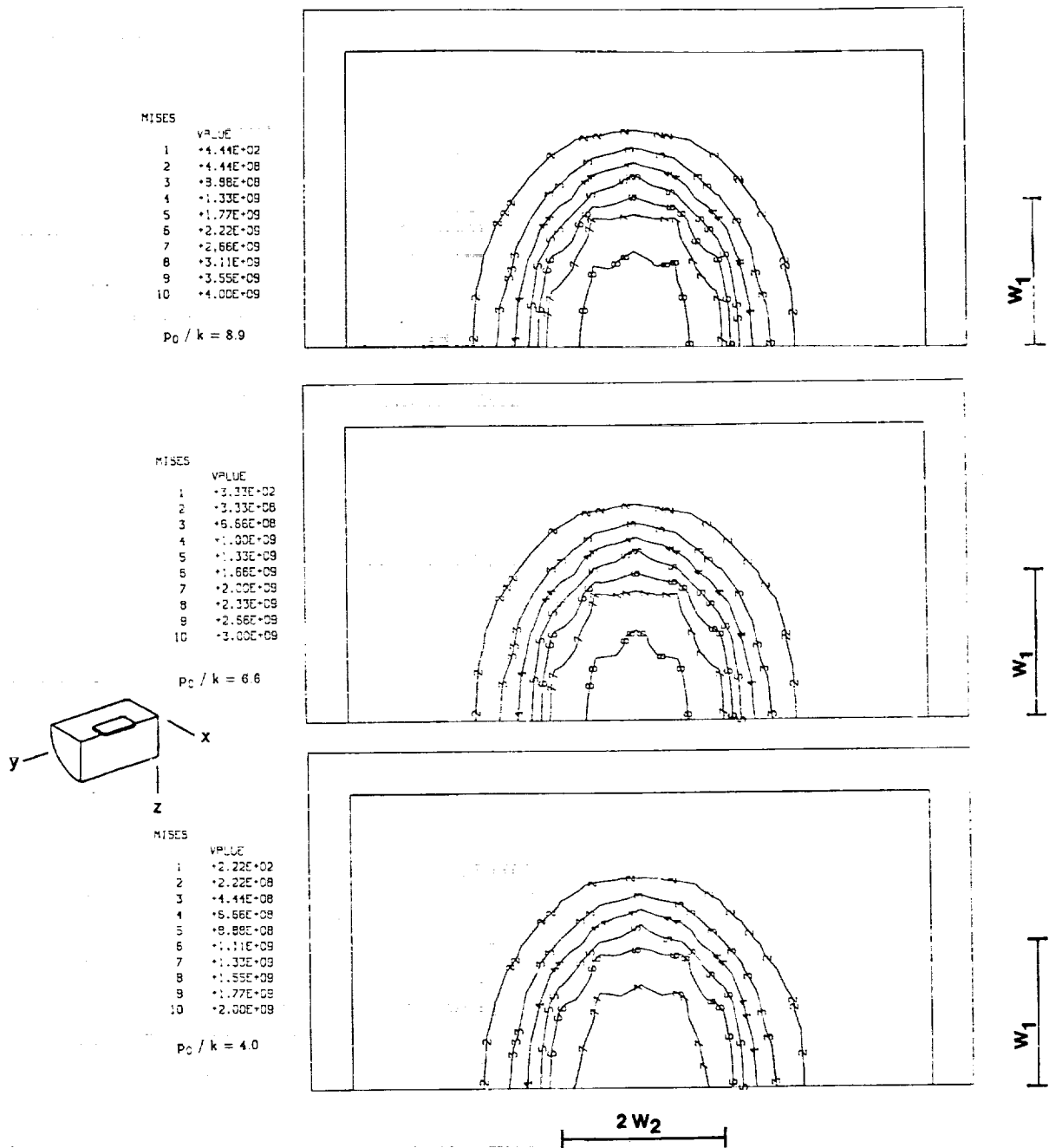


Figure 3.3.1 Contour distribution of equivalent (Mises) stresses on the surface of the mesh (viewed along the z-axis), for high, medium and low pressures. The size of the contact is indicated in the figure. The schematic drawing shows the viewed slice. The values are expressed in N/m^2 (Pascals).

figures except those representing residual values), the load is at the center of the mesh, and the contours are directly under the contact pressure. The elliptical nature of the contact is evident from the shape of the contours (the size of the contact widths is indicated on the figure). A constant ratio of semi-major to semi-minor contact width was used for all the calculations⁹. The equivalent stress is as high as 3.11 GPa at the center of the contact for the high pressure case (2.33 GPa and 1.33 GPa for the medium and low pressure cases, respectively). Figure 3.3.2 shows the distribution of equivalent Mises stresses for the side view, i.e. along the -x-axis, for the three pressure levels. It is interesting to note in these figures that the contours which indicate an equivalent stress above the kinematic yield strength ($\sigma_k = 1050.0$ MPa) extend up to the surface for the high pressure case (contours 4 and higher), reach close to the surface for the medium pressure case (contours 5 and higher), and are completely confined to the subsurface region for the low pressure case (contours 6 and higher). The same observations may be made with reference to the contours shown in Figure 3.3.3. This figure shows the front view of the equivalent Mises stress contours for a set of elements located at the center of the mesh, as indicated in the schematic drawing.

The translating 3-D Hertzian pressure produces highly complex stress distributions in the half space. This is clearly evident in Figures 3.3.4 through 3.3.8, which show stress contours for the second contact. Figure 3.3.4 shows the contact stress distribution (along the z direction) on the top surface. The contours provide evidence of the elliptical nature of the contact, elongated along the x-axis (perpendicular to the rolling direction). Figure 3.3.5 depicts the distribution of shear stress, σ_{xy} , near the top surface, viewed along the z-axis. The peak values for the antisymmetric distribution of this stress component are present at the edge of the contact, and range from plus to minus 166.0 MPa for the high pressure case, from plus to minus 133.0 MPa for the medium pressure case, and from -88.8 MPa to 77.7 MPa for the low pressure case. The most favorable conditions for crack propagation driven by this stress component would take place on a yz plane, i.e. perpendicular to the surface, and close to the edge of the contact.

Figure 3.3.6 shows the distribution of circumferential stress, σ_{yy} , viewed along the -x direction. As previously observed by Kulkarni et al. (1990a) for the case of a contact elongated along the rolling direction, a small region of tensile stress develops at the surface on either side of the semi-minor contact width. For the high pressure case, the magnitude of this tensile stress component reaches up to 333.0 MPa. However, the

⁹ The ratio $w_1/w_2 = 1.77$.

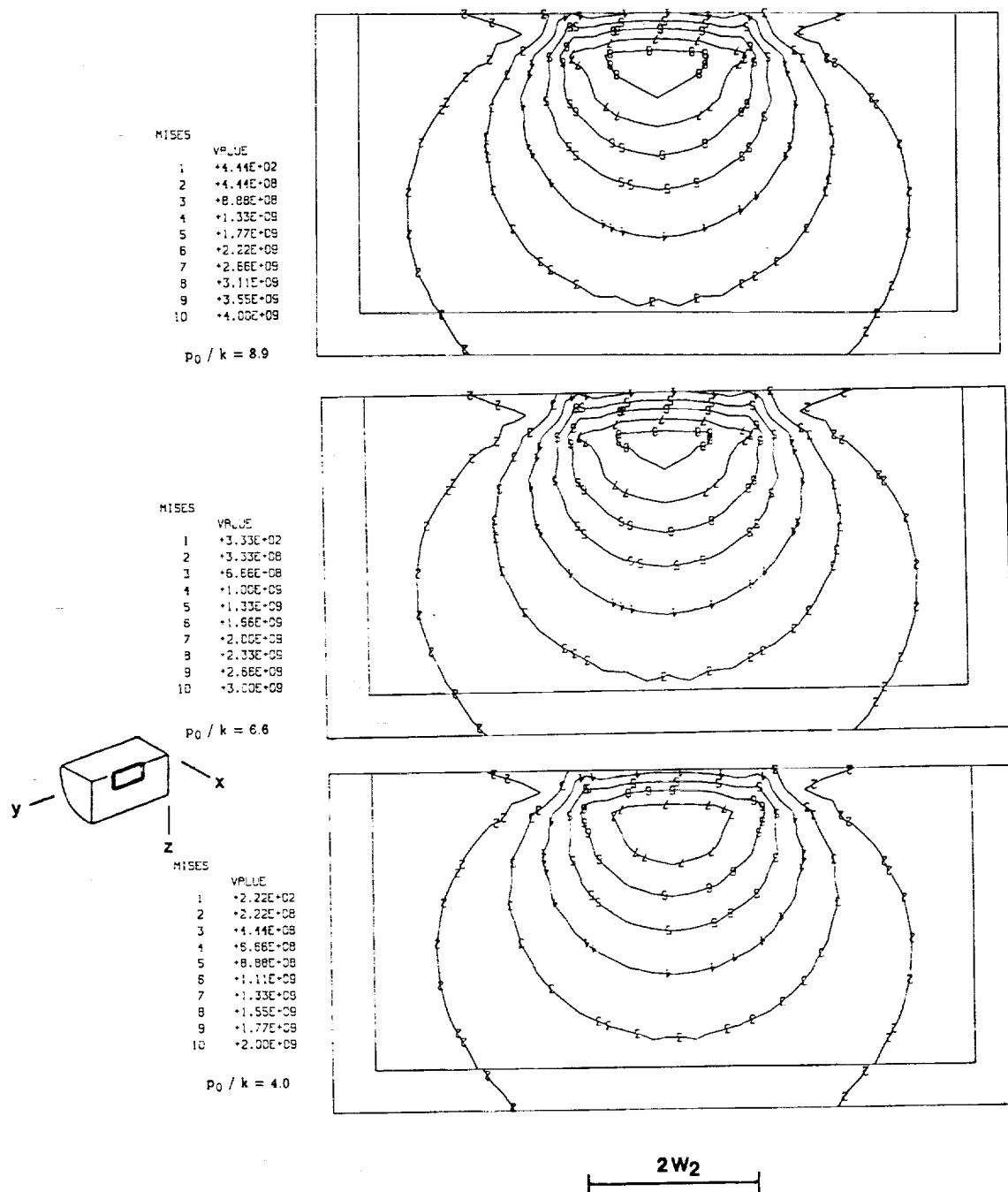
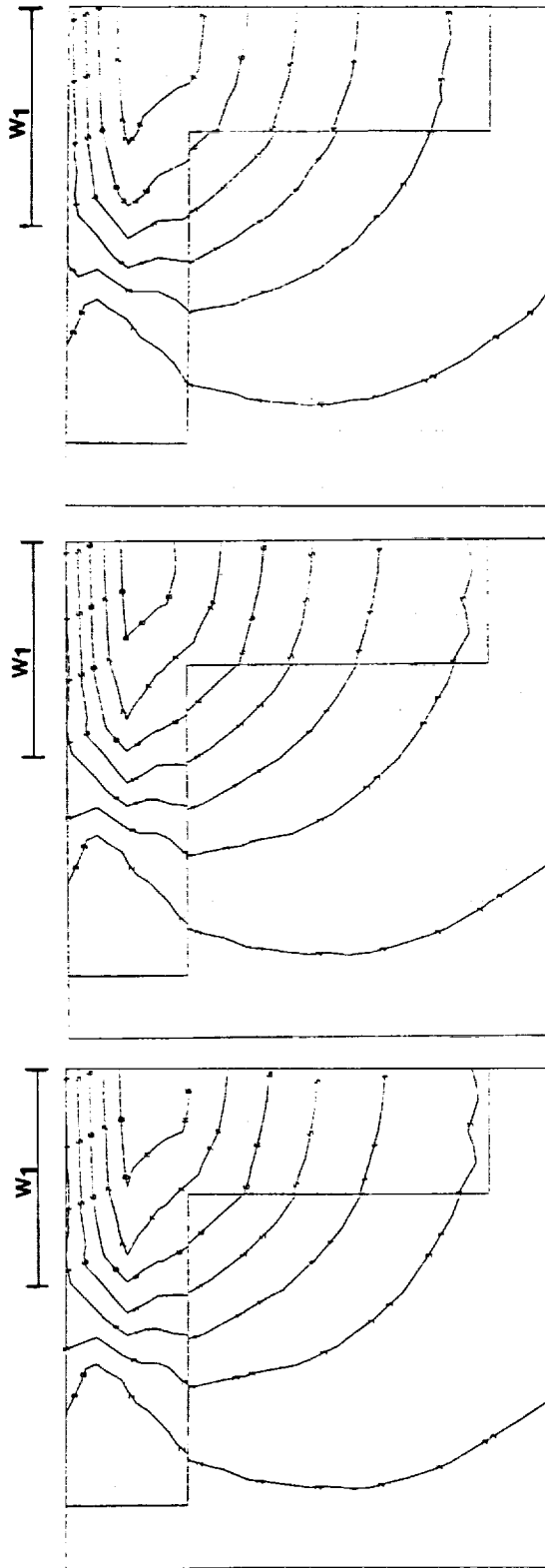


Figure 3.3.2 Contour distribution of equivalent (Mises) stresses on the side of the mesh (viewed along the x-axis), for high, medium and low pressures. The size of the contact is indicated in the figure. The schematic drawing shows the viewed slice. The values are expressed in N/m^2 (Pascals).



MISES	VALUE
1	*4.44E+02
2	*4.44E+08
3	*8.88E+08
4	*1.33E+09
5	*1.77E+09
6	*2.22E+09
7	*2.66E+09
8	*3.11E+09
9	*3.55E+09
10	*4.00E+09

$P_0 / k = 8.9$

MISES	VALUE
1	*3.33E+02
2	*3.33E+08
3	*6.66E+08
4	*1.00E+09
5	*1.33E+09
6	*1.66E+09
7	*2.00E+09
8	*2.33E+09
9	*2.66E+09
10	*3.00E+09

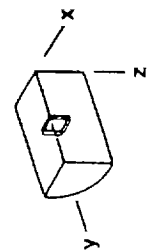
$P_0 / k = 6.0$

MISES	VALUE
1	*2.22E+02
2	*2.22E+08
3	*4.44E+08
4	*6.66E+08
5	*8.88E+08
6	*1.11E+09
7	*1.33E+09
8	*1.55E+09
9	*1.77E+09
10	*2.00E+09

$P_0 / k = 4.0$

Figure 3.3.3

Contour distribution of equivalent (Mises) stresses on a set of elements at the center of the mesh (viewed along the y-axis), for high, medium and low pressures. The size of the contact is indicated in the figure. The schematic drawing shows the observed slice. The values are expressed in N/m^2 (Pascals).



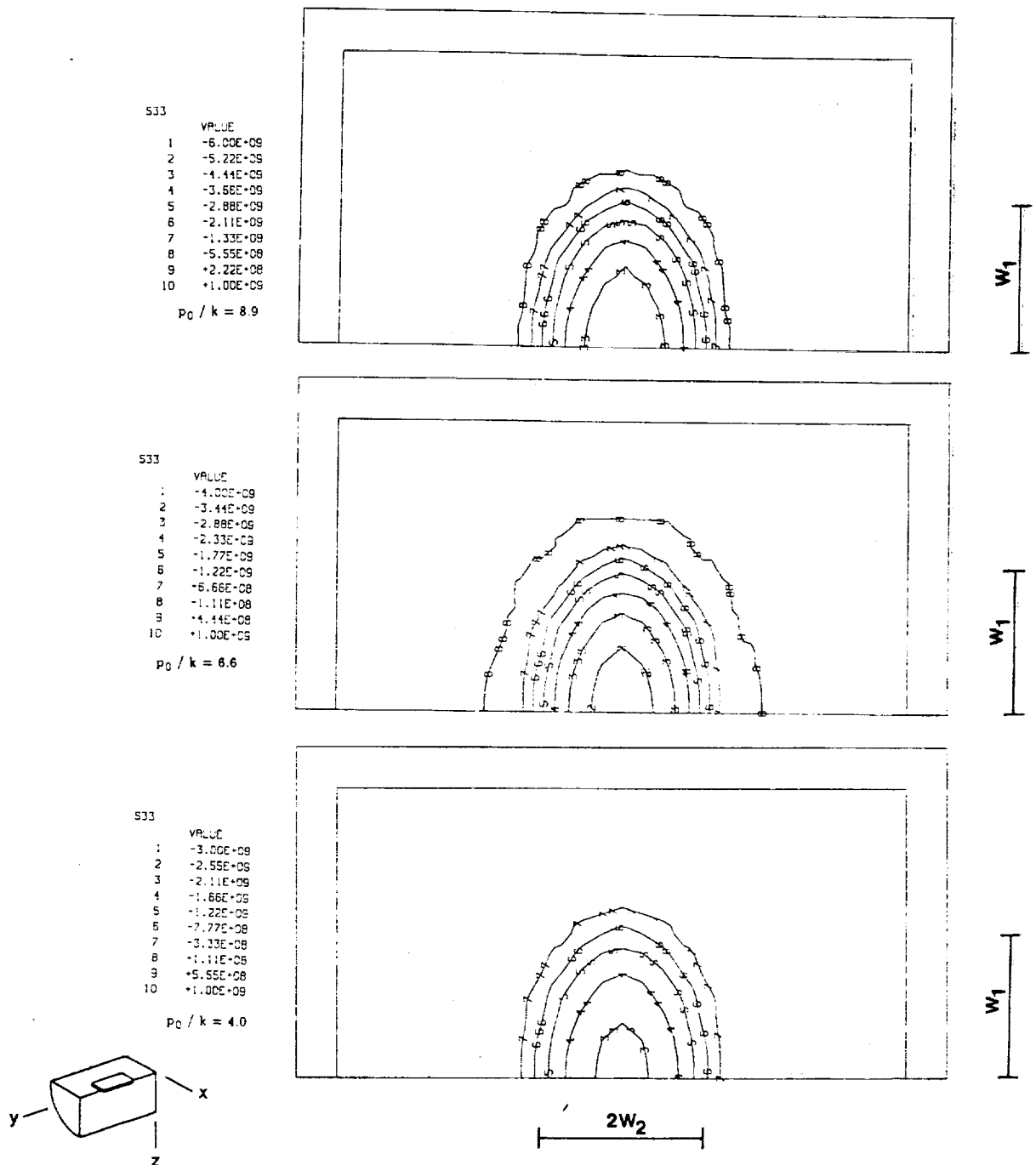


Figure 3.3.4 Contour distribution of direct, σ_{zz} , stresses viewed along the z -axis (top surface), for high, medium and low pressures. The size of the contact is indicated in the figure. The schematic drawing shows the observed slice. The values are expressed in N/m^2 (Pascals).

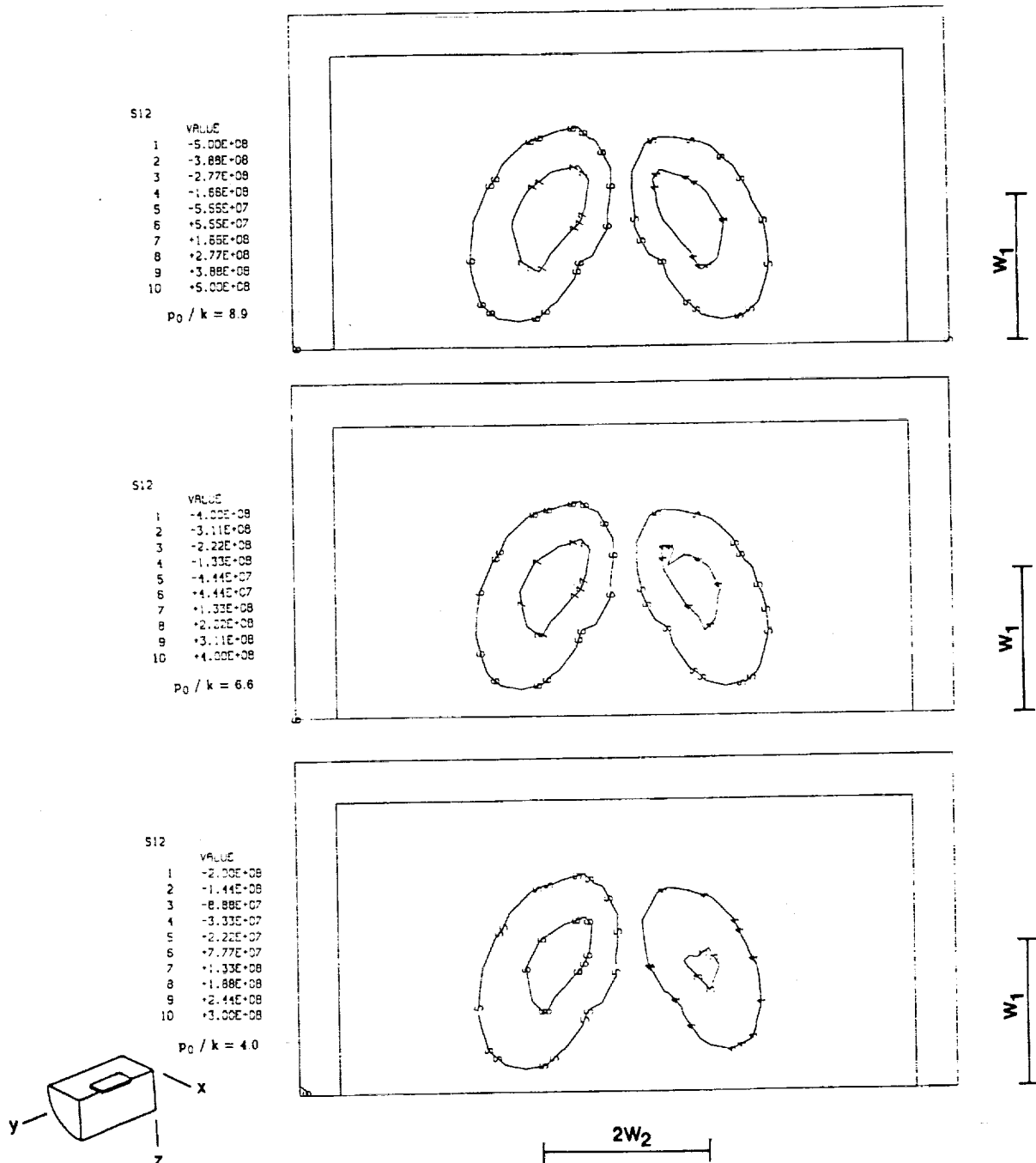


Figure 3.3.5 Distribution of shear stresses, σ_{xy} , viewed along the z-axis. The figure indicates the size of the contact as well as the values for the contours. The stresses are indicated in N/m² (Pascal). The schematic drawing shows the portion of the mesh under observation.

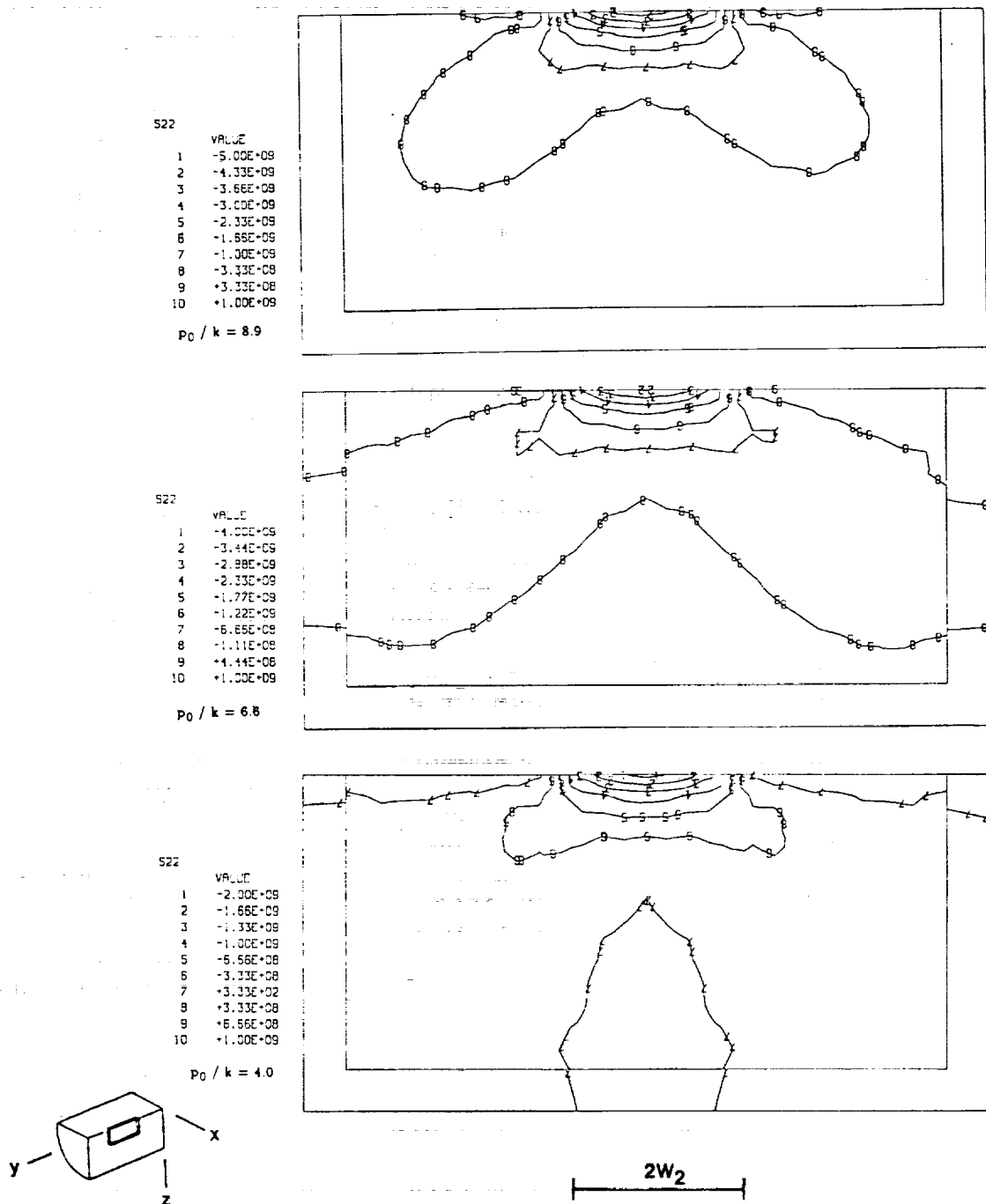


Figure 3.3.6 Distribution of circumferential, σ_{yy} , direct stresses under the surface. The pressure distribution has been translated halfway through one pass. The schematic drawing indicates the slice of material under observation. The values for the contours are in units of N/m^2 (Pascals).

volume of material affected by the tensile stresses is not large. Figure 3.3.7 shows the subsurface antisymmetric distribution of shear stress, σ_{yz} . This stress component peaks at a depth of approximately $0.3w_1$. The magnitude of this stress is, however, almost seven times as large as the previously mentioned values for σ_{xy} . The peak values for this stress range from plus to minus 1100.0 MPa for the high pressure case, from plus to minus 1000.0 MPa for the medium pressure case, and from plus to minus 555.0 MPa for the low pressure case. The most favorable orientation for a crack to grow with this shear stress component for driving force would be on planes parallel to the surface.

Figure 3.3.8 presents the contour distribution of axial stress, σ_{xx} , for a slice of material at the center of the mesh. There is evidence of tensile axial stress at the edge of the contact, however, with the exception of the high pressure case where the stress approaches 444.0 MPa, it is negligible. In all cases though, the volume of material affected by the tensile stress is small. Figure 3.3.9 presents the distribution of shear stress, σ_{xz} , under the contact. The peak value of this shear stress takes place at the edge of the contact, at a depth of approximately $0.32w_1$. The magnitude of the shear stress is also larger than σ_{xy} , but smaller than σ_{yz} . The peak values are 1000.0 MPa for the high pressure case, 700.0 MPa for the medium pressure case, and 433.0 MPa for the low pressure case. The distribution is also expected to be antisymmetric but with respect to the plane of symmetry of the mesh, i.e. y-z.

The plastic strain increments, $d\epsilon_{ij}^p$, for each translating increment are used to calculate the equivalent plastic strain by integrating them over the history of loading, based on a von Mises yield function and for the appropriate kinematic hardening flow rule. The equivalent plastic strain, ϵ_{eq}^p , is thus a measure of the degree of plasticity attained at a material point. Figure 3.3.10 shows the equivalent plastic strain contours half way through the second translation of the pressure distribution, viewed along the z-axis (top surface). Figure 3.3.11 shows the equivalent plastic strain distribution from a side view. The peak plastic activity takes place in all cases at a depth of approximately $0.25w_1$. For the high pressure case, the peak equivalent plastic strain reaches values as high as 0.004; for the other two cases the maxima are equal to 0.00233 and 0.00044 for the medium and low pressures, respectively. Figure 3.3.12 shows the distribution of equivalent plastic strains viewed along the y-axis, it is evident that as the pressure increases, so does the volume of material affected by irreversible plasticity.

Another indication of the degree of plasticity is the plastic work, given by the integral of the product $\sigma_{ij} \cdot d\epsilon_{ij}^p$ over the loading history of the material point. This irrecoverable work leads to damage accumulation by exhaustion of ductility, which in turn is responsible for crack initiation and

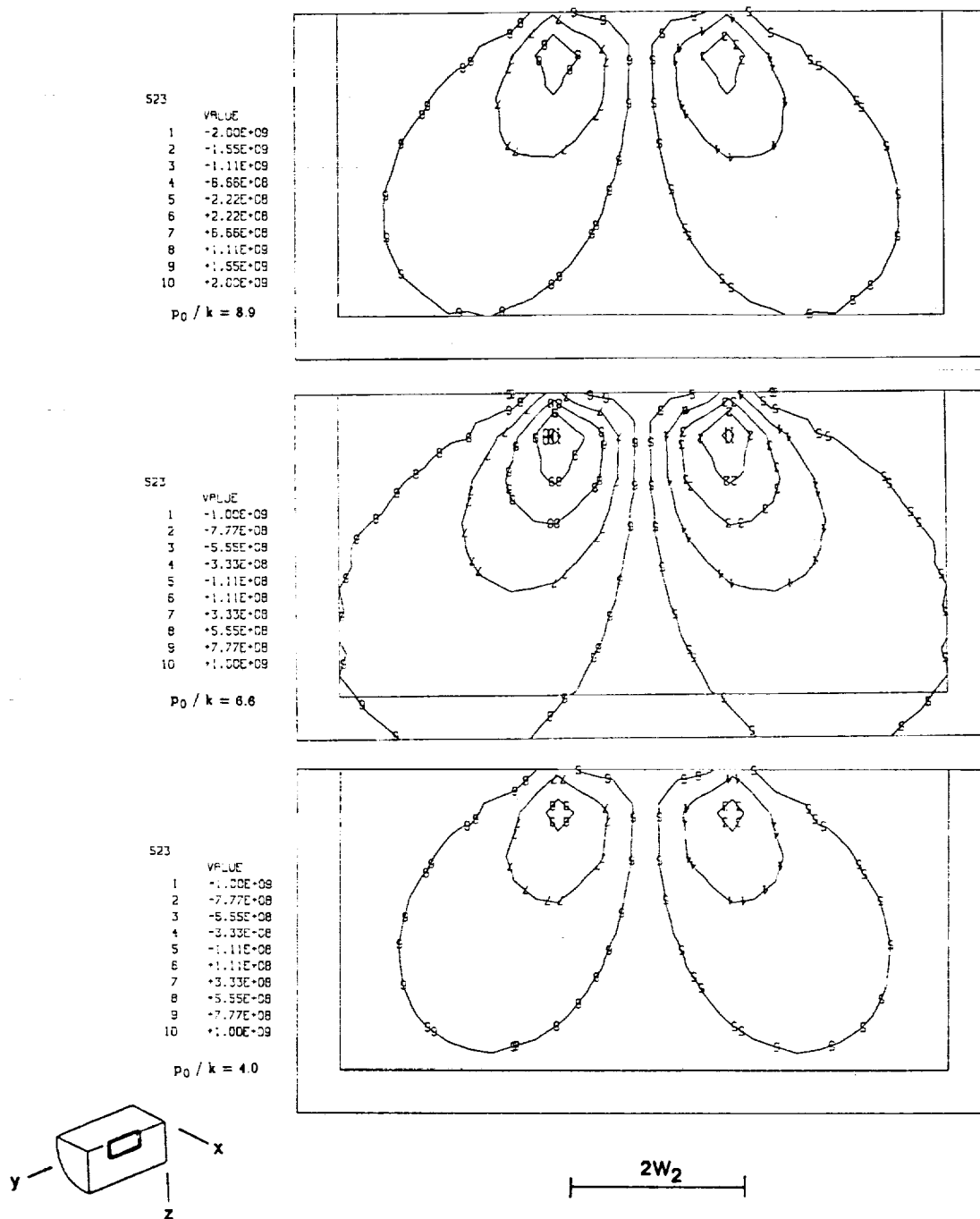
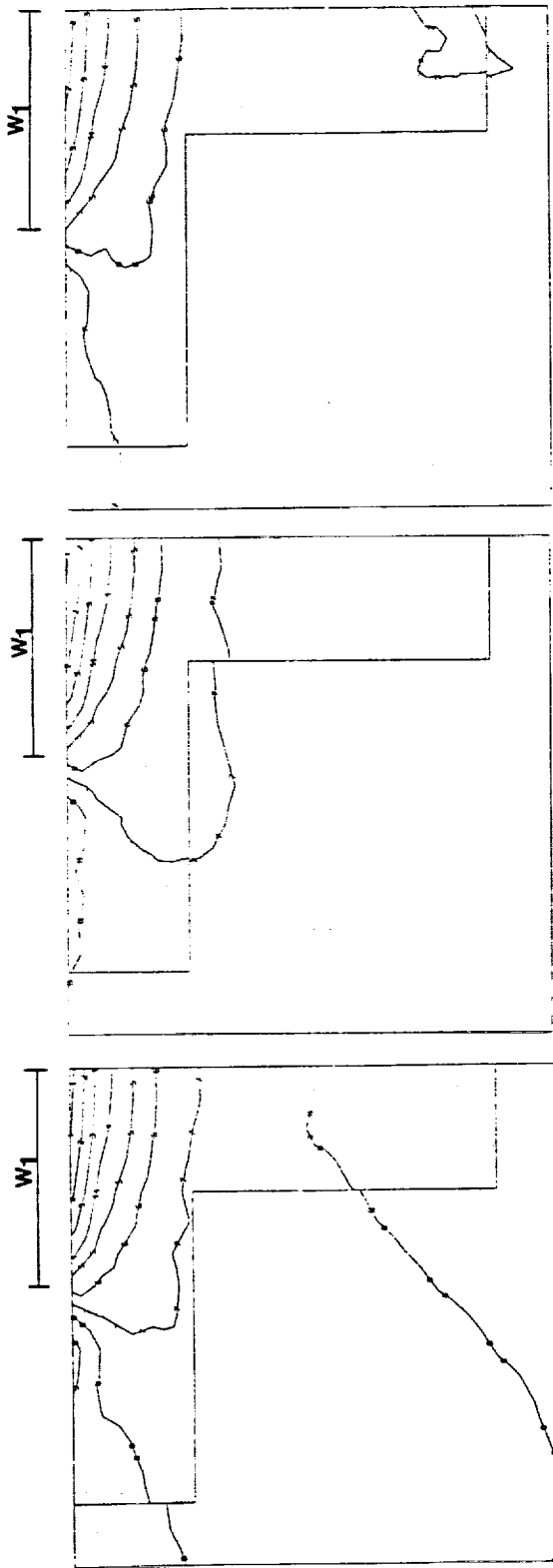


Figure 3.3.7

Antisymmetric distribution of shear stress, σ_{yz} , viewed along the x-direction. The schematic drawing shows the portion of the mesh under observation. The stresses are in units of N/m^2 (Pascals).



S11	VALUE
1	-4.00E+09
2	-3.44E+09
3	-2.88E+09
4	-2.32E+09
5	-1.76E+09
6	-1.20E+09
7	-6.44E+08
8	-1.11E+08
9	4.44E+07
10	1.00E+08

$p_0 / k = 8.9$

S11	VALUE
1	-3.00E+09
2	-2.55E+09
3	-2.11E+09
4	-1.66E+09
5	-1.22E+09
6	-7.77E+08
7	-3.33E+08
8	1.11E+08
9	5.55E+07
10	1.00E+08

$p_0 / k = 6.6$

S11	VALUE
1	-2.00E+09
2	-1.66E+09
3	-1.33E+09
4	-1.00E+09
5	-6.66E+08
6	-3.33E+08
7	3.33E+07
8	3.33E+07
9	6.66E+07
10	1.00E+08

$p_0 / k = 4.0$

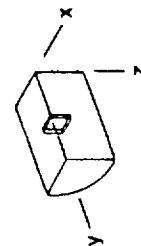
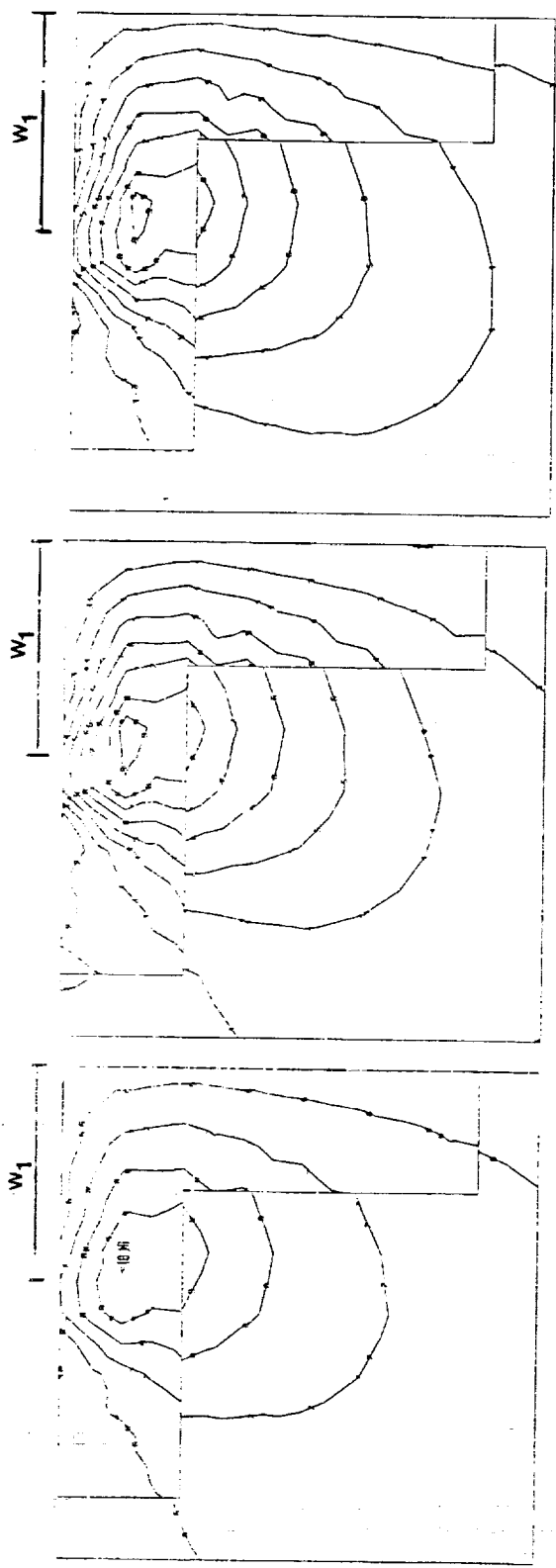


Figure 3.3.8

Distribution of normal, σ_{xx} , stresses viewed along the $-y$ direction. The contours are shown for the material at the center of the mesh directly under the contact, as indicated in the schematic drawing. The stresses are in units of N/m^2 (Pascals).



S13	VALUE
1	-1.00E+08
2	-3.33E+07
3	+3.33E+07
4	+1.00E+08
5	+1.66E+08
6	+2.33E+08
7	+3.00E+08
8	+3.66E+08
9	+4.33E+08
10	+5.00E+08

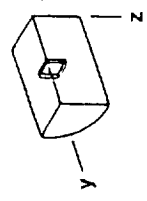
$P_0 / k = 4.0$

S13	VALUE
1	-9.99E+07
2	+1.00E+08
3	+1.00E+08
4	+2.00E+08
5	+3.00E+08
6	+4.00E+08
7	+5.00E+08
8	+6.00E+08
9	+7.00E+08
10	+8.00E+08

$P_0 / k = 6.6$

S13	VALUE
1	1.00E+09
2	-7.77E+08
3	-5.55E+08
4	-3.33E+08
5	-1.11E+08
6	+1.11E+08
7	+3.33E+08
8	+5.55E+08
9	+7.77E+08
10	+1.00E+09

$P_0 / k = 8.9$



x Figure 3.3.9

Contour distribution of shear stresses, σ_{xz} , under the surface and immediately below the contact, at the center of the mesh. The schematic drawing shows the portion of material under consideration. The contours show the stresses in units of N/m^2 (Pascals).

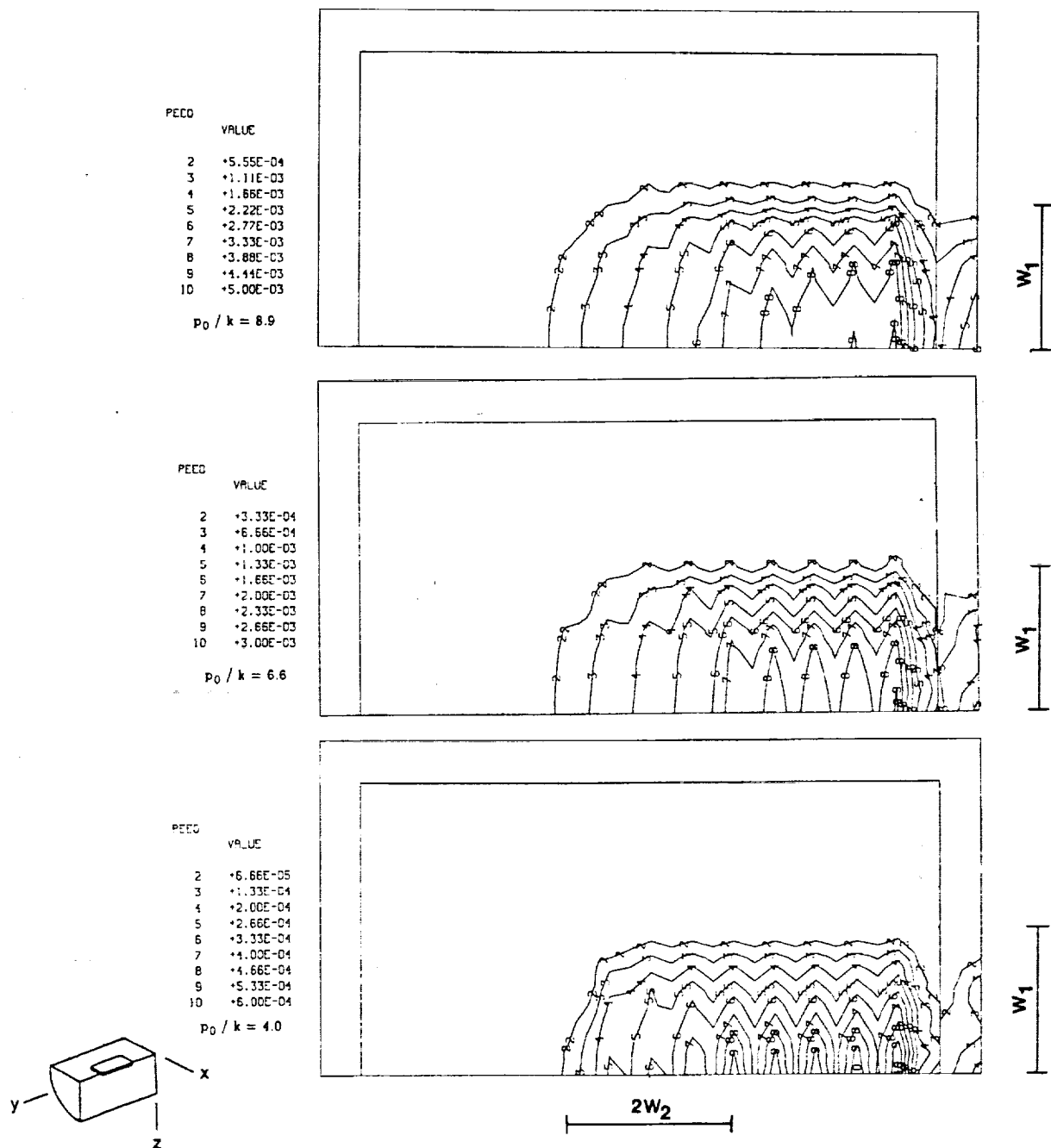


Figure 3.3.10 Distribution of iso-contours for the equivalent plastic strains, viewed along the z-direction. The dimension of the contacts are indicated in the figure. The schematic shows the slice of material under observation.

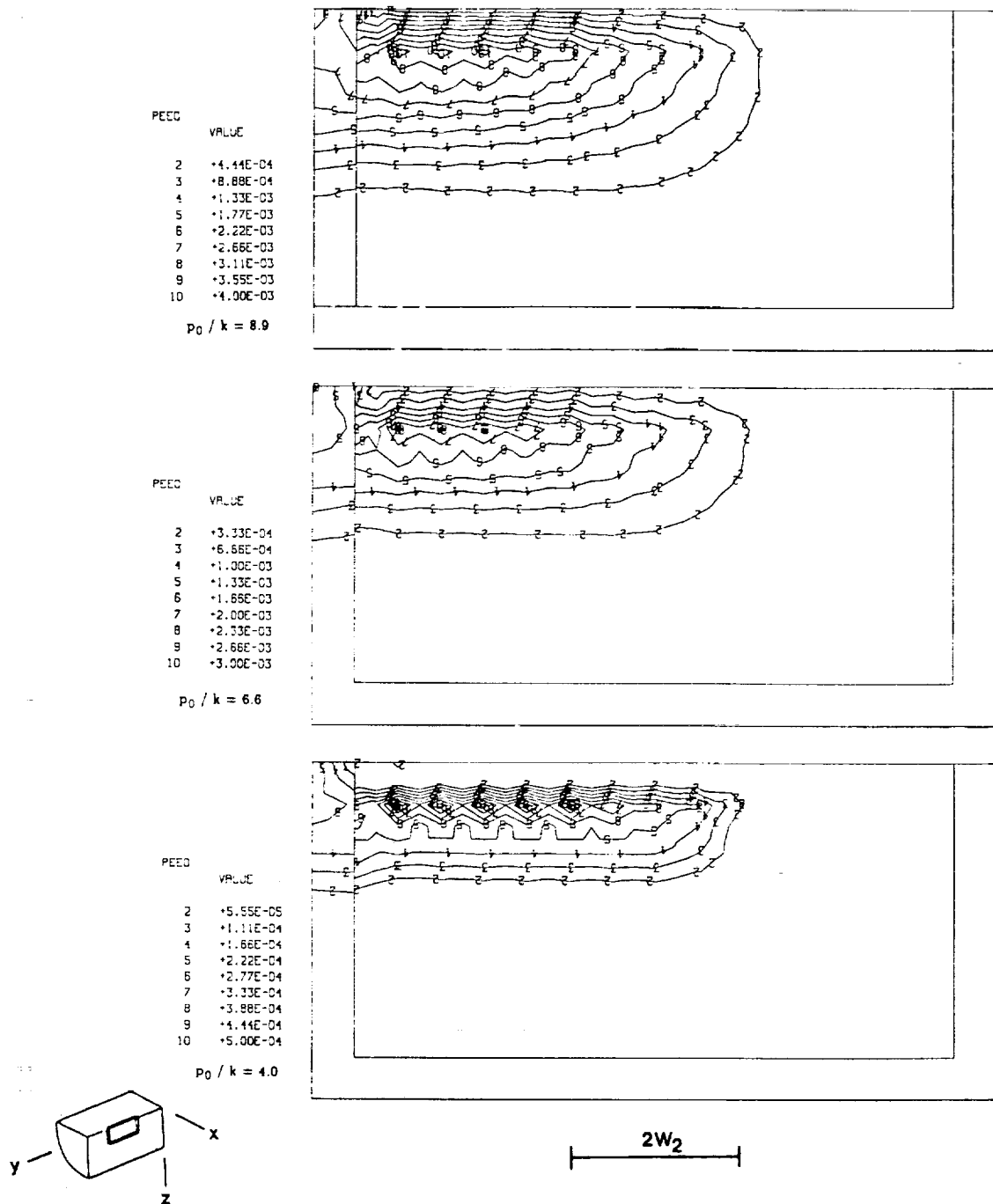


Figure 3.3.11 Distribution of equivalent plastic strains under the surface, viewed along the x-direction. The schematic drawing shows the slice of mesh under consideration.

ORIGINAL PAGE IS
OF POOR QUALITY

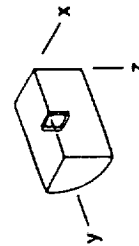
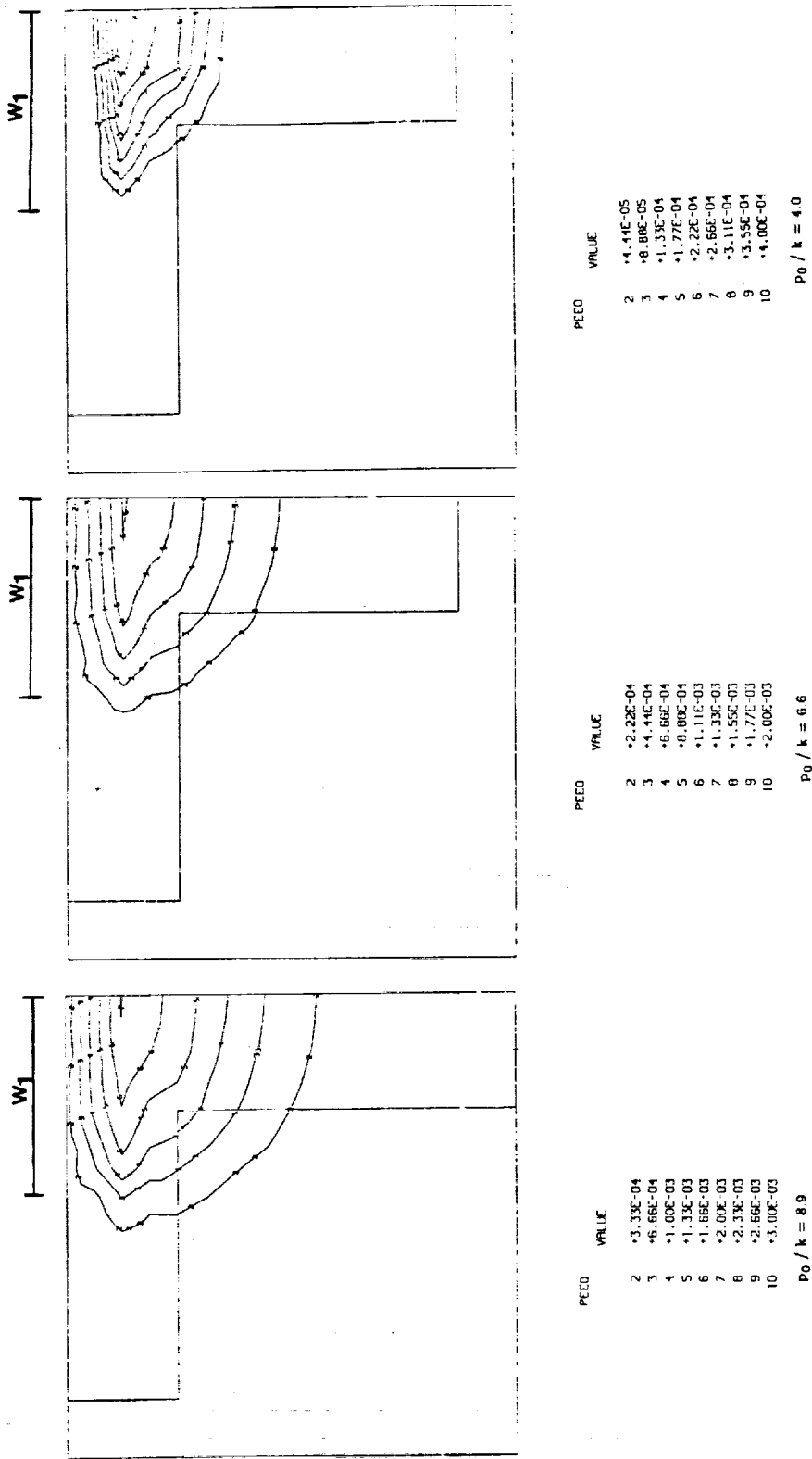


Figure 3.3.12 Distribution of equivalent plastic strains under the surface, viewed along the y-direction for a slice of material located at the center of the mesh as indicated in the schematic drawing.

propagation, thus leading ultimately to failure. Figure 3.3.13 shows the contours of plastic energy viewed along the x-axis. Figure 3.3.14 presents the subsurface distribution perpendicular to the z-axis; this figure indicates that the maximum dissipation of energy by irrecoverable plastic work takes place at a depth of $0.3w_1$ in all three cases. Moreover, the maximum of plastic work occurs directly under the contact (centered with the pressure distribution). However, the volume of material exposed to cyclic plasticity increases with the peak pressure.

In the case of two dimensional rolling, line contact (a rigid cylinder rolling over a flat half-space), the flat surface remains flat during rolling and the mechanically admissible residual stress state permits only two components, σ_{xx}^r and σ_{yy}^r , which vary as a function of the distance from the surface. The deformation mechanism is one of ratchetting parallel to the surface. In the case of point contact, which is a three dimensional problem, all six components of residual stress can exist, and are present. Their magnitude is not only a function of the depth from the surface (z distance) but also a function of their distance from the center plane (x distance). The ploughing of the material introduces a strain gradient in the axial direction; this region is surrounded by material which has not been plastically deformed. Upon unloading, this material tries to recover its original shape, thus resulting in residual stresses.

Figures 3.3.15 through 3.3.17 show the distribution of direct residual stresses at integration points located at a distance of $0.125w_1$ from the yz plane, at the center of the mesh. The residual stresses are normalized with respect to the kinematic shear yield strength, k_k , and are plotted as a function of the depth below the surface, normalized with respect to the semi-major contact width, w_1 . Each plot presents the results for the three contact pressures used in the calculations. Table 3.3.1 compares the peak direct residual stresses obtained for the present calculations with previous values reported in the literature.

Figures 3.3.18 through 3.3.21 show iso-contours of the half equivalent plastic strain range for the three different loadings (high: $p_0/k \approx 9$, medium: $p_0/k \approx 6$, low: $p_0/k \approx 4$) for pure rolling, and for rolling-plus-sliding at the high load level (Fig. 3.3.21). The contours are for a slice of material located at the center of the mesh, as shown on the schematics. Figure 3.3.22 shows a comparison of the variation in the half plastic strain range with depth, for the three different loads under pure rolling, and the high load under rolling plus sliding (these values are taken at the same locations as Figs. 3.3.18-21).

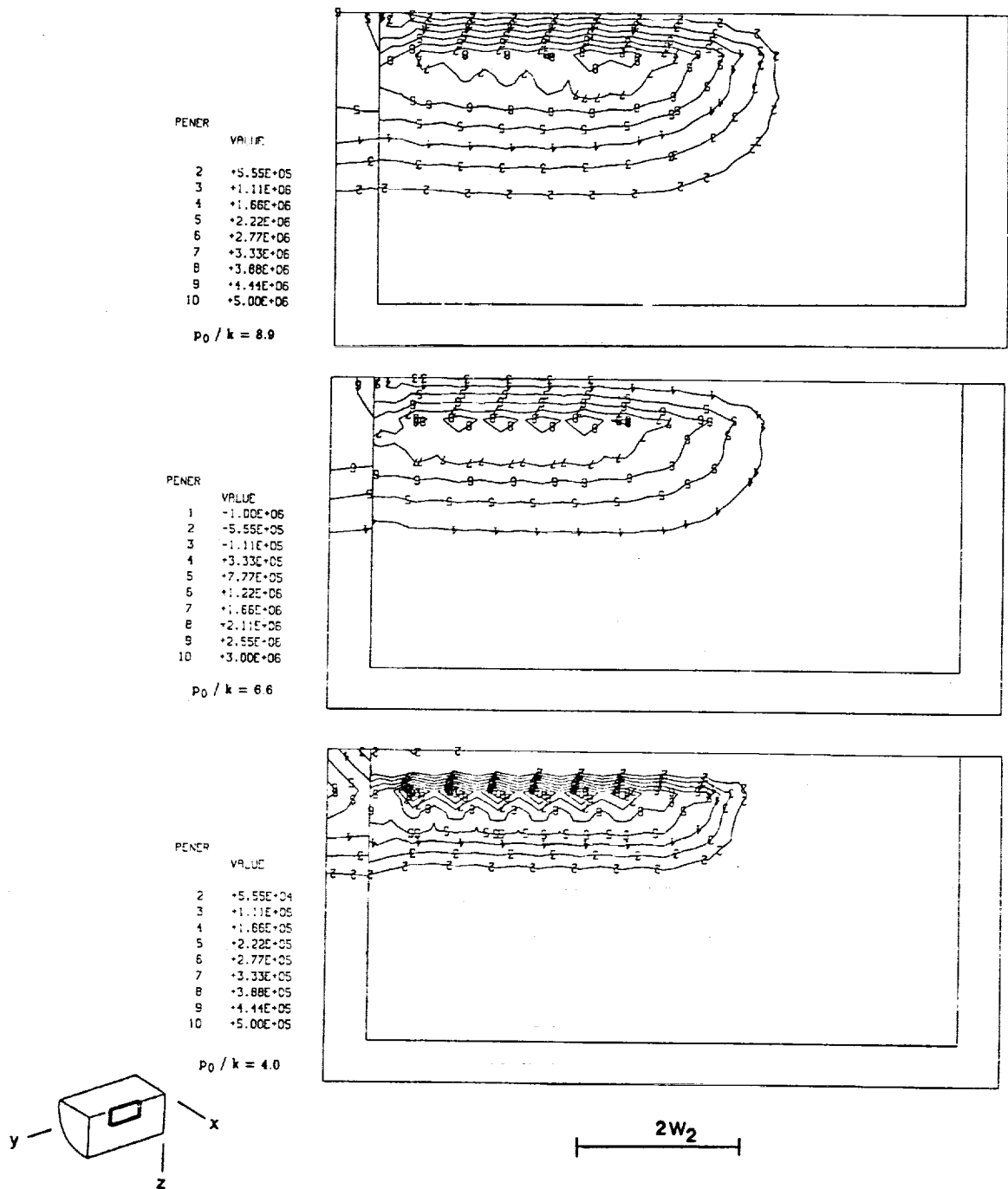


Figure 3.3.13 Contour distribution of the amount of energy dissipated as irrecoverable plastic work per unit volume, viewed along the x direction. The contours are in units of N.m (Joules).

ORIGINAL PAGE IS
OF POOR QUALITY

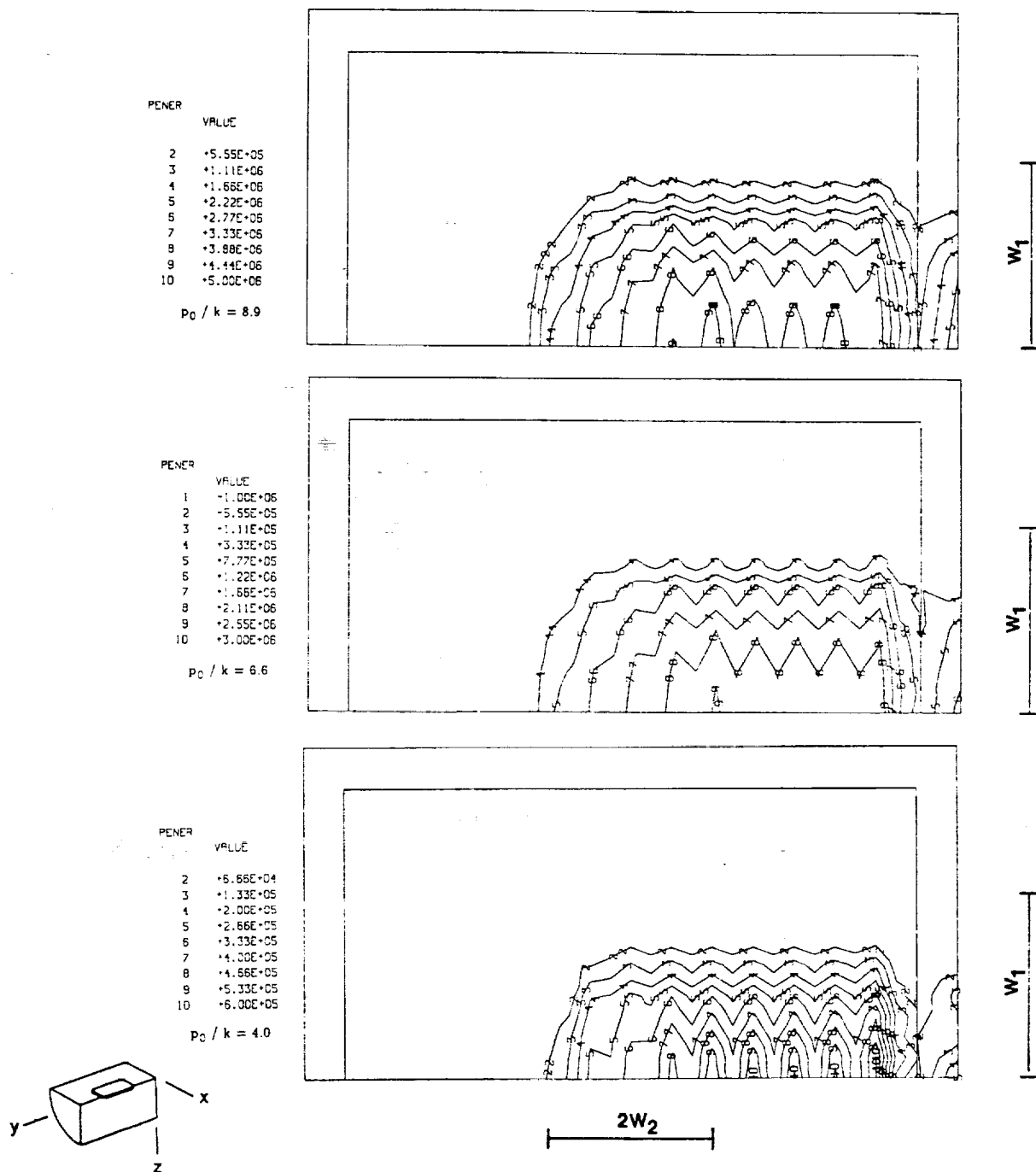


Figure 3.3.14 Contour distribution of energy dissipated by plastic work, viewed along the z-direction on the slice of material indicated in the schematic drawing. The contours are in units of N.m (Joules).

ORIGINAL PAGE IS
OF POOR QUALITY

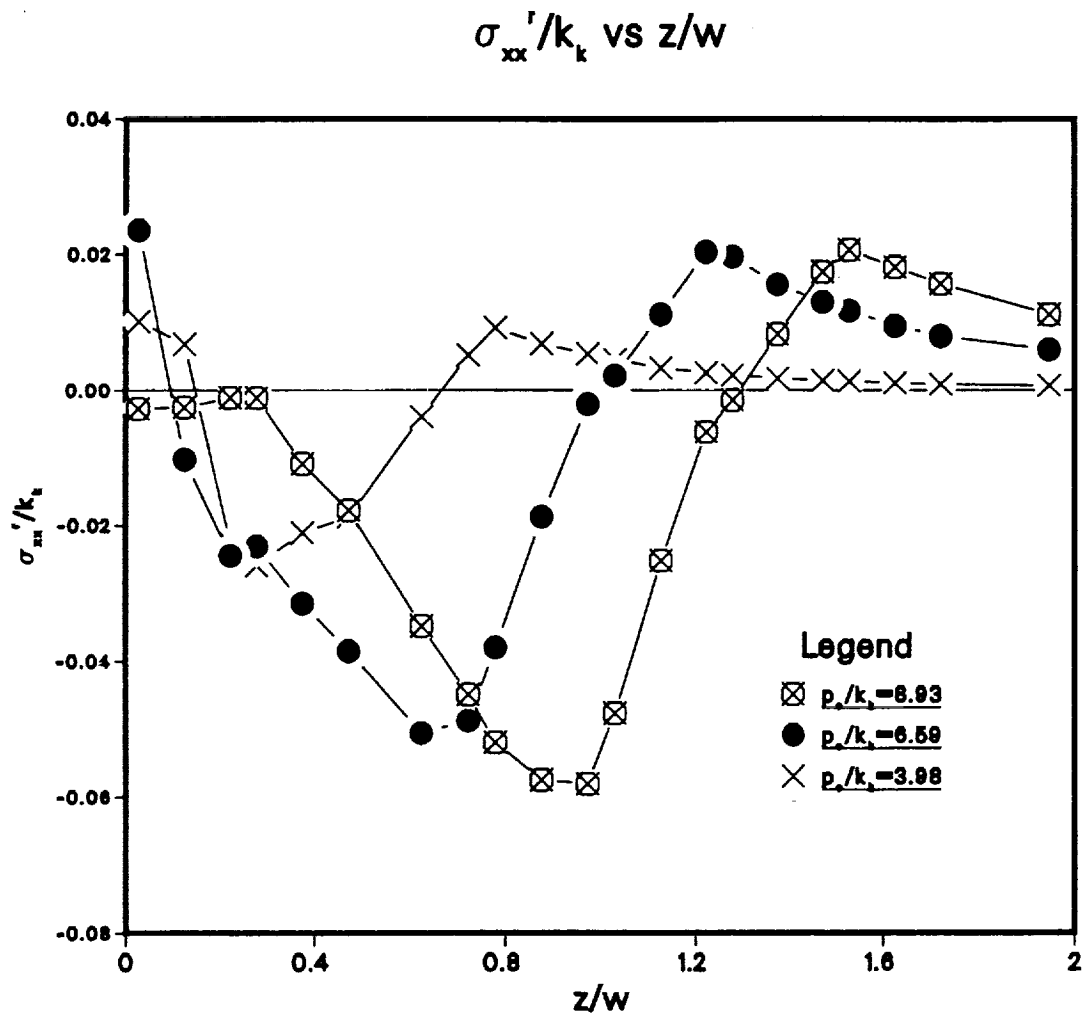


Figure 3.3.15 Distribution of residual direct stresses at the center of the mesh in the axial direction (normalized with respect to the kinematic shear yield strength) as a function of the depth (normalized with respect to the semi-major contact width). Results for the three different loadings are indicated in the Fig.

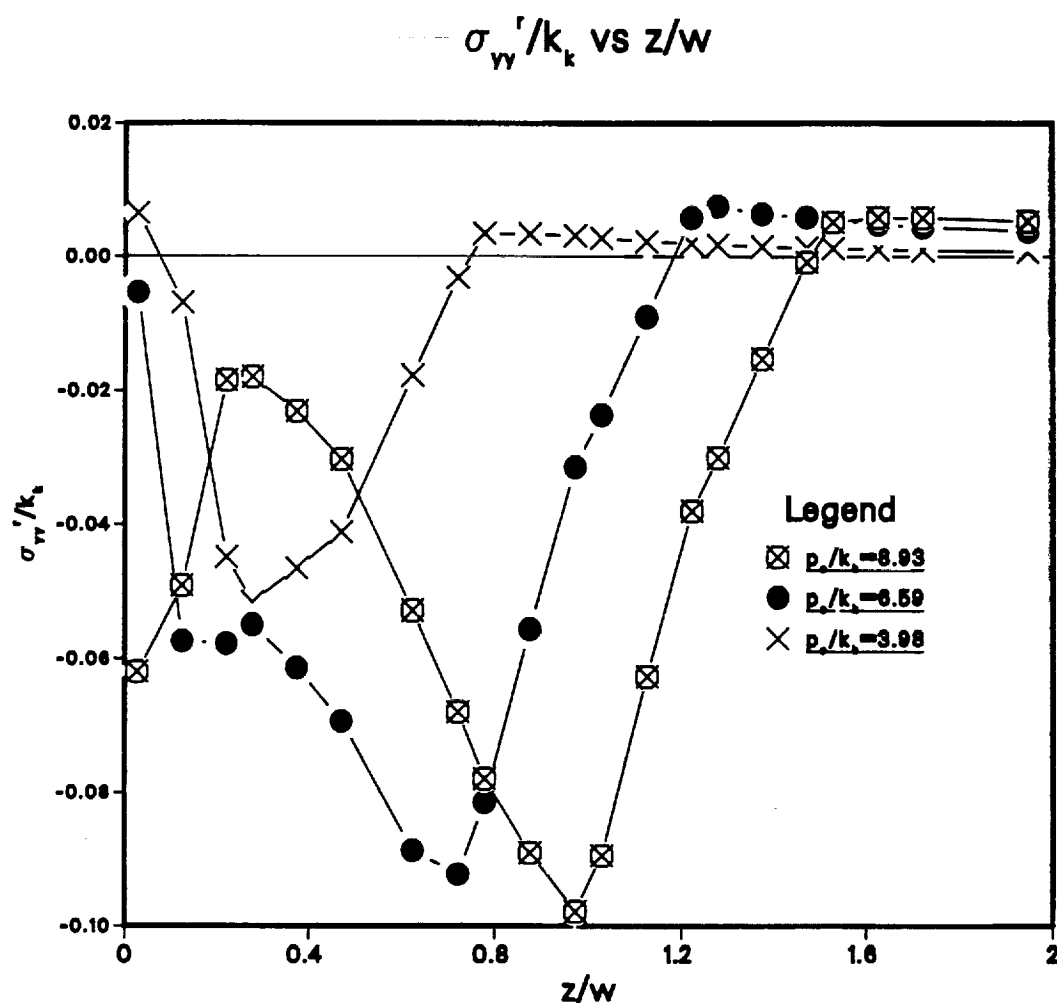


Figure 3.3.16 Distribution of residual direct stresses at the center of the mesh in the circumferential direction (normalized with respect to the kinematic shear yield strength) as a function of the depth (normalized with respect to the semi-major contact width). Results for the three different loadings are indicated in the Fig.

Table 3.3.1 Direct residual stresses

Reference	σ^r_{xx}	σ^r_{yy}	σ^r_{zz}
Groom (1983)	-150	-180	-30
Bower and Cheesewright(1988)	-150	-220	-60
Bhargava (1988), $p_o/k_k=5$	-70	-63	NA
McDowell and Moyar(1986)	NA	-212	NA
Kulkarni ¹⁰ (1990a), $p_o/k_k=9.2$	-115	-180	-40
Present Work:			
$p_o/k_k=8.93$	-36 14	-59 6	-16 14
pure rolling $p_o/k_k=6.59$	-32 19	-56 7	-16 18
$p_o/k_k=3.98$	-16 7	-32 5	-7 6
roll. + slid. $p_o/k_k=8.93$	-45 110	-121 247	-68 58

Note 1: The peak compressive and tensile residual stresses are presented for the three different contact pressures under pure rolling, and also for the rolling plus 0.2 percent sliding case.

Note 2: All the stresses are expressed in MPa, and for the present work, for the second pass of the load.

¹⁰ The contact ellipsoid was elongated along the rolling direction for this 3D calculation.

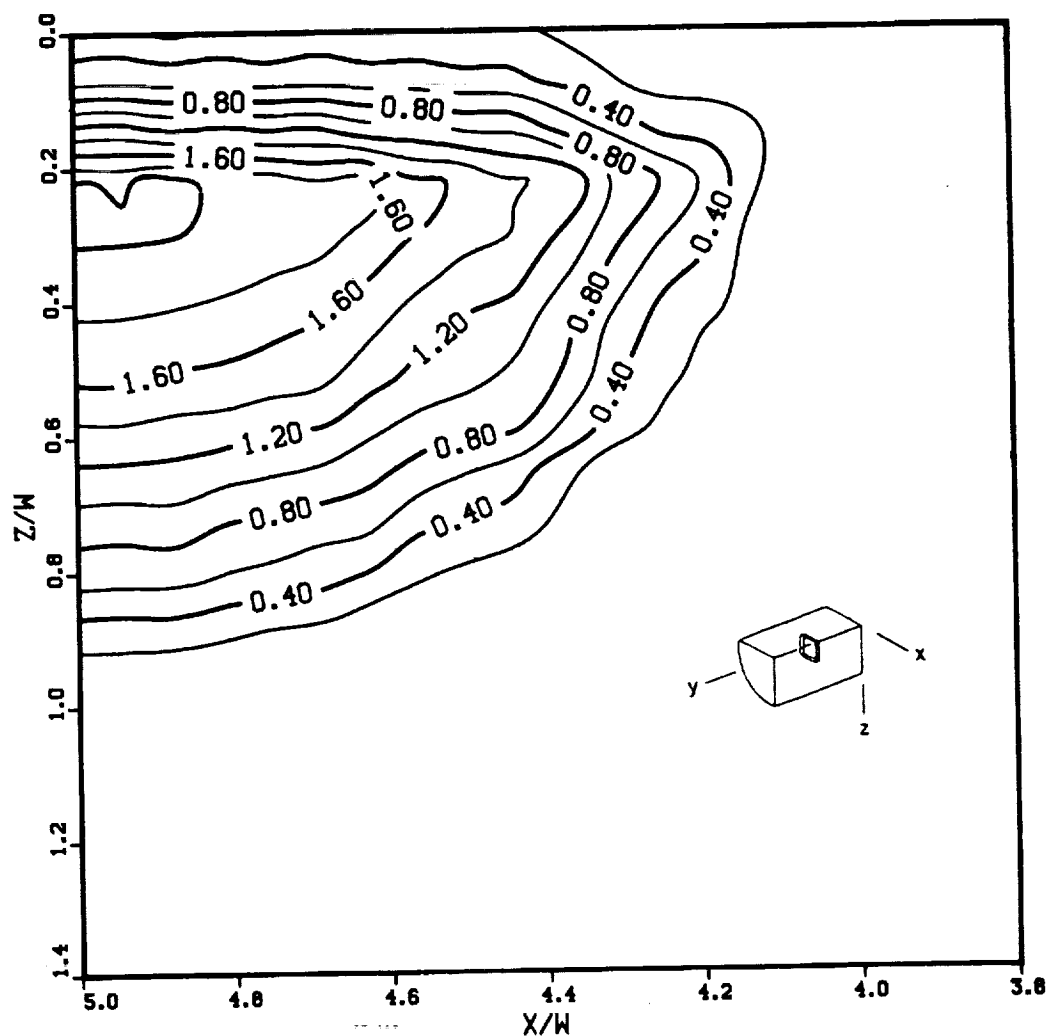


Figure 3.3.18 Iso-contours of the half equivalent plastic strain range for pure rolling with high loading ($p_0/k \approx 9$). The contours are for a slice of material located at the center of the mesh, as shown on the schematics. Strain values are shown magnified $\times 10^3$.

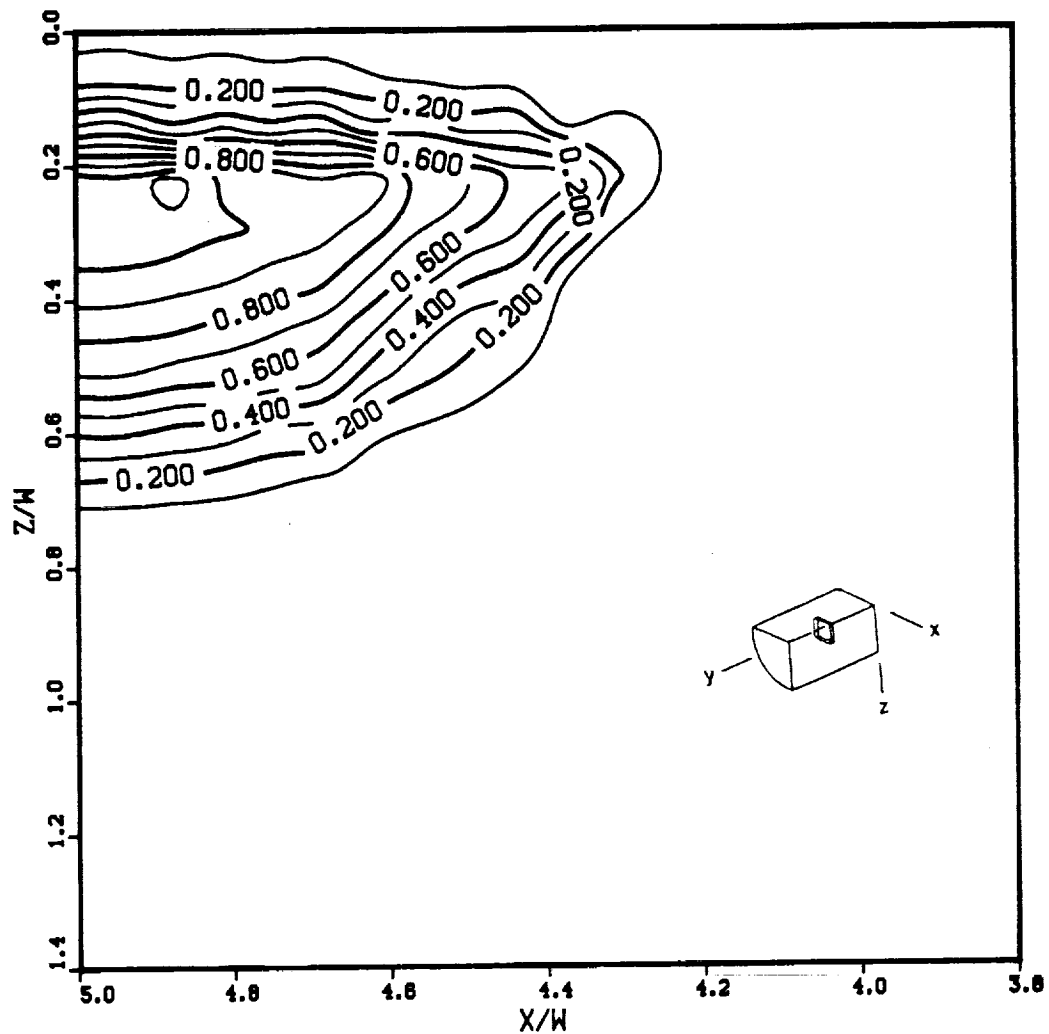


Figure 3.3.19 Iso-contours of the half equivalent plastic strain range for pure rolling with medium loading ($p_0/k \approx 6$). The contours are for a slice of material located at the center of the mesh, as shown on the schematics. Strain values are shown magnified $\times 10^3$.

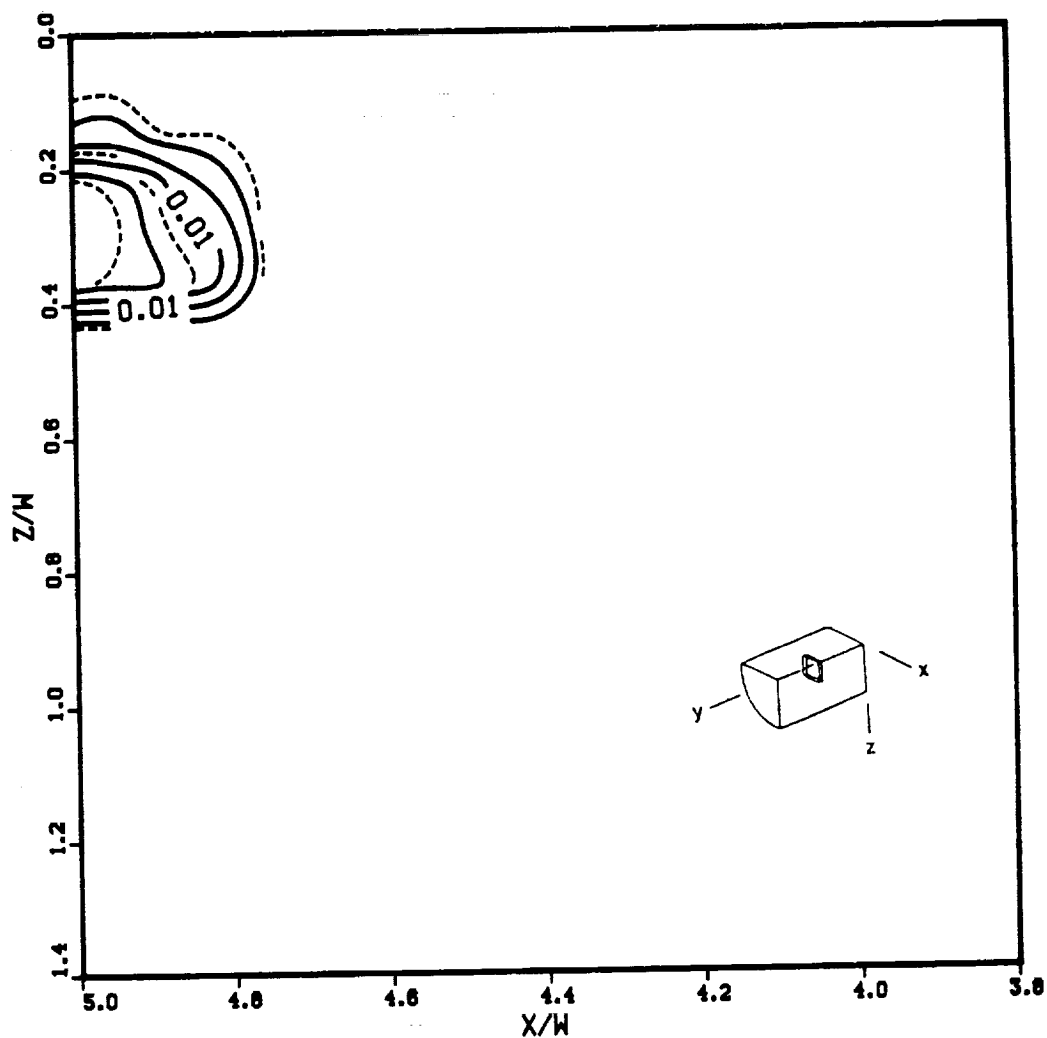


Figure 3.3.20 Iso-contours of the half equivalent plastic strain range for pure rolling with low loading ($p_0/k \approx 4$). The contours are for a slice of material located at the center of the mesh, as shown on the schematics. Strain values are shown magnified $\times 10^3$.

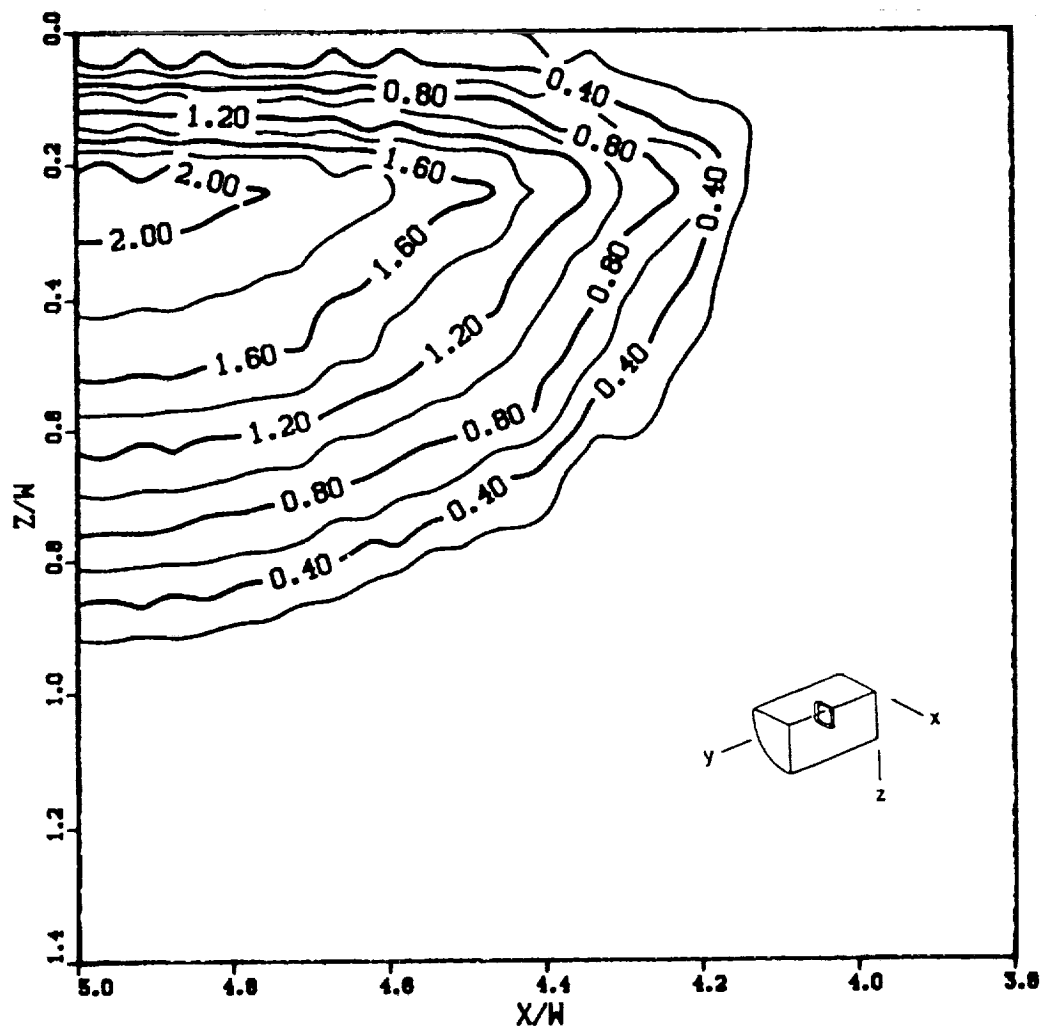


Figure 3.3.21 Iso-contours of the half equivalent plastic strain range for rolling-plus-sliding with high loading ($p_0/k \approx 9$). The contours are for a slice of material located at the center of the mesh, as shown on the schematics. Strain values are shown magnified $\times 10^3$.

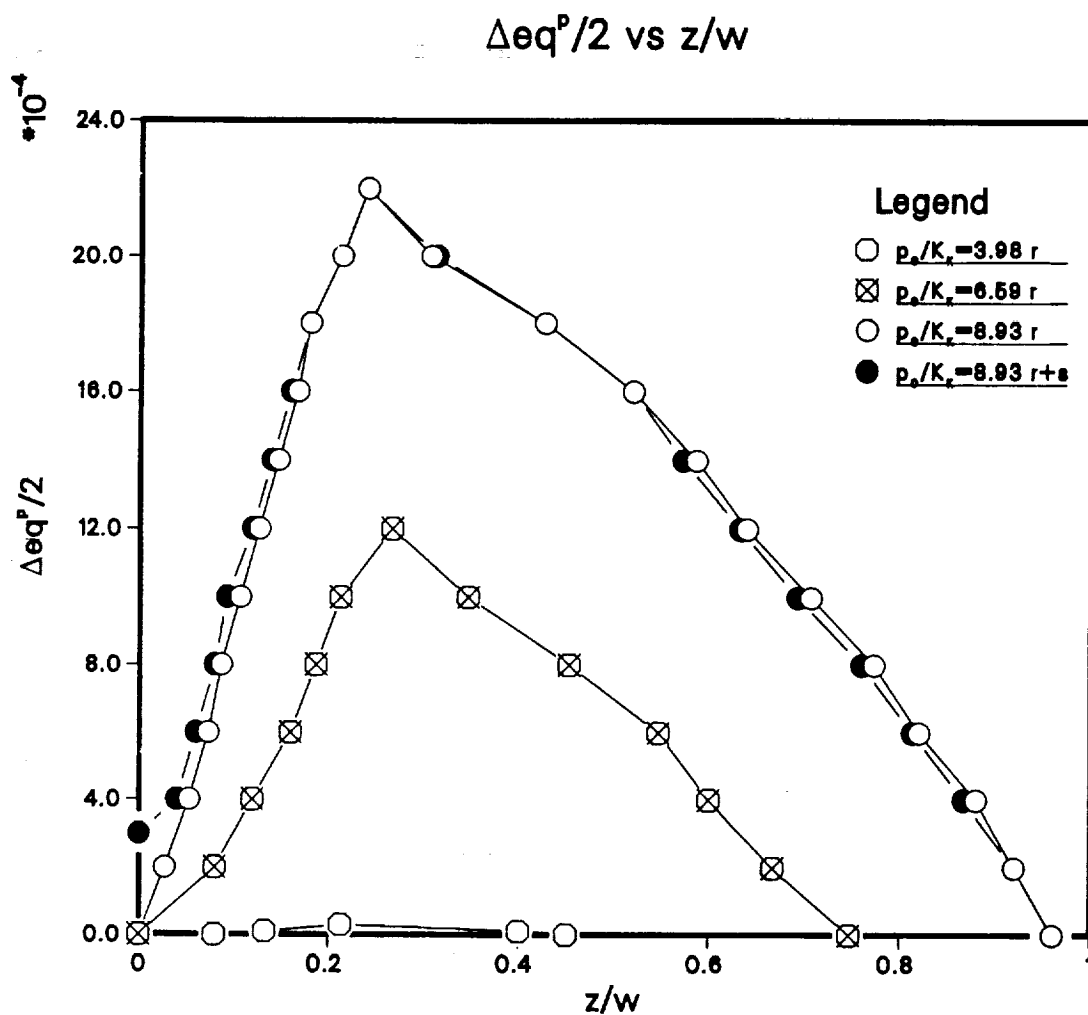


Figure 3.3.22 Comparison of the variation in the half plastic strain range with depth, for the three different loads under pure rolling, and the high load under rolling-plus-sliding (these values are taken at the same locations as Figs. 3.3.18-21)

3.4 Three Dimensional Rolling Contact of Hardened Aluminum

The Mises equivalent stress distribution for the Aluminum properties is shown in Figure 3.4.1¹¹. This figure shows the equivalent stress contours on two different sections of the mesh in the vicinity of the contact, as indicated in the schematic drawings. The peak value of the equivalent stress occurs at a depth of approximately $0.5w$ below the surface.

Figure 3.4.2 illustrates the equivalent plastic strain contours underneath the contact. The equivalent plastic strain, ϵ^P_{eq} , is obtained by calculating the equivalent plastic strain increment, $d\epsilon^P_{eq}$, for each incremental pressure translation, and integrating it over the entire loading history. It is a cumulative measure of plasticity in the half space. Plastic strain activity extends to a depth of approximately $1w$ below the surface and the peak plastic strain is located at a depth of approximately $0.4w$, as shown in Figure 3.4.2.

The distribution of the continuing cyclic plasticity during the first and second contact sequences is shown in Figure 3.4.3. This shows the variation with depth of equivalent plastic strain range, $\Delta\epsilon^P$, which peaks at a relative depth of $z/w = 0.45$. The magnitude of ϵ^P is non-zero up to a relative depth of $z/w = 1.5$ for the first contact. However, for the second contact (or steady state), ϵ^P extends only to a relative depth of $z/w = 1.0w$. The magnitude of peak ϵ^P remains essentially the same between the first and the second contacts.

The residual stresses developed as a result of plastic deformation of the rim at the end of the second contact are illustrated in Figures 3.4.4 through 3.4.7. Contours of axial, σ_x , and circumferential, σ_y , residual stress contours are shown in Figures 3.4.4 and 3.4.5. Residual stresses become tensile very close to the surface, within a relative depth of $z/w = 0.2$. Figures 3.4.6 and 3.4.7 illustrate the variation of σ_x and σ_y with relative depth. Peak residual stresses are compressive and are located at approximately $z/w = 0.9$.

The cyclic shear stress-shear strain history experienced by the model for the two contacts is shown in Figure 3.4.8. The point for which the stress-strain values are obtained is located at a relative depth: $z=0.4w$. The non-fully reversed hysteresis loop for the first contact is fully reversed for the second contact. Thus the idealized ELKP material behavior allows no ratchetting or unidirectional accumulation of plastic strains.

The permanent microstructural damage in 7075-T6 alloy is

¹¹ The distribution of individual stress and strain components are presented in Appendix 3.

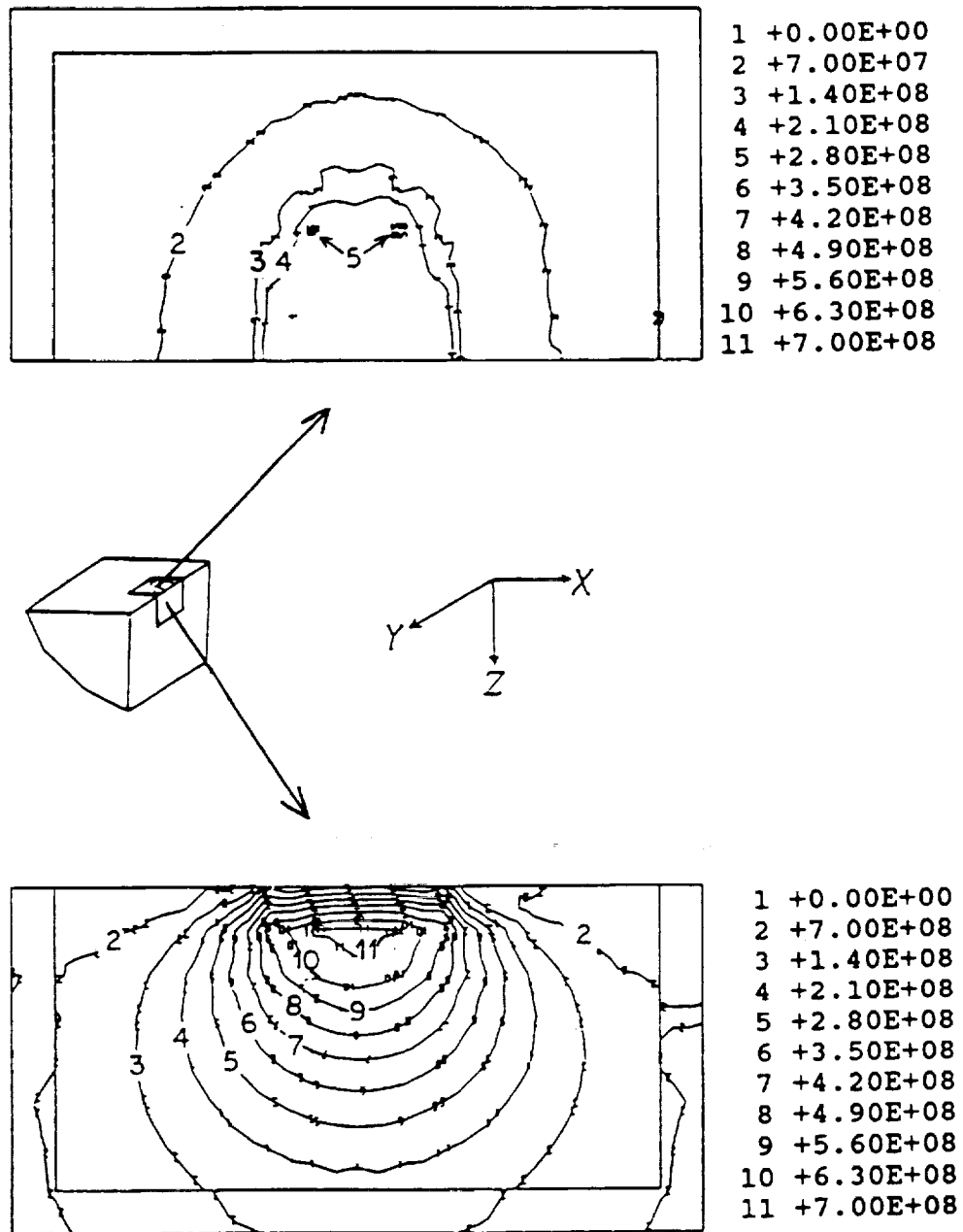


Figure 3.4.1. Contours of von Mises equivalent stress on two different sections of the mesh (the sections are schematically indicated by the side of each figure). The numbers on the individual contours represent different equivalent values of the contours.

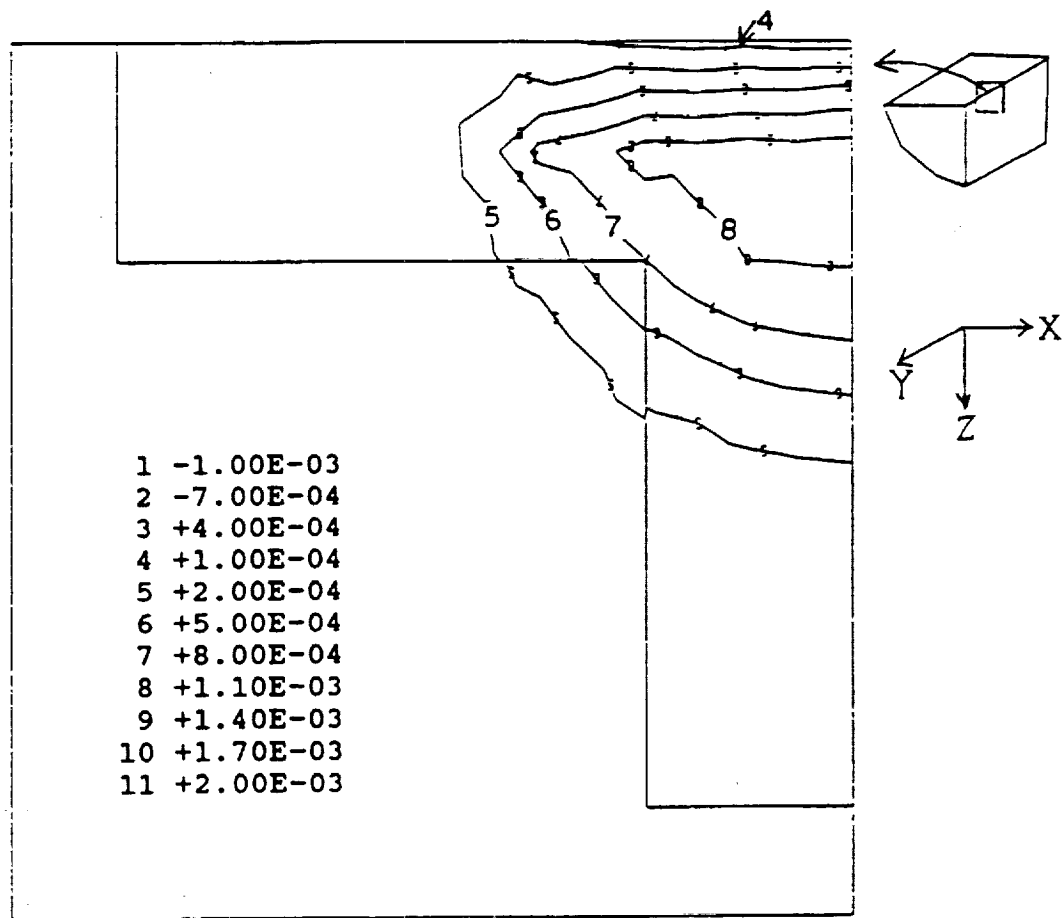


Figure 3.4.2 Equivalent plastic strain contours representing the plastic strain history as the pressure ellipsoid completes one translation.

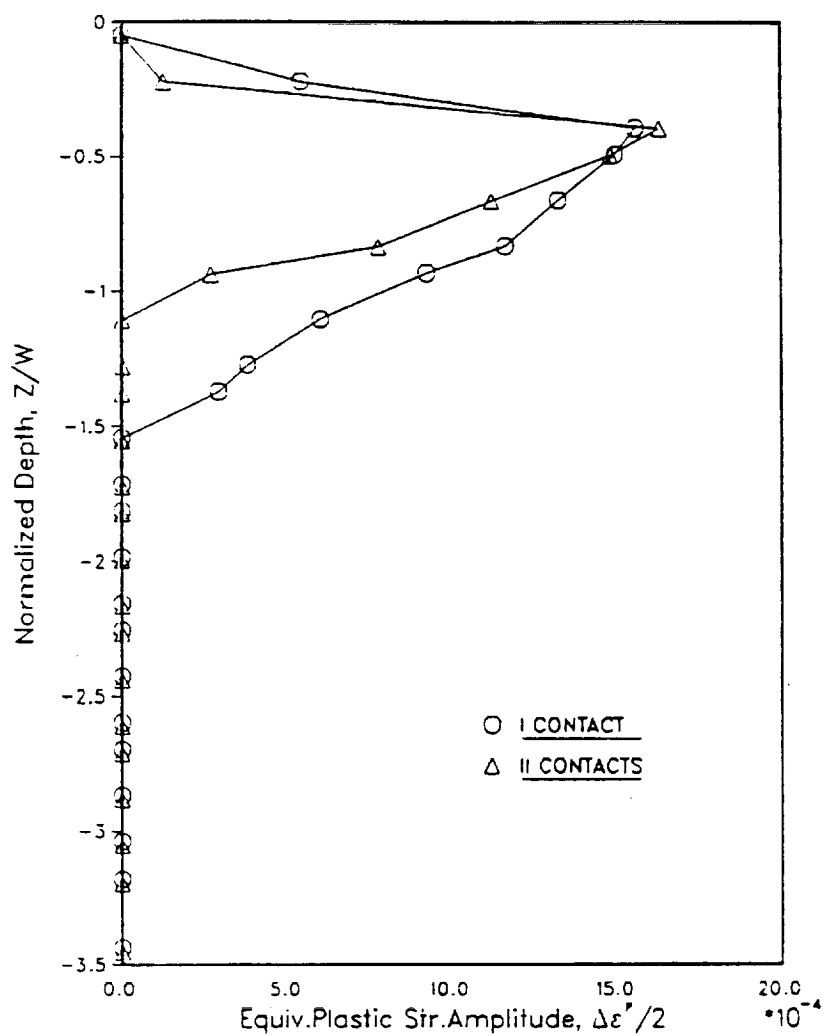


Figure 3.4.3 Variation of the half-equivalent plastic strain range, plastic strain range, $\epsilon_p/2$, with normalized depth, for the first and second contacts.

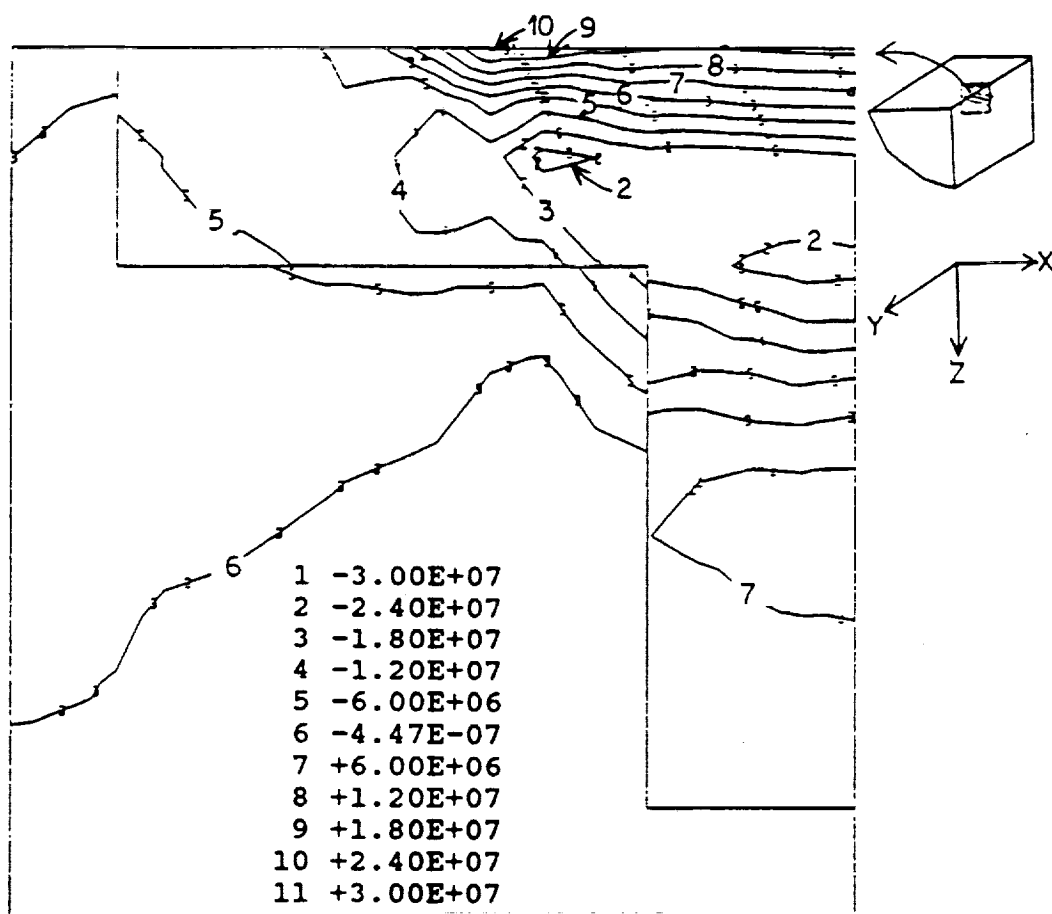


Figure 3.4.4 Contours of the out-of-plane (or axial) residual stress, σ_x^r . The stress values are tensile close to the rolling surface (as indicated by the contour levels 7 through 11).

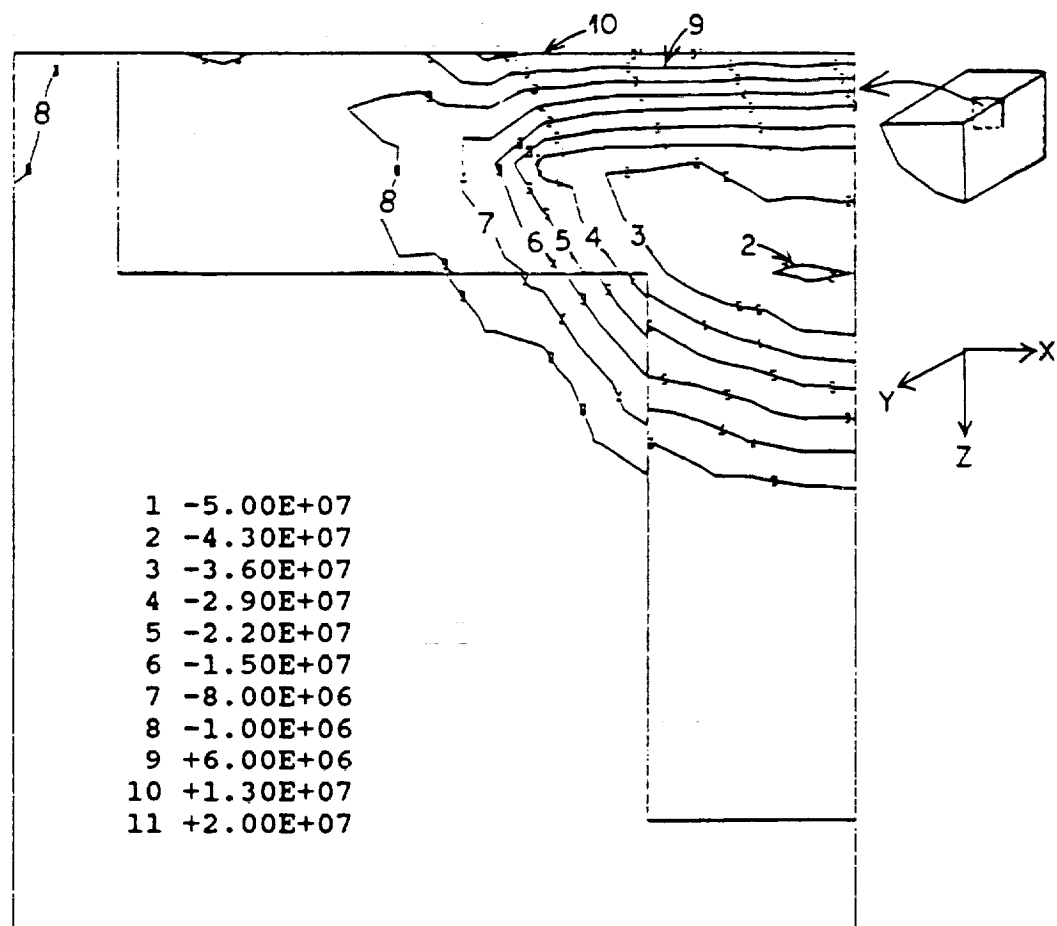


Figure 3.4.5 Contours of the circumferential residual stress, σ_{r_y} . The stress values are tensile close to the rolling surface (as indicated by the contour levels 9 through 11).

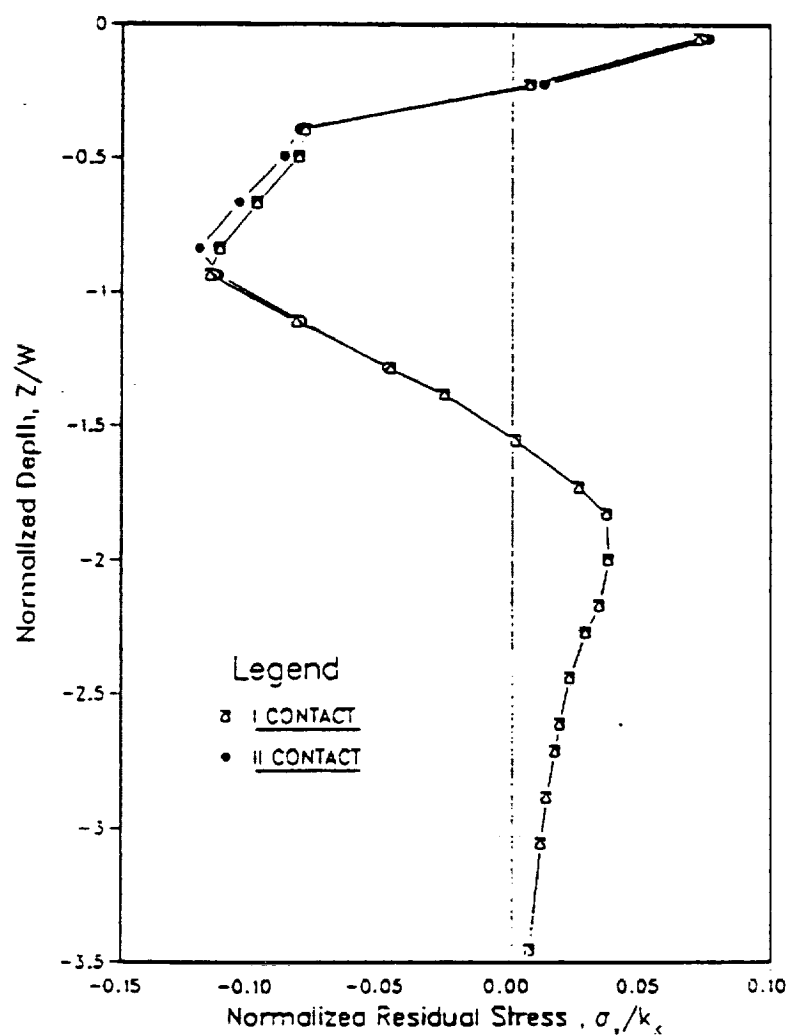


Figure 3.4.6 Variation of the out-of-plane (or axial) residual stress, σ^r_x , with normalized depth. The values of σ^r_x are obtained from integration points located near the middle of the mesh, where the effects of the boundary are not significant.

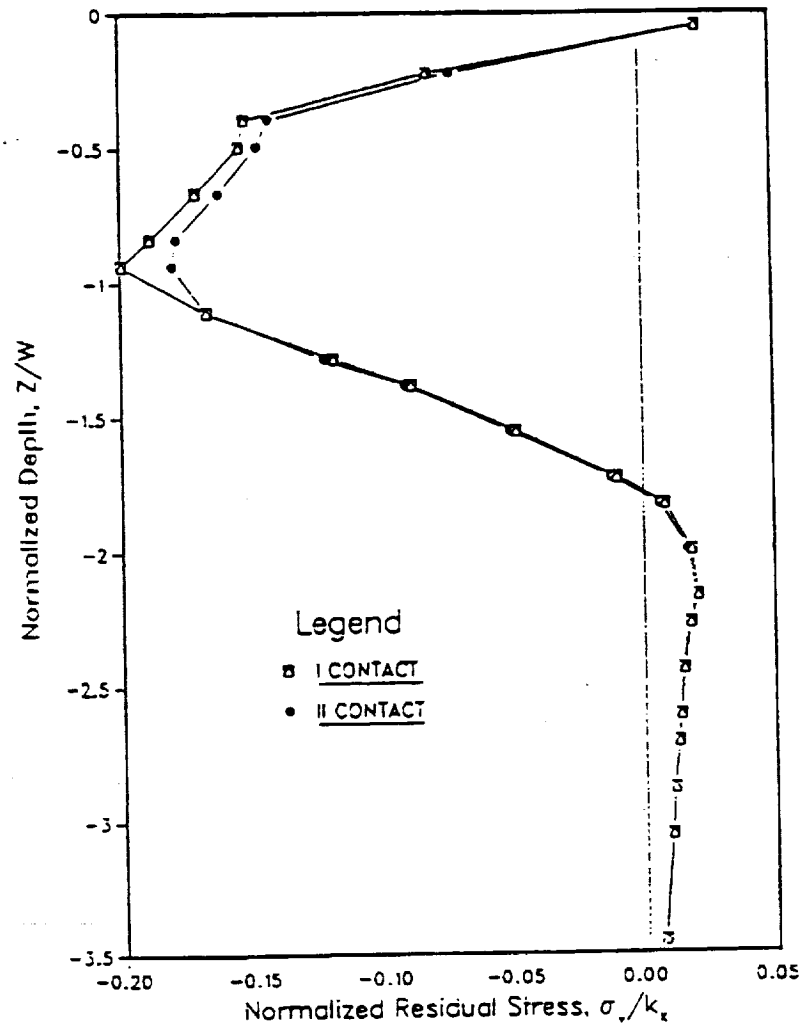


Figure 3.4.7 Variation of the circumferential residual stress, σ_r , with normalized depth. The values of σ_r are obtained from integration points located near the middle of the mesh, where the effects of the boundary are not significant.

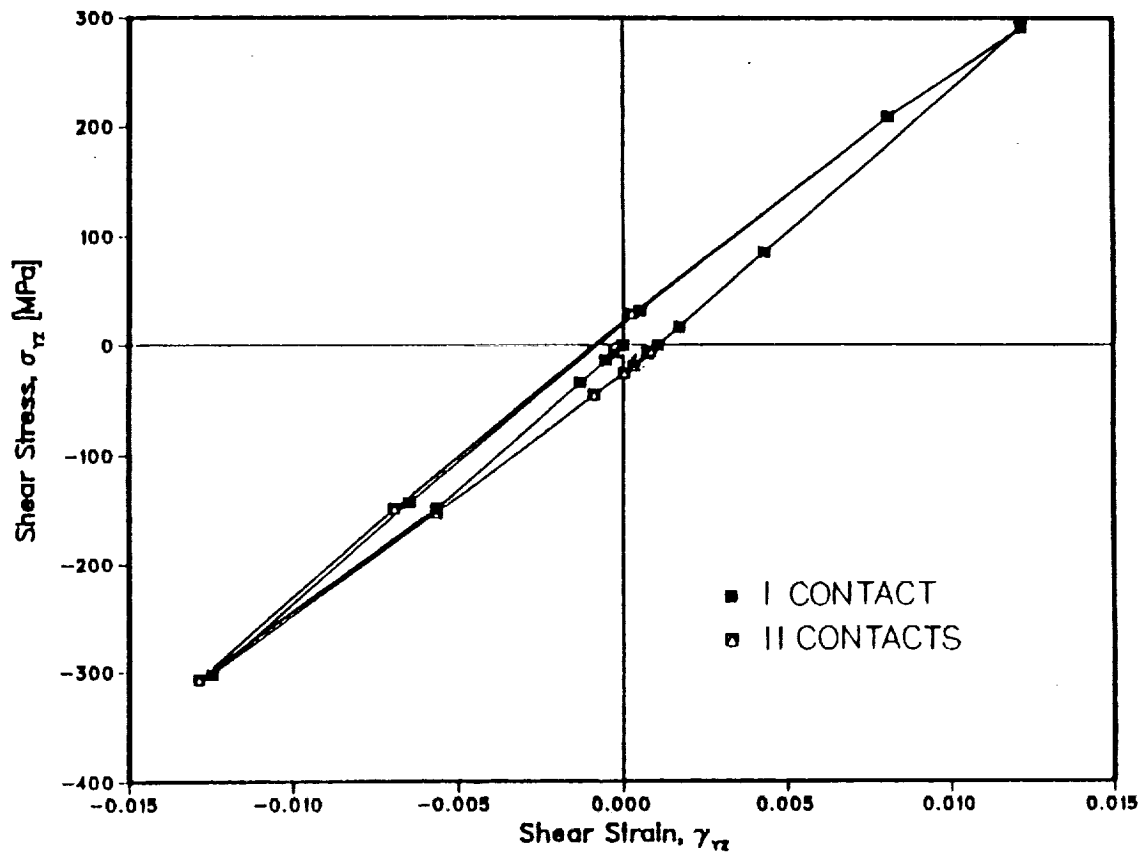


Figure 3.4.8 In-plane shear stress-shear strain history experienced by a point in the model at a relative depth: $z = 0.4 w$. This is also the location of the maximum continuing plastic strain, ϵ^P .

caused by continuing plasticity in the rim. The damage is characterized by the early formation of slip bands underneath the contact, resulting in a gradual destruction of the grain structure followed by sub-surface crack initiation. As illustrated in Figures 3.4.9 and 3.4.10, the shape and the extent of microstructural damage correlate very well with the equivalent plastic strain distribution obtained from finite element calculations.

Sub-surface cracks occur within the plastic zone at depths: $0.1 \leq z/w \leq 1.2$ underneath the running track (here, the normalizing parameter is the semi-minor axis of the contact ellipse, $w = 0.102$ mm). The distribution of sub-surface cracks as a function of depth is shown in Figure 3.4.11. The equivalent plastic strain variation drawn to the same scale is also shown in Figure 3.4.11. While the extent to which cracks occur below the surface correlates well with the extent of continuing plasticity, the majority of the cracks do not occur at $z/w = 0.4$ where the plastic strain peaks. Instead, a large number of cracks are found closer to the surface at $z/w = 0.20$. The distribution of crack length below the surface is shown in Figure 3.4.12. Again, the longest cracks are located at $z/w = 0.20$, while the average length of cracks at $z/w = 0.40$ is approximately 10x smaller. A plausible explanation of the high occurrence of long cracks at $z/w = 0.20$ from the surface is that the compressive residual stresses decrease in magnitude at this depth. For instance, the circumferential and the out-of-plane residual stress distributions, illustrated in Figure 3.4.12 shows that high levels of compressive residual stresses at depths: $0.30 \leq z/w \leq 1.2$ gradually diminish and become tensile at depths: $z/w \leq 0.2$. Therefore, the process of crack initiation and growth resulting from peak plastic activity is impeded by the presence of high compressive residual stresses.

The following sequence of events occurs in 7075-T6 aluminum before the final spall failure. Directly underneath the contact at depths: $z \approx 1.0w$, slip lines gradually develop as a result of continuing cyclic plasticity in the initial stages, i.e., $N \leq 10^3$ cycles. These slip lines probably represent plastic activity in the primary slip systems. As the plastic damage continues, i.e., $10^3 \leq N \leq 10^6$, more slip systems are activated. Gradually the slip bands become less discrete giving a destroyed appearance to the grain structure. The only visible slip bands at this stage are either very close to the surface: $z/w \leq 0.1$, or at the outer edges of the damaged region: $z/w \geq 1.2$, where the plastic strain tapers off. Small cracks nucleate within the damaged region: $0.10 \leq z/w \leq 1.2$. Smaller levels of compressive residual stress favor both the initiation and the growth of cracks at $z/w \approx 0.2$. As one of the crack branches reaches the surface, a chunk of material breaks off, leaving behind a spall pit. As this process continues, the spall pit grows larger and deeper into the rim. These steps are schematically illustrated in Figure 3.4.13.

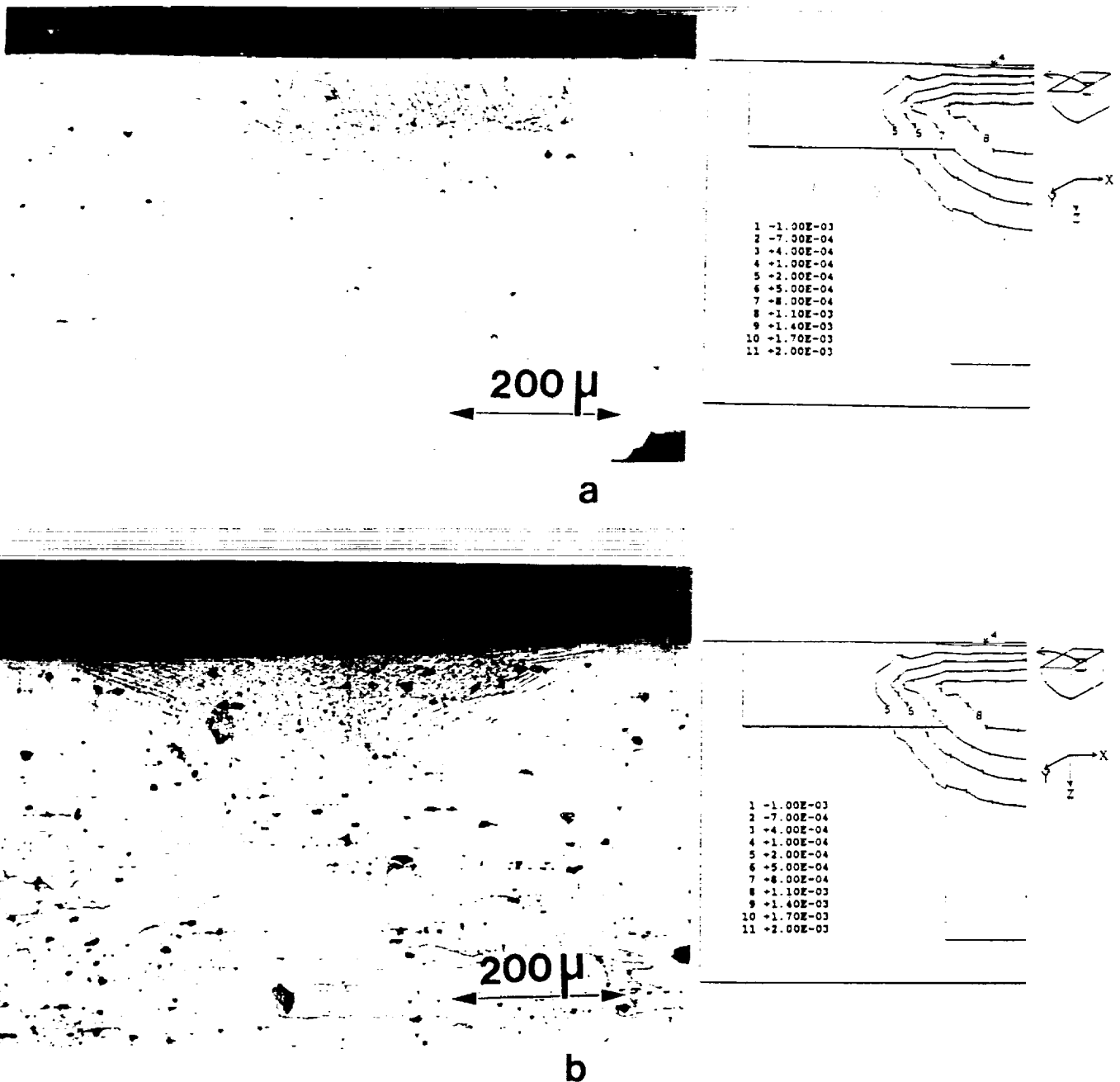


Figure 3.4.9 Comparison of plastic strain contours obtained from finite element calculations and the microstructural changes produced by rolling: (a) after 10^3 contacts, and (b) after 2.3×10^6 contacts. The microstructure and the adjoining contours are shown on the same scale.

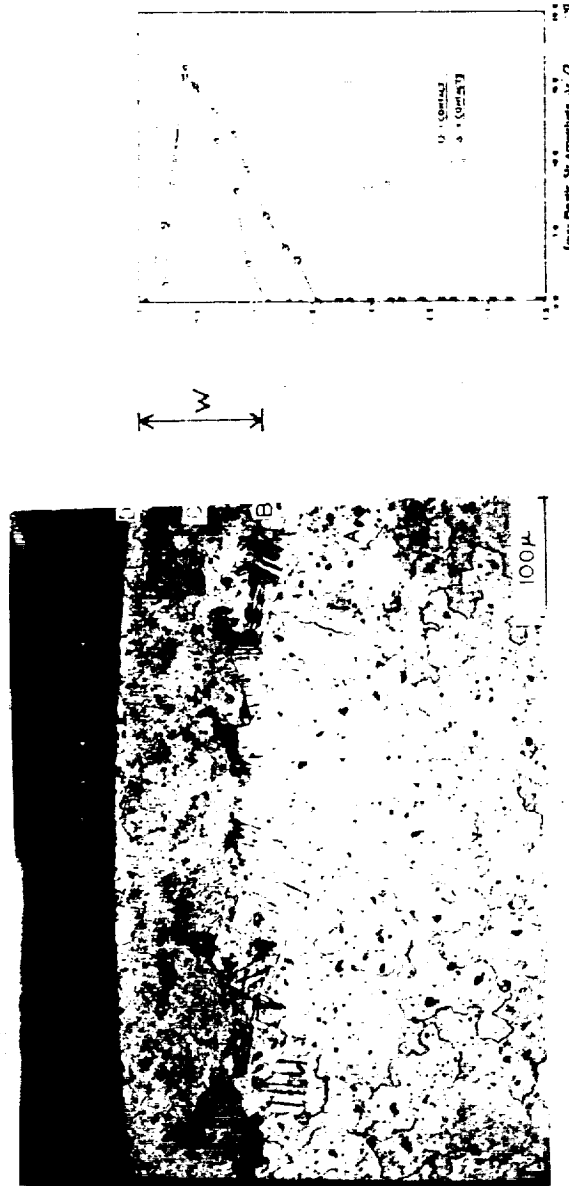


Figure 3.4.10 Comparison of half-equivalent plastic strain range distribution obtained from finite element calculations and the microstructural changes produced by rolling on a section parallel to the rolling direction.

ORIGINAL PAGE IS
OF POOR QUALITY

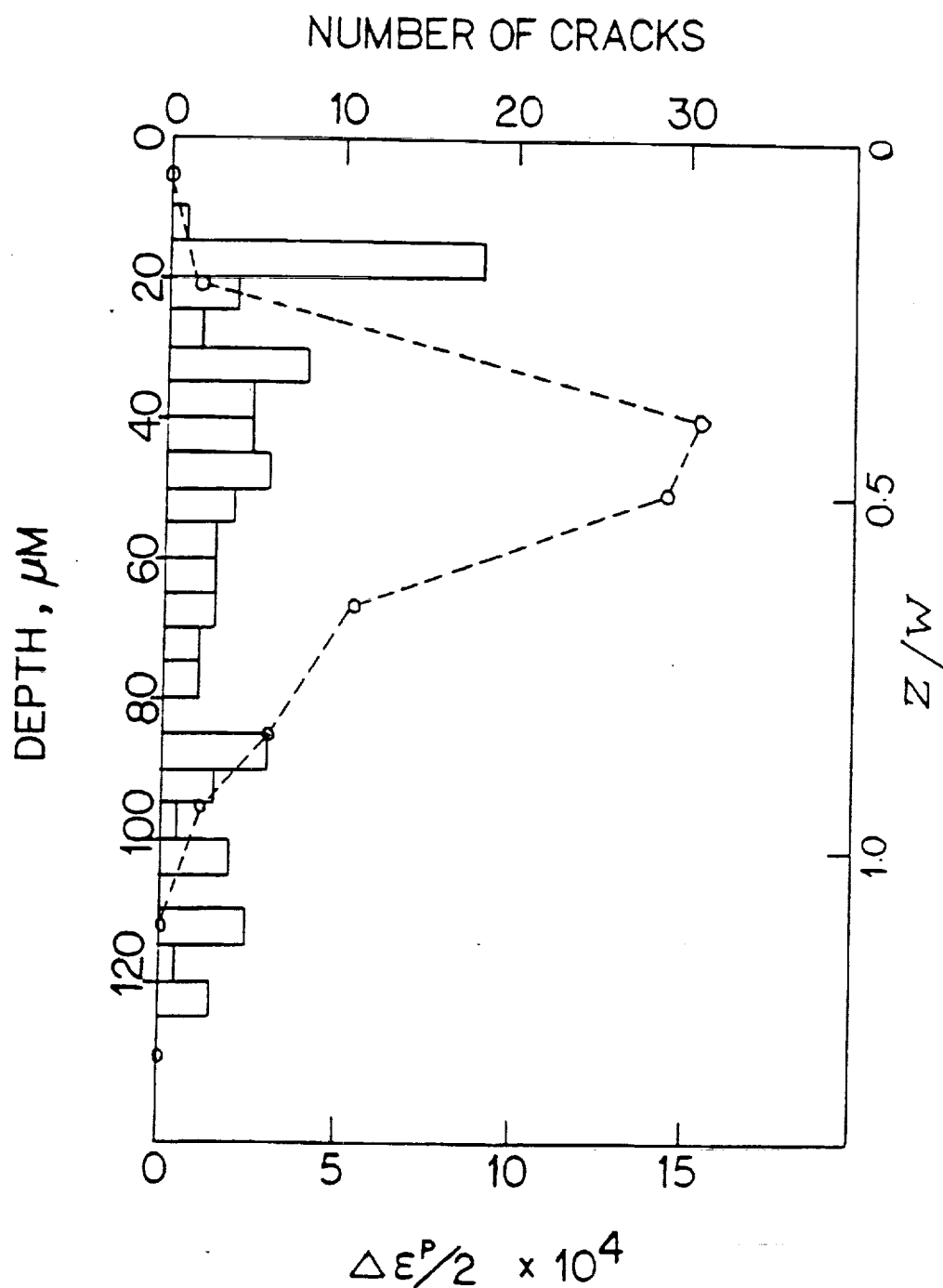


Figure 3.4.11 Distribution of sub-surface cracks with depth below the surface. The variation of the equivalent plastic strain amplitude, $\Delta\epsilon^P/2$, is indicated by dashed lines.

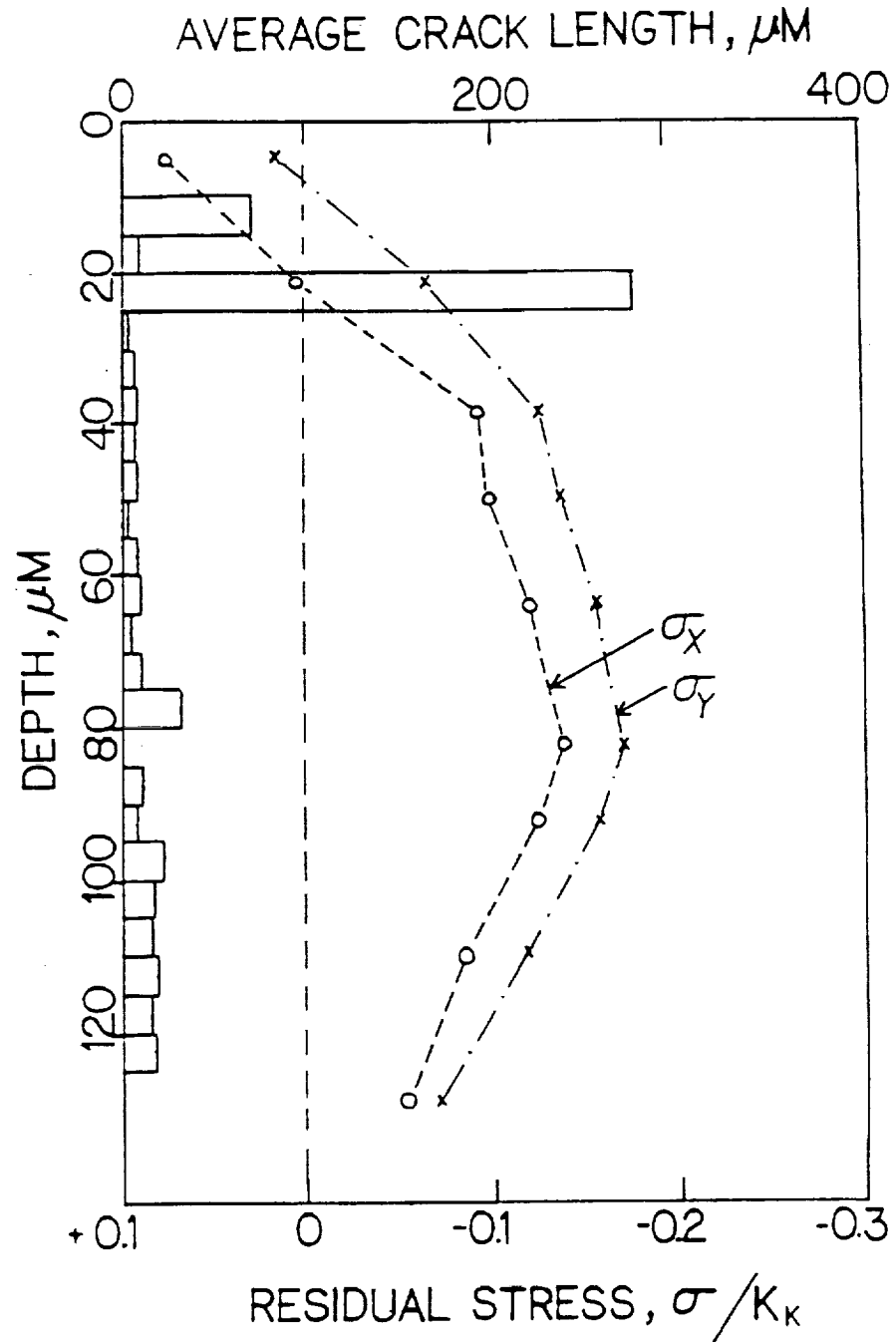


Figure 3.4.12 Distribution of sub-surface crack length with depth below the surface. The variation of the axial (σ_x) and circumferential (σ_y) residual stresses are indicated by the dashed lines.

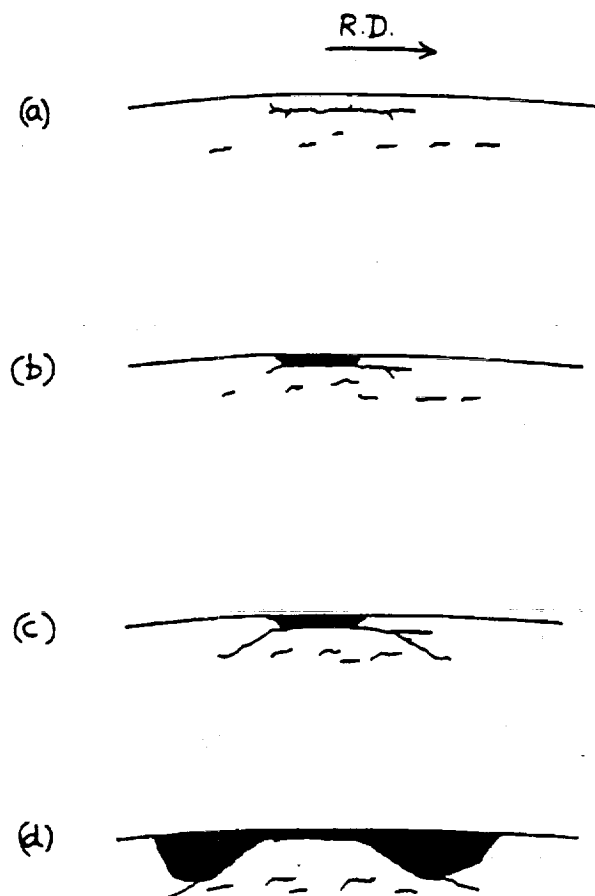


Figure 3.4.13 Schematic diagram of spall formation in 7075-T6 aluminum.

The implication of these results is that compressive residual stresses retard the process of sub-surface crack nucleation and growth even in the presence of continuing plasticity. Hence, longer lives can be obtained by artificially installing residual compressive stresses in a relatively shallow region under the surface, i.e., $z/w \leq 0.25$, or by altering the properties of this shallow layer. The rolling contact performance is strongly determined by the cyclic stress-strain response of the material. In spite of the microstructural differences between bearing steels and 7075-T6 aluminum, the cyclic stress-strain response of these two materials is qualitatively similar. Therefore, the extension of the relationship between residual stresses, cyclic plasticity and sub-surface crack nucleation from 7075-T6 aluminum to bearing steels is justifiable.

Some of the major limitations of the present work are noteworthy. Cyclic axial tests do not reproduce the non-proportional straining and rotation of principal shear directions that result from repeated rolling contact above shakedown. When the principal shear directions do not rotate, the cyclic damage is limited to a fewer number of favorably oriented slip systems and the damage is more intense. In addition, the absence of hydrostatic stresses and the larger stressed volume shorten the life in cyclic axial fatigue tests. This is a likely explanation for the 10^3 -fold difference between the rolling contact life and the cyclic axial tests. Also, in 7075-T6 aluminum, the precipitate particles are important contributors to strength¹². However, the effect of particles is ignored in the current study.

Future extension of the current study must treat (a) the strain rate effects on cyclic stress-strain response, (b) non-linearity of the kinematic hardening behavior, (c) the effect of particles, (d) thermal effects, and (e) anisotropy and texture effects. More work is needed to characterize the process of slip band appearance at a sub-microstructural scale.

3.5 Two Dimensional Rolling-Plus-Sliding with Heat Generation

Figure 3.5.1 shows the normalized residual stresses as a function of normalized depth, y/w (after unloading followed by cooling to the ambient temperature). Both the axial (σ_z) and the circumferential (σ_x) stresses are found to be tensile up to a depth of approximately 0.5 y/w . Figures 3.5.2 and 3.5.3 compare the circumferential and axial residual stresses

¹² Indeed, during the axial fatigue tests, a noticeable difference between the elastic slope in tension and compression was observed. This is probably an effect induced by the precipitate particles.

respectively for the thermo-mechanical and mechanical loading cases. Significant differences in magnitude and nature are observed. Fig. 3.5.4 presents the residual equivalent plastic strain contours for a section of the mesh, and Fig. 3.5.5 shows the residual equivalent plastic strain variation with depth. Peak plastic activity occurs slightly below the surface. Figure 3.5.6 shows a section of the residual state of the mesh (after cooling to the ambient temperature). The surface temperatures half way through the passes are shown in Fig. 3.5.7. The temperature distribution is asymmetric about $x/w = 0.0$. Fig. 3.5.8 shows the temperature contours half way through the third pass. Figures 3.5.9 and 3.5.10 present the hysteresis loops for the second and third passes, respectively. The loop is found to be closed after the third pass (second thermo mechanical pass) indicating fully reversed plasticity.

The analyses reveal that the incorporation of ELKP material properties greatly reduces the plastic strains generated compared with those resulting from perfect plasticity. The peak residual equivalent plastic strain (ϵ_p) obtained here, 2.5×10^{-3} ($p_0/k=5.0$, $\mu=0.1$), is equal to $1/25$ of the value obtained by Kulkarni et al. (1989): 6.0×10^{-2} ($p_0/k=5.0$, $\mu=0.1$), for elastic perfectly plastic behavior under the same operating conditions. From Fig. 3.5.5 it can be seen that heating does not have a large effect on the residual strains, but the peak strain occurs at a lesser depth. Further, it should be noted that no plastic strains extend beyond a depth of $2w$ (see Figs. 3.5.4 and 3.5.5).

A similar trend is seen for the residual stresses. The normalized stresses are found to be tensile, consistent with the findings of Kulkarni et al. (finite element model, 1988), and Muro et al. (X-ray measurements, 1973). But the magnitudes are far smaller than those obtained by Kulkarni et al. who reported a peak normalized circumferential residual stress of 1.7, clearly due to the difference in material properties. The residual stresses are found to be highly tensile and less compressive as compared to the non-heating case. The ratio of peak tensile stress to peak compressive stress is close to 2.5 for circumferential residual stresses, and 2.0 for axial residual stresses. A value of 2.0 has been reported by Muro et al. (1973), determined by X-ray measurements (see Figs. 3.5.1 and 3.5.2). The peak circumferential residual stresses are found to be about 1.4 times the peak axial residual stresses (Fig. 3.5.3). It should be noted that the residual stresses vanish at a depth of $2w$ as do the residual strains. The highest temperature after three passes is found to be 590 C. The temperature increment per pass decreases with each pass but the thermal steady state is not reached (Fig. 3.5.7). The temperature contours half way through the third pass show high temperatures away from the position of the load in the direction opposite to the translation of the load. Temperature gradients are seen to vanish after a depth of $0.5w$. This steep temperature gradient produces very high

RESIDUAL STRESSES

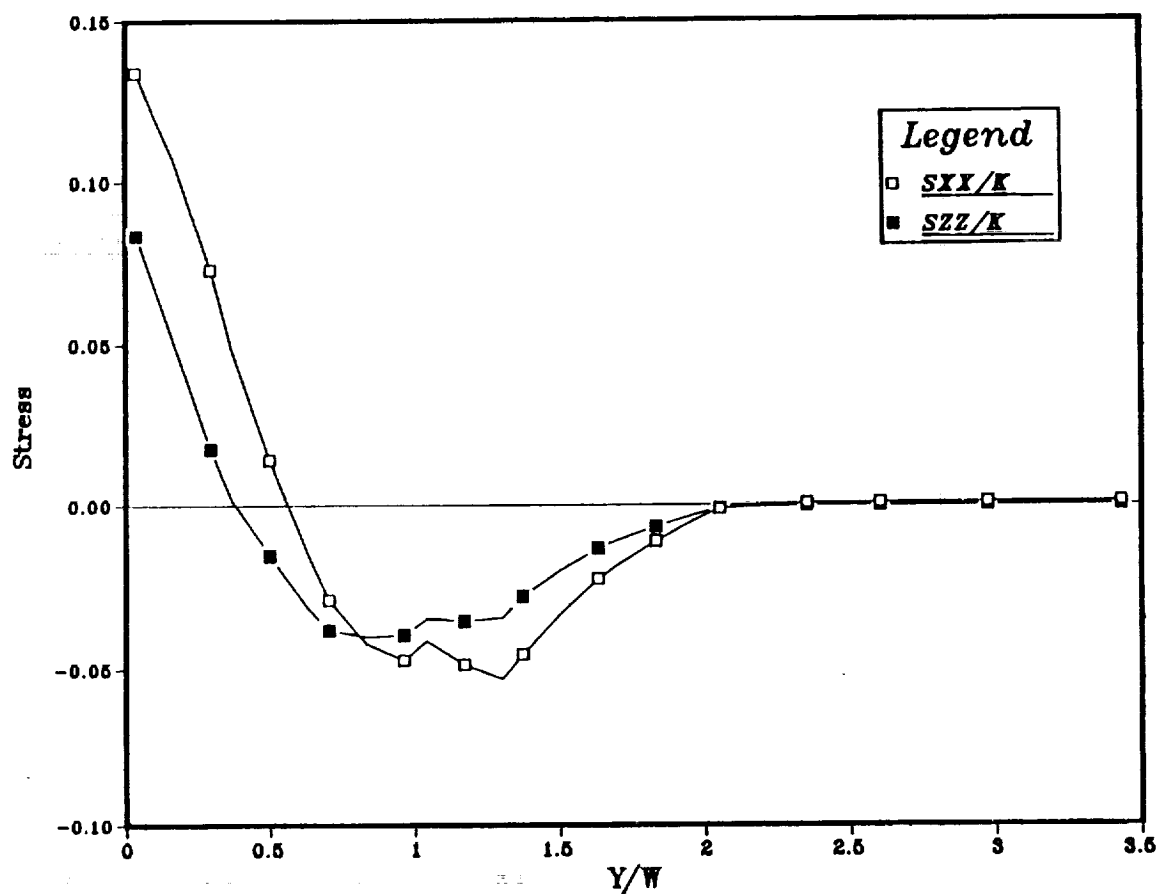


Figure 3.5.1 Normalized residual stresses as a function of the normalized depth, y/w . Mechanic unloading followed by cooling to the ambient temperature.

RESIDUAL CIRCUMFERENTIAL STRESSES

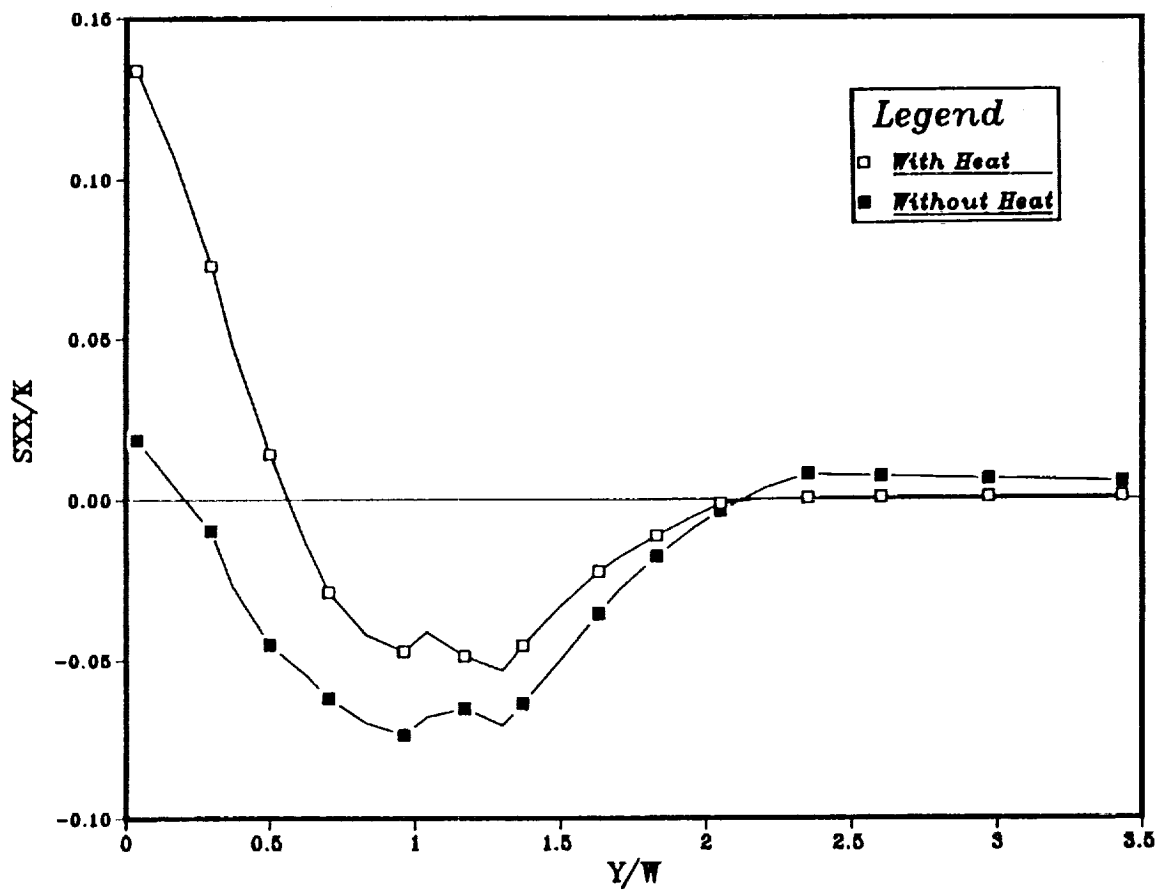


Figure 3.5.2 Circumferential residual stresses for thermomechanical (open symbols) and pure mechanical loading (filled symbols).

AXIAL RESIDUAL STRESSES

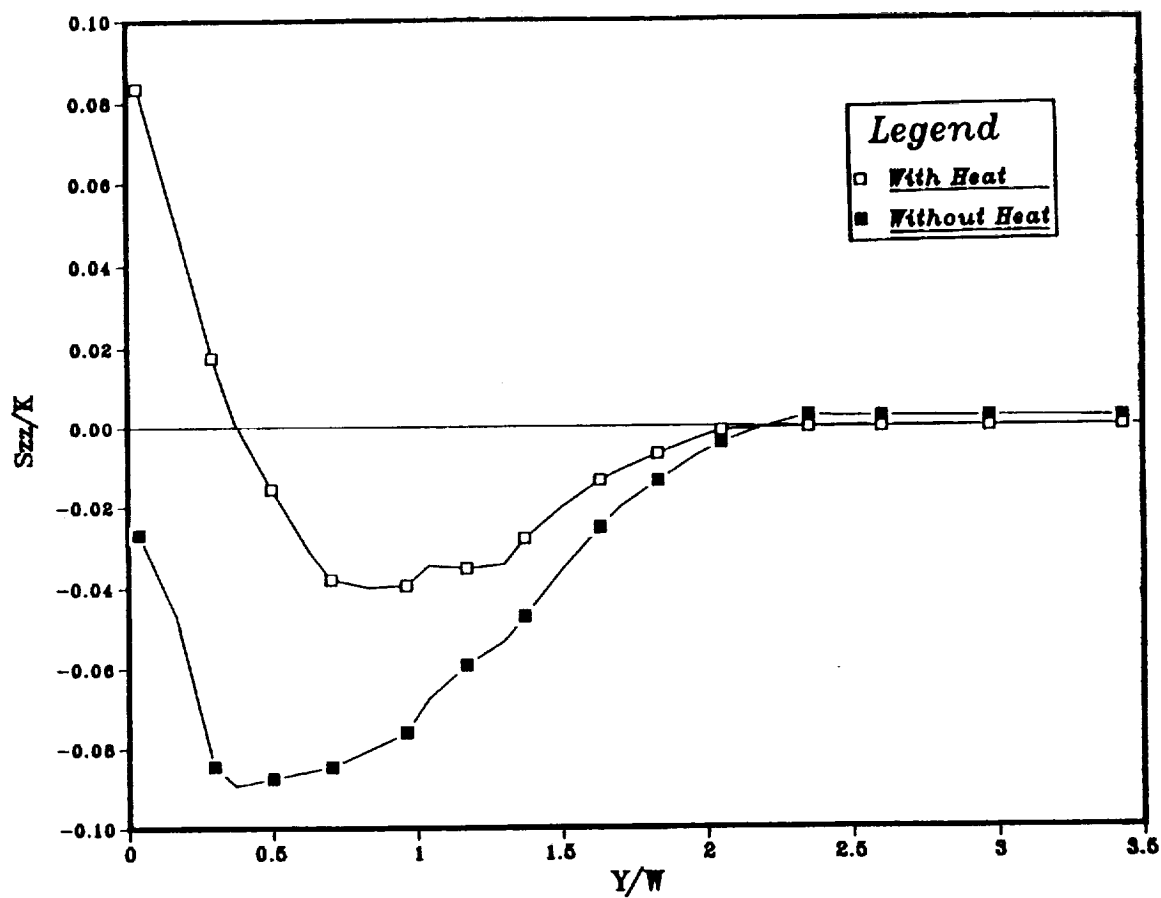


Figure 3.5.3 Axial residual stresses for thermomechanical (open symbols) and pure mechanical loading (filled symbols), for a point located at the center of the mesh.

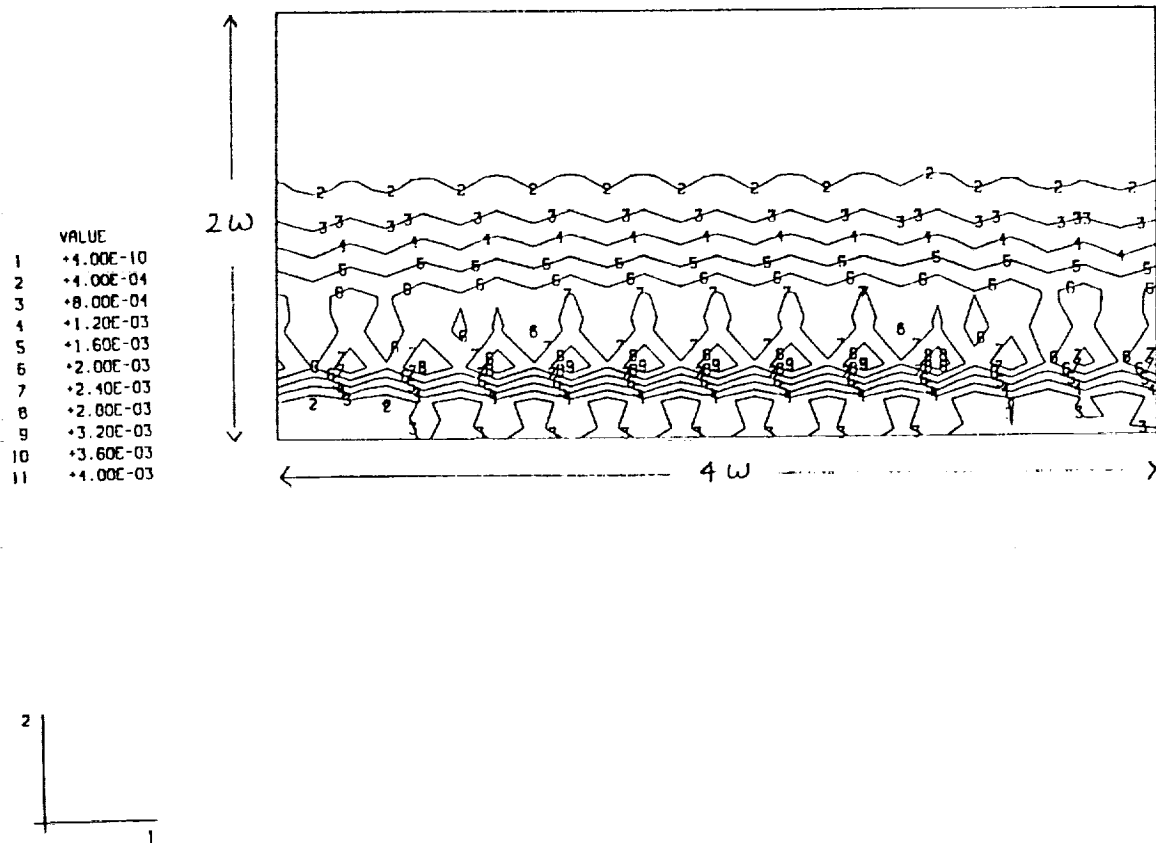


Figure 3.5.4 Residual equivalent plastic strain contours.

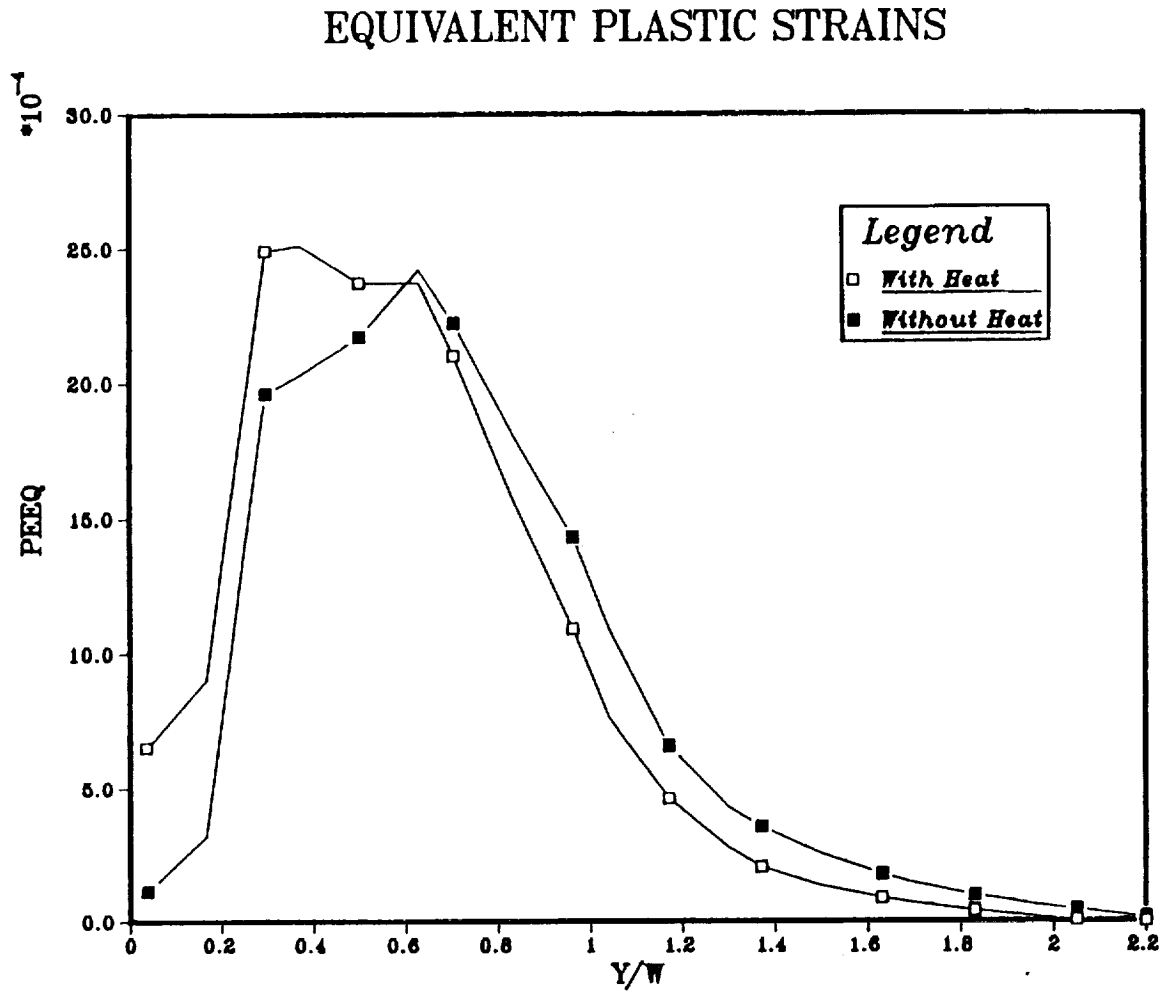


Figure 3.5.5 Residual equivalent plastic strain variation with depth for a point located at the center of the mesh.

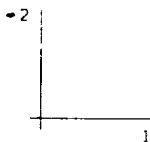
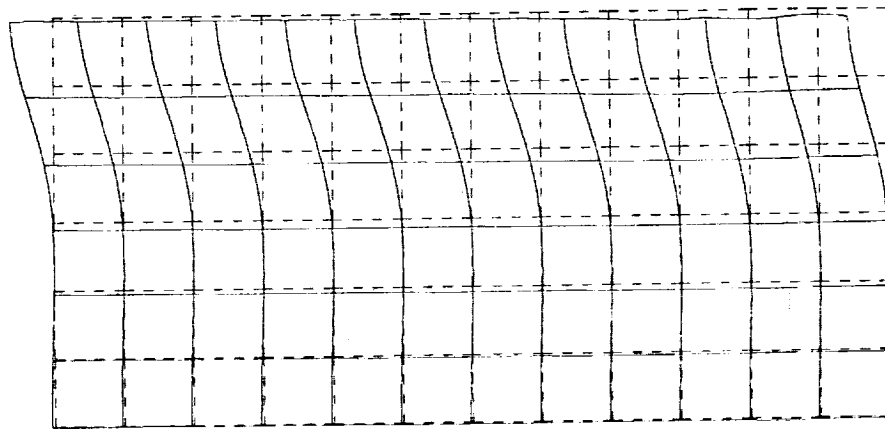


Figure 3.5.6 Deformed residual configuration of the mesh after cooling to room temperature. Magnification factor x590.

SURFACE TEMPERATURES

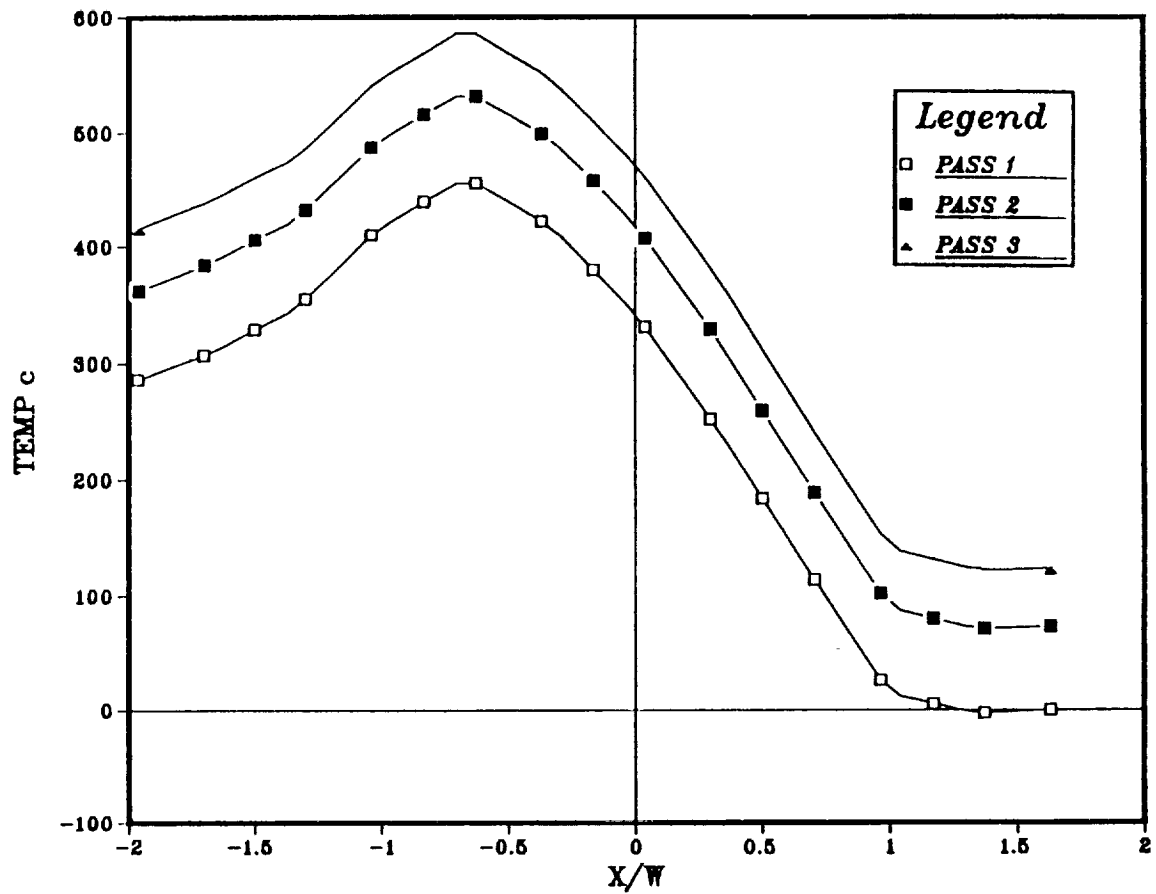


Figure 3.5.7 Distribution of surface temperature halfway through the pass, for different passes.

	VALUE
1	+7.00E-05
2	+7.00E+01
3	+1.40E+02
4	+2.10E+02
5	+2.80E+02
6	+3.50E+02
7	+4.20E+02
8	+4.90E+02
9	+5.60E+02
10	+6.30E+02
11	+7.00E+02

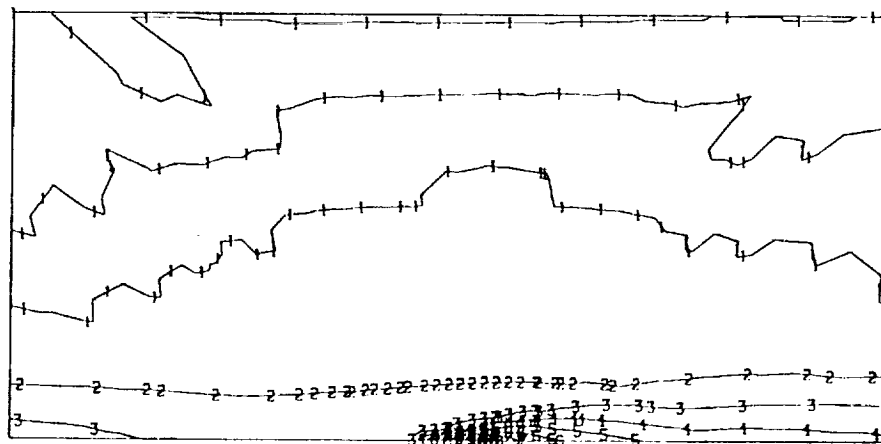


Figure 3.5.8 Temperature contours half way through the third pass.

HYSTERESIS LOOP,PASS 2

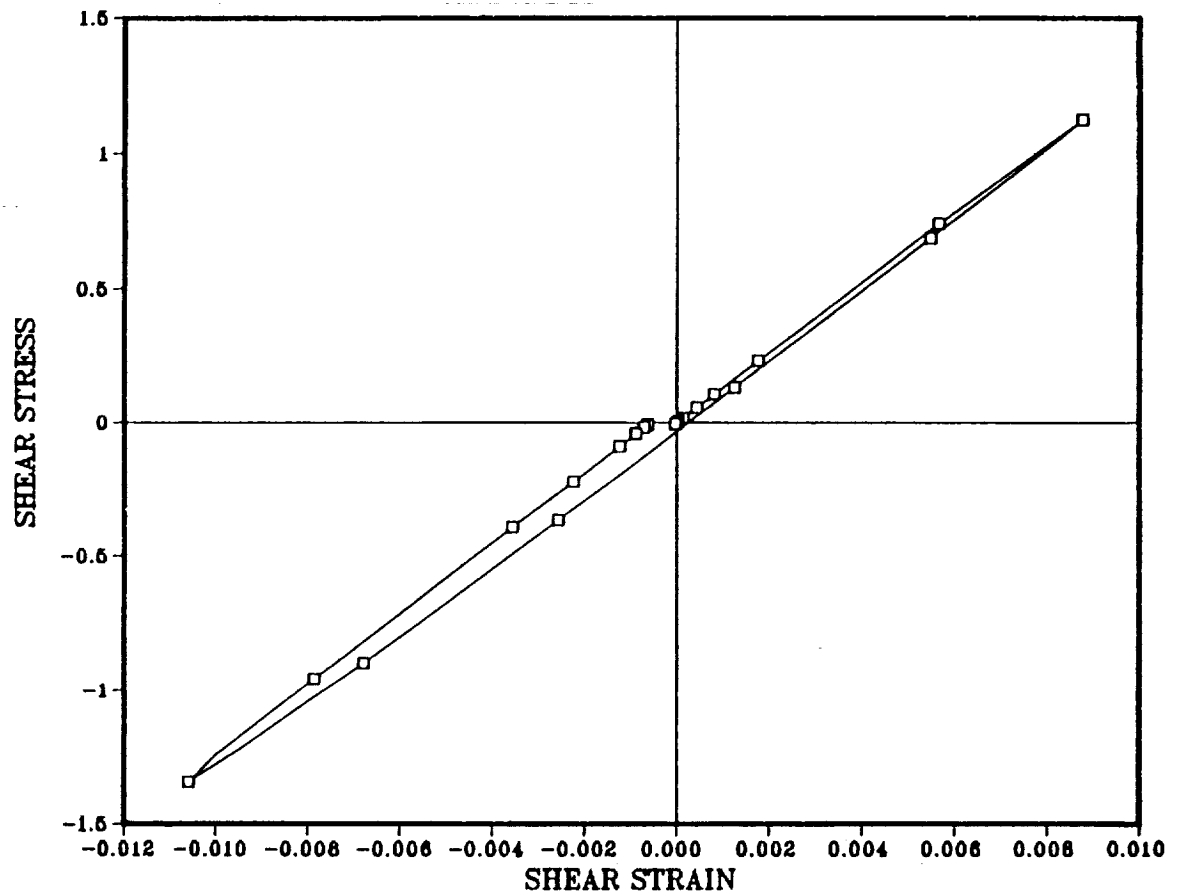


Figure 3.5.9 Hysteresis loop, shear stress versus shear strain, for the second pass

HYSTERESIS LOOP,PASS 3

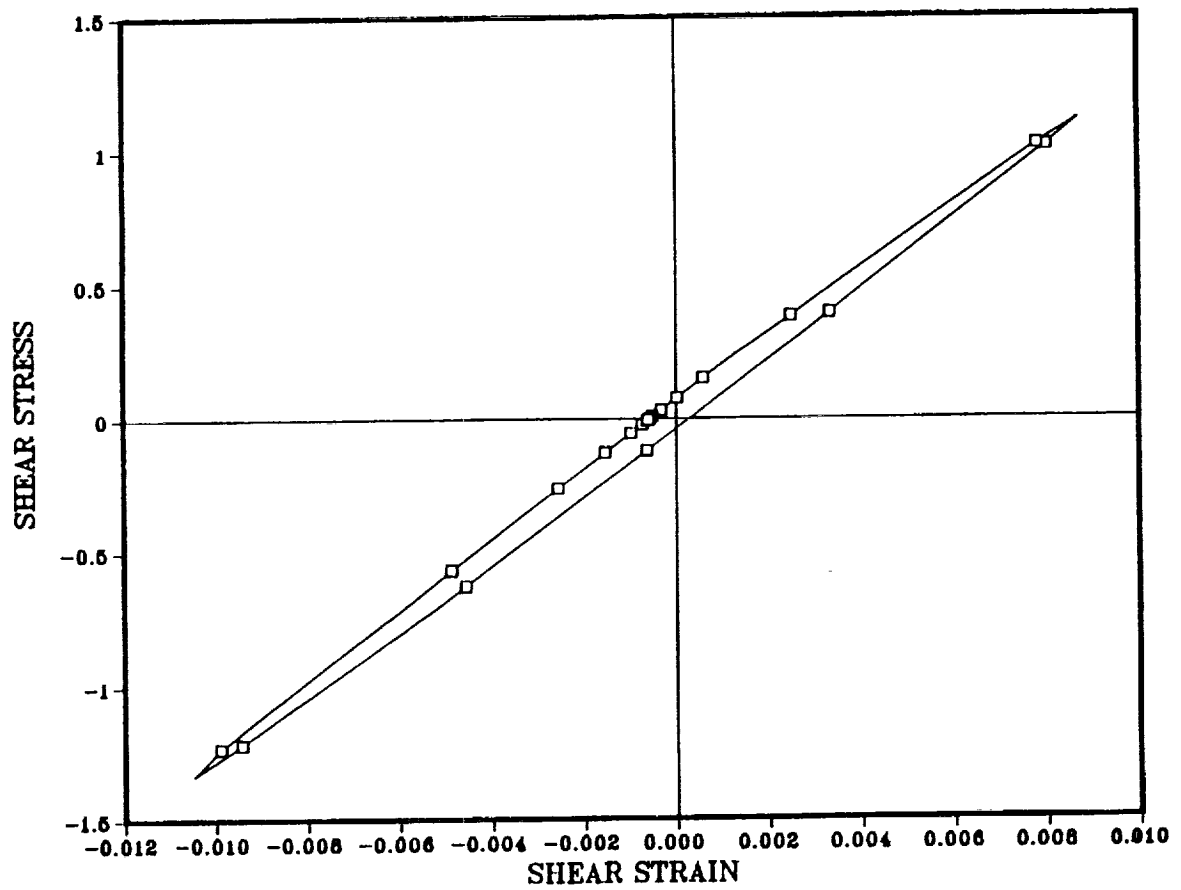


Figure 3.5.10 Hysteresis loop, shear stress versus shear strain, for the third pass

compressive stresses. This is followed by a nonuniform thermal contraction during cooling which appears to be the reason for the residual tensile stresses. These transient residual tensions (due to the translating thermo-mechanical load) suggest a possible mechanism for thermo-cracking. The hysteresis loops show that plasticity is fully reversed after two passes as reported by Ham et al. (1989).

Temperature dependence of thermo-physical properties is complicated and difficult to implement. Of the thermal properties, α , the thermal diffusivity, usually co-varies with the thermal conductivity, K , at intermediate and high temperatures. As a rule ρ decreases and c_p increases with increasing temperatures, while k increases or decreases with temperature, depending on the material. The most important thermal parameter is $h(T)$, the coefficient for forced convection (film coefficient). In forced convection $h(T)$ varies from 10 to 10^4 $W/m^2 K$, and depends on geometry, flow conditions and physical properties. An attempt at a boundary layer analysis to solve the heat transfer problem and define $h(T)$ for a specific contact situation is recommended. Of the mechanical properties, E , Young's modulus, decreases, while ν , Poisson's ratio, increases with increase in temperature.

Accounting for the changes in mechanical properties with temperature is recommended for further study; the material will soften at high temperatures and this could significantly alter the residual stresses and strains.

3.6 Conclusions

Three dimensional finite element calculations of repeated frictionless rolling contact have been carried out for ELKP properties of an AISI 440C bearing steel, at relative Hertzian pressures of $p_0/k_k \approx 4.0, 6.6$ and 8.9 , using the geometry of the 3-ball-rod contact fatigue testing machine. The subsurface stresses, plastic strains, residual stresses and plastic work done are evaluated. Equivalent stresses above the kinematic yield strength extend to the surface only for the highest load level. The peak equivalent plastic strain occurs at approximately $0.25w_1$ ($w_1/w_2 = 1.77$) for all load cases; the values of these strains are 4.4×10^{-4} , 2.33×10^{-3} , and 4.0×10^{-3} , for the low, medium and high loads, respectively.

Three dimensional finite element calculations of repeated frictionless rolling contact have been carried out for ELKP properties of the 7075-T6 aluminum alloy, at a relative Hertzian pressure of $p_0/k_k \approx 5.7$, using the geometry of the 3-ball-rod contact fatigue testing machine. The subsurface stresses, plastic strains, and residual stresses are evaluated. The peak plastic strain amplitude, $\Delta \epsilon_{\max}^p/2 = 1.6 \times 10^{-3}$, occurs at a relative depth of $z/w = 0.4$ below the surface. Peak residual stresses obtained

are $\sigma_x^r(\max) = 26.4$ MPa, and $\sigma_y^r(\max) = 39.7$ MPa, occurring at a relative depth of $z/w = 0.9$.

Two dimensional finite element calculations of repeated rolling-plus-sliding contact have been carried out for ELKP properties of an AISI 440C bearing steel, at relative Hertzian pressures of $p_o/k_k = 5.0$. Plastic strains, residual stresses and temperature distributions are presented. Plastic strains are shown to be considerably lower for ELKP properties than for an elastic-perfectly-plastic material (Kulkarni et al., 1989). Steep temperature gradients close to the surface produce high compressive stresses; the ensuing cooling causes residual tensile stresses, a possible mechanism for thermo-cracking. Thermo-mechanical behavior is highly dependent on the material properties, which also may be temperature dependent. A more precise definition of these properties, especially the thermal film coefficient, is recommended.

4. EVALUATION OF THE FRACTURE MECHANICS DRIVING FORCE FOR SPALL GROWTH

4.1 Background

This section reviews and extends calculations of the fracture mechanics driving force for cyclic crack growth under rolling contact (see Keer and Bryant, 1983, O'Reagan et al., 1985, Bastias et al., 1989, and Hanson and Keer, 1991, for reviews of the problem). Observations of the spall process in 440C samples, described in Section 5.4, as well as observations of spall damaged HPOTP bearings (Bhat and Dolan, 1982, 1983), indicate that the spalls nucleate close to the surface. The number of cycles needed by surface-breaking, micron-size crack nuclei to grow to a spall is one component of the contact life.

The analysis of the growth component is a difficult task, particularly for the conditions in the HPOTP bearing. First, there are several features that can add to the K - crack growth driving force produced the Hertzian stresses. These include stationary pressure spikes arising from surface irregularities, the pressure of lubricant in the crack cavity, centrifugal and tensile residual stresses superimposed on the Hertzian stresses and thermal stresses. The contributions from these sources are not necessarily in phase. Secondly, there are Mode I, II and III contributions to the driving force whose combined effect is difficult to predict. Thirdly, the driving force is modified by the crack face friction and the non-planar crack profile, features that are difficult to quantify. Fourth, only a few studies have examined the actual 3-dimensional crack configuration (Kaneta and Murakami, 1991, Hanson and Keer, 1991). Finally, analyses of the driving force are difficult to test because the centrifugal stresses, lubrication and thermal conditions in the HPOTP bearing are not reproduced in the 3-ball-rod testing machine.

The sources of driving force are examined more fully in Section 4.2. A new analysis by Bower (1989) for a 2 dimensional surface breaking crack with entrapped lubricant is applied in Section 4.3 to define the fracture mechanics driving force for conditions of interest. Results of driving force calculations for the different sources are compared in Section 4.4. The corresponding threshold crack sizes for growth are examined in Section 4.5. Actual measurements of the growth life are presented in Section 5.4. Fracture mechanics predictions of crack growth are compared with the measurements in Section 6.3.

4.2 Contributions to the Spall Growth Driving Force.

4.2.1 Hertzian Stresses. Under pure rolling contact, the Hertzian stresses -- those associated with perfectly smooth,

idealized contacting surfaces -- are largely compressive and, by themselves, fail to generate a Mode I crack driving force¹³. Low levels of tensile stress are generated close to the surface for the case of rolling-plus-sliding with friction but these are not likely to produce significant Mode I K-values for small, as-nucleated cracks. Two-dimensional treatments of sub-surface cracks (O'Reagan et al., 1985) show that the cyclic shear stresses generated under rolling contact do produce Mode II and Mode III K-values. The peak values occur well below the surface at relative depths $y \approx w$ (where $2w$ is the contact width) provided crack face friction is ignored. However, even the peak values are modest because the friction and interlocking between the rough crack faces impede the crack face sliding. For lubricated contact, the Mode II and Mode III K-values diminish as the surface is approached. This is also true for surface-breaking cracks. Keer and Bryant (1983) find that the K-values of 2-dimensional surface-breaking cracks are very small for crack lengths just beyond the nucleation stage, i.e. $a \approx 10 \mu\text{m}$. In general, the driving forces produced by 3-dimensional cracks are even smaller (Kaneta and Murakami, 1990). The conclusion to be drawn from this is that the mechanical effects of pure rolling contact of idealized smooth surfaces do not promote the growth of micron-size surface or near-surface cracks. Other contributions to the K-driving force must be considered to account for the formation of spalls.

4.2.2 Stationary Pressure Spikes from Surface Irregularities. The analyses of Goglia et al., 1984, de Mul et al., 1987, and Elsharkawy and Hamrock, 1991 reveal that small, sub-microns-size irregularities in the running track surface, i.e., asperities, dents and grooves, produce large, local perturbations of the Hertzian pressure. These are in the form of narrow, stationary pressure spikes that rise and fall as the contact passes over the asperity. The spikes can be expected to assist the nucleation of near-surface cracks and then intensify the K_{II} - and K_{III} -values generated, thereby facilitating their growth until they attain a size comparable to the dimensions of the surface irregularity. Evidence of this is contained in early work showing direct relations between surface roughness and contact life (Soda and Yamamoto, 1982), the deleterious effects of debris dents (Lorosch, 1982) and the measurements reported in Sections 5.4 and 5.5. No work has yet been done to analyze the contributions of stationary spikes to the crack growth driving force.

4.2.3 Entrapped Lubricant. Experiments by Way (1935), Dawson (1961), and Clayton and Hill (1986) show that spalls do

¹³ The Modes I, II and III correspond with the opening mode, in-plane mode and out-of-plane mode of crack loading, respectively.

not form in the absence of a lubricating fluid. The cracks always propagate in the direction of the load or, stated in another way, cracks only form with negative inclinations (Nakajima et al., 1983, Fujita, 1984). Also, when one rolling element drives another, the driven element fails first (Soda and Yamamoto (1982), Nakajima (1983)). Hanson and Keer (1991) have rationalized these observations, noting that under the above conditions, the mouth of a surface-breaking crack is open and can accept lubricant before closing under the action of the contact pressure. The effects of lubricant were treated by Keer and Bryant (1983), Kaneta et al. (1985, 1987) who assumed that the entrapped lubricant transmits the pressure from the mouth of the crack to the crack tip. This mechanism produces both Mode I and Mode II crack driving forces. Recently, Bower (1988) has employed the distribute dislocation technique of Keer and Bryant (1983) to calculate the stress intensity factors for 2 dimensional surface breaking cracks. Bower proposes that the crack mouth closes as the contact moves over the crack, pushing entrapped liquid into the crack and forcing the crack faces apart, producing a significant Mode I crack driving force. This mechanism is sensitive to the direction of rolling. The implications of the Bower analysis for short, surface breaking cracks are examined in Section 4.4. A more recent treatment of 3-dimensional cracks with entrapped lubricant has been reported by Kaneta and Murakami, 1991.

4.2.4 Thermal stresses. The localized frictional heating attending rolling-plus-sliding can enhance crack growth directly by way of the cyclic thermal stresses and indirectly through thermal stress-induced-plasticity and the resulting tensile residual stresses. In addition, the attending reductions in clearances can increase the contact pressure and the heat generation. The latter is part of the scenario proposed by Bhat and Dolan (1982, 1983) for failures of the HPOTP bearing. Goshima and Keer (1990) have analyzed the contribution of thermoelastic contact on the crack driving force. The influence of thermal-mechanical contact on plasticity-induced residual stresses is examined in Section 3.5.

4.2.5 Centrifugal and Residual Stresses. Centrifugal and residual stresses are ordinarily not cyclic in nature. However, when the compressive Hertzian contact stresses are superimposed on centrifugal (tensile) stresses or circumferential tensile residual stresses, Mode I K -driving forces are obtained (Mendelson and Ghosn, 1986). In addition, the centrifugal and tensile residual stresses reduce the stress normal to the crack faces, and, by way of the crack face friction, increase the Mode II- and Mode III- components of the driving force (Chen et al., 1988). Consistent with this, evidence of improvements in the contact life produced by compressive residual stresses has been reported by a number of workers (Fujita and Yoshida, 1978, Clark, 1985, Xiao et al., 1990). Elasto-plastic calculations of

rolling contact indicate that significant, circumferential, tensile residual stresses are generated when the rolling element is overloaded or subjected to sliding and overheated, at contact pressures well above shakedown (Bhargava et al., 1990, Kulkarni, 1991). Mendelson and Ghosn (1986) have used a boundary integral method to calculate the stress intensity factors for a surface breaking, vertical crack. Their analysis accounts for the centrifugal stress but assumes the crack faces to be frictionless and does not take the effects of entrapped lubricant into account.

4.2.6 Cyclic Plasticity. Cyclic plasticity increases the crack tip displacements which are responsible for the cyclic crack growth. This effect appears to be small for hardened bearing steel because the plastic hardening rate is close to the elastic stiffness (Bastias, 1990). However, the contribution of plasticity could be important at elevated temperatures and in regions of the bearing softened by overheating.

4.3 Evaluation of The Mode I and Mode II Driving Force for Surface-Breaking Cracks with Entrapped Liquid.

4.3.1 Analytical Procedure. As noted in Section 4.2.3., Bower (1989) has used the distributed dislocation technique to evaluate the Mode I and Mode II crack driving force for 2 dimensional, surface-breaking cracks with entrapped liquid. This section offers additional calculations of the driving forces for cracks with the usual inclinations. The calculations employed the techniques devised by Bower and were facilitated by software made available by him. The theoretical model, which is illustrated in Figure 4.1, consists of a 2-dimensional surface breaking crack of length, a , in a half space. The definition of the crack inclination θ is that employed by Bhargava et al. (1990). The Hertzian pressure distribution, and the associated frictional shear tractions, are applied on the surface of the half space, and incrementally translated from left to right. They are characterized by the peak Hertzian pressure, p_0 , and the maximum tangential traction, q_0 . Two different tractive forces were examined: (a) the negative or "driving" traction experienced by the slower rotating, "driven" element or follower which is directed opposite to the rolling direction and (b) the positive or "braking" traction experienced by the faster rotating driver which is directed in the rolling direction. The calculations were performed for: (i) dry conditions, (ii) lubricated conditions with Hertzian pressure over the crack mouth acting in the crack cavity, (iii) $q_0/p_0 = -0.01, -0.05, -0.10, 0.01, 0.05$ and 0.10 (iv) crack face friction values of $\mu^c = 0$ and 0.2 , (v) crack inclinations of $\theta = -20^\circ$ and -30° and (vi) relative crack depths $0.2 < x/h < 1.0$. While the main objective of this work was to extend the driving force calculations to the threshold crack size, the Bowers algorithms proved to be unstable for crack depths shallower than $a/w = 0.5$. It should be noted

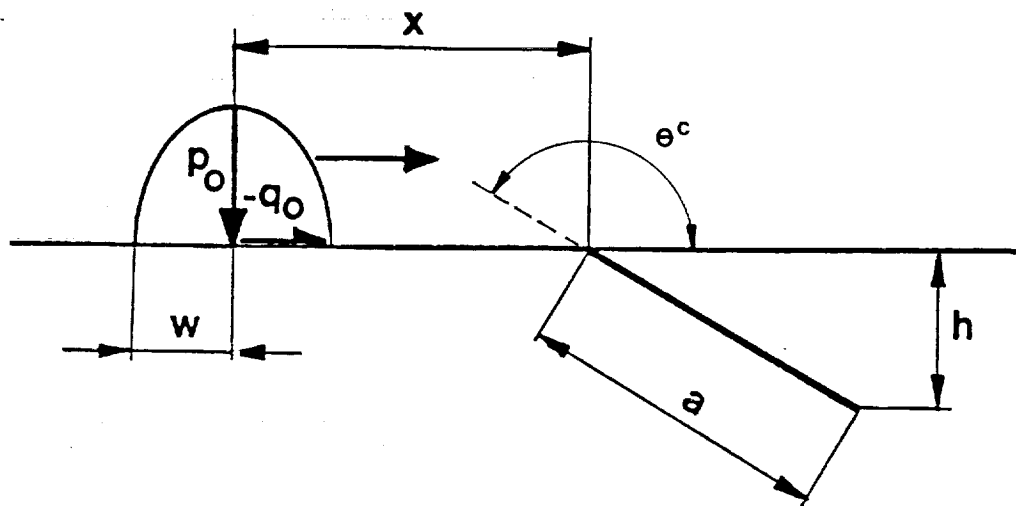


Figure 4.1

Geometry and nomenclature used for the surface breaking crack problem which was solved using the Bowers (1989) analytical solution. The load was translated from left to right. The traction q_0 is considered positive when its direction coincides with the rolling direction.

that negative tractions are expected to increase the crack mouth opening and permit more fluid to enter the crack cavity before it is closed by the contact pressure than is the case for positive tractions. However, the Bower model does not account for differences in the crack mouth opening arising from the sign and magnitude of the tractions.

4.3.2. Results. Results for dry contact are summarized in Figures 4.2 - 4.12. In these cases a Mode I component is not produced because there is no liquid to be trapped in the crack cavity. The calculations show that the potency of the surface-breaking crack, given by the normalized driving force range, $\Delta K_{II}/(p_0/a)$, decreases as the crack becomes shorter and shallower. For an $a=10\text{ }\mu\text{m}$ -long, $\mu^C=0.2$, $\theta^C = -20^\circ$ -inclined crack in a driven element, subjected to a Hertzian pressure, $p_0=2.5\text{ GPa}$, a traction ratio, $q_0/p_0=-0.05$: $\Delta K_I=0$, and $\Delta K_{II}/(p_0/a)\approx 0.1$ (for the extrapolation shown in Figure 4.11 with dashed lines. This means that $\Delta K_{II} \approx 0.7$, which is likely to be well below the threshold.

The results for lubricated contact and cracks with entrapped liquid are summarized in Figures 4.13 - 4.31. These show that the potency of the cracks increases as the crack becomes shorter and shallower for the a/w -range examined. The normalized driving force must reach a maximum with a/w and then approach zero for vanishingly small a/w , but the position of the maximum could not be defined (see Figure 4.29). While the ΔK_{II} -driving force for the same $a = 10\text{ }\mu\text{m}$ -long crack and contact pressure cited in the previous paragraph is much larger with lubricant pressure, the uncertainties in the interpolation (see Figure 4.29) prevent a numerical evaluation. The Mode I values for the lubricated case are about 3x larger than the Mode II values and could well be above the threshold. The Mode II driving force values are about 25% greater with positive tractions than with negative tractions in the lubricated case, a difference that is not observed in the absence of lubrication. The Mode I - ΔK -values, presented in Figure 4.21, are independent of the sign of the traction and the values of the crack face friction.

4.4 Comparisons of the Contributions to the Driving Force for Surface Breaking Cracks.

To facilitate a comparison of the crack growth driving force arising from centrifugal stresses, entrapped liquid and thermal effects, the results of the different 2- and 3-dimensional analyses were reduced to the relations between the normalized driving force and the normalized crack length and compiled in Table 4.1 and in Figure 4.32. Most of the analyses have been performed for crack lengths, a , comparable to the semi-contact width, w , i.e. $a/w \approx 1.0$, rather than the threshold crack length, e.g. $0.001 < a/w < 0.01$. In some cases, such as small subsurface

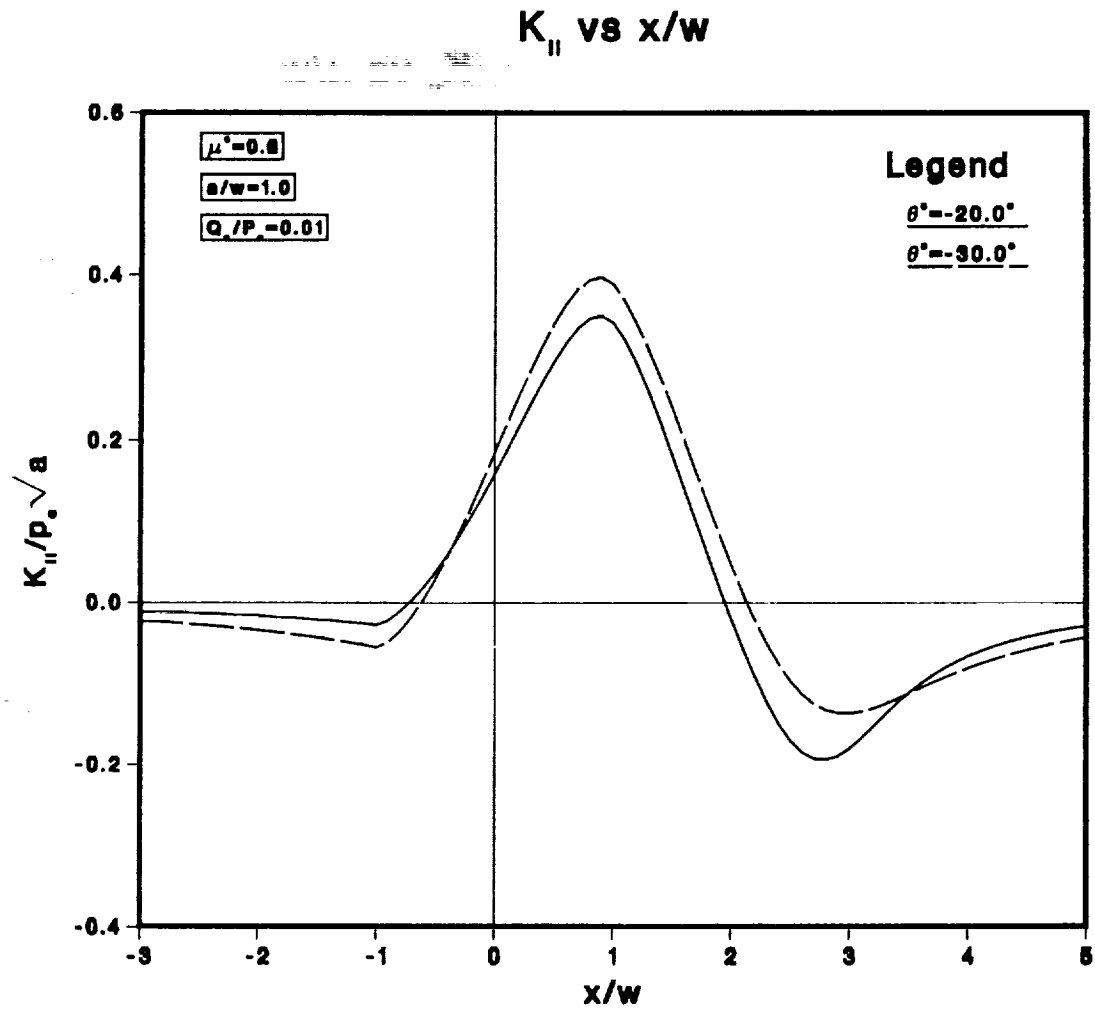


Figure 4.2

Variation of the normalized, Mode II stress intensity factor versus the normalized distance between the contact and the crack mouth for dry contact, a relative crack length, $a/w = 1$, crack inclinations $\theta = -20^\circ$ and -30° , the traction ratio, $q_0/p_0 = 0.01$, and crack face friction, $\mu^c = 0$.

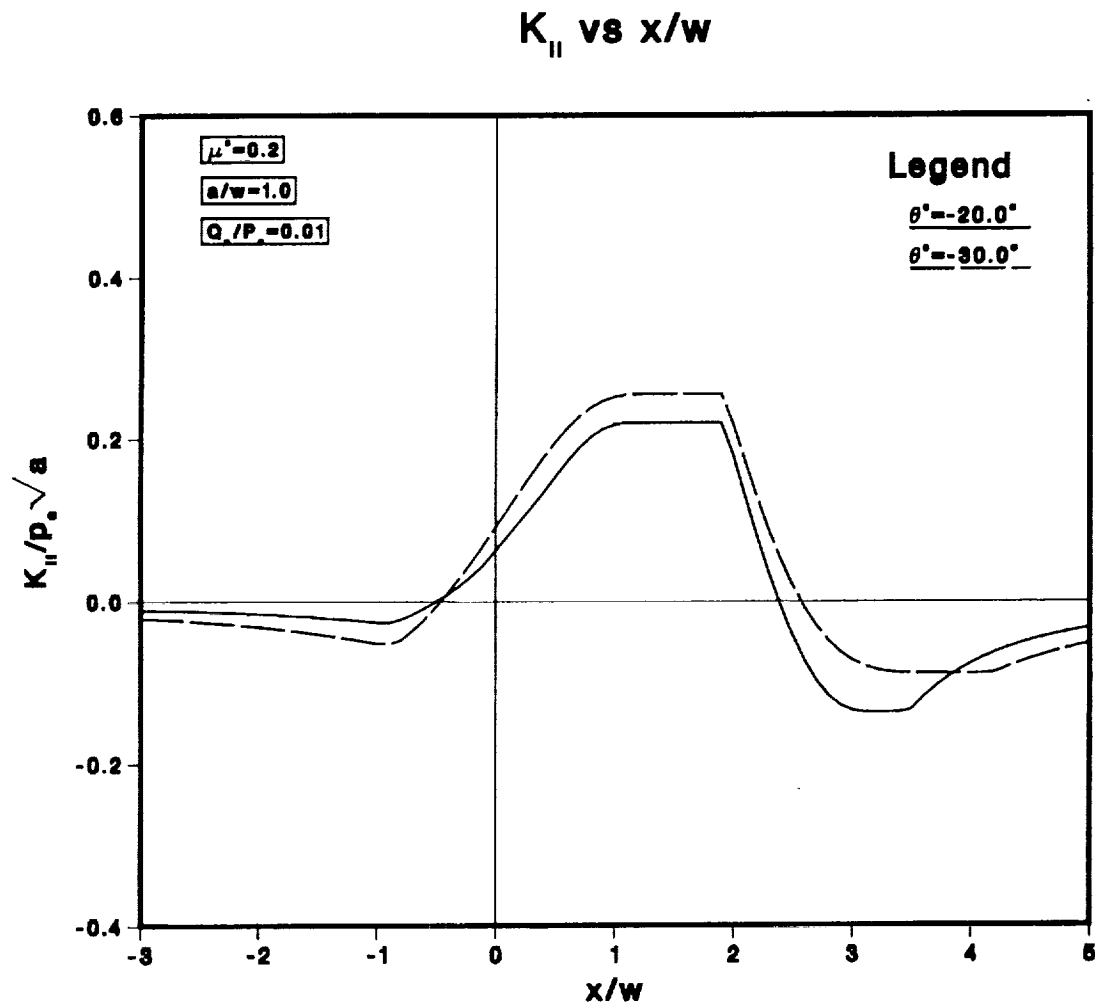


Figure 4.3

Variation of the normalized, Mode II stress intensity factor versus the normalized distance between the contact and the crack mouth for dry contact, a relative crack length, $a/w = 1$, crack inclinations $\theta = -20^\circ$ and -30° , the traction ratio, $q_0/p_0 = 0.01$, and crack face friction, $\mu^c = 0.2$.

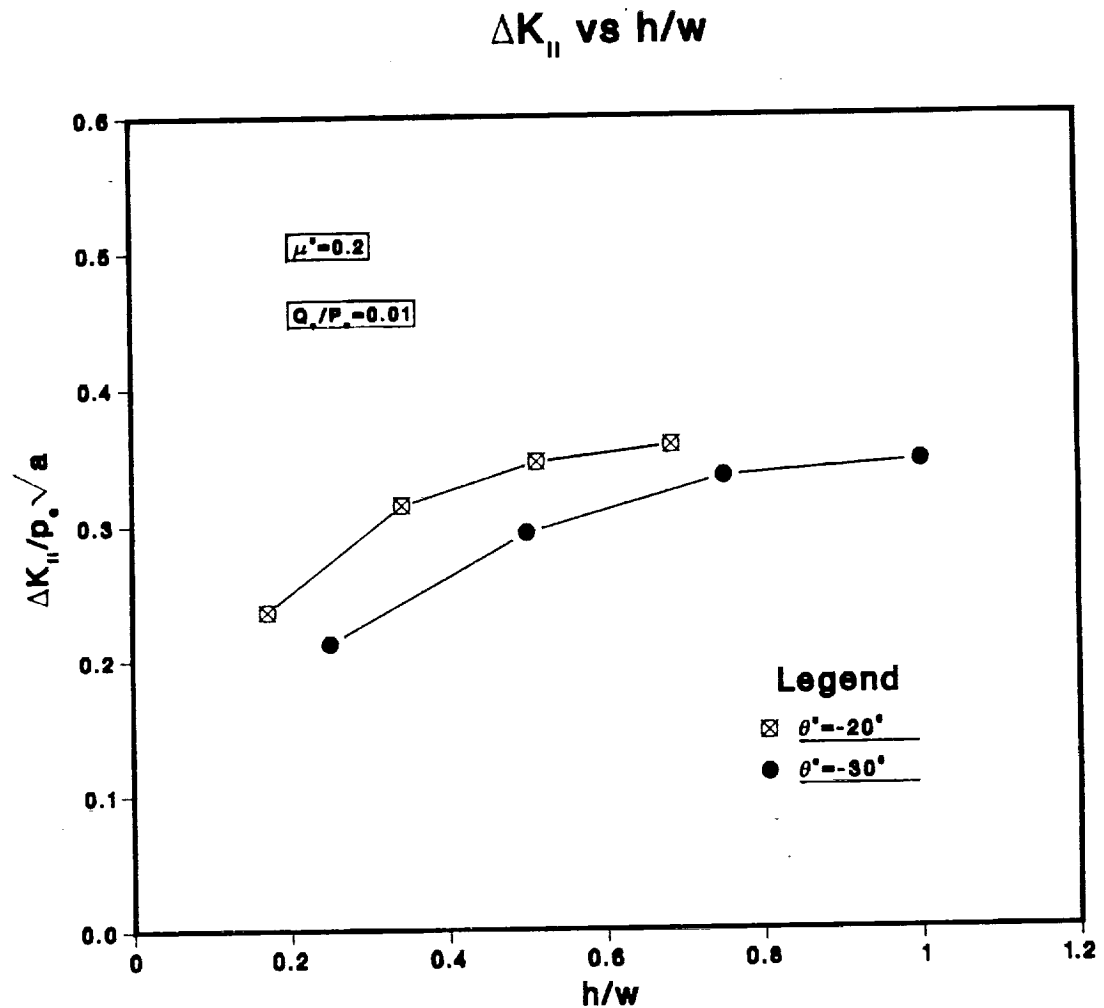


Figure 4.4

Variation of the normalized Mode II crack tip driving force versus the normalized crack tip depth for dry contact, crack inclinations, $\theta = -20^\circ$ and -30° , the traction ratio, $q_0/p_0 = 0.01$, and crack face friction, $\mu^c = 0.2$.

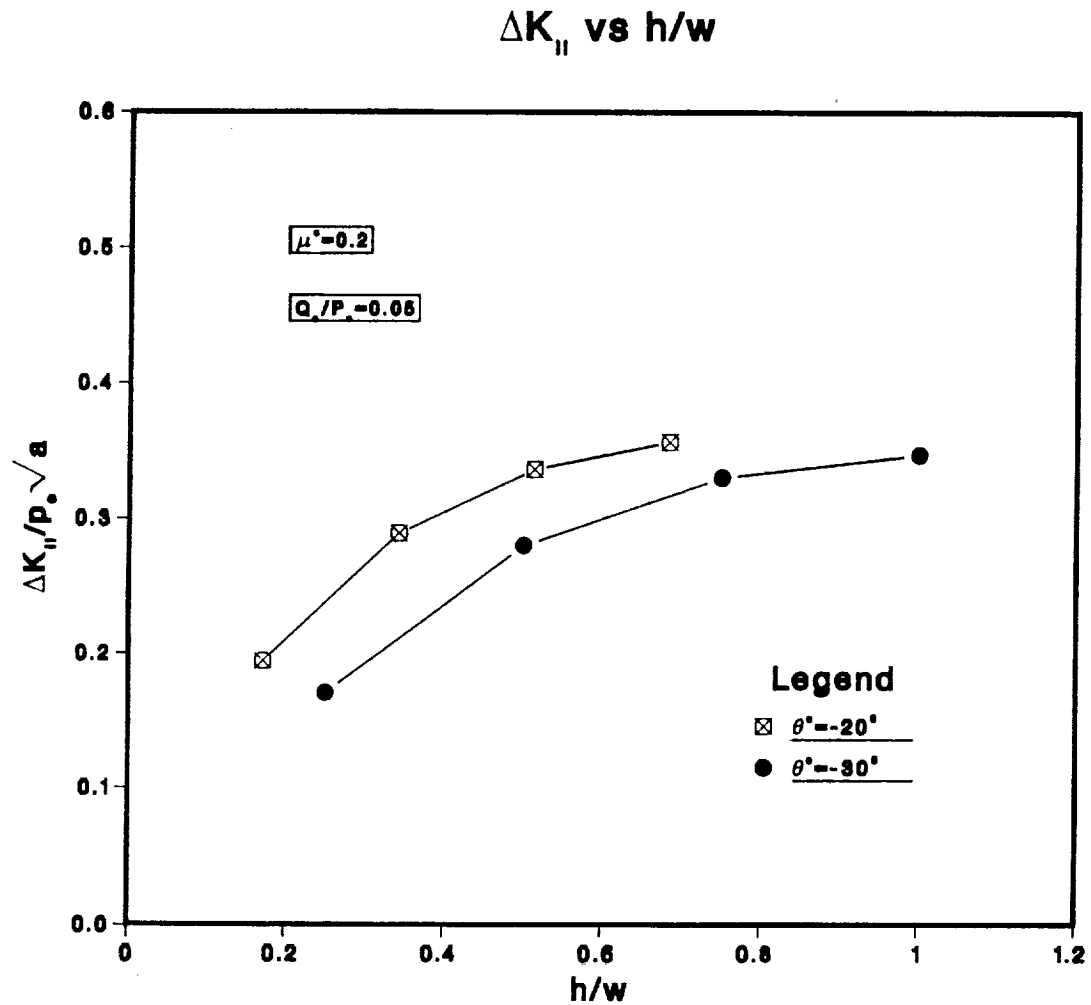


Figure 4.5

Variation of the normalized Mode II crack tip driving force versus the normalized crack tip depth for dry contact, crack inclinations, $\theta = -20^\circ$ and -30° , the traction ratio, $q_0/p_0 = 0.05$ and crack face friction, $\mu^c = 0.2$.

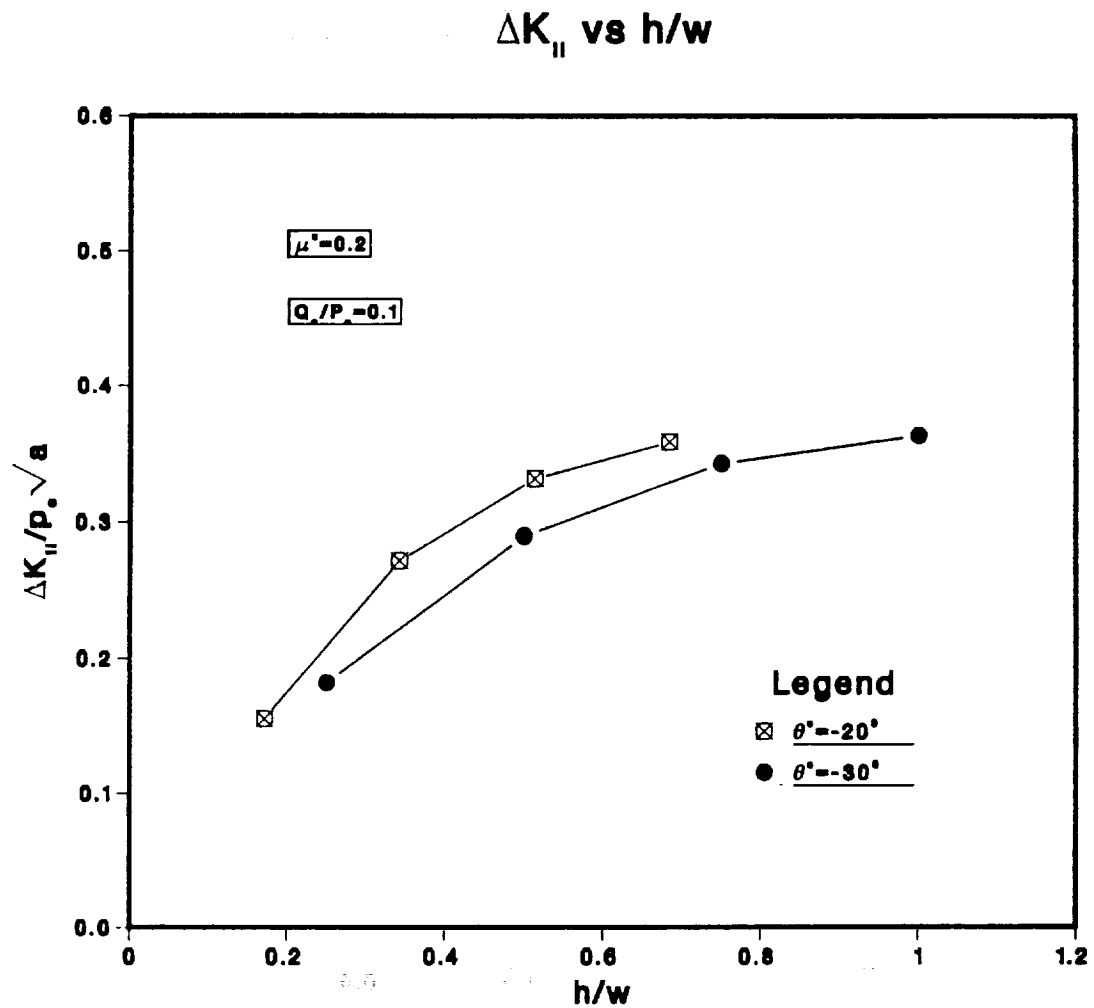


Figure 4.6

Variation of the normalized Mode II crack tip driving force versus the normalized crack tip depth for dry contact, crack inclinations, $\theta = -20^\circ$ and -30° , the traction ratio, $q_0/p_0 = 0.1$ and crack face friction, $\mu^c = 0.2$.

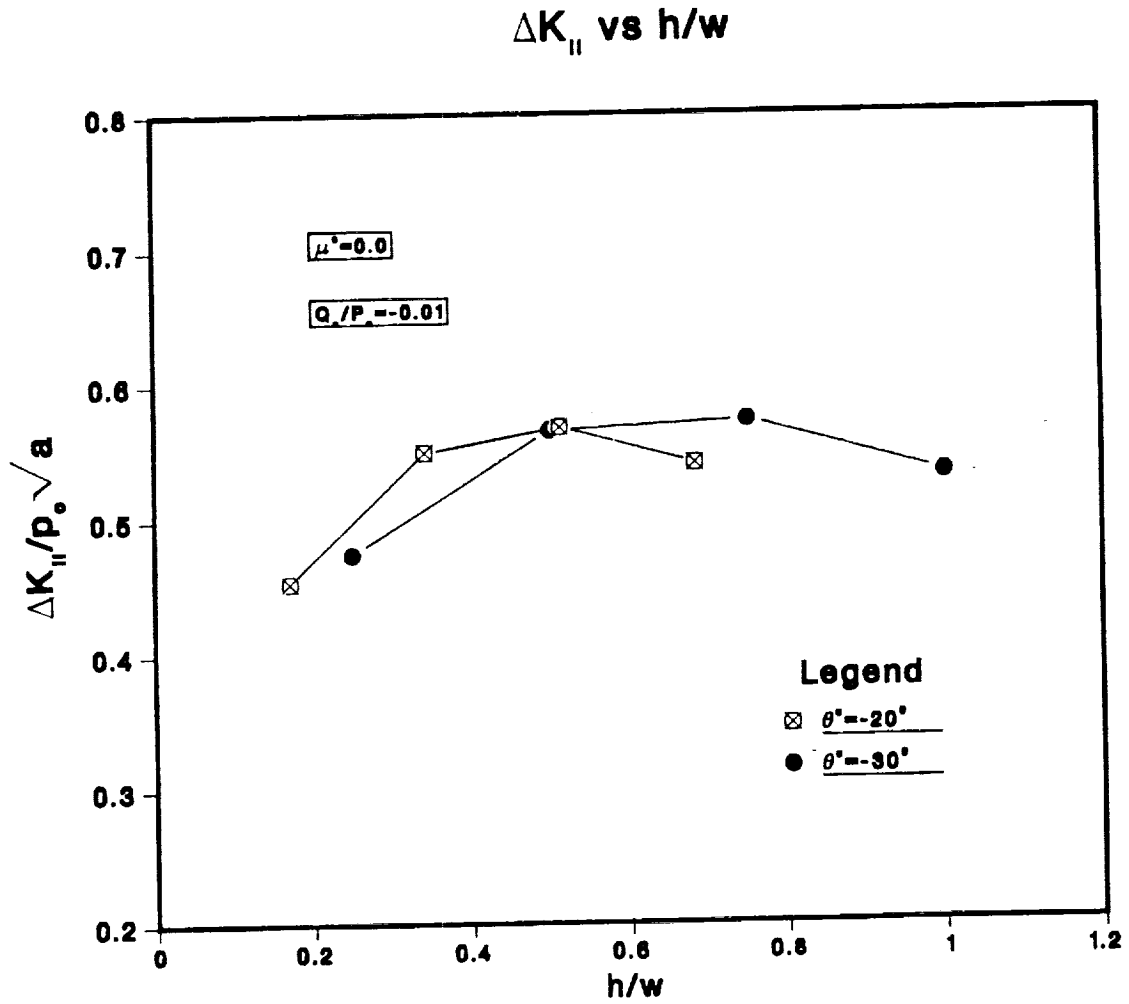


Figure 4.7

Variation of the normalized Mode II crack tip driving force versus the normalized crack tip depth for dry contact, crack inclinations, $\theta = -20^\circ$ and -30° , the traction ratio, $q_0/p_0 = -0.01$ and crack face friction, $\mu^c = 0$.

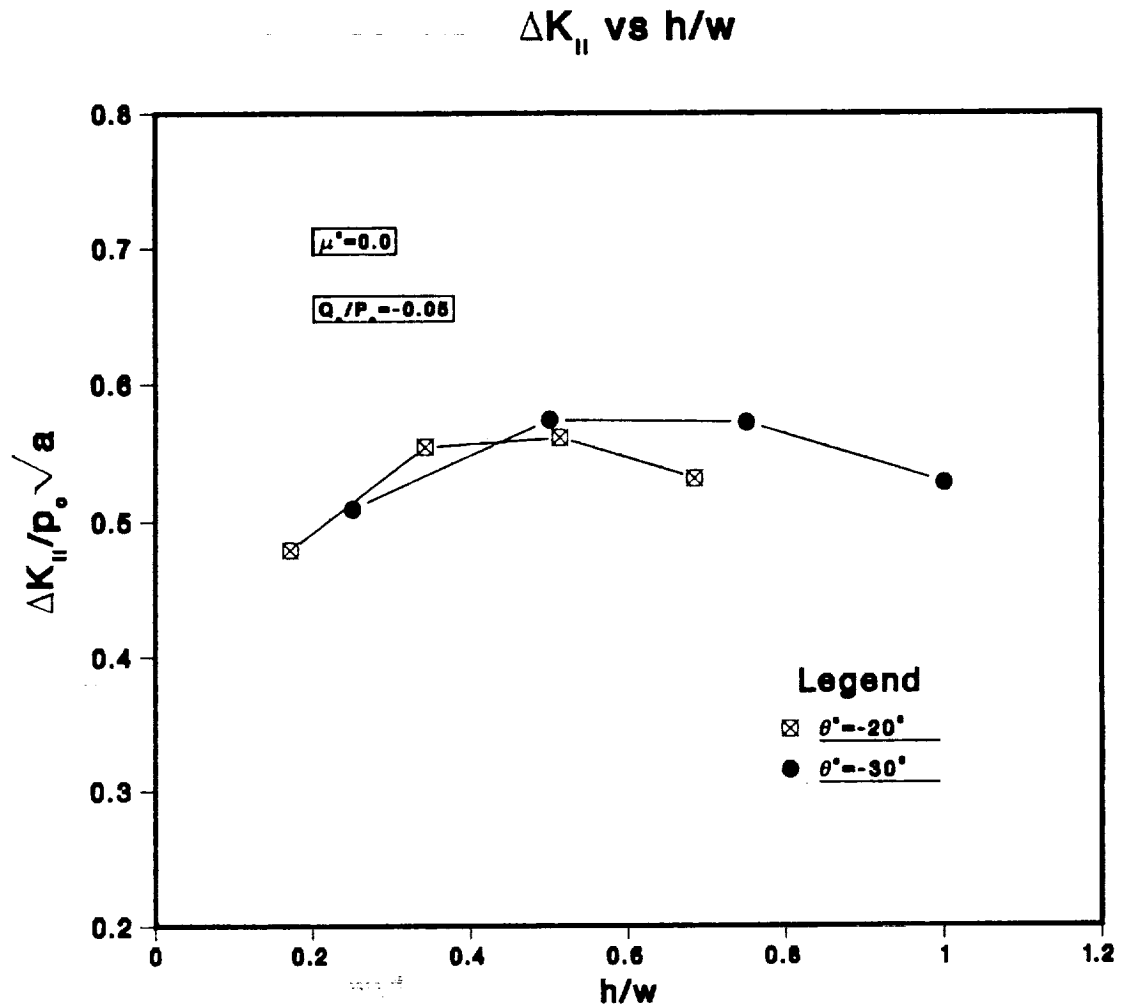


Figure 4.8

Variation of the normalized Mode II crack tip driving force versus the normalized crack tip depth for dry contact, crack inclinations, $\theta = -20^\circ$ and -30° , the traction ratio, $q_0/p_0 = -0.05$ and crack face friction, $\mu^C = 0$.

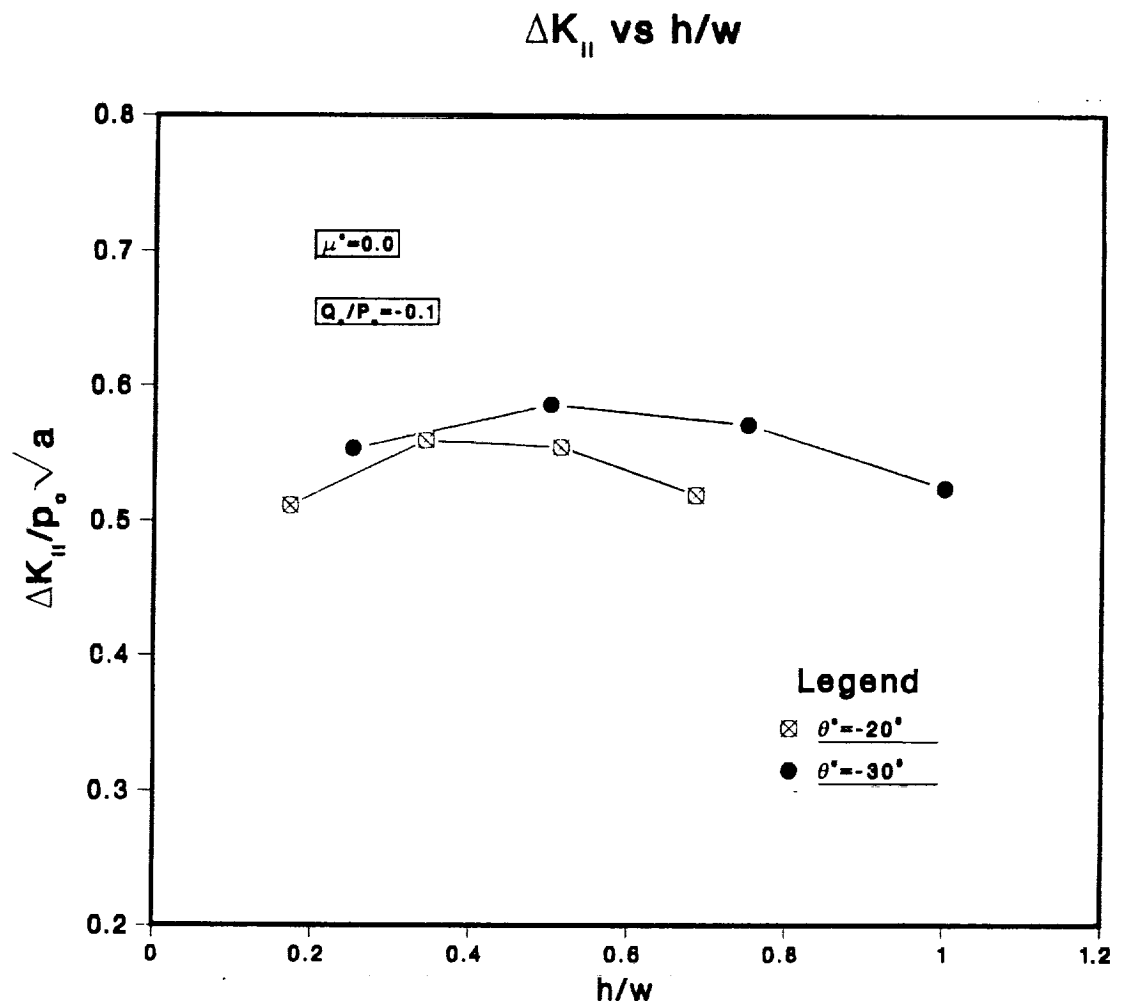


Figure 4.9

Variation of the normalized Mode II crack tip driving force versus the normalized crack tip depth for dry contact, crack inclinations, $\theta = -20^\circ$ and -30° , the traction ratio, $q_0/p_0 = -0.1$ and crack face friction, $\mu^c = 0$.

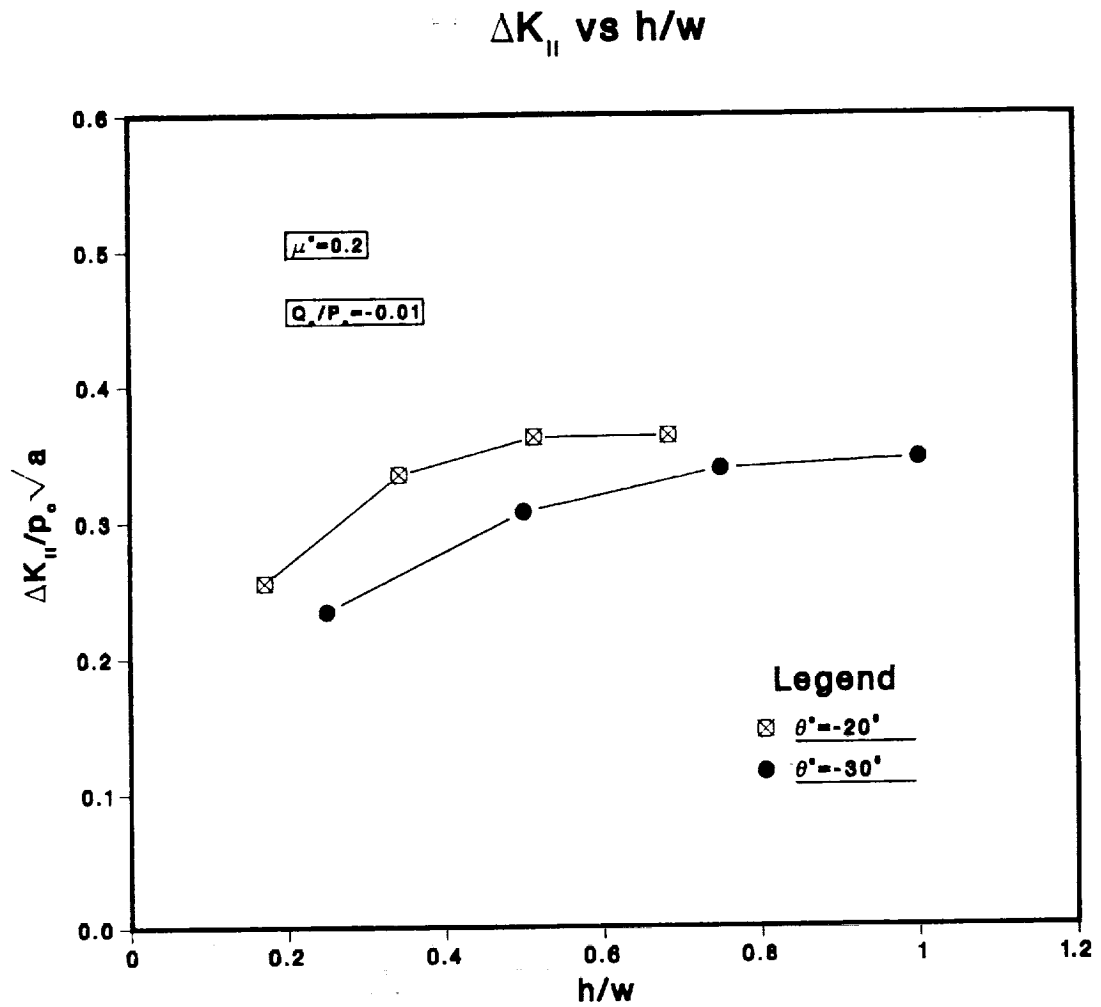


Figure 4.10

Variation of the normalized Mode II crack tip driving force versus the normalized crack tip depth for dry contact, crack inclinations, $\theta = -20^\circ$ and -30° , the traction ratio, $q_0/p_0 = -0.01$ and crack face friction, $\mu^C = 0.2$.

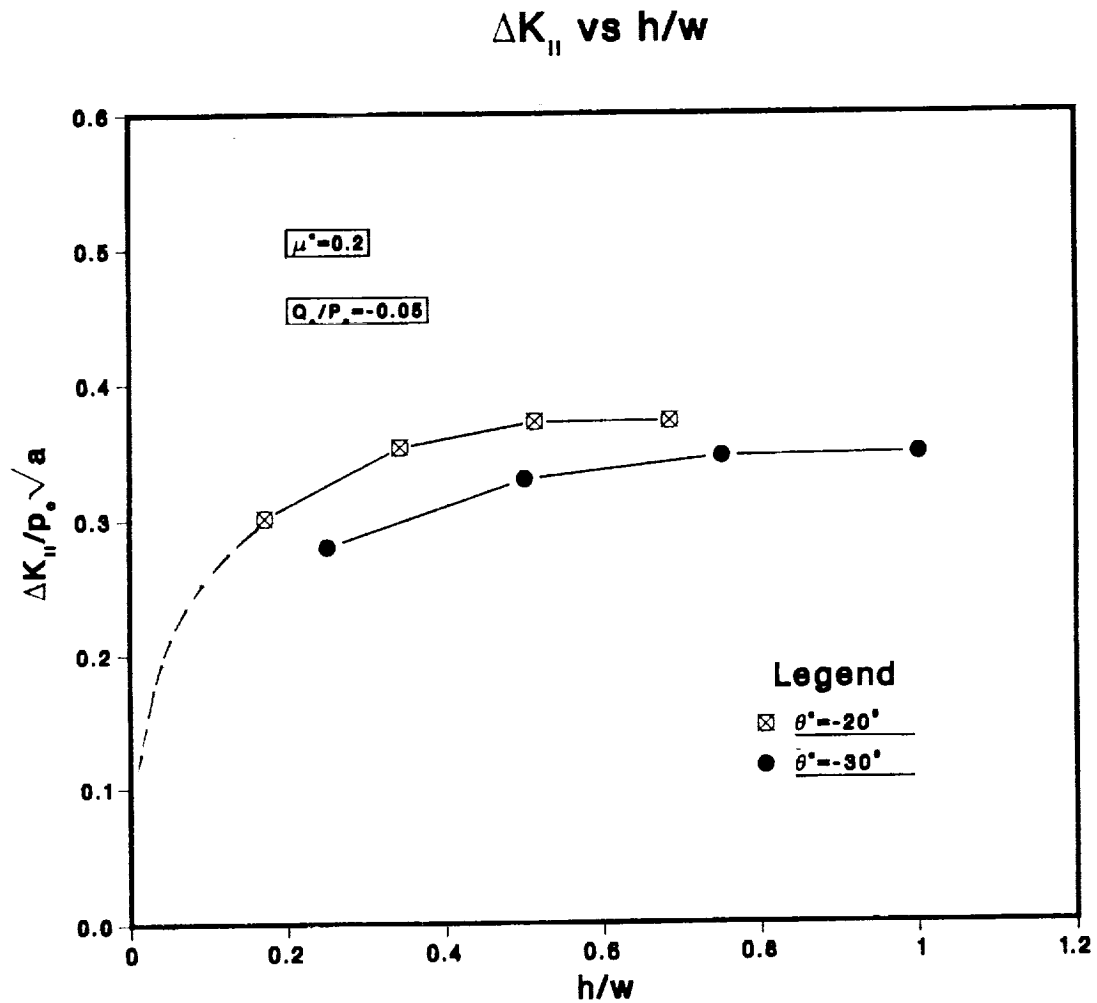


Figure 4.11

Variation of the normalized Mode II crack tip driving force versus the normalized crack tip depth for dry contact, crack inclinations, $\theta = -20^\circ$ and -30° , the traction ratio, $q_0/p_0 = -0.05$ and crack face friction, $\mu^c = 0.2$.

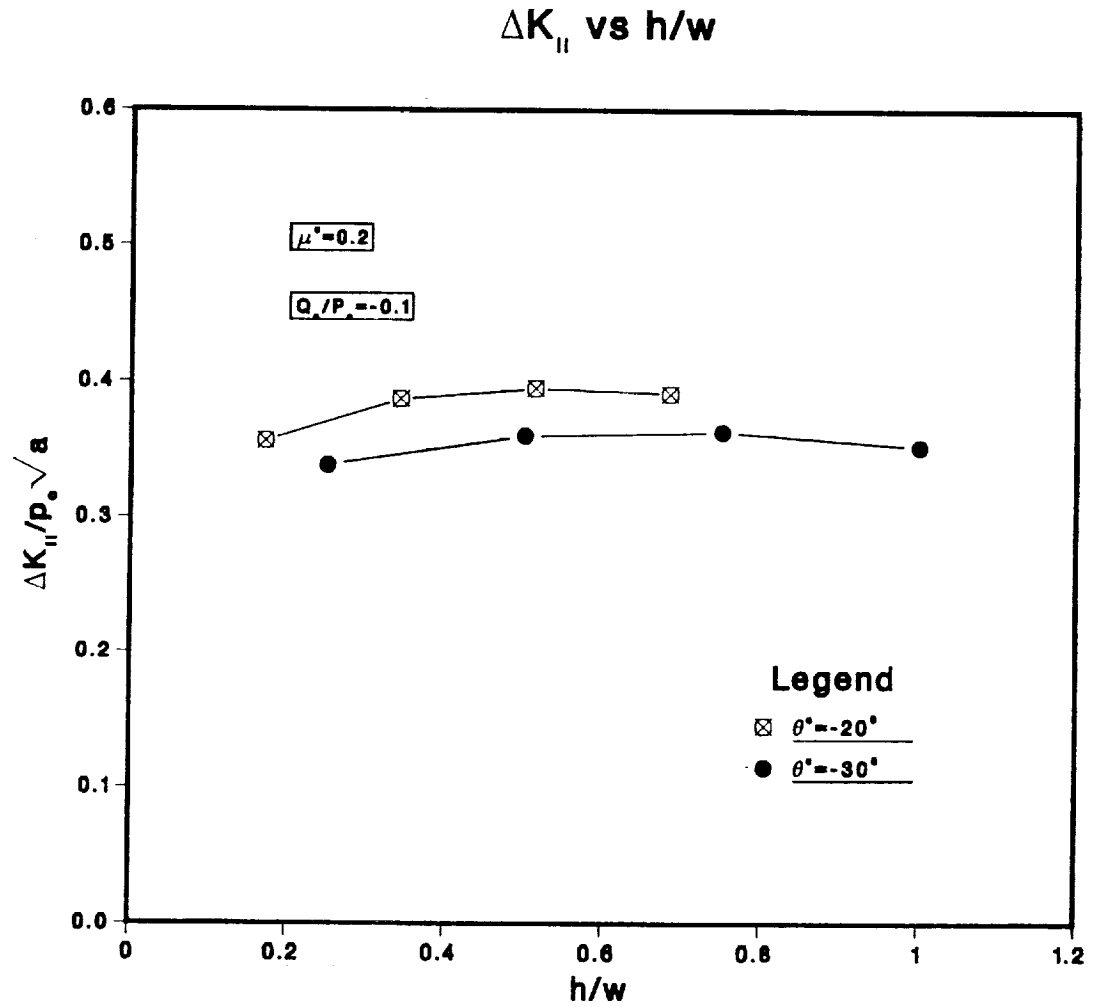


Figure 4.12

Variation of the normalized Mode II crack tip driving force versus the normalized crack tip depth for dry contact, crack inclinations, $\theta = -20^\circ$ and -30° , the traction ratio, $q_0/p_0 = -0.1$ and crack face friction, $\mu^c = 0.2$.

K_{II} AND K_I vs x/w

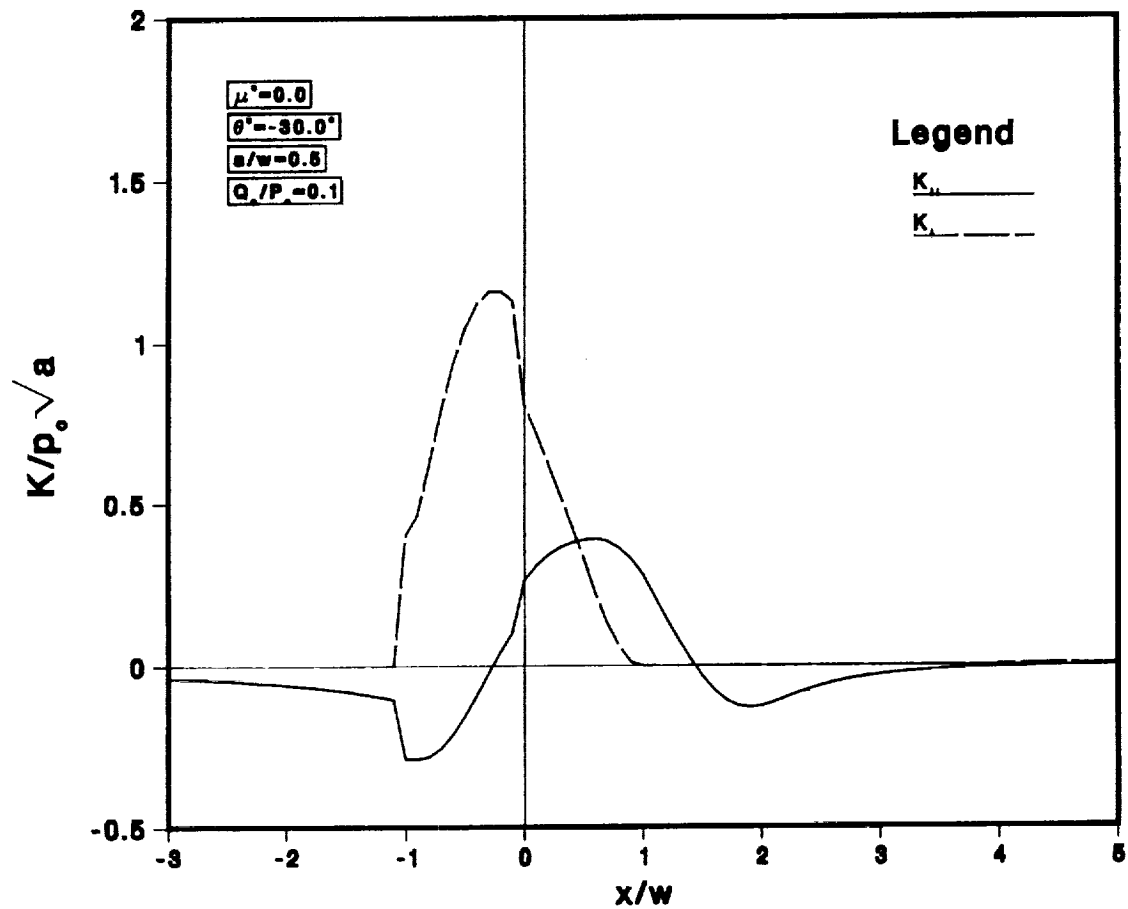


Figure 4.13 Variation of the normalized, Mode I and Mode II stress intensity factor versus the normalized distance between the contact and the crack mouth for lubricated contact, a relative crack length, $a/w = 0.5$, crack inclinations $\theta = -30^\circ$, the traction ratio, $q_0/p_0 = 0.1$, and crack face friction, $\mu^c = 0$.

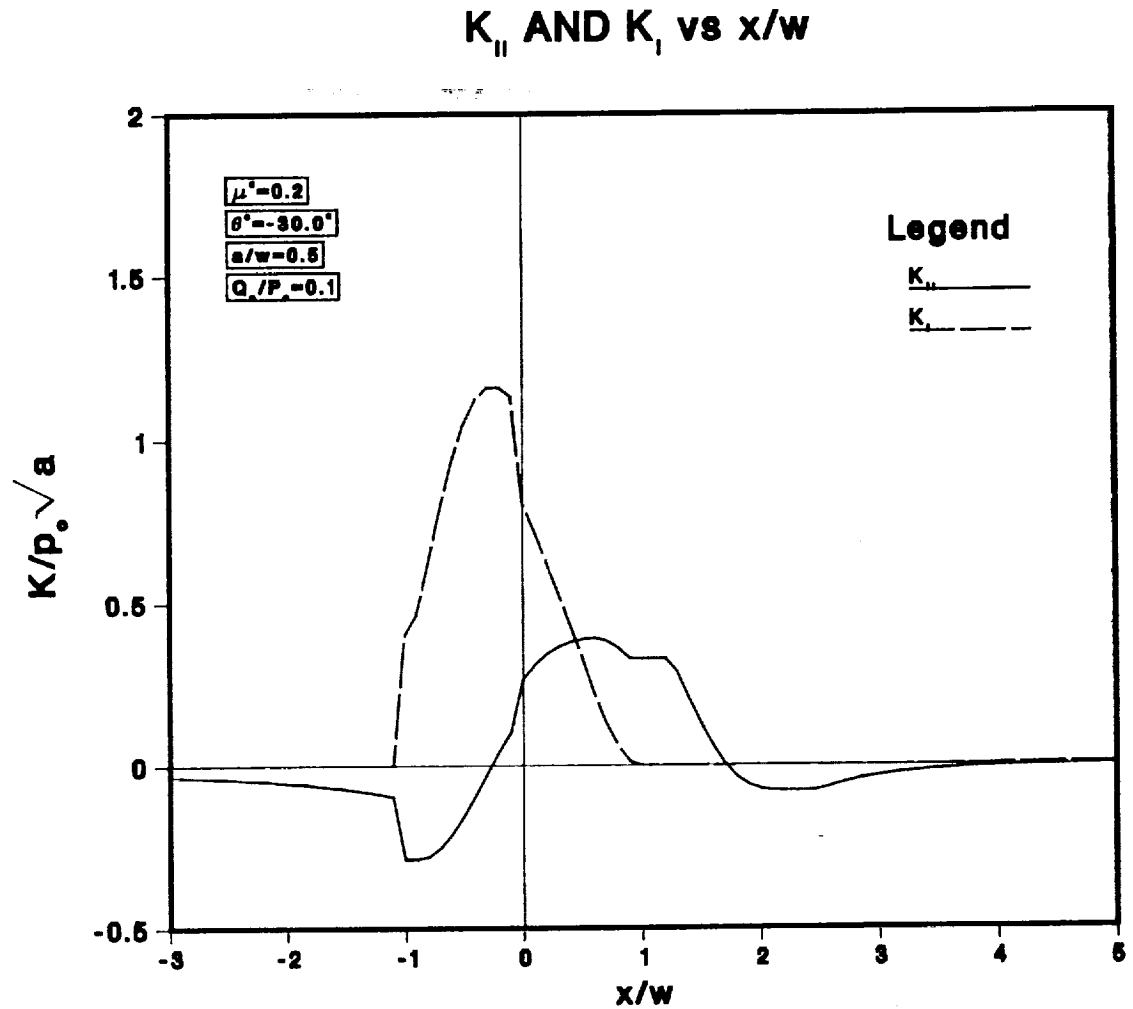


Figure 4.14

Variation of the normalized, Mode I and Mode II stress intensity factor versus the normalized distance between the contact and the crack mouth for lubricated contact, a relative crack length, $a/w = 0.5$, crack inclinations $\theta = -30^\circ$, the traction ratio, $q_0/p_0 = 0.1$, and crack face friction, $\mu^c = 0.2$.

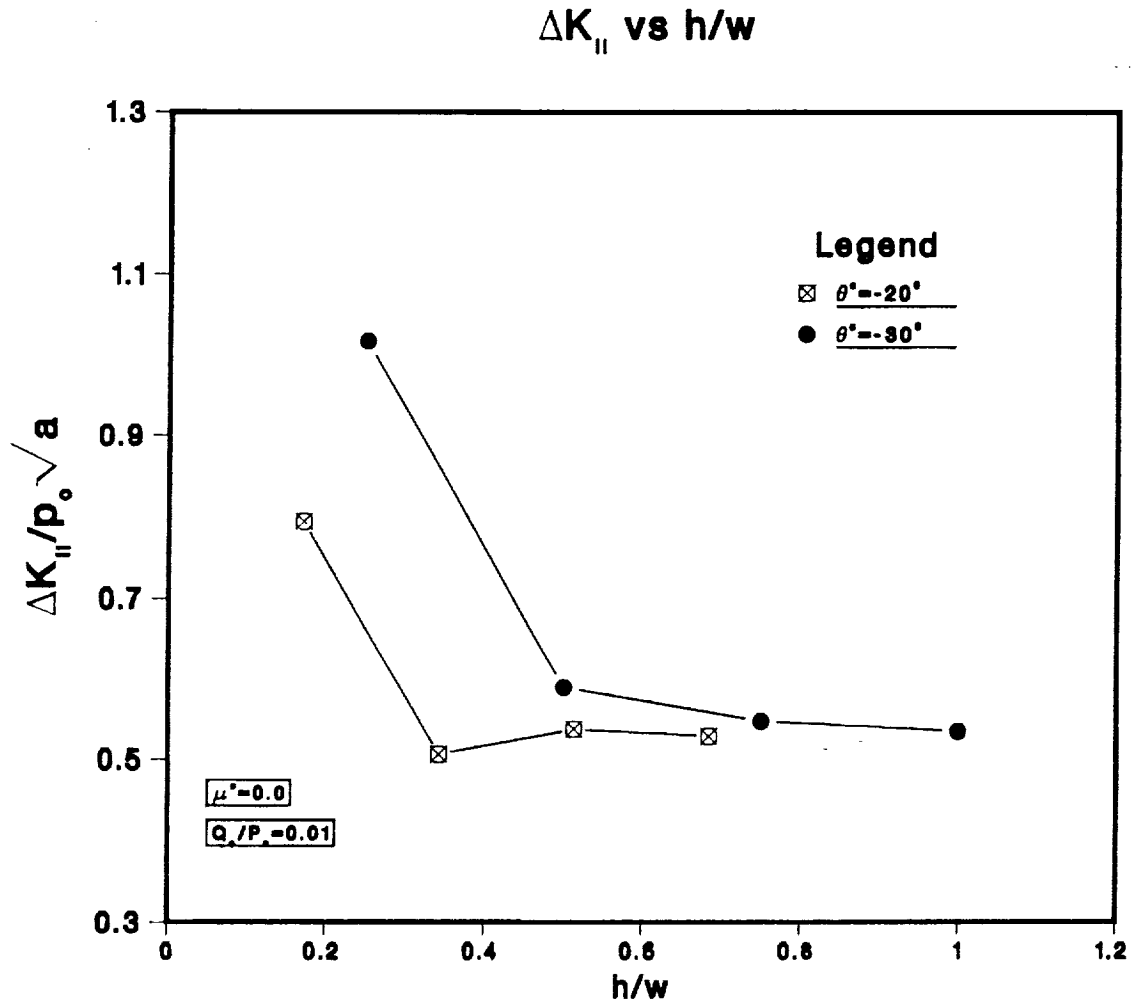


Figure 4.15

Variation of the normalized Mode II crack tip driving force versus the normalized crack tip depth for lubricated contact, crack inclinations, $\theta = -20^\circ$ and -30° , the traction ratio, $q_0/p_0 = 0.01$ and crack face friction, $\mu^c = 0$.

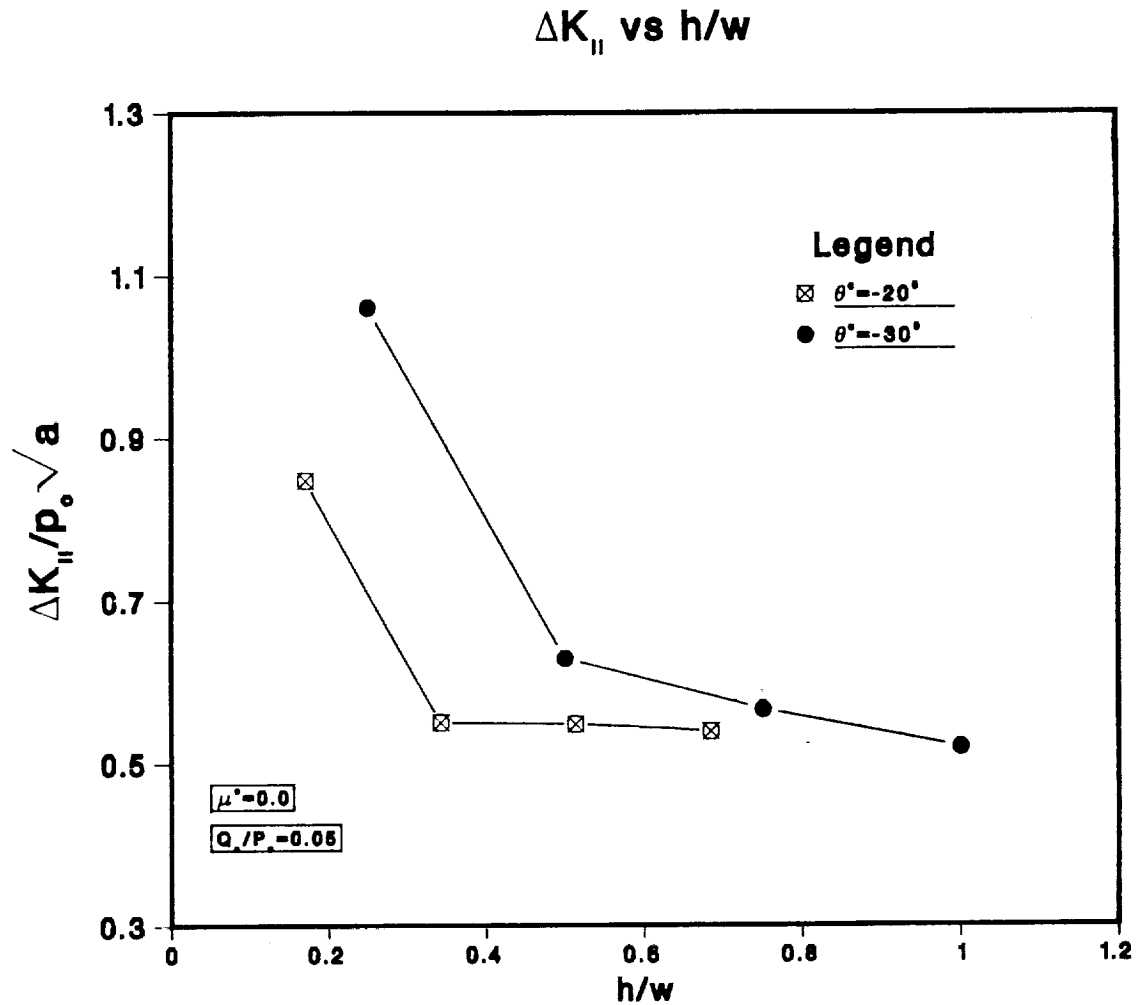


Figure 4.16 Variation of the normalized Mode II crack tip driving force versus the normalized crack tip depth for lubricated contact, crack inclinations, $\theta = -20^\circ$ and -30° , the traction ratio, $q_0/p_0 = 0.05$ and crack face friction, $\mu^c = 0$.

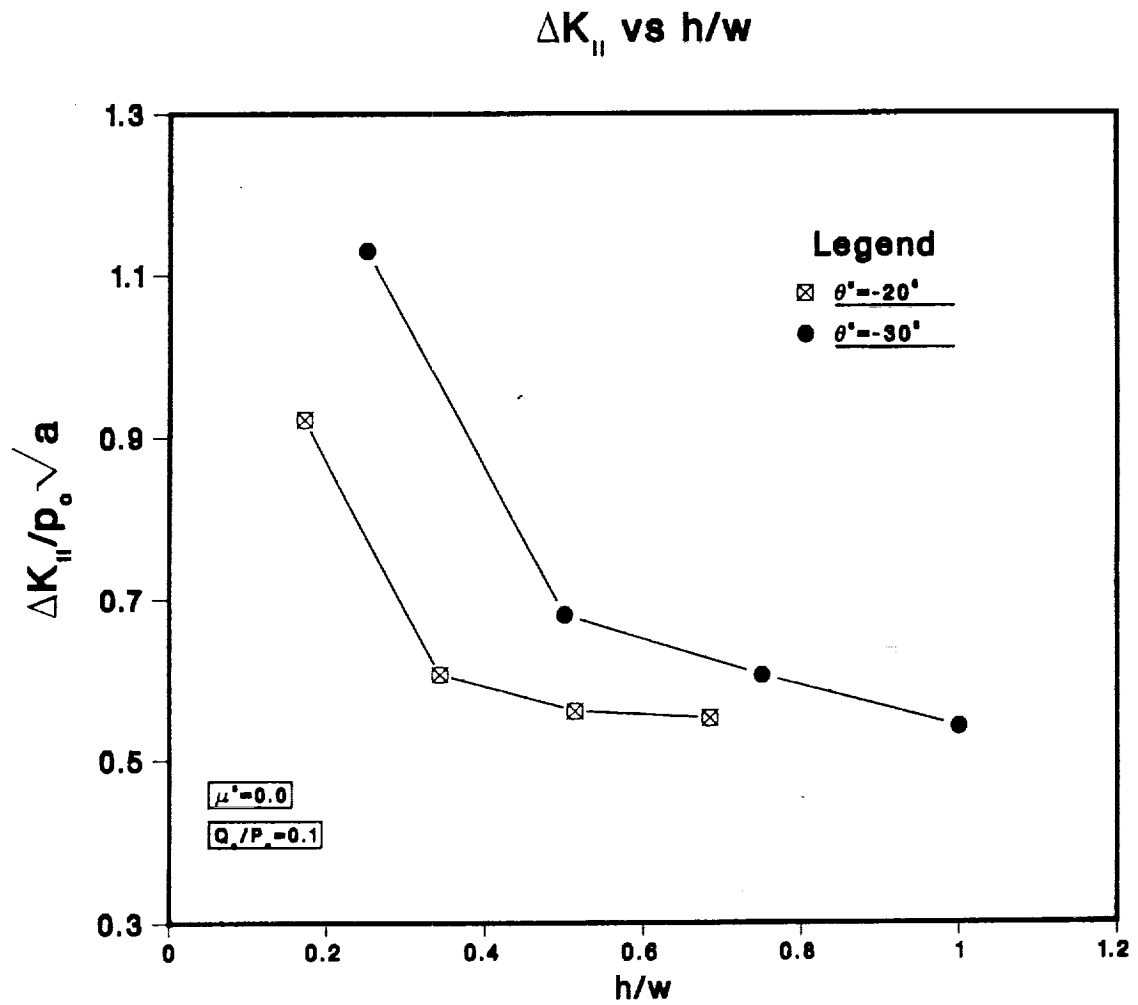


Figure 4.17 Variation of the normalized Mode II crack tip driving force versus the normalized crack tip depth for lubricated contact, crack inclinations, $\theta = -20^\circ$ and -30° , the traction ratio, $q_0/p_0 = 0.1$ and crack face friction, $\mu^c = 0$.

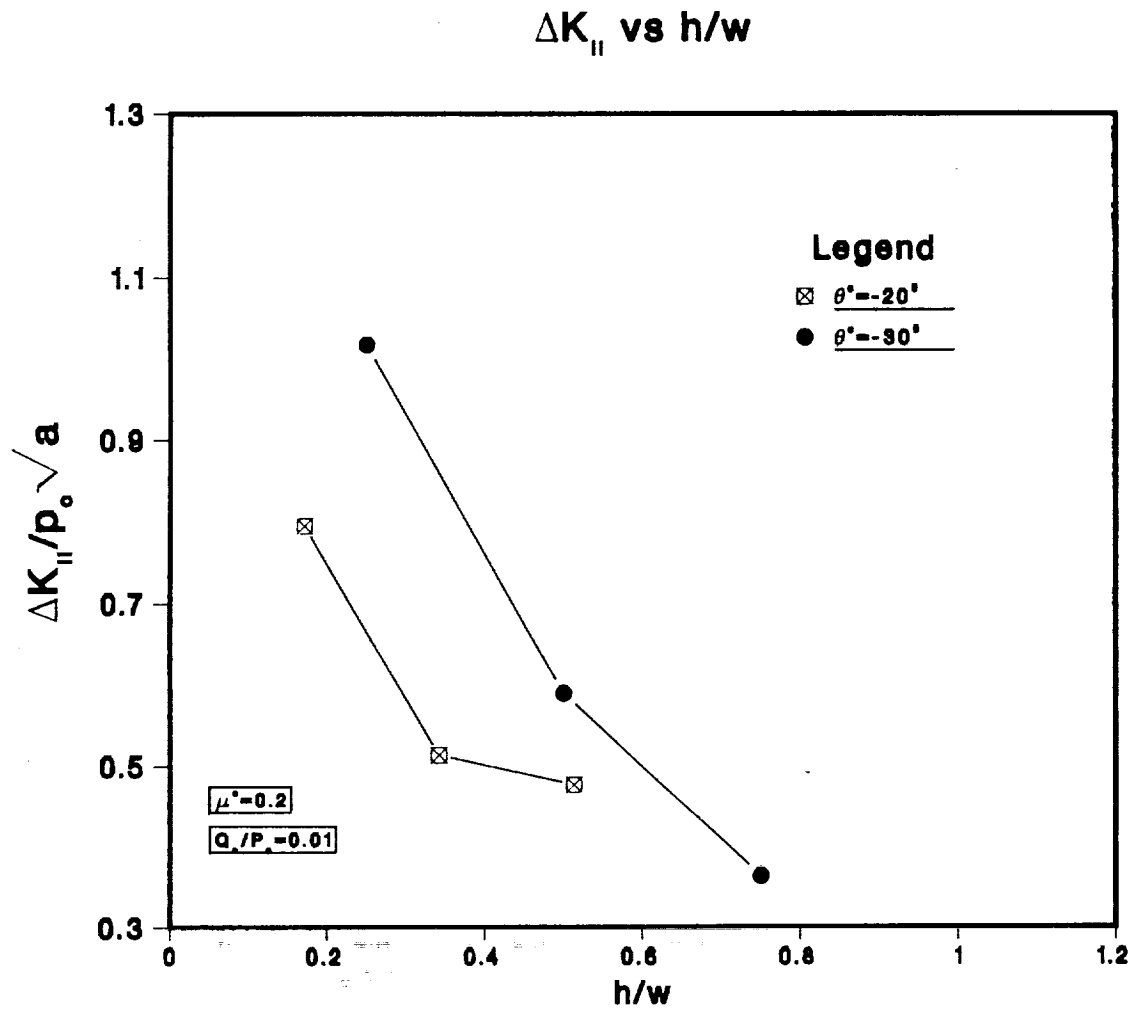


Figure 4.18 Variation of the normalized Mode II crack tip driving force versus the normalized crack tip depth for lubricated contact, crack inclinations, $\theta = -20^\circ$ and -30° , the traction ratio, $q_0/p_0 = 0.01$ and crack face friction, $\mu^c = 0.2$.

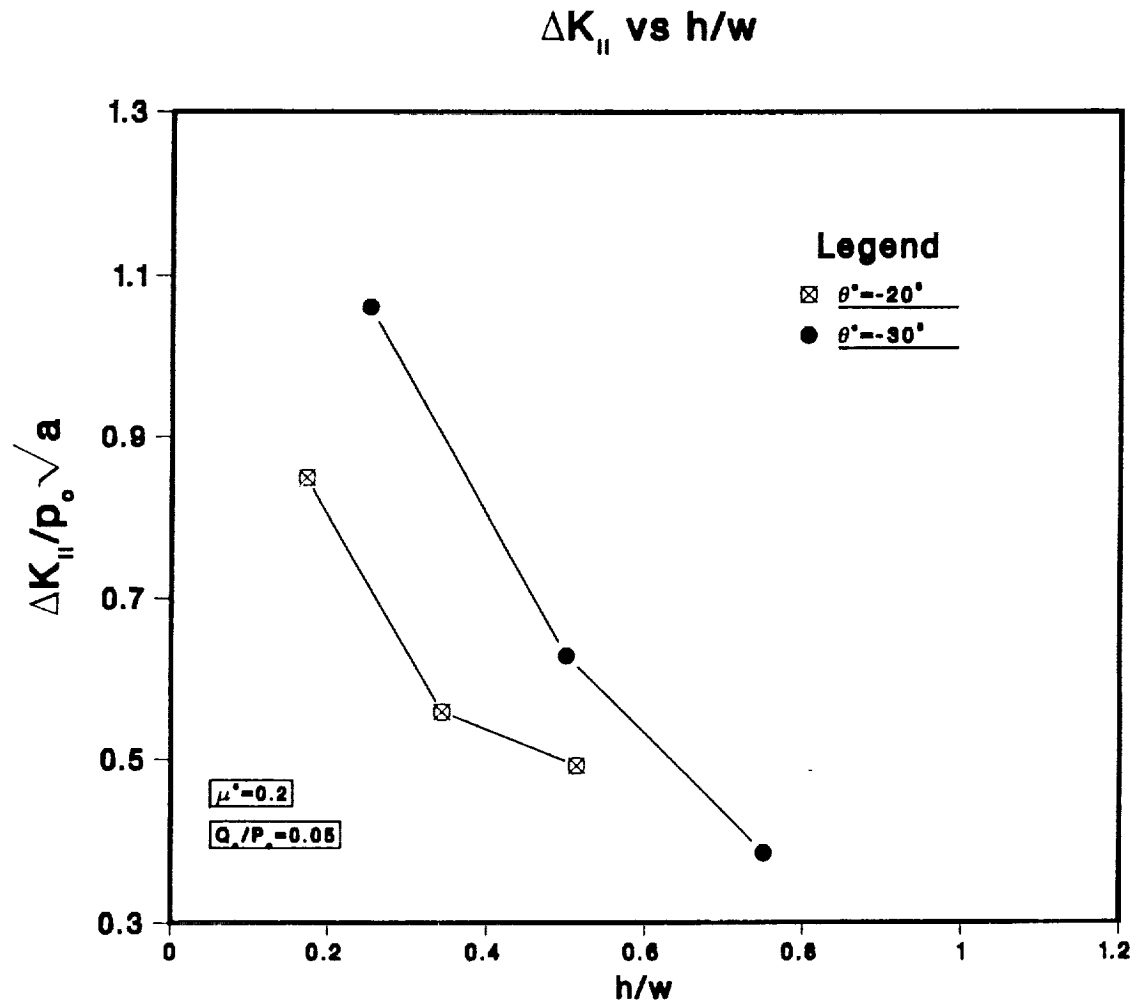


Figure 4.19 Variation of the normalized Mode II crack tip driving force versus the normalized crack tip depth for lubricated contact, crack inclinations, $\theta = -20^\circ$ and -30° , the traction ratio, $q_o/p_o = 0.05$ and crack face friction, $\mu^c = 0.2$.

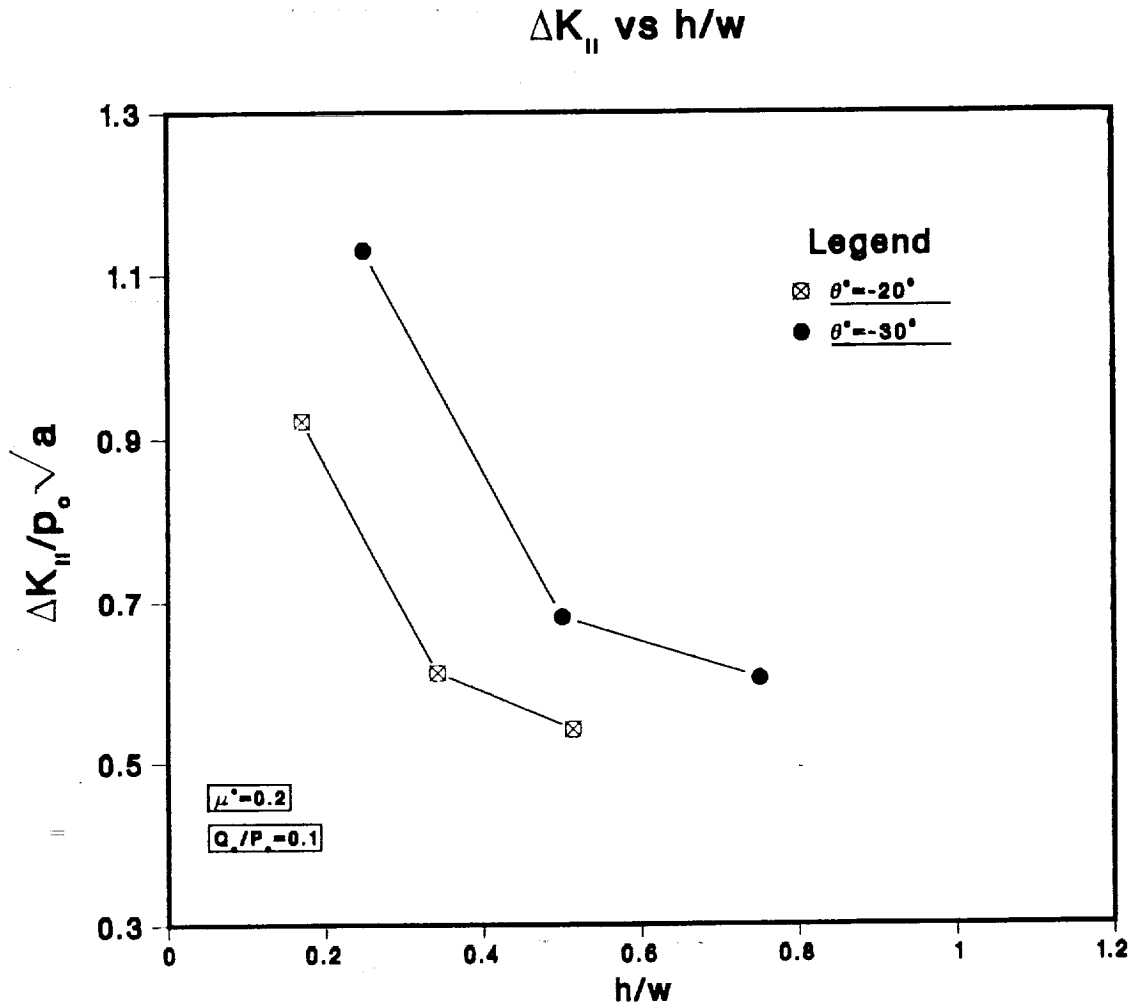


Figure 4.20

Variation of the normalized Mode II crack tip driving force versus the normalized crack tip depth for lubricated contact, crack inclinations, $\theta = -20^\circ$ and -30° , the traction ratio, $q_0/p_0 = 0.1$ and crack face friction, $\mu^c = 0.2$.

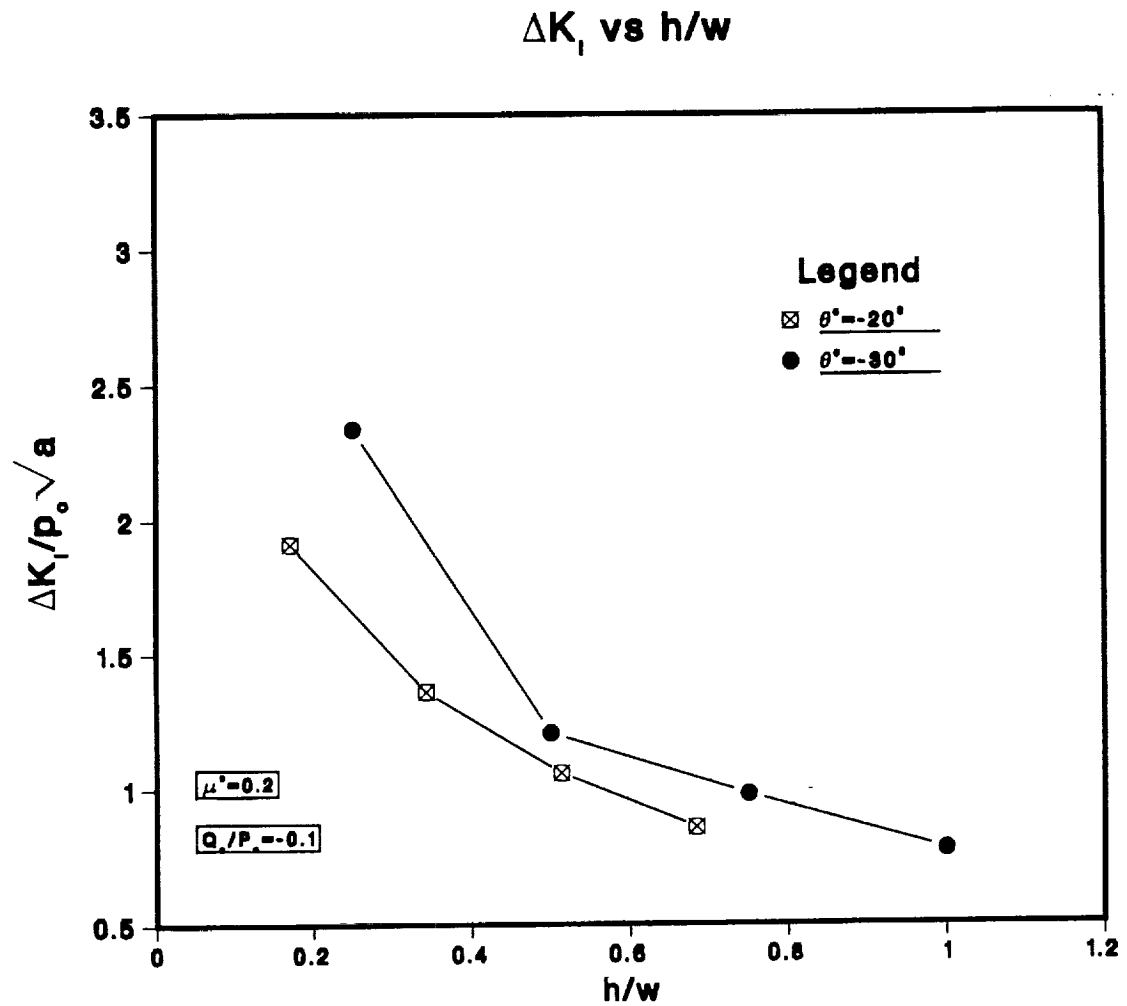


Figure 4.21 Variation of the normalized Mode I crack tip driving force versus the normalized crack tip depth for lubricated contact, crack inclinations, $\theta = -20^\circ$ and -30° . The Mode I values are independent of the traction ratio and the crack face friction.

K_{II} AND K_I vs x/w

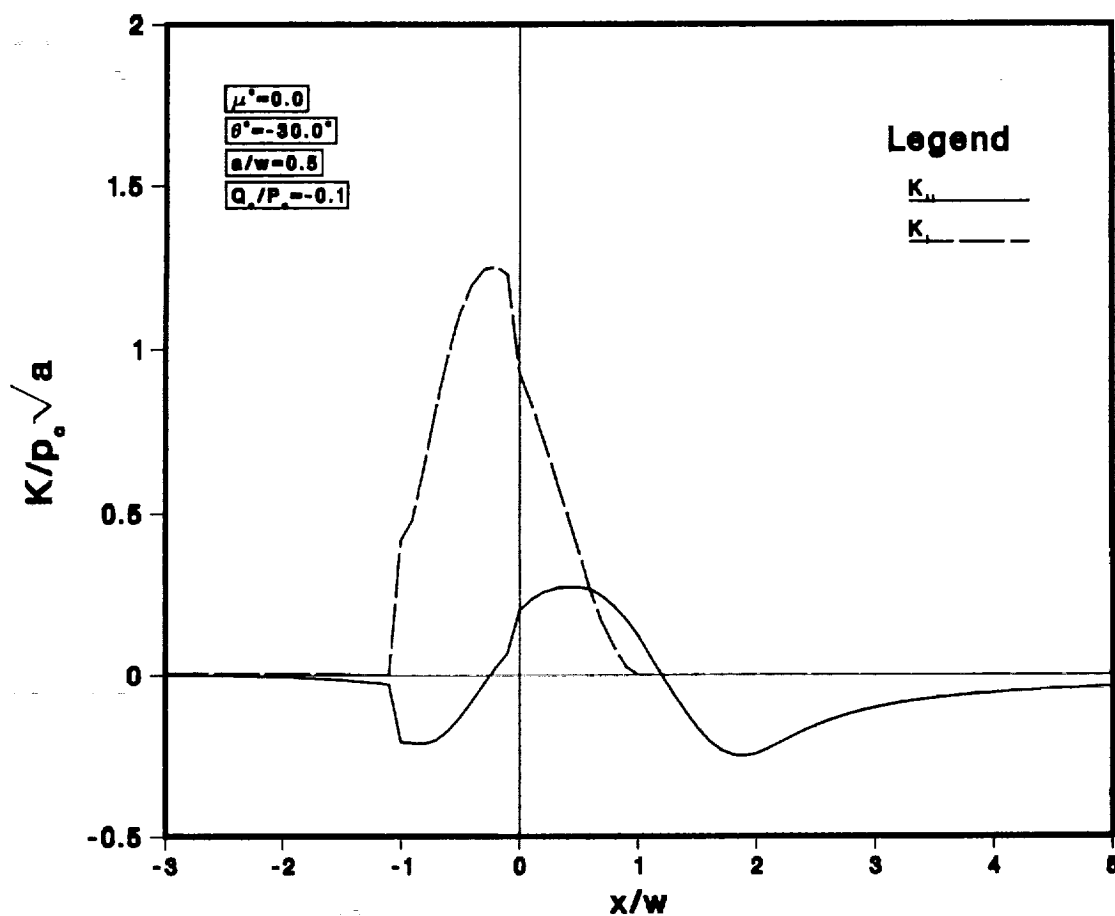


Figure 4.22

Variation of the normalized, Mode I and Mode II stress intensity factor versus the normalized distance between the contact and the crack mouth for lubricated contact, a relative crack length, $a/w = 0.5$, crack inclinations $\theta = -20^\circ$, the traction ratio, $q_0/p_0 = -0.1$, and crack face friction, $\mu^c = 0$.

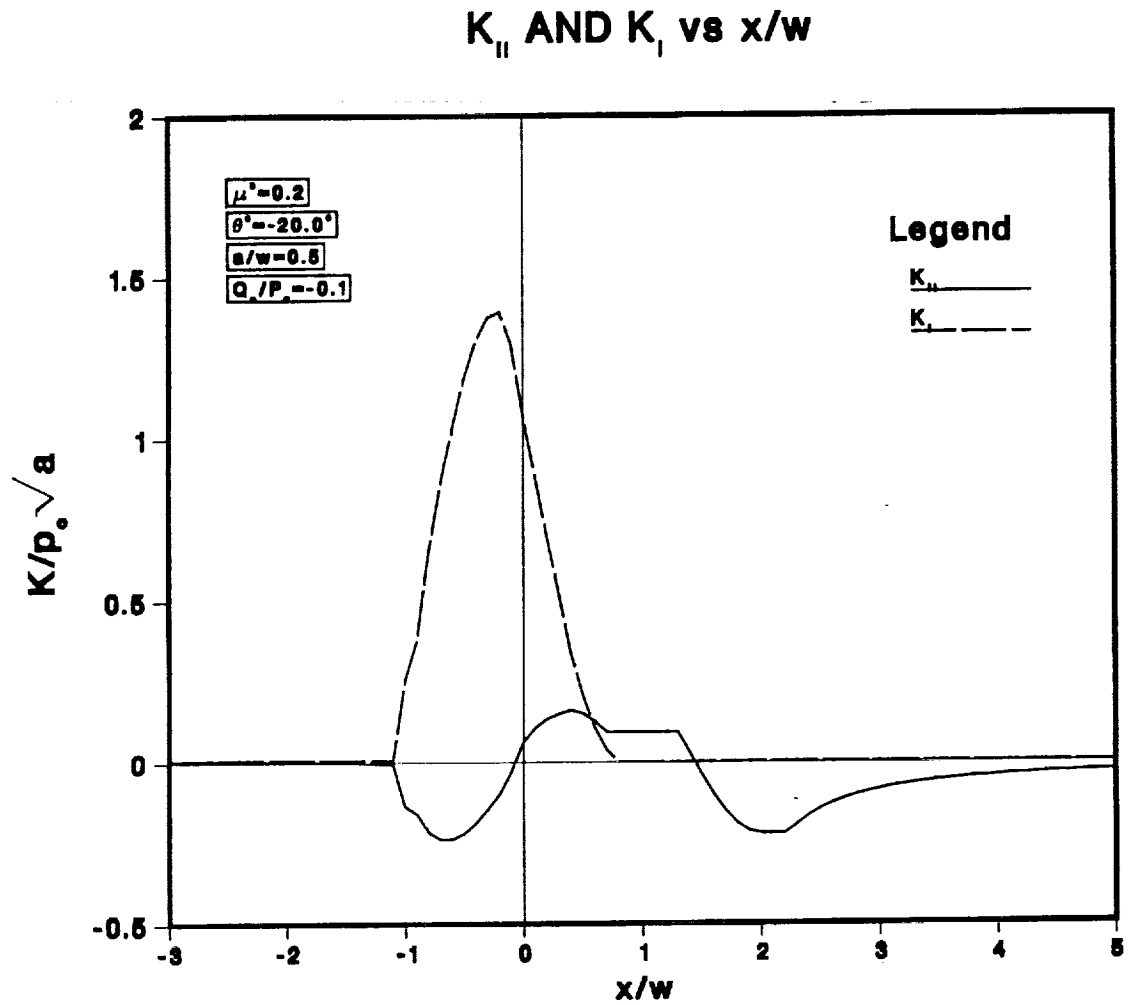


Figure 4.23 Variation of the normalized, Mode I and Mode II stress intensity factor versus the normalized distance between the contact and the crack mouth for lubricated contact, a relative crack length, $a/w = 0.5$, crack inclinations $\theta = -30^\circ$, the traction ratio, $q_0/p_0 = -0.1$, and crack face friction, $\mu^c = 0.2$.

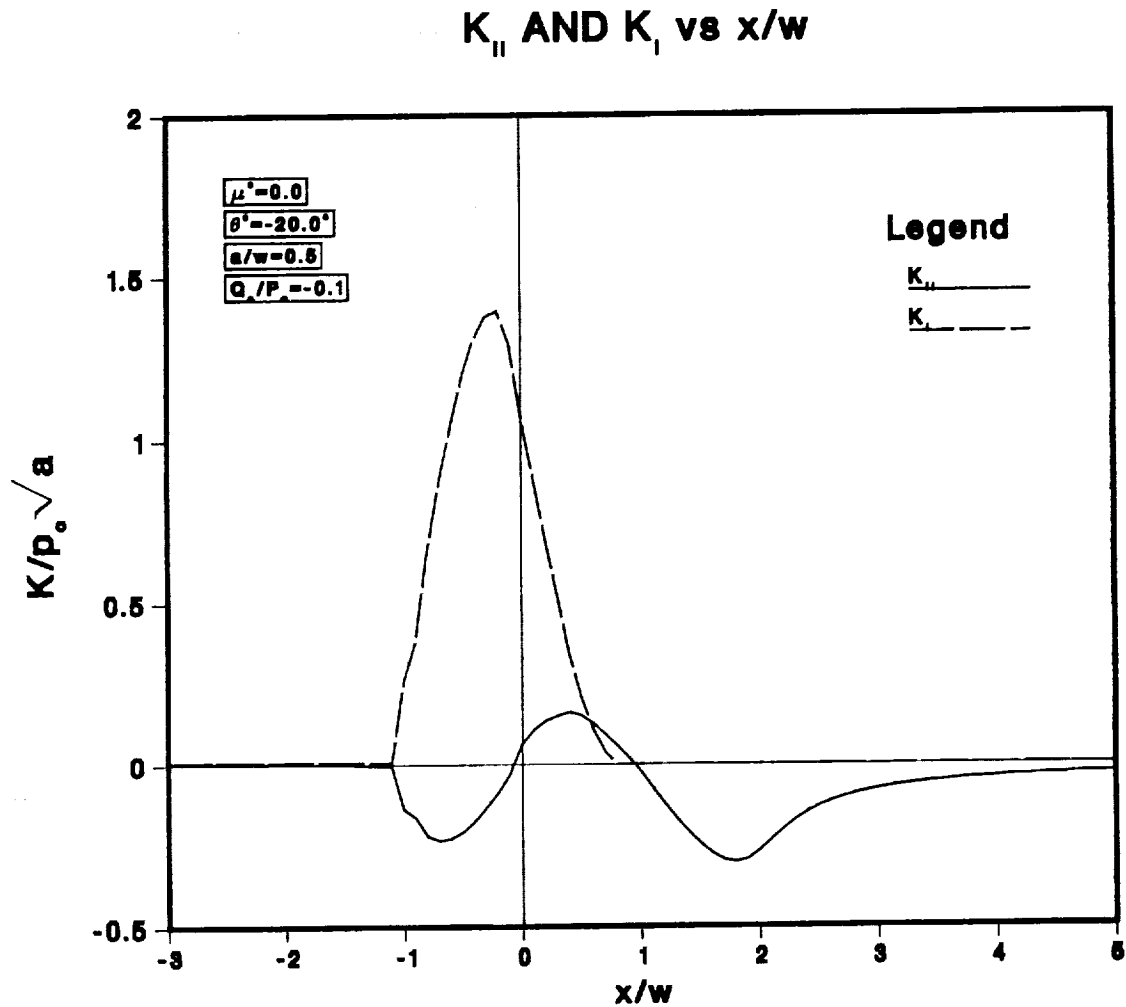


Figure 4.24

Variation of the normalized, Mode I and Mode II stress intensity factor versus the normalized distance between the contact and the crack mouth for lubricated contact, a relative crack length, $a/w = 0.5$, crack inclinations $\theta = -30^\circ$, the traction ratio, $q_0/p_0 = -0.1$, and crack face friction, $\mu^c = 0$.

K_{II} AND K_I vs x/w

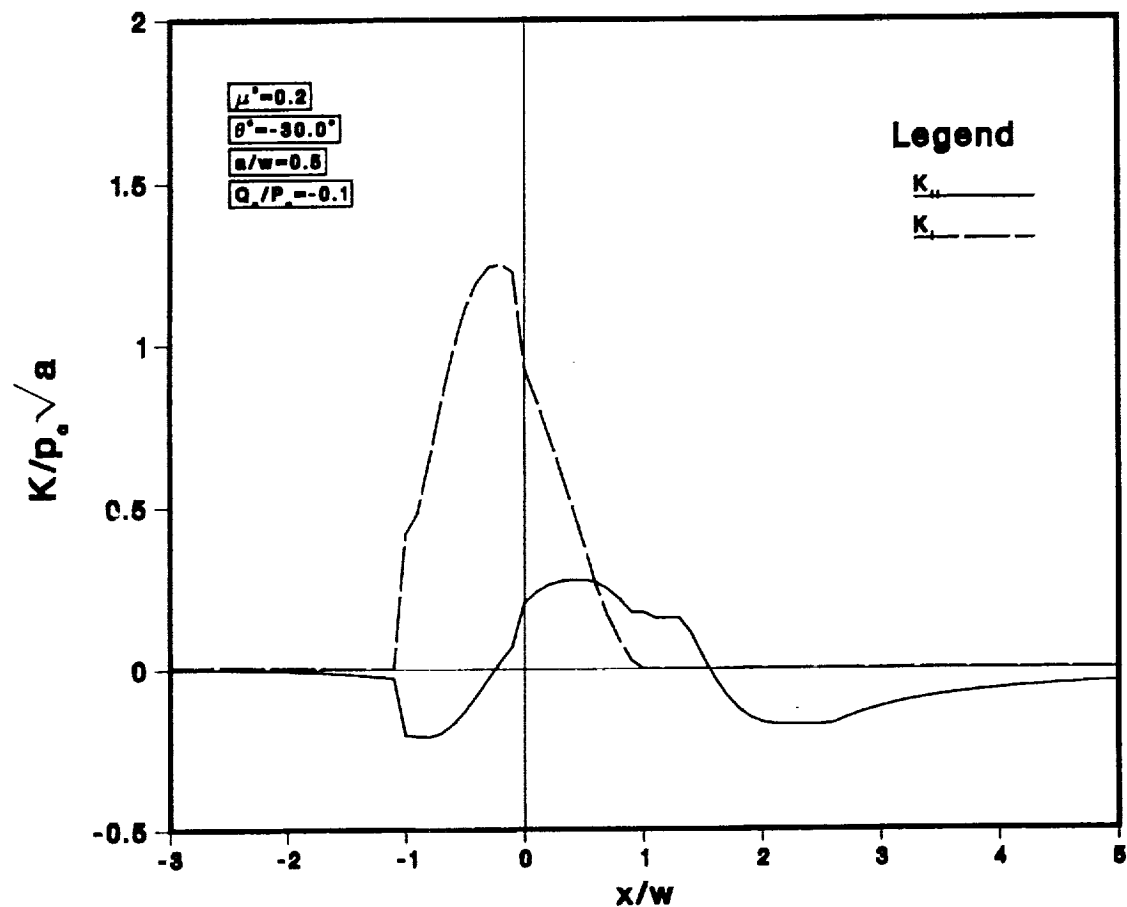


Figure 4.25 Variation of the normalized, Mode I and Mode II stress intensity factor versus the normalized distance between the contact and the crack mouth for lubricated contact, a relative crack length, $a/w = 0.5$, crack inclinations $\theta = -30^\circ$, the traction ratio, $q_0/p_0 = -0.1$, and crack face friction, $\mu^c = 0.2$.

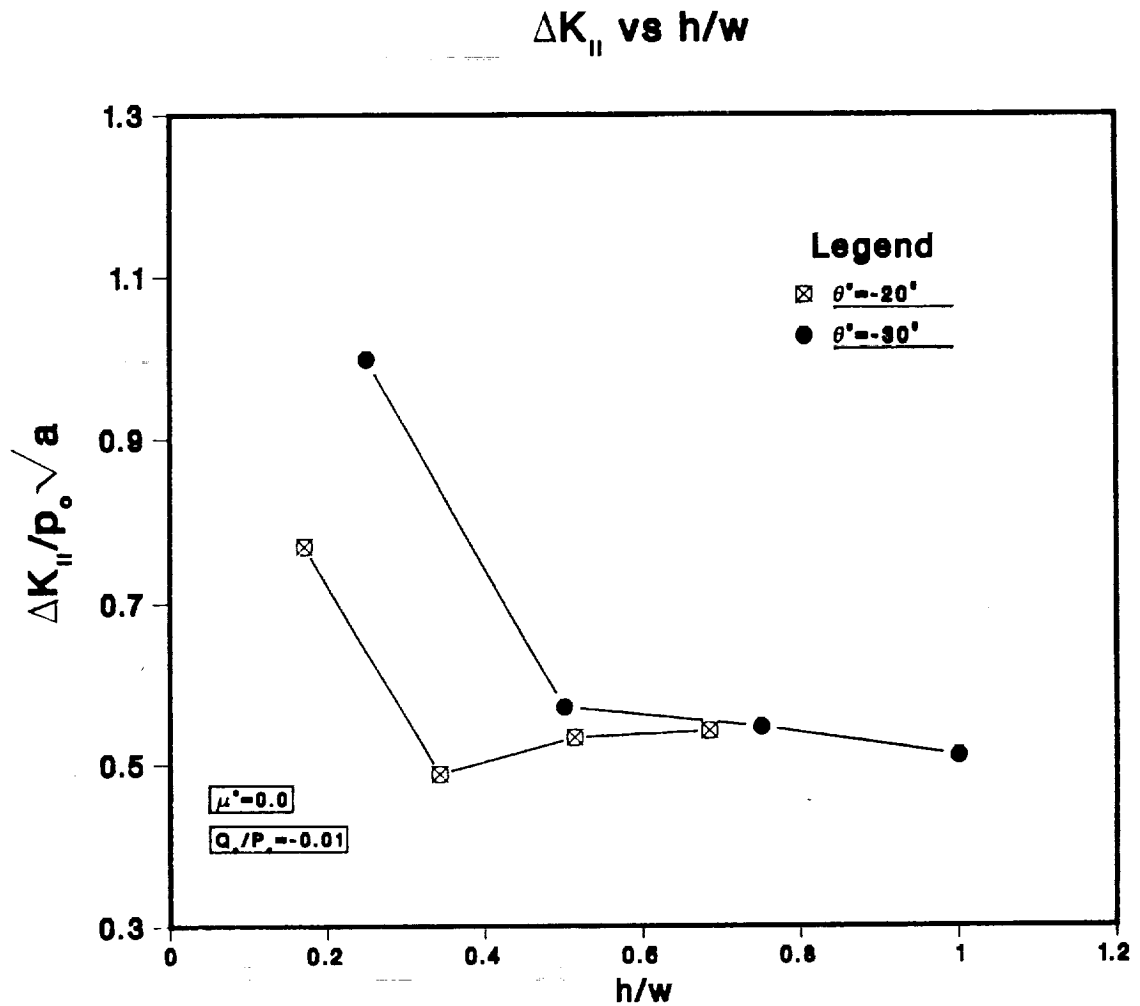


Figure 4.26

Variation of the normalized Mode II crack tip driving force versus the normalized crack tip depth for lubricated contact, crack inclinations, $\theta = -20^\circ$ and -30° , the traction ratio, $q_0/p_0 = -0.01$ and crack face friction, $\mu^c = 0$.

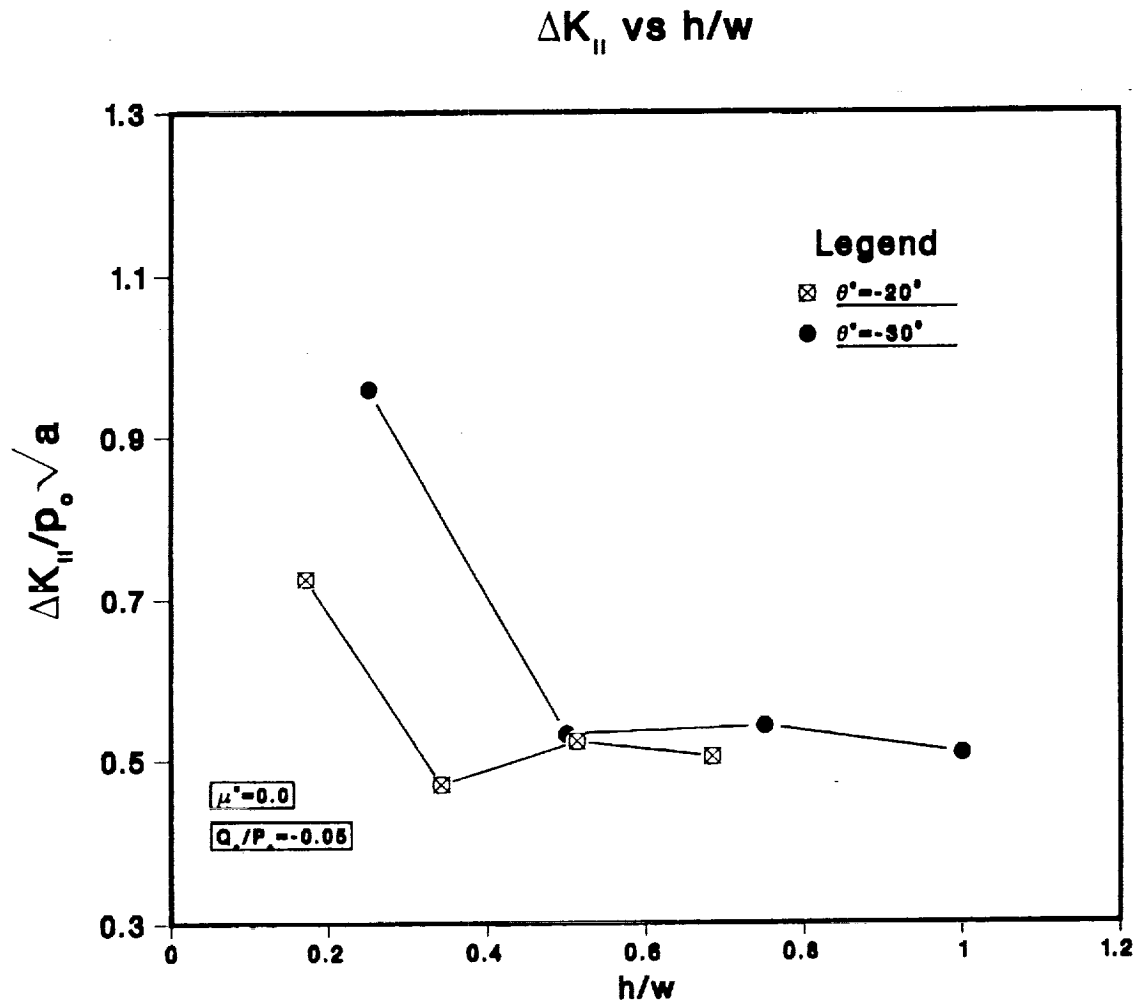


Figure 4.27

Variation of the normalized Mode II crack tip driving force versus the normalized crack tip depth for lubricated contact, crack inclinations, $\theta = -20^\circ$ and -30° , the traction ratio, $q_0/p_0 = -0.05$ and crack face friction, $\mu^c = 0$.

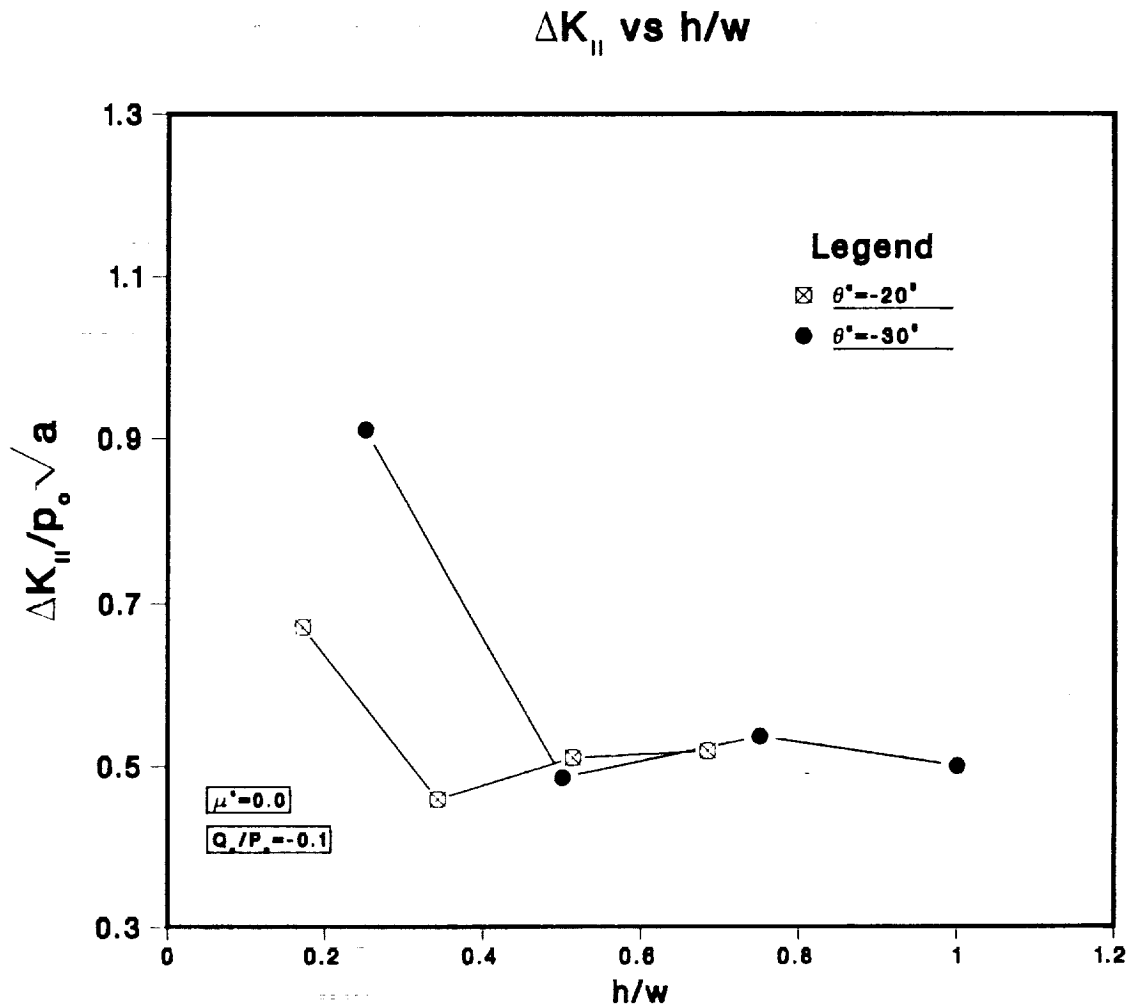


Figure 4.28

Variation of the normalized Mode II crack tip driving force versus the normalized crack tip depth for lubricated contact, crack inclinations, $\theta = -20^\circ$ and -30° , the traction ratio, $q_0/p_0 = -0.1$ and crack face friction, $\mu^c = 0$.

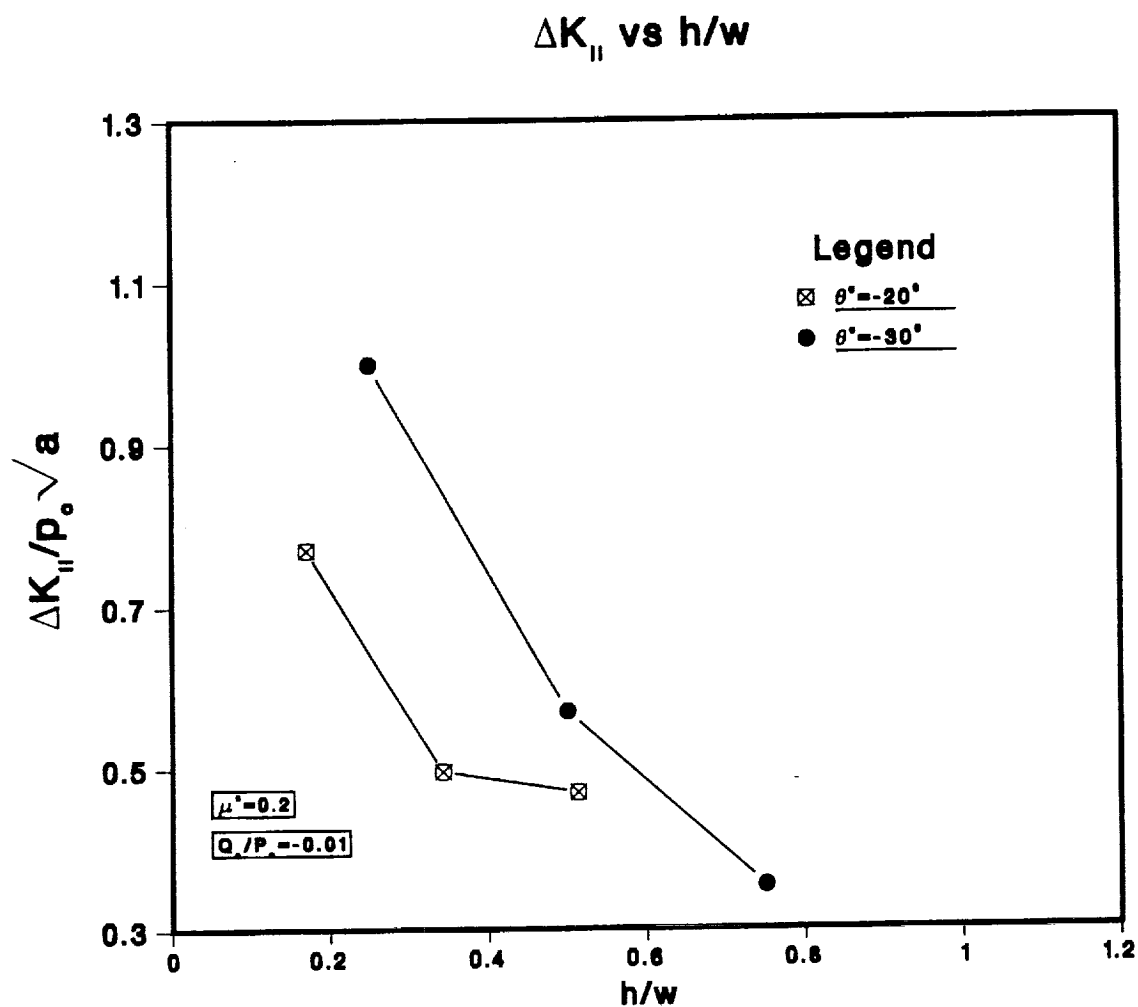


Figure 4.29 Variation of the normalized Mode II crack tip driving force versus the normalized crack tip depth for lubricated contact, crack inclinations, $\theta = -20^\circ$ and -30° , the traction ratio, $q_0/p_0 = -0.01$ and crack face friction, $\mu^c = 0.2$.

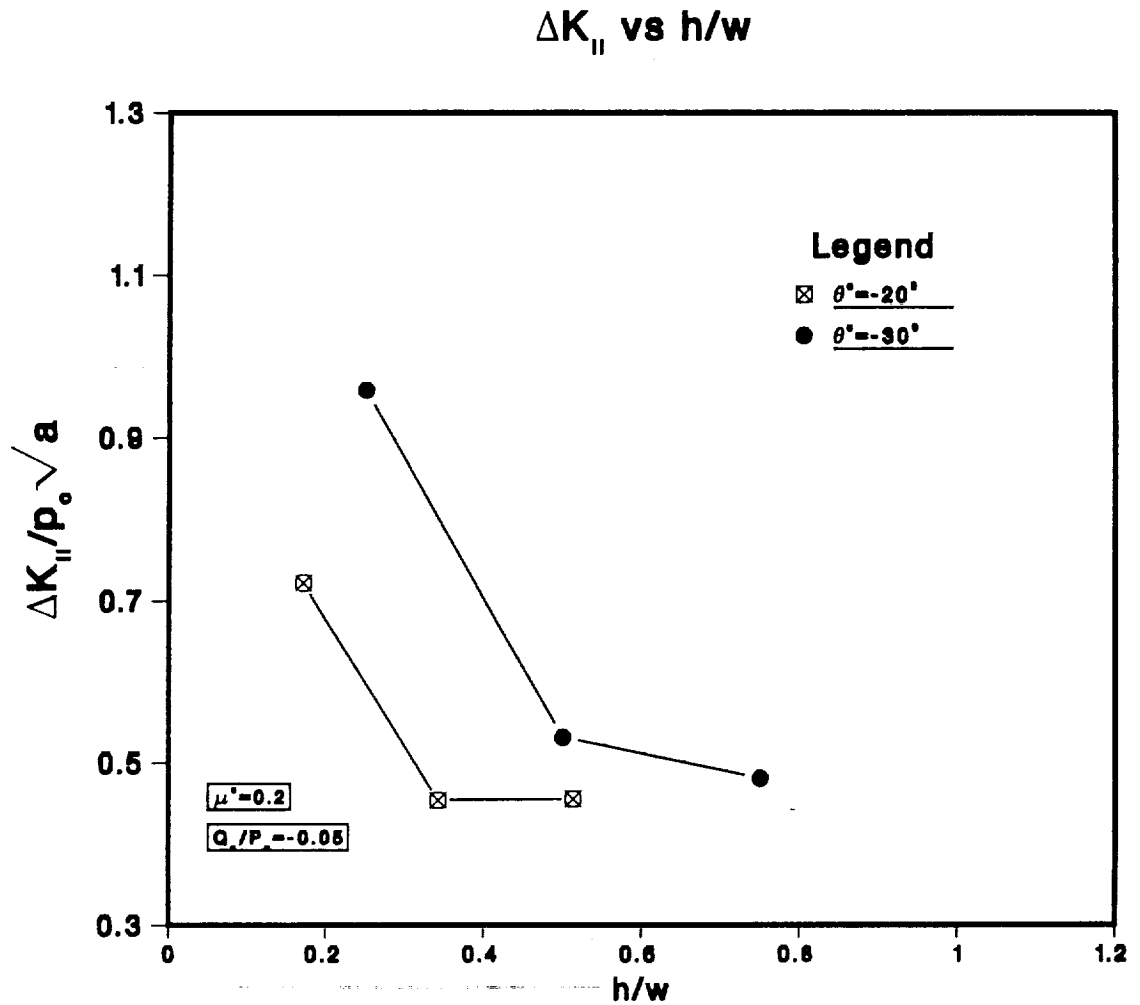


Figure 4.30

Variation of the normalized Mode II crack tip driving force versus the normalized crack tip depth for lubricated contact, crack inclinations, $\theta = -20^\circ$ and -30° , the traction ratio, $q_0/p_0 = -0.05$ and crack face friction, $\mu^c = 0.2$.

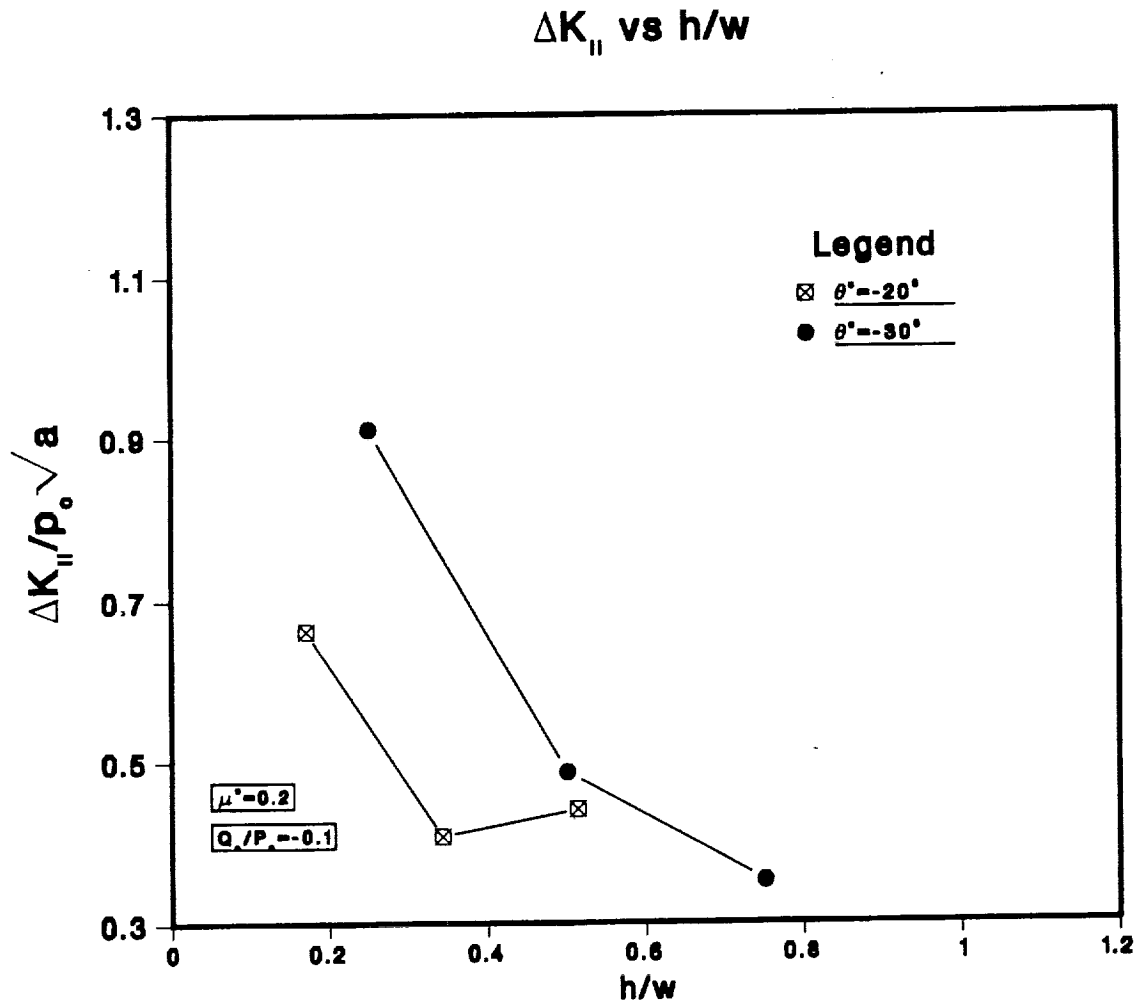


Figure 4.31 Variation of the normalized Mode II crack tip driving force versus the normalized crack tip depth for lubricated contact, crack inclinations, $\theta = -20^\circ$ and -30° , the traction ratio, $q_0/p_0 = 0.1$ and crack face friction, $\mu^c = 0.2$.

Table 4.1 SUMMARY OF FRACTURE MECHANICS K DRIVING FORCE
CALCULATIONS FOR SURFACE BREAKING CRACKS SUBJECTED TO
ROLLING CONTACT

Contact Conditions	$\frac{a}{w}$	$\frac{q_o}{p_o}$	μ^c	$\frac{a}{b}$	θ	Mode	$\frac{\Delta K}{p_o \sqrt{w}}$	Ref.
2D, Dry	0.5	-0.01	0.2	∞	20°	II	0.18	[1]
2D, Dry	1.0	-0.01	0.2	∞	20°	II	0.33	[1]
2D, Dry	1.5	-0.01	0.2	∞	20°	II	0.44	[1]
2D, Lubric.	0.5	-0.01	0.2	∞	20°	II	0.54	[1]
2D, Lubric.	1.0	-0.01	0.2	∞	20°	II	0.49	[1]
2D, Lubric.	1.5	-0.01	0.2	∞	20°	II	0.57	[1]
2D, Lubric.	0.5	-0.01	-	∞	20°	I	1.36	[1]
2D, Lubric.	1.0	-0.01	-	∞	20°	I	1.36	[1]
2D, Lubric.	1.5	-0.01	-	∞	20°	I	1.30	[1]
2D, Lubric.	0.5	-0.05	0.25	∞	25°	II	0.68	[2]
2D, Lubric.	0.5	-0.05	0.25	∞	25°	I	1.44	[2]
2D, Dry, Cent.	1.0	0	0	∞	90°	II	0.97	[3]
2D, Dry, Cent.	2.0	0	0	∞	90°	II	1.13	[3]
2D, Dry, Cent.	1.0	0	0	∞	90°	I	0.09	[3]
2D, Dry, Cent.	2.0	0	0	∞	90°	I	0.27	[3]
2D, Dry, TC	0.05	0.1	0	∞	30°	II	0.078	[4]
2D, Dry, TC	0.10	0.1	0	∞	30°	II	0.131	[4]
2D, Dry, TC	0.20	0.1	0	∞	30°	II	0.209	[4]
3D, Lubric.	0.2	0	0.5	0.5	45°	II	0.035	[5]
3D, Lubric.	0.1	0	0.5	2.0	45°	II	0.053	[5]
3D, Lubric.	0.2	-0.1	0.5	0.5	45°	I	0.15	[5]
3D, Lubric.	1.0	-0.1	-	0.5	45°	I	0.25	[5]
3D, Lubric.	0.1	-0.1	-	2.0	45°	I	0.12	[5]
3D, Lubric.	0.5	-0.1	-	2.0	45°	I	0.20	[5]
3D, Lubric.	1.0	-0.1	-	2.0	45°	I	0.20	[5]

Ref.: [1] This Report

[2] Bower, A.F. (1989)

[3] Mendelson, A., and Ghosh, L.J. (1986)

[4] Goshima, T., and Keer, L.M. (1990)

[5] Kaneta, M., and Murakami, Y. (1990)

Note 1: The values indicated under Ref. [3] were obtained for:

Roller Diam: 0.5 in Roller Length: 0.57322 in

No. Rollers: 28 Shaft Speed: 25,500 RPM

Shaft - IR: 2.0 in, OR: 2.30233 in

Inner Raceway - IR: 2.3 in, OR: 2.6 in

Outer Raceway - IR: 3.1 in, OR: 3.35 in

Interference fit of inner raceway

onto the shaft at 0 RPM : 0.00233 in

Note 2: The values for Ref. [4] are for: thermal loading
parameter (τ) = 10, and for a Peclet number (Pe) = 100.

Key TC - Thermal Contact Dry - No Lubricant in Crack
Cent - Centrifugal Forces Lubric - Pressure in Crack
due to lubric.

cracks, the relation between the normalized driving force and crack length is parabolic¹⁴ (O'Reagan et al., 1985) and this facilitates interpolations. However, this is not the case for the surface breaking cracks examined here and any interpolations to small crack lengths must be done with caution even though the driving force for vanishingly small cracks does approach zero.

The results in Figure 4.32 reveal that pressure from fluid in the crack cavity, centrifugal stresses and thermal stresses each add significantly to the ΔK -driving force, particularly for relatively short cracks, $a/w < 0.1$. However, they are not necessarily additive because they do not peak at the same relative contact location. Fluid in the crack cavity is especially potent since it generates Mode I values that are even larger than the Mode II values. The compilation suggests that all but the smallest, surface breaking, lubricated cracks may grow in Mode I. It is also evident that the driving forces generated by 3 dimensional cracks are $\approx 20\%$ of the values obtained for 2-dimensional cracks. Since the real spall nuclei are 3-dimensional (see Section 5.4), the 3-D results of Kaneta and Murakami (1990) appear to be most relevant for estimating growth on the 3-ball-rod testing machine. The following expressions approximate the variation of the driving force with crack length for this case:

$$\Delta K_I = A (a/w)^B p_0 \sqrt{w} \dots\dots\dots (4.1)$$

where $A = 2.3$ and $B = 0.3$.

4.5 Evaluation of Threshold Crack Sizes.

Insight into the significance of the driving force values can be obtained by installing a separate set of curves describing the conditions at the threshold for growth. By inserting specific values of the peak contact pressure, p_0 , and the threshold value of ΔK , curves describing the driving force requirements for different threshold flaw sizes can be generated. These curves are overlayed in Figures 4.33-4.34 on the results of the driving force analyses in Figure 4.32 for 2 contact pressures and 2 estimates of the threshold, $\Delta K_{\text{threshold}}$. The coincidence of the results from a particular driving force source and the threshold curves define the critical crack size for growth in each case. Cracks smaller than the threshold would either not be expected to grow, or to enlarge much more slowly as part of the crack nucleation process. Since crack nucleation is assisted by hard particles and inclusions, the critical flaw size can be viewed as a rough measure of the tolerable inclusion size.

¹⁴ $\Delta K/p_0\sqrt{a} = A$ or $\Delta K/(p_0\sqrt{w}) = A \sqrt{(a/w)}$ where A is a constant.

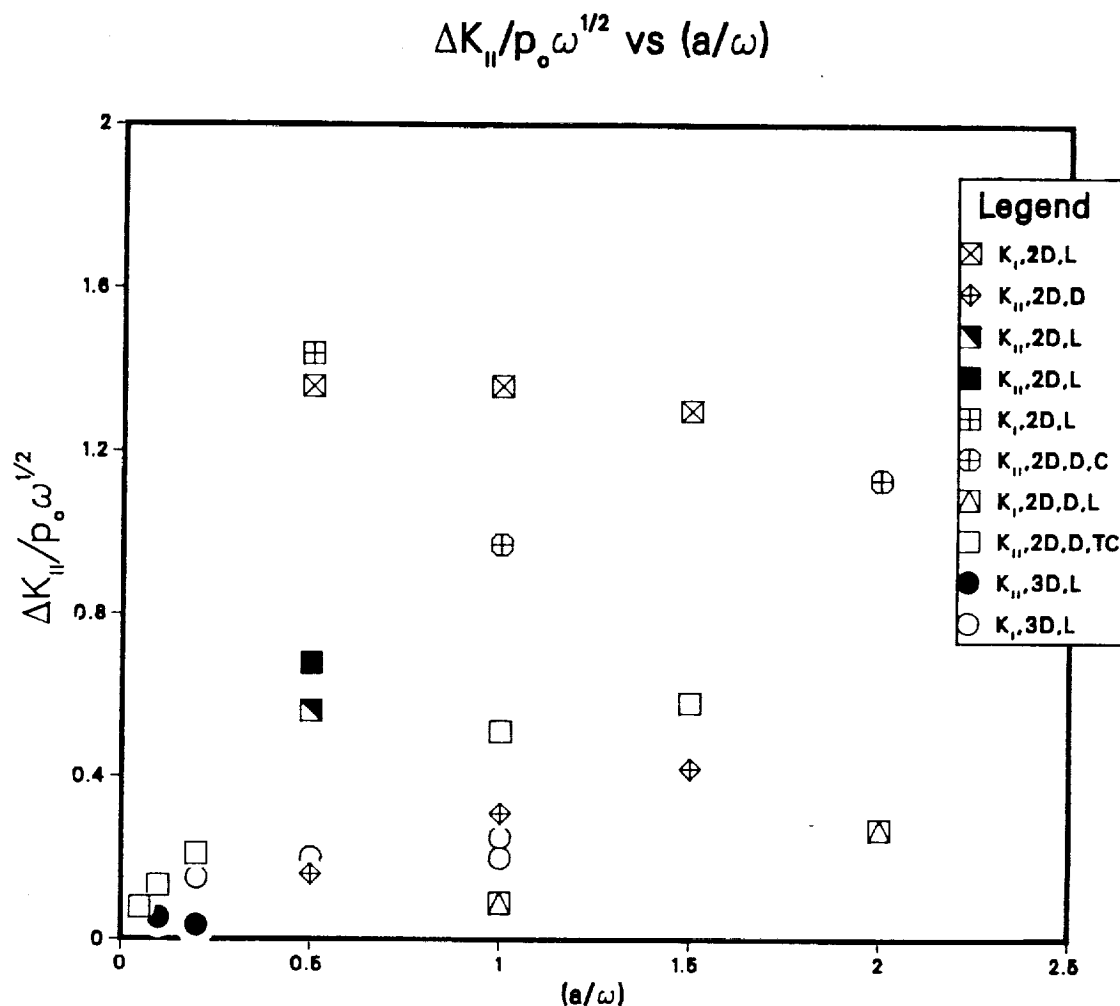


Figure 4.32

Normalized, Mode I and Mode II stress intensity factor ranges reported by different investigators for different sources of the cyclic crack growth driving force and for different relative crack lengths. Details can be found in Table 4.1. The following abbreviations are used: 2D - 2-dimensional, 3D - 3-dimensional, D - dry, L - lubricated, C - centrifugal stress and T - thermal stress.

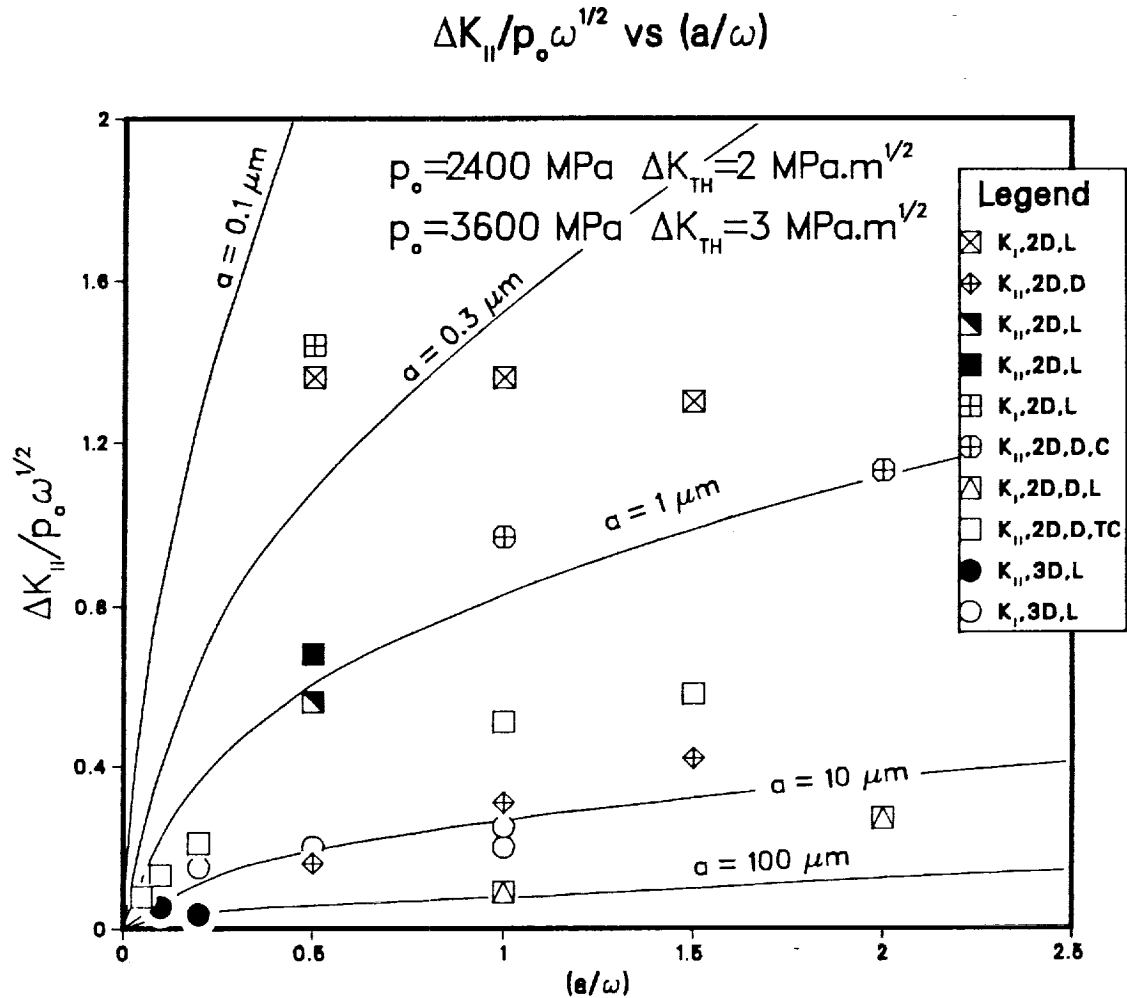


Figure 4.33

Curves describing the conditions at the threshold for cyclic crack growth for either a Hertzian contact pressure, $p_o = 2.4 \text{ GPa}$ and a $\Delta K_{THRESH} = 2 \text{ MPa}$ or $p_o = 3.6 \text{ GPa}$ and a $\Delta K_{THRESH} = 3 \text{ MPa}$. These are overlaid on data points representing the normalized, Mode I and Mode II stress intensity factor ranges reported for different sources of the cyclic crack growth driving force in Figure 4.32. The coincidence defines the conditions for the onset of crack growth in each case. The following abbreviations are used: 2D - 2-dimensional, 3D - 3-dimensional, D - dry, L - lubricated, C - centrifugal stress and T - thermal stress.

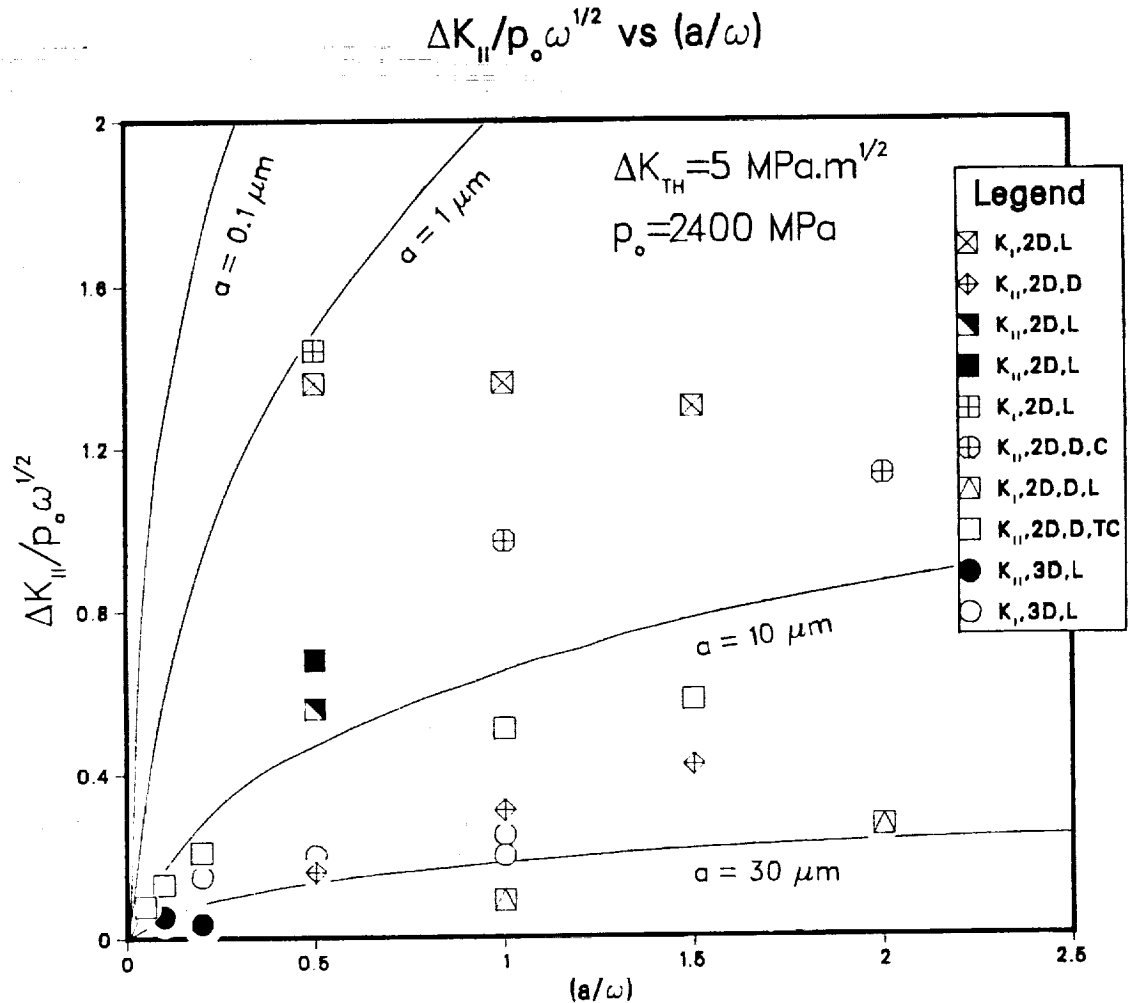


Figure 4.34

Curves describing the conditions at the threshold for cyclic crack growth for a Hertzian contact pressure, $p_o = 2.4 \text{ GPa}$ and a $\Delta K_{THRESH} = 5 \text{ MPa}$. These are overlaid on data points representing the normalized, Mode I and Mode II stress intensity factor ranges reported for different sources of the cyclic crack growth driving force in Figure 4.32. The coincidence defines the conditions for the onset of crack growth in each case. The following abbreviations are used: 2D - 2-dimensional, 3D - 3-dimensional, D - dry, L - lubricated, C - centrifugal stress and T - thermal stress.

surfaces, a Hertzian pressure of $p_0 = 2.4$ GPa and a K_I -threshold = 5 MPa, 3-dimensional, surface breaking cracks (and inclusions) with dimensions, $a \approx 10$ μm can be tolerated in a perfectly smooth well lubricated bearing. The centrifugal stress contribution appears to be negligible. The defect tolerance will be reduced somewhat by thermal stresses arising from loss of lubrication and sliding. The $a \approx 10$ μm defect dimension is larger than the inclusions normally encountered in bearing grade 440C. Consistent with this, the contact lives of 440C samples which contain ≈ 10 μm - surface breaking cracks exceed $N = 6 \cdot 10^8$ contacts when they are tested at $p_0 = 2.4$ GPa in the 3-ball-rod tester. The cracks do not grow under these conditions. At higher contact pressures the same $a \approx 10$ μm surface cracks do grow into spalls and reduce the contact life dramatically (see Section 5.4).

4.6 Conclusions

Efforts have been made to extend the Bower treatment of 2-dimensional, surface breaking cracks with fluid in the crack cavity to smaller relative crack lengths, but the Bower algorithm proved unstable for $a/w < 0.5$. In the range $0.5 < a/w < 1.5$, the values of the normalized driving force, $K/p_0/a$ decrease with the relative crack length, a/w , for lubricated contact, but increase for dry contact

A compilation of K -driving force values of surface breaking cracks has been assembled. This reveals that fluid in the crack cavity, centrifugal stresses, and thermal stresses add significantly to the crack driving force, particularly for relatively short cracks, $a/w < 0.1$. Fluid in the crack cavity is especially potent, producing relatively large Mode I driving force values. The driving forces generated by 3-dimensional cracks are $\approx 20\%$ of the values calculated for 2-dimensional cracks.

As a result of the modest driving force generated by small, 3-dimensional cracks, surface cracks as large as $a \approx 10$ μm would not be expected to grow in idealized smooth, well lubricated bearings with a Mode I, $K_{\text{THRESH}} = 5$ MPa subjected to a Hertzian Pressure, $p_0 = 2.4$ GPa. This is consistent with experimental results described in Section 5.4.

5. ROLLING CONTACT FAILURE

5.1 Background

The life of an element subjected to rolling contact loading is limited by the premature spalling and heavy wear of the bearing races and balls. The spalls are mainly surface initiated, proceeding in both balls and races, and propagate inward with distinctive geometric features.

The spalling process is driven by the surface frictional tractions, Soda (1981), and by the stationary pressure spikes originated at surface irregularities, Hamrock (1990). Additional complications may be caused by: a) the presence of subsurface secondary particles or inclusions, which may lead to subsurface initiated cracks, b) strain induced phase transformations, i.e. retained austenite decomposition, carbide dissolution, c) lubrication conditions at the surface, or d) thermally induced stress fluctuations (as treated in Section 3.5), which eventually contribute to the Modes I and II driving forces (as indicated in Section 4.4).

This section describes experiments conducted on 440C bearing steel in order to gain a better understanding of the mechanisms leading to spall failure under different conditions.

5.2 Experimental Materials and Procedures

The rolling experiments were carried out on the 3-ball-rod rolling contact fatigue tester developed by the ball and roller bearing group at Federal-Mogul, and furnished by NTN Bower. The design and operation of the tester machine has been described by Glover (1982).

The test material is AISI 440C, martensitic stainless steel, heat treated to a hardness of 59-61 HRC. The test samples were subjected to the following heat treatment:

- a) Austenitized at 1930 ± 30 °F for 1 hour at temperature.
- b) Hardened by quenching in liquid nitrogen.
- c) Tempered one hour (minimum) at 325 ± 25 °F.
- d) Cooled in air to 70 ± 10 °F.
- e) Cold soaked in liquid nitrogen for 30 minutes.
- f) Tempered for 1 hour at 325 ± 25 °F.

The geometry of the samples is shown in Figure 5.1. The test

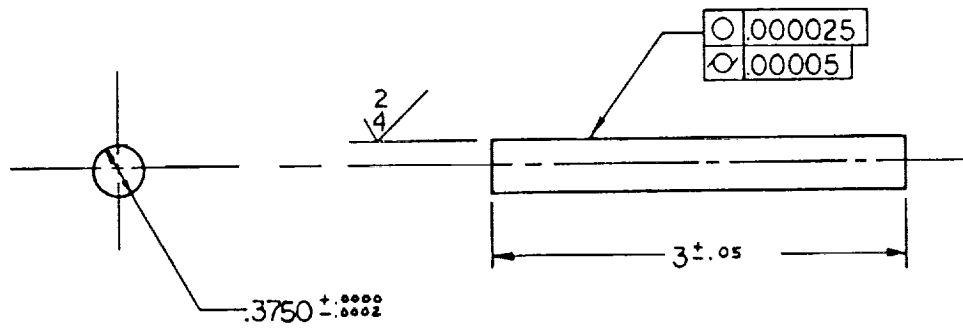


Figure 5.1 Test specimen design according to Glover (1982), all the dimensions are in inches.

samples were ground to a surface finish of 6.5 AA ($0.165 \mu\text{m}$), with a roundness of $1.27\text{--}1.54 \mu\text{m}$ (a more detailed study of the surface finish is included in Figure 5.2). Each rod can be used to perform up to 8 individual tests.

The balls used in the RCF tester are made of AISI 52100 bearing grade steel. Two different sets of balls were used during the tests. The first set consisted of balls with smooth surface, i.e. 0.34 AA ($8.6 \times 10^{-3} \mu\text{m}$), and the second set consisted of balls which are abrasive blasted to increase the surface roughness, i.e. 4.28 AA ($0.11 \mu\text{m}$). A more detailed surface analysis of both types of balls can be seen in Figures 5.3a and b. The chemical compositions for both the 440C and the 52100 steels are shown in Table 5.1.

5.2.1 Rolling Contact Testing: A total of 21 individual tests (see Table 5.2), distributed among three specimens were conducted. After each test the balls were replaced to insure uniform testing conditions. Exxon grade 2380 turbine oil was used as a lubricant in all the tests. The oil was applied by drip feed at a rate of 10 drops per minute. A spring load of 253.6 N was used in all the tests. The peak Hertzian pressure was calculated to be equal to 5.4 GPa.

Six tests were conducted under similar conditions to determine the amount of scatter in the results (Test Series 1). An attempt was also made to vary the content of retained austenite in the specimens by soaking in liquid nitrogen for different lengths of time; a total of 10 tests were devoted to this purpose (Test Series 2). Three more tests were conducted with smooth balls in order to register any differences in the failure life, location and size of spalls, or the surface appearance after the test (Test Series 3). Two additional tests were conducted using rough balls in order to study the contacting surface (Test Series 4). The tests were interrupted after a short time after starting to examine and photograph the surface under the scanning electron microscope. After examination, the specimens were inserted back into the RCF tester. The tests were continued until spalling failure occurred.

The fatigue test results summarized in Table 5.2 have been analyzed using the two-parameter Weibull statistics. The Weibull estimates for the two cases are summarized in Tables 5.3 and 5.4, respectively. Graphical representation of the test data is illustrated in Figure 5.4. The procedure adopted to obtain the Weibull parameters is similar to the graphical method described by Lipson and Sheth (1973). A computer program was written to evaluate the L10 and L50, as well as the characteristic lives, and the upper and lower bounds for the 75% confidence levels, by using a binomial distribution method.

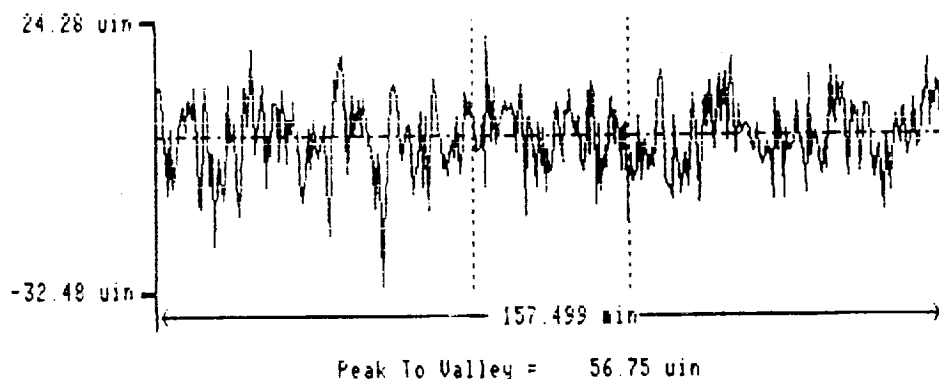
Table 5.1 Composition of 440C and 52100

Steel	C	Mn	Si	Cr	Ni	Mo	Cu	Al	P	S
440C	1.05	.44	.44	17.11	.10	.48	.04	.02	<.022	<.001
52100	1.02	.34	.32	1.45	0.13	.05	.16	---	<.09	<.014

Balance Fe.

F1 - Analysis
 F2 - Graph
 F3 - Dump
 F4 - Expand
 F5 - Exclude
 F6 - Z-Range

Mode	Cut Off	Filter	Reference	Ignore
ROUGHNESS	.030 in	ISO	STRAIGHT	0 %
RCF ROD 440-C GROUND				



F1 - Analysis

Mode	Cut Off	Filter	Reference	Ignore
ROUGHNESS	.030 in	ISO	STRAIGHT	0 %
RCF ROD 440-C GROUND				

Rt1 = 45.57 uin
 Rpa = 28.62 uin
 Ry = 56.50 uin
 Rt1 = 56.50 uin
 Rt2 = 55.62 uin
 Rt3 = 39.22 uin
 Rt4 = 36.85 uin
 Rt5 = 39.66 uin

Lo = 157.499 min
 Rp = 24.28 uin
 Rv = 32.48 uin
 Rt = 56.75 uin

SLOPE = .11 Deg

Ra = 6.47 uin
 Rq = 8.14 uin
 Rsk = -.3
 Rku = 3.4
 Delq = 2.22 Deg
 Lanq = 1.322 min
 S = 625.10 uin
 Sa = 1.227 min
 R3z = 34.54 uin
 R3y = 43.39 uin

Figure 5.2

Surface roughness of 440-C RCF test sample. (a) Shows the profilometer trace, with a peak-to-valley value of 56.75 μ in, (b) shows an analysis of the profile, worth noticing the surface finish of 6.5 μ in, and (c) the roundness analysis indicates a good value, i.e. 50-60 μ in.

ORIGINAL PAGE IS
 OF POOR QUALITY

F1 - Analysis
 F2 - Graph
 F3 - Dump
 F4 - Expand
 F5 - Exclude
 F6 - Z_Range

Mode	Cut Off	Filter	Reference	Ignore
ROUGHNESS	030 in	ISO	CONVEX	0 %
RCF MASTER BALL #1 LOT #1230 <i>Grit blasted</i>				



Peak To Valley = 97.63 uin

F1 - Analysis

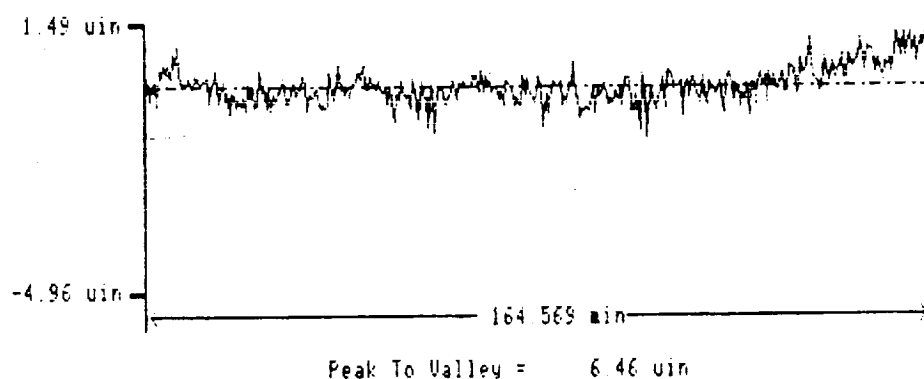
Mode	Cut Off	Filter	Reference	Ignore
ROUGHNESS	030 in	ISO	CONVEX	0 %
RCF MASTER BALL #1 LOT #1230				

Rt = 40.82 uin	Lo = 163.293 min	Ra = 4.18 uin
Rpm = 24.29 uin	Rp = 48.34 uin	Rq = 6.11 uin
Ry = 88.78 uin	Rv = 49.38 uin	Rsk = 1.4
Rt1 = 23.93 uin	Rt = 97.63 uin	Rku = 16.4
Rt2 = 27.18 uin		Delq = 2.81 Deg
Rt3 = 42.57 uin	RADIUS = .25026 in	Lamq = 1.097 min
Rt4 = 29.71 uin	Diameter = .50051 in	S = 582.37 uin
Rt5 = 88.78 uin		Sm = 1.022 min
		R3z = 24.58 uin
		R3y = 38.02 uin

Figure 5.3.a Surface roughness analysis of a 52100 RCF ball. The ball has been grit (sand) blasted to a surface finish of 4.18 μ in, for a peak-to-valley of 97.63 μ in.

F1 - Analysis
 F2 - Graph
 F3 - Dump
 F4 - Expand
 F5 - Exclude
 F6 - Z-Range

Mode	Cut Off	Filter	Reference	Ignore
ROUGHNESS	.030 in	ISO	CONVEX	0 %
RCF NEW BALL BEFORE SANDBLASTING PROCESS				



F1 - Analysis

Mode	Cut Off	Filter	Reference	Ignore
ROUGHNESS	.030 in	ISO	CONVEX	0 %
RCF NEW BALL BEFORE SANDBLASTING PROCESS				

R11 = 2.73 uin	Lo = 164.569 min	Ra = .34 uin
Rp1 = .82 uin	Rp = 1.49 uin	Rq = .47 uin
Ry = 5.54 uin	Rv = 4.96 uin	Rsk = -.8
Rt1 = 1.79 uin	Rt = 6.46 uin	Rku = 15.2
Rt2 = 2.45 uin		Delq = .12 Deg
Rt3 = 1.77 uin	RADIUS = .25020 in	Lamq = 1.359 min
Rt4 = 5.54 uin	Diameter = .50041 in	S = 556.87 uin
Rt5 = 2.11 uin		Su = 1.312 min
		R3z = 1.68 uin
		R3y = 1.98 uin

Figure 5.3.b Surface roughness analysis of a 52100 RCF ball. The ball has been lapped to a surface finish of 0.34 μ in, for a peak-to-valley of 6.34 μ in.

Table 5.2 Result of Rolling Tests

Test Series 1: Study of the contacting surfaces and scatter in the experimental data (combined with Test Series 3 for the statistical analysis shown in Table 5.3)

Test #	Specimen ID	Track #	Machine Head	Hours in LN ₂	Ball Lot ¹⁵	Hours to Failure	Stress Cyclesx10 ⁶
1	A1	L1	1	0	R	22.0	11.33
2	A2	L1	1	0	R	10.4	5.36
3	A2	L3	1	0	R	6.4	3.30
4	A2	L5	1	0	R	2.4	1.24
5	A2	L7	1	0	R	2.4	1.24
6	A2	L9	1	0	R	10.4	5.36

Test Series 2: Retained austenite study.

7	A1	L3	1	1	R	27.8	14.32
8	A1	L5	1	2	R	7.5	3.86
9	A1	L6	2	3	R	22.1	11.38
10	A1	L7	1	3	R	15.2	7.82
11	A1	L8	2	3	R	14.2	7.31
12	A2	L2	2	2	R	3.9	2.00
13	A2	L4	2	2	R	6.4	3.30
14	A2	L6	2	2	R	1.0	0.52
15	A2	L8	2	2	R	16.6	8.54
16	A2	L10	2	2	R	3.4	1.75

Test Series 3: Initial study of ball roughness effect.

17	A1	L2	2	3	S	30.4	15.65
18	A1	L9	1	3	S	14.0	7.20
19	A1	L10	2	3	S	63.6	32.75

Test Series 4: Study of the contacting surfaces and scatter in the experimental data (combined with Test Series 3 for the statistical analysis shown in Table 5.3)

20	A6	L2	2	0	R	19.6	10.09
21	A6	L3	2	0	R	5.3	2.7

¹⁵ R=Rough Lot, S=Smooth Lot

Table 5.3 Two-Parameter Weibull Estimate for Case 1

Study of the contacting surfaces and scatter in the experimental data are combined here. The results shown under Test Series 1 and 4 in Table 5.2

<u>Item</u>	<u>Cycles</u>	<u>Median Ranks</u>
1	0.124×10^7	0.08300
2	0.124×10^7	0.20210
3	0.273×10^7	0.32130
4	0.330×10^7	0.44040
5	0.536×10^7	0.55960
6	0.536×10^7	0.67870
7	0.101×10^8	0.79790
8	0.113×10^8	0.91700
Slope = 1.24469		L10 = 0.94748×10^6
Intercept = -19.37923		L50 = 0.43041×10^7
Characteristic Life = 0.57778×10^7		
Correlation = 0.9633787		

Table 5.4 Two-Parameter Weibull Estimate for Case 2

Study of the effect of retained austenite in the fatigue life using the results shown as Test Series 2 in Table 5.2.

<u>Item</u>	<u>Cycles</u>	<u>Median Ranks</u>
1	0.520×10^6	0.10910
2	0.175×10^7	0.26550
3	0.200×10^7	0.42180
4	0.330×10^7	0.57820
5	0.386×10^7	0.73450
6	0.854×10^7	0.89090
Slope = 1.11034		L10 = 0.49944×10^6
Intercept = -16.81940		L50 = 0.27247×10^7
Characteristic Life = 0.37904×10^7		
Correlation = 0.9825556		

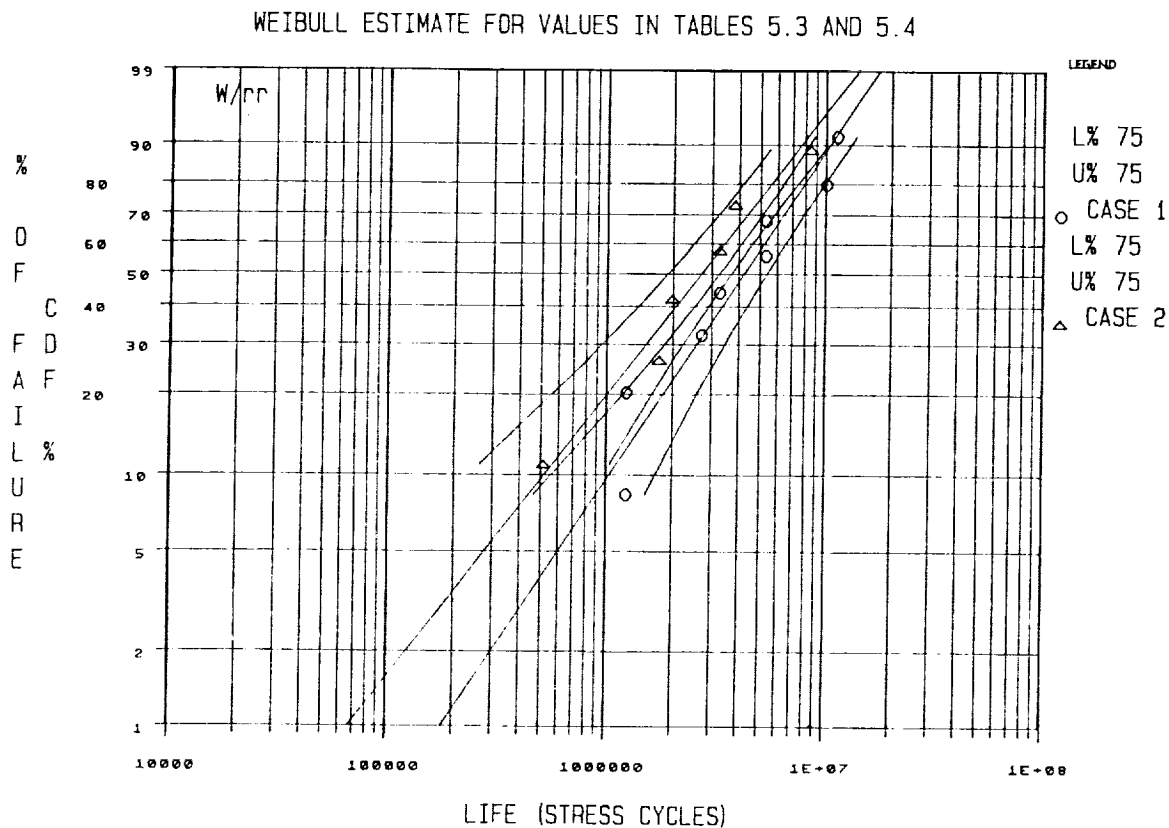


Figure 5.4

Weibull plot for the RCF test results presented in Tables 5.3 and 5.4, peak pressure, $p_0 = 5.4$ GPa. Case 1 (circles) represent the statistical analysis of the results of the Test Series 1 and 4 from Tables 5.2. Case 2 (triangles) are the results of the study of the influence of retained austenite on the fatigue life, i.e. Test Series 3 from Table 5.2.

In order to perform the statistical analysis of the data included in Table 5.2, the samples were grouped in two different categories: a) Tests Series 1 and 4 were combined since they represent similar test conditions, b) Six tests from Test Series 2, each with two hours of liquid nitrogen immersion, were selected to represent similar test conditions. The results show that the Weibull slopes for the two cases are within the range: $0.8 < e < 1.5$ as expected for bearing steels, according to Harris (1984). While the L10 lives for the two cases are comparable, the L50 life for Case 1 is approximately 60% higher than the L50 life for Case 2. This difference may be due to the transformation of the retained austenite after the immersion in liquid nitrogen. In the case of Test Series 3, the use of smooth balls resulted in a relatively longer failure life.

5.2.2 Artificial Defects: Following a procedure similar to the one adopted by Lorosch (1982), the running tracks of 440C specimens were artificially indented by a 120° sphero-conical Rockwell "Brale" penetrator. The load applied to obtain the hardness indents was approximately 10 kg, and the diameter of the indentation was approximately equal to 0.1 mm. Spalls consistently initiated close to the hardness impression in all cases. The specimen surface near the hardness impression was periodically studied and photographed using the scanning electron microscope. The general features of the spall produced by the hardness indent are very similar to the 'classical' spall indicated by Kumar (1987) in early reports. After the crack had initiated, the specimen was inserted back in the RCF tester and run to failure.

A total of 30 experiments were run at three different peak Hertzian pressures, $p_0 = 3.3, 4.0$ and 5.45 GPa. For each pressure, two sets of five samples were run, one without and one with a hardness impression. All these experiments were run with rough balls. Summaries of the rolling tests for the three pressure levels are presented in Tables 5.5, 5.7 and 5.9. In addition to these, Tables 5.6, 5.8 and 5.10 present the Weibull parameters for the tests without and with hardness impressions for the three cases. The results were also plotted on Weibull charts¹⁶; Figure 5.5 shows the results for the tests run under a peak pressure of $p_0 = 3.3$ GPa, and Figures 5.6 and 5.7.a present the results on the same probability paper for the tests conducted at $p_0 = 4.0$ and 5.45 GPa, respectively.

In order to ascertain the influence of the microasperities on the total life of the sample, an additional set of 13 experiments was run at a peak Hertzian pressure of $p_0 = 5.41$ GPa

¹⁶ The percent of failure is expressed as a function of the number of stress cycles.

Table 5.5(a) Rolling experiments without hardness impression
($p_o = 3300$ MPa)

Test #	Specimen ID	Track ID	Machine Head	Hardness Indent	Ball Lot ¹⁷	Hours to Failure	Stress Cycles
1	A9	L1	1	No	R	87.7	45.17×10^6
2	A9	L2	1	No	R	57.3	29.51×10^6
3	A9	L3	1	No	R	25.4	13.08×10^6
4	A9	L4	1	No	R	69.1	35.59×10^6
5	A9	L5	1	No	R	57.8	29.77×10^6

Table 5.5(b) Rolling experiments with hardness impression
($p_o = 3300$ MPa)

Test #	Specimen ID	Track ID	Machine Head	Hardness Indent	Ball Lot	Spall Growth Life in Stress Cycles ¹⁸
1	A9	L6	1	Yes	R	10.15×10^6
2	A9	L7	1	Yes	R	7.11×10^6
3	A9	L8	1	Yes	R	16.07×10^6
4	A9	L9	1	Yes	R	9.06×10^6
5	A9	L10	1	Yes	R	12.52×10^6

¹⁷ R = Rough lot, S = Smooth lot.

¹⁸ Spall Growth Life = (Total failure life with hardness impression) - (Life at first observation of cracks).

Table 5.6(a) Weibull parameters for rolling test without
hardness impression ($p_o = 3300$ MPa)

<u>Item</u>	<u>Cycles</u>	<u>Median Ranks</u>
1	0.1308×10^8	0.1294
2	0.2951×10^8	0.3147
3	0.2977×10^8	0.5000
4	0.3559×10^8	0.6853
5	0.4517×10^8	0.8706
Slope	= 2.11496	$L_{10} = 0.12361 \times 10^8$
Intercept	= -36.78784	$L_{50} = 0.30123 \times 10^8$
Characteristic Life	= 0.35822×10^8	
Mean Life	= 0.31719×10^8	
Correlation	= 0.9503689	

Table 5.6(b) Weibull parameters for rolling test with
hardness impression ($p_o = 3300$ MPa)

<u>Item</u>	<u>Cycles</u>	<u>Median Ranks</u>
1	0.7110×10^7	0.1294
2	0.9060×10^7	0.3147
3	0.1015×10^8	0.5000
4	0.1252×10^8	0.6853
5	0.1607×10^8	0.8706
Slope	= 3.28743	$L_{10} = 0.6186 \times 10^7$
Intercept	= -53.65850	$L_{50} = 0.1097 \times 10^8$
Characteristic Life	= 0.12266×10^8	
Mean Life	= 0.11038×10^8	
Correlation	= 0.9842627	

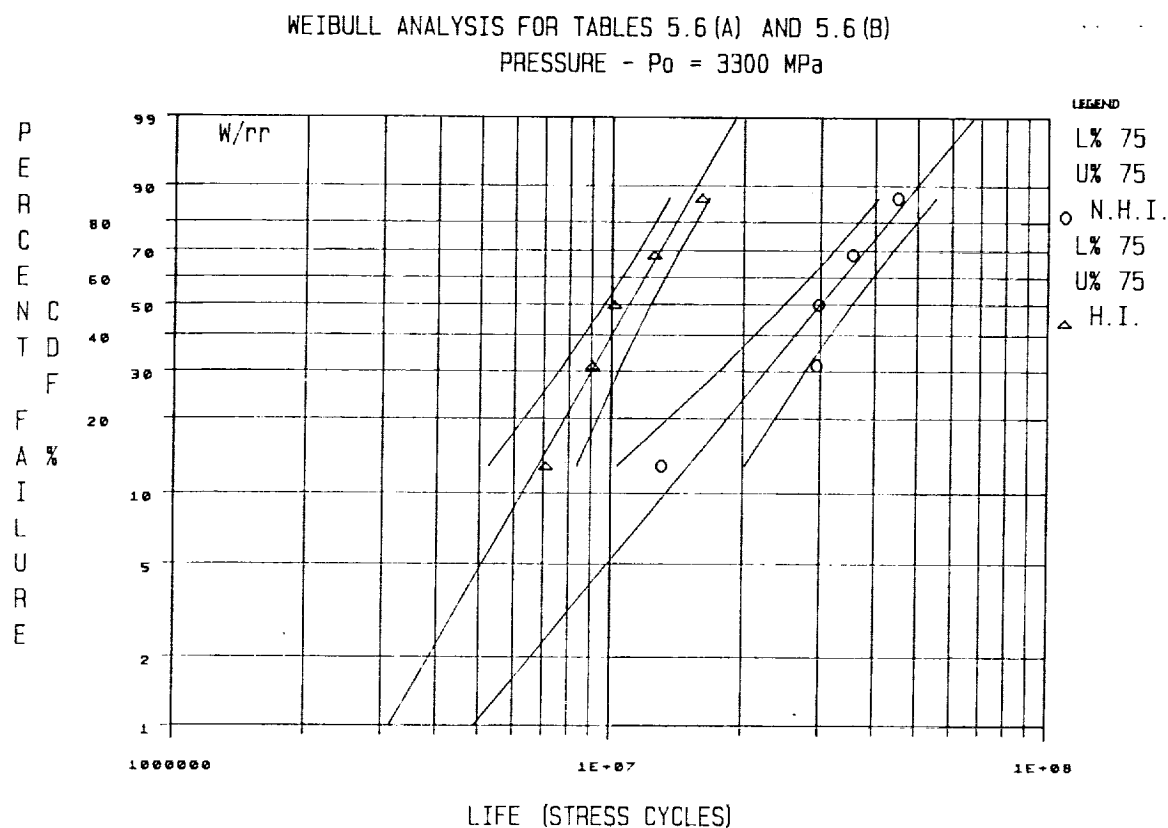


Figure 5.5

Weibull plot for the RCF test results presented in Tables 5.6.a (circles) and 5.6.b (triangles), peak pressure, $p_0 = 3.3 \text{ GPa}$. The two outer lines represent the limits of the 75% certainty band.

Table 5.7(a) Rolling experiments without hardness impression
($p_0 = 4000$ MPa)

Test #	Specimen ID	Track ID	Machine Head	Hardness Indent	Ball Lot	Hours to Failure	Stress Cycles
1	A8	L4	1	No	R	19.0	9.785×10^6
2	A8	L5	1	No	R	48.5	24.980×10^6
3	A8	L6	1	No	R	21.4	11.020×10^6
4	A8	L7	1	No	R	25.7	13.240×10^6
5	A8	L8	1	No	R	30.5	15.710×10^6

Table 5.7(b) Rolling experiment with hardness impression
($p_0 = 4000$ MPa)

Test #	Specimen ID	Track ID	Machine Head	Hardness Indent	Ball Lot	Spall Growth Life in Stress cycles
1	A8	L9	1	Yes	R	5.974×10^6
2	A8	L10	1	Yes	R	7.828×10^6
3	A8	L11	1	Yes	R	4.017×10^6
4	A8	L12	1	Yes	R	3.966×10^6
5	A8	L13	1	Yes	R	4.172×10^6

Table 5.8(a) Weibull parameters for rolling test without hardness impression ($p_o = 4000$ MPa)

<u>Item</u>	<u>Cycles</u>	<u>Median Ranks</u>
1	0.9785×10^7	0.1294
2	0.1102×10^8	0.3147
3	0.1324×10^8	0.5000
4	0.1571×10^8	0.6853
5	0.2498×10^8	0.8706
Slope	= 2.63138	$L_{10} = 0.72331 \times 10^7$
Intercept	= -36.78784	$L_{50} = 0.14799 \times 10^8$
Characteristic Life	= 0.17011×10^8	
Mean Life	= 0.15142×10^8	
Correlation	= 0.9281409	

Table 5.8(b) Weibull parameters for rolling test with hardness impression ($p_o = 4000$ MPa)

<u>Item</u>	<u>Cycles</u>	<u>Median Ranks</u>
1	0.3966×10^7	0.1294
2	0.4917×10^7	0.3147
3	0.4172×10^7	0.5000
4	0.5974×10^7	0.6853
5	0.7828×10^7	0.8706
Slope	= 2.94662	$L_{10} = 0.2749 \times 10^7$
Intercept	= -45.93936	$L_{50} = 0.5210 \times 10^7$
Characteristic Life	= 0.5901×10^7	
Mean Life	= 0.5279×10^7	
Correlation	= 0.8593127	

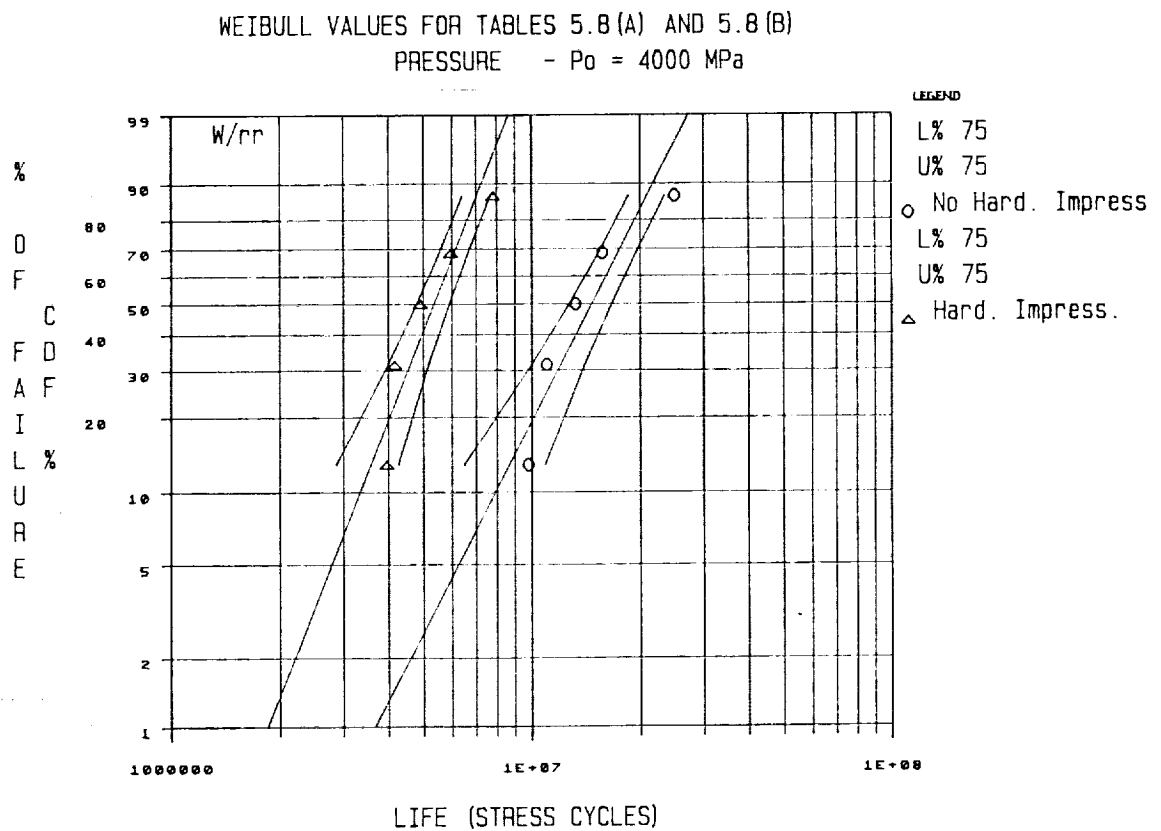


Figure 5.6

Weibull plot for the RCF test results presented in Tables 5.8.a (circles) and 5.8.b (triangles), peak pressure, $p_o = 4.0 \text{ GPa}$. The two outer lines represent the limits of the 75% certainty band.

Table 5.9(a) Rolling experiment without hardness impression
($p_o = 5450$ MPa)

Test #	Specimen ID	Track ID	Machine Head	Hardness Indent	Ball Lot	Hours to Failure	Stress Cycles
1	A7	L4	1	No	R	8.1	4.17×10^6
2	A7	L5	1	No	R	8.5	4.38×10^6
3	A7	L8	1	No	R	7.2	3.71×10^6
4	A7	L9	1	No	R	14.2	7.31×10^6
5	A7	L10	1	No	R	12.2	6.28×10^6

Table 5.9(b) Rolling experiment with hardness impression
($p_o = 5450$ MPa)

Test #	Specimen ID	Track ID	Machine Head	Hardness Indent	Ball Lot	Spall Growth Life in Stress Cycles
1	A7	L11	1	Yes	R	0.695×10^6
2	A7	L12	1	Yes	R	1.210×10^6
3	A8	L1	1	Yes	R	1.416×10^6
4	A8	L2	1	Yes	R	2.678×10^6
5	A8	L3	1	Yes	R	4.532×10^6

Table 5.10(a) Weibull parameters for rolling test without hardness impression ($p_0 = 5450$ MPa)

<u>Item</u>	<u>Cycles</u>	<u>Median Ranks</u>
1	0.3708×10^7	0.1294
2	0.4172×10^7	0.3147
3	0.4378×10^7	0.5000
4	0.6283×10^7	0.6853
5	0.7313×10^7	0.8706
Slope = 3.32260		
Intercept = -51.73905		
$L_{10} = 0.29419 \times 10^7$		
$L_{50} = 0.51865 \times 10^7$		
Characteristic Life = 0.57913×10^7		
Mean Life = 0.52146×10^7		
Correlation = 0.928257		

Table 5.10(b) Weibull parameters for rolling test with hardness impression ($p_0 = 5450$ MPa)

<u>Item</u>	<u>Cycles</u>	<u>Median Ranks</u>
1	0.6953×10^6	0.1294
2	0.1210×10^7	0.3147
3	0.1416×10^7	0.5000
4	0.2678×10^7	0.6853
5	0.4532×10^7	0.8706
Slope = 1.38991		
Intercept = -20.43612		
$L_{10} = 0.4812 \times 10^6$		
$L_{50} = 0.1866 \times 10^7$		
Characteristic Life = 0.24294×10^7		
Mean Life = 0.22133×10^7		
Correlation = 0.9734292		

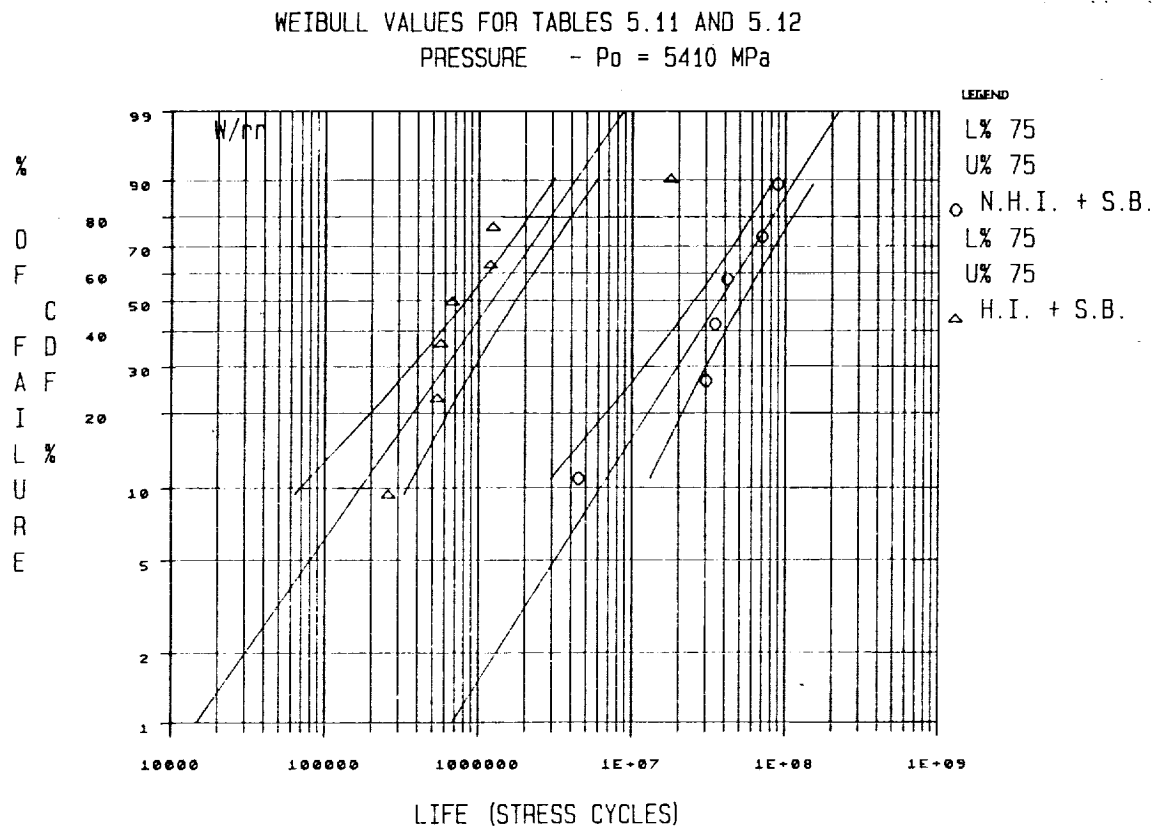


Figure 5.7.a Weibull plot for the RCF test results presented in Tables 5.10.a (circles) and 5.10.b (triangles), peak pressure, $p_0 = 5.45 \text{ GPa}$. The two outer lines represent the limits of the 75% certainty band.

with and without hardness impression¹⁹, but employing smooth balls. Tables 5.11 and 5.12 show the rolling test results and the significant Weibull distribution parameters. The results are presented in Weibull charts in Figure 5.7.b.

5.2.3 Spall Replication and Sectioning Techniques: Before an accurate 3-dimensional finite element model of a crack under rolling contact loading can be implemented, more needs to be known about the geometry of the spalls. Typical spall angles and dimensions, as well as their relationship to the applied load, the geometry of the system, the lubrication, etc., have to be accurately defined. Spalls created during the experimental phase of this program were studied using two different methods: a) a replication technique, and b) a mechanical sectioning followed by scanning microscopy observation.

The first procedure consists of the following steps: 1) the sample was degreased using methanol in an ultrasonic cleaner, 2) a medium viscosity plastic material (vinyl polysiloxane) was then prepared and applied on a glass microslide, 3) the sample, with the spall under study facing down, was pressed against the plastic and held in position for approximately 15 minutes, 4) the sample was removed from the plastic. In order to check the degree of fidelity with which this method reproduces the topological features of the spall, the replicas were gold coated and observed under the scanning electron microscope. Figure 5.8 shows photographs of a spall and the resulting gold coated replica.

The samples were mounted on the adjustable stage of a Sloan Dektak Surface Profile measuring device²⁰, which allowed up to 100 μm displacement in the radial direction²¹. The stylus of the profilometer was positioned on the replica at a distance of approximately 0.3 mm from the spall (this position was taken as the origin in the y direction). The stage was moved along the axial direction at a rate of 0.01 cm/min. Figure 5.9 shows traces obtained with the profilometer, as well as their relative location on the spall. A total of 18 traces were taken for each spall at intervals of approximately 0.05 mm each. The traces were then digitized and used to create a 3-dimensional drawing of the

¹⁹ Two samples were not used for the calculations because they presented lives which were completely different from the rest of the population.

²⁰ This equipment has a sensitivity ranging from 25 Angstrom units to a maximum of 1×10^6 Angstrom.

²¹ Relative to the spall, x is the axial direction, y is the circumferential direction, and z is the radial direction.

Table 5.11 Rolling test results without hardness
impression and smooth balls ($p_0=5410$ MPa)

Test #	Specimen ID	Track ID	Machine Head	Hardness Indent	Ball Lot	Total Life in Stress Cycles
1	440-1	10	2	No	S	30.2×10^6
2	440-1	11	2	No	S	70.3×10^6
3	440-1	12	2	No	S	4.49×10^{622}
4	440-1	5	2	No	S	89.1×10^6
5	440-1	6	2	No	S	34.7×10^6
6	440-1	10	2	No	S	41.6×10^6

Weibull Distribution Parameter

$L_{10} = 21.0 \times 10^6$
 $L_{50} = 51.7 \times 10^6$
 Mean Life = 54.5×10^6
 Slope = 2.09
 Correlation = 0.9386

Table 5.12 Rolling Test Results With Hardness
Impression and smooth balls ($p_0=5410$ MPa)

Item #	Specimen ID	Track ID	Machine Head	Hardness Indent	Ball Lot	Growth Life in Stress Cycles
1	440-L1	5	2	Yes	S	0.57×10^6
2	440-L2	4	2	Yes	S	0.54×10^6
3	440-L3	4	2	Yes	S	0.67×10^6
4	440-L3	5	2	Yes	S	0.26×10^6
5	440-L3	8	2	Yes	S	17.9×10^{623}
6	440-L3	9	2	Yes	S	1.24×10^6
7	440-L3	10	2	Yes	S	1.19×10^6

Weibull Distribution Parameter

$L_{10} = 2.45 \times 10^5$
 $L_{50} = 7.07 \times 10^5$
 Mean Life = 7.71×10^5
 Slope = 1.7789
 Correlation = 0.9700

22 This sample was not used for the Weibull distribution calculations.

23 This sample was not used for the calculations because the total life is significantly different than the rest of the population.

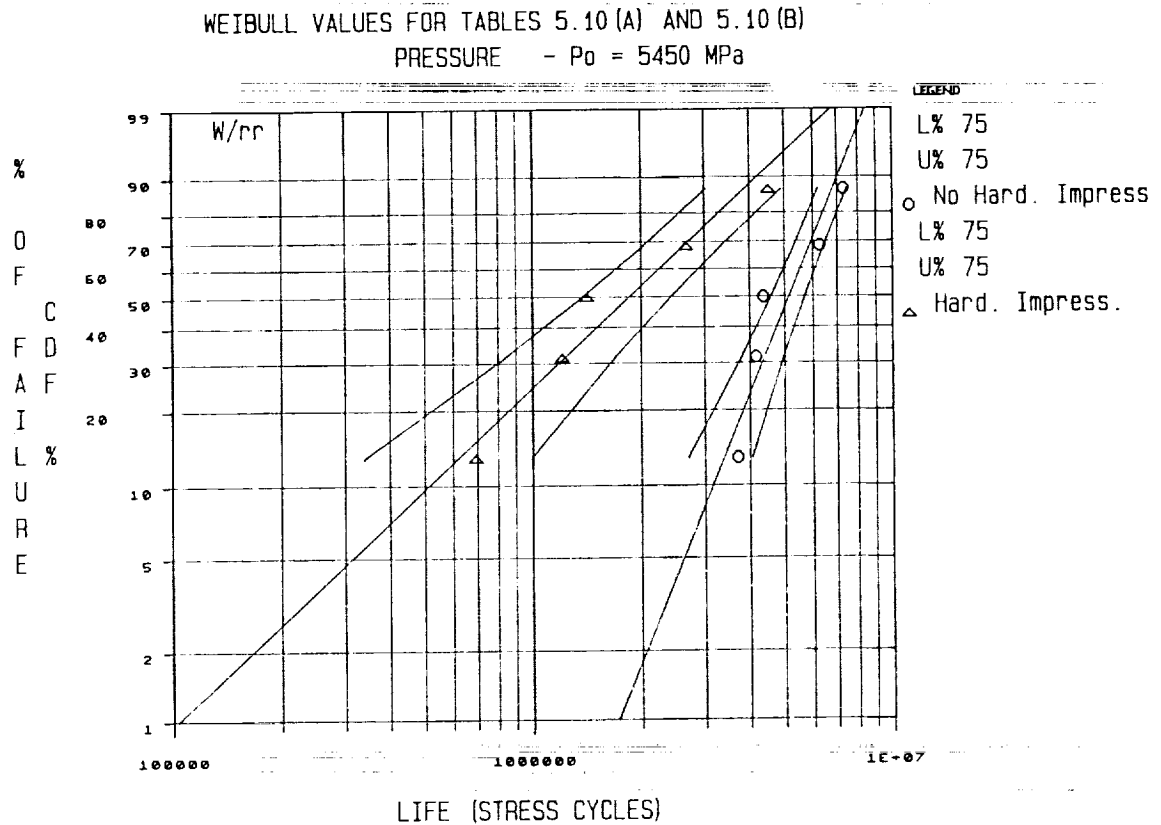


Figure 5.7.b Weibull plot for the RCF test results presented in Tables 5.11 (circles) and 5.12 (triangles), peak pressure, $p_0 = 5.41 \text{ GPa}$. The two outer lines represent the limits of the 75% certainty band.



R.D. ←



Figure 5.8 Spall and gold coated replica of a spall in sample A7, track L5. Viewed at 300X in both cases.

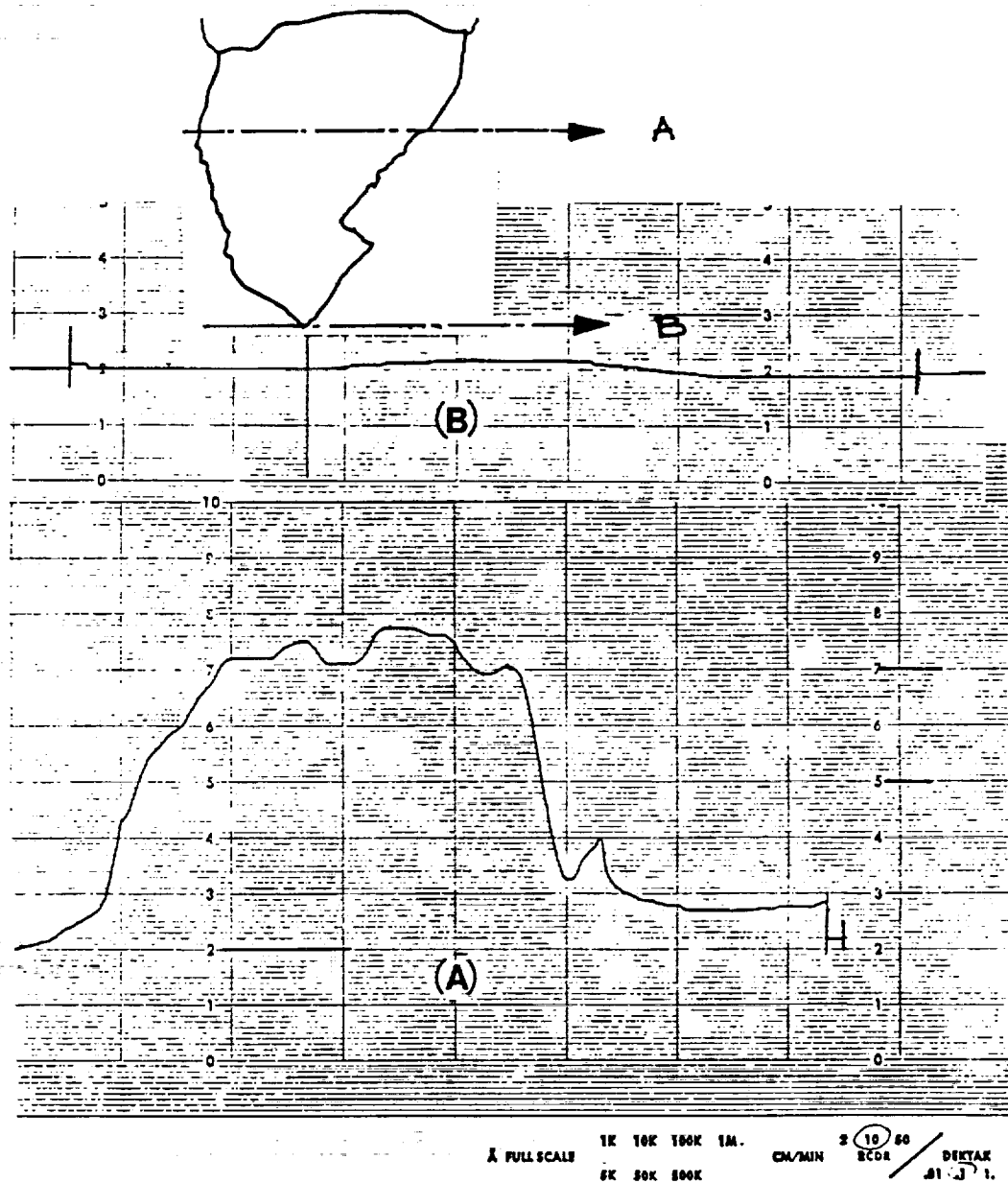


Figure 5.9 Traces of the spall's surface obtained with the Dektak Surface Profilometer. The scales are indicated in the figure, as well as the relative position of the traces in the spall.

ORIGINAL PAGE IS
OF POOR QUALITY

spall; Figure 5.10 shows this drawing as well as the corresponding iso-contour map²⁴.

Some effort has been devoted in the past to characterizing the geometry of the spall failures. Shao et al. (1987) and Soda (1981) have reported cracks running at 20° to 30° to the surface. Bhat and Dolan (1982, 1983) have detected crack inclinations of 10° to 20°; Voskamp (1988) has indicated the presence of cracks running parallel to the surface. Kumar et al. (1987), among others, have pointed out the following general features of the spalls: a) the V-shaped spalls point in the rolling (forward) direction, b) the cracks grow laterally and circumferentially making a small angle with the running surface, c) the cracks grow deeper as they extend in the direction opposite to the rolling direction, and present a stepped like character, d) the cracks break through to the surface at the shallow end, thus producing a cantilever flap supported by an "unbroken" ligament at the deeper end, e) due to secondary cracks running perpendicular to the main crack front, portions of the flap behind the crack front break off periodically producing wear fragments.

In order to systematically check these observations, spalls produced for the present project were sectioned and observed in a transmission electron microscope. The sectioning was done with a high speed silicon carbide cutting blade; water was used as a lubricant. Spalls were sectioned along the axial and circumferential directions. After sectioning, the spalls were mounted in conducting resins (Conductomet) and polished with polishing paper grits 240, 320, 400 and 600. Pictures were taken in a Hitachi scanning electron microscope.

Table 5.13 summarizes the results obtained from the observations²⁵. Figure 5.11 shows a schematic representation of a typical spall and the nomenclature used for the different dimensions and angles. Figures 5.12.a-d show spalls viewed along the radial direction and, after the sectioning, in the circumferential direction. In the radial view, the presence of a micropit right before the V-apex of the spall is evident (Figure 5.12.a). Figures 5.12.b and c show spalls formed in the vicinity of hardness impressions. The top views also indicate the presence of a surface breaking radial crack; this can also be seen in the circumferential cut. The linking of this radial crack with the horizontal subsurface crack results in the detachment of another

²⁴ The 3-dimensional drawing and the iso-contour maps are created by a Fortran program which makes use of the subroutine DISSPLA from Integrated Software Systems Corp.

²⁵ All these results are for a peak Hertzian pressure of $p_0 = 5.45$ GPa, for which the semi-minor and -major contact widths are $w_2 = 0.22$ mm and $w_1 = 0.40$ mm respectively.

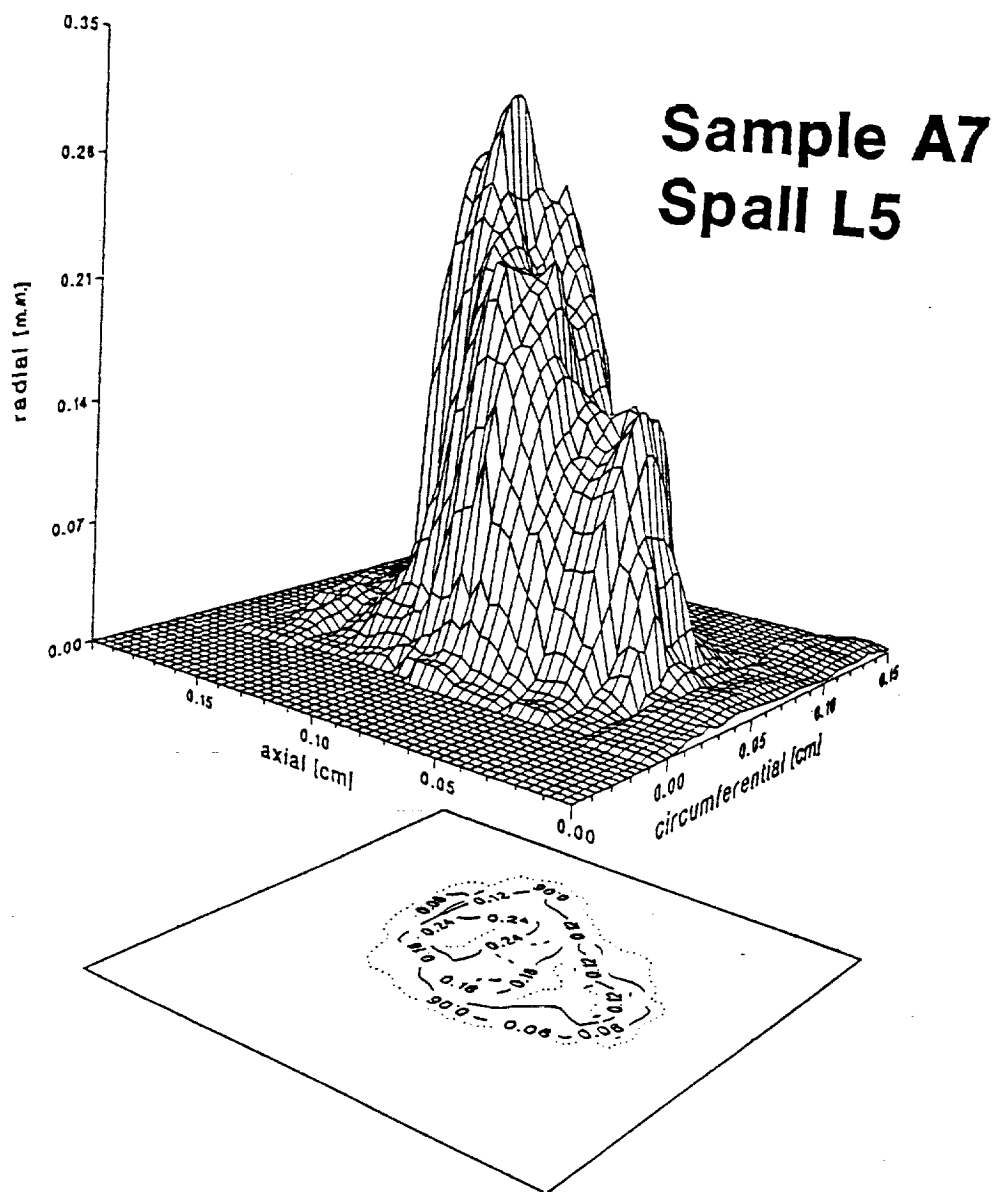


Figure 5.10 3-Dimensional digitized view of spall A7-L5 created under a pressure of $p_0 = 5.45$ GPa. The digitized 3D view results from the traces obtained with a surface profilometer on the surface of the plastic replica. The projection on a plane perpendicular to the radial direction shows the height iso-contours in the spall.

Table 5.13 Spalls Geometry

Samp. ID	Track ID	Hard. Imp.	Ball Lot	W_{ax}^m (mm)	$\frac{W_{max}}{W_{th}}$	L_{max} (mm)	α ($^{\circ}$)	Cut	β ($^{\circ}$)	D (mm)
A1	L1	N	R	0.965	1.20	0.72	62	C	21	0.096
A3	L1	Y	R	0.824	1.02	0.78	54	C	21	0.130
A3	L2	Y	R	0.929	1.15	0.86	62	C	20	0.149
A7	L1	N	R	0.988	1.23	0.99	NA	C	NA	0.138
A7	L3	N	R	0.812	1.00	0.34	NA	C	20	0.075
A7	L7	N	R	1.032	1.28	1.04	30	C	24	0.142
A7	L10	N	R	1.082	1.34	0.91	61	C	13	0.130
A1	L2	N	S	NA	NA	NA	NA	A	54/68	0.115
A1	L3	N	R	0.747	0.93	0.57	55	A	21/45	0.089
A3	L3	Y	R	0.845	1.05	0.85	50	A	44	0.142
A7	L4	N	R	0.853	1.06	0.95	30	A	67/65	0.089
								A	53/60	0.130
A7	L5	N	R	0.952	1.18	1.12	45	A	10	0.075
A7	L8	N	R	0.900	1.12	1.07	51	A	67/65	0.108

W_{max} - Maximum width of the spall, along axial direction (mm).

L_{max} - Maximum length of the spall, in the circumferential direction (mm).

α - Angle at the apex of the spall ($^{\circ}$).

β - Angle(s) observed in the respective cut ($^{\circ}$).

D - Depth, maximum depth for the circumferential cuts, and local depth for the axial cuts.

C - Circumferential cut.

A - Axial cut.

N.A. - Not available

All the tests included in this table were run at a peak Hertzian pressure of 5.45 GPa.

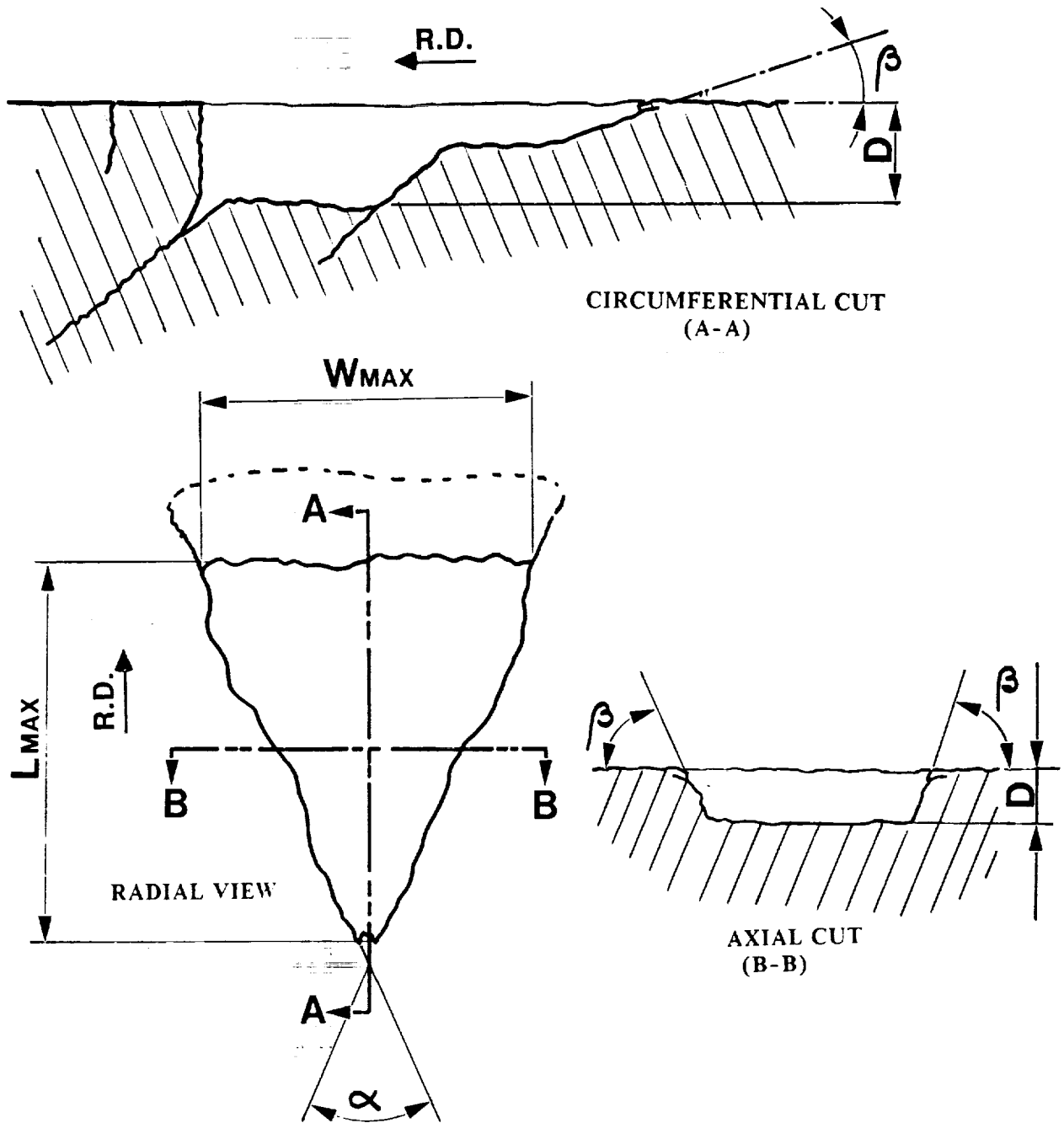


Figure 5.11

Schematic representation of a spall indicating the nomenclature used in Table 5.13, angles are measured with respect to the surface of the sample.

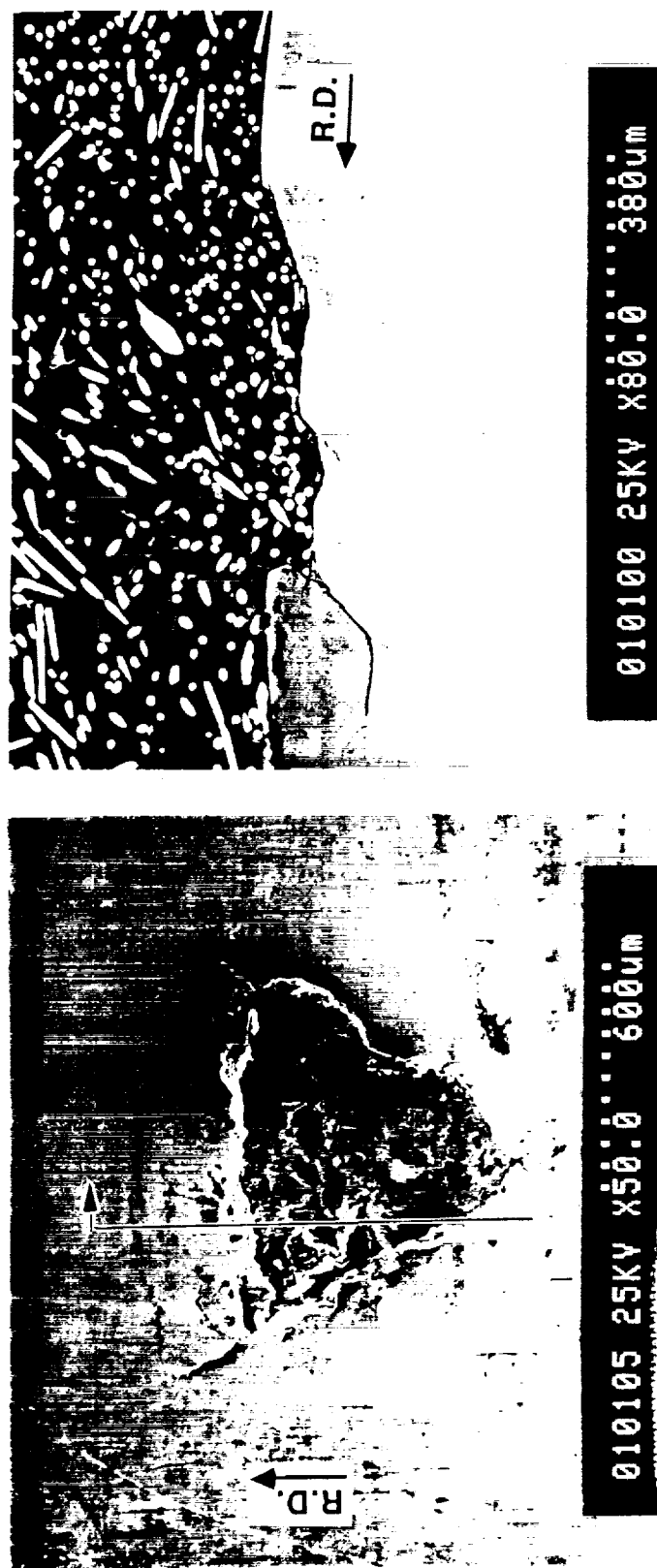


Figure 5.12.a Radial view of spall Al-L1 at 50X, and 80X view of a circumferential cut of the same spall. This sample was tested at a peak pressure of $p_0=5.45$ GPa. A micropit can be observed at the tip of the V-shaped spall. Rough balls were used for this test.

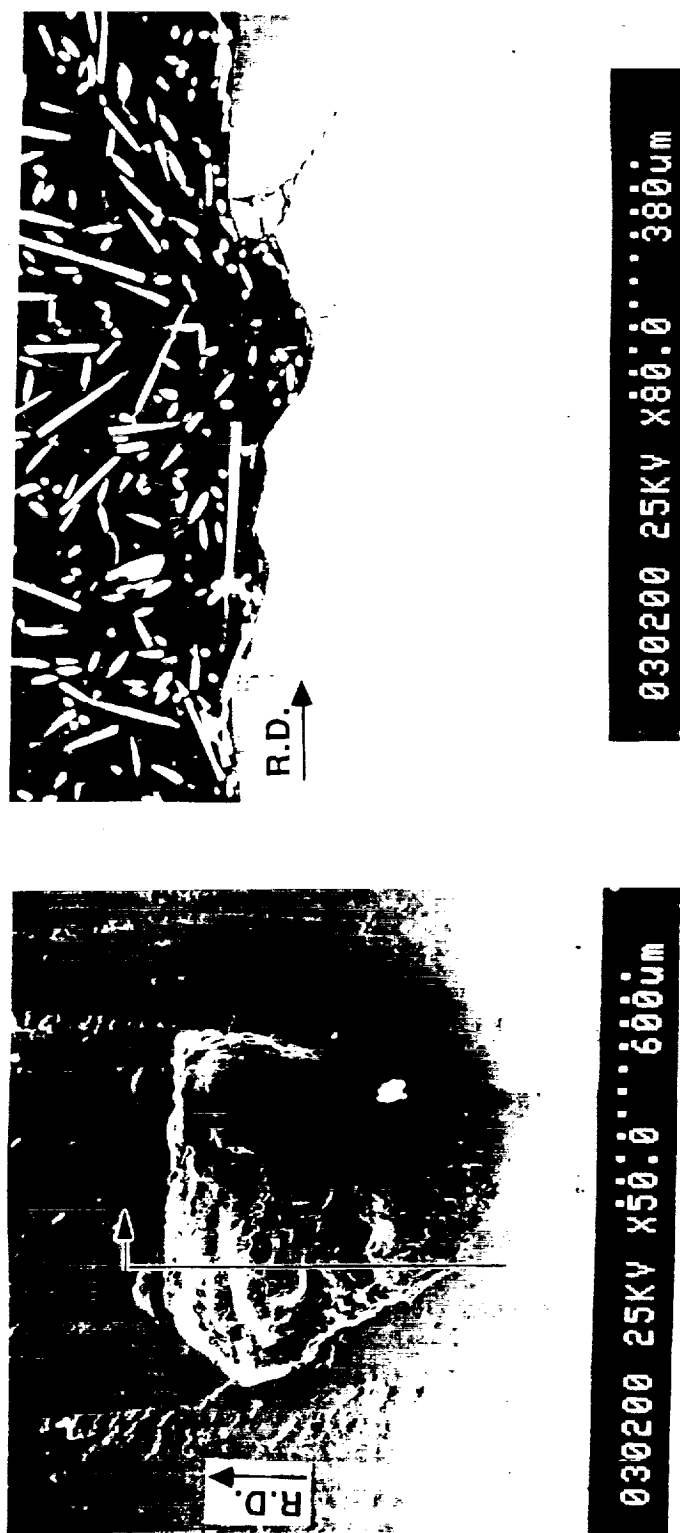


Figure 5.12.b Radial view of spall A3-L2 at 50X, and 80X view of a circumferential cut of the same spall. This sample was tested at a peak pressure of $p_0=5.45$ GPa. A $120\text{ }\mu\text{m}$ hardness impression can be observed near the tip of the spall. Rough balls were used for this test.

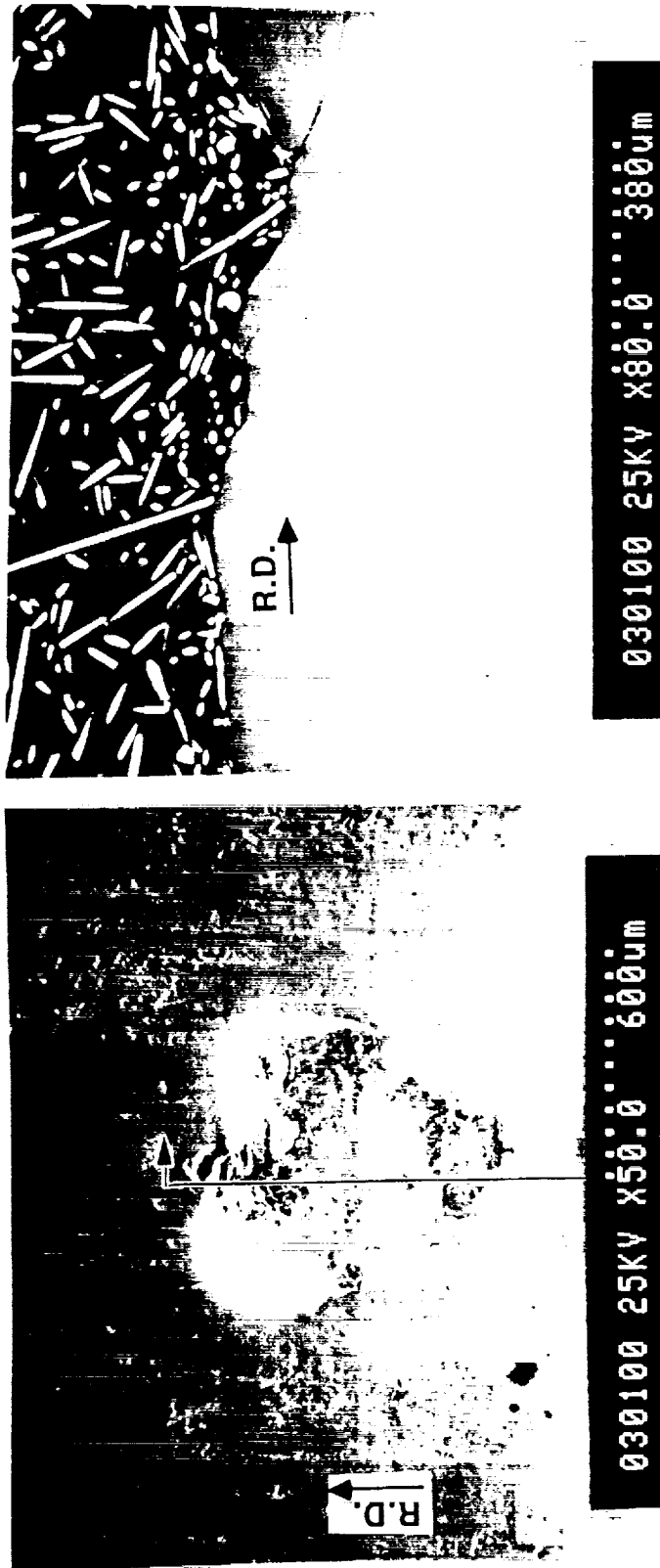


Figure 5.12.c Radial view of spall A3-L1 at 50X, and 80X view of a circumferential cut of the same spall. This sample was tested at a peak pressure of $p_0=5.45$ GPa. A $120\ \mu\text{m}$ hardness impression can be observed near the tip of the spall. Rough balls were used for this test.

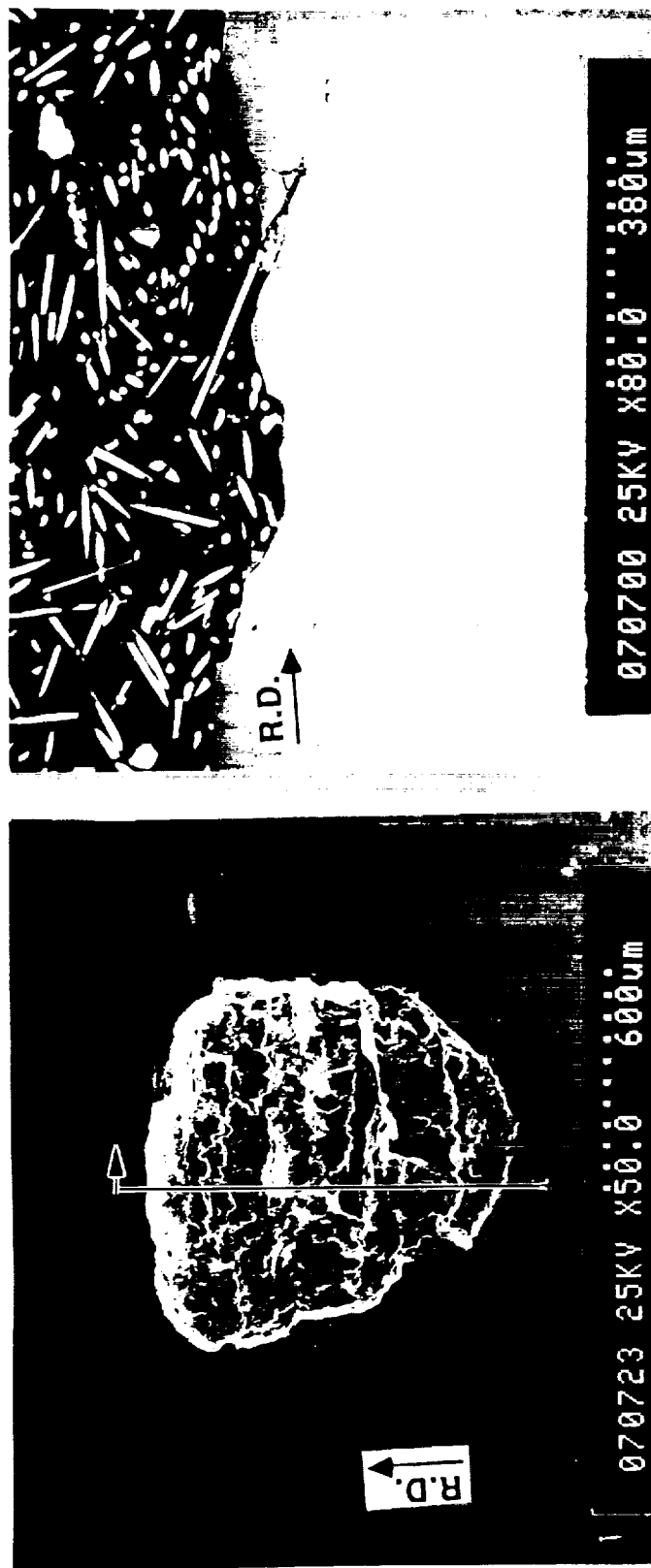


Figure 5.12.d Radial view of spall A7-L7 at 50X, and 80X view of a circumferential cut of the same spall. This sample was tested at a peak pressure of $p_0=5.45$ GPa. Rough balls were used for this test

ORIGINAL PAGE IS
OF POOR QUALITY

cantilever flap. Figures 5.13.a-d show top views of several spalls, as well as the result of axial sectioning. The axial cuts reveal the presence of subsurface cracks propagating in the axial direction.

5.3 Retained Austenite

The cyclic straining of the material under the contact may induce the gradual transformation of the retained austenite present in the matrix²⁶. Test Series 2, see Table 5.2, sought to find a connection between the change in life and a probable change in retained austenite content. However, any changes in life are not obvious from the Table. More testing may be required before any conclusions may be drawn.

5.4 Nucleation vs. Growth

Experimental measurements summarized in Figure 5.14²⁷ show that the life of ground, 440C steel rods employed by the 3-ball-rod tester is reduced by about 10x when the conventional, lapped balls are replaced by the standard rough balls recommended for use with the testing machine. The installation of a 120 μm -diameter, 30 μm -deep dent (Rockwell C hardness indent) reduces the contact life with rough balls by an additional factor of 3x to 10x.

Since the effect of surface finish is confined to depths comparable to the asperity height, the implications of these results is that the lives of ground 440C bars obtained with the rough balls (standard conditions) and with smooth balls are controlled by the near surface mode. This is consistent with the findings of Lorosch shown in Figure 5.15 for the 52100 grade. This figure shows that only the elements with the longest lives, i.e. $N \gg 10^8$ contacts at $p_0 = 5.4$ GPa, are of the subsurface mode.

The installation of artificial dents makes it possible to follow the progress of spall nucleation and growth. Figures 5.16.a through c show the evolution of a surface initiated defect, in the proximity of a hardness impression. These pictures were taken from sample A6, subjected to $p_0 = 5.4$ GPa, after 4, 6 and 10.3 hours (approximately 2.1, 3.1 and 5.3 million cycles respectively). Figure 5.17 also shows the effect of a small surface indent in the raceway of a sample subjected to a rolling contact pressure of $p_0/k = 8.9$.

²⁶ The retained austenite may be as high as 45%.

²⁷ This figure is obtained from the results presented in Tables 5.5(a)-5.12.

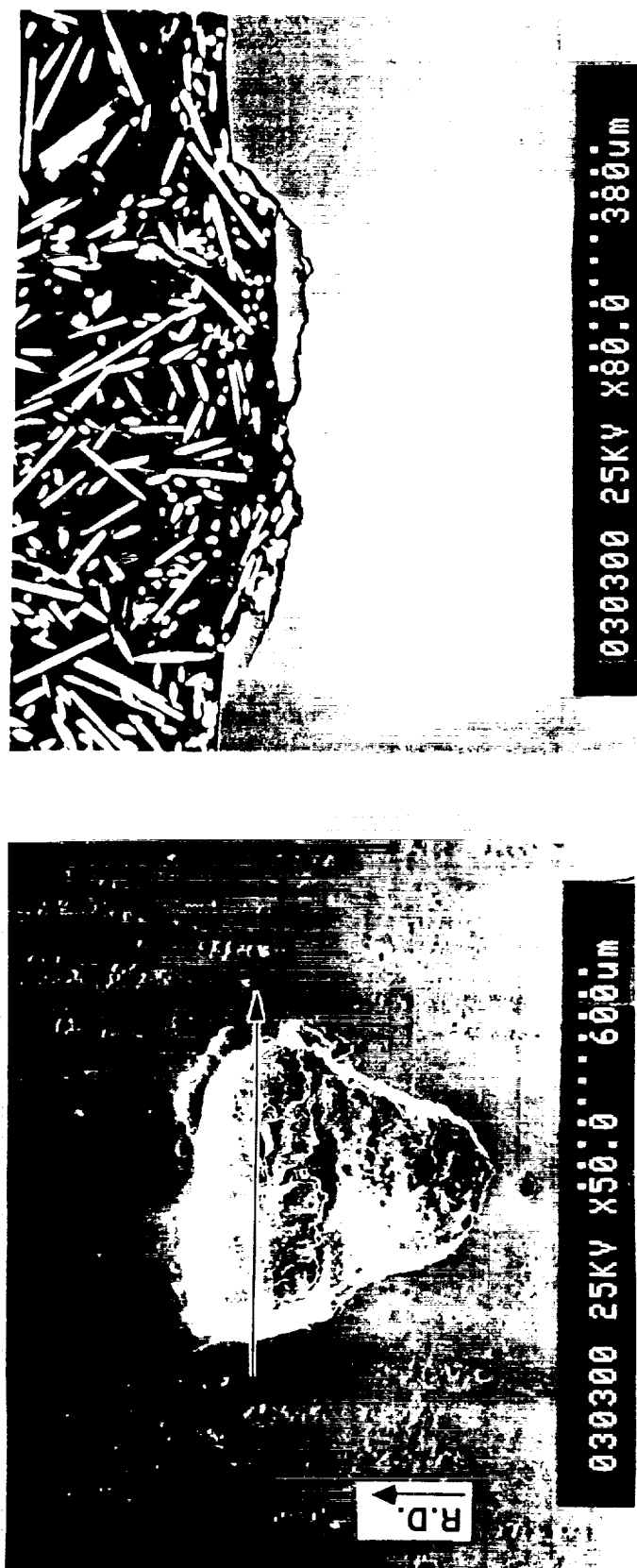


Figure 5.13.a Radial view of spall A3-L3 at 50X, the axial cut is shown at 80X. This experiment was run under a peak pressure of $p_0=5.45$ GPa, with rough balls. A micro pit can be seen near the tip of the spall.

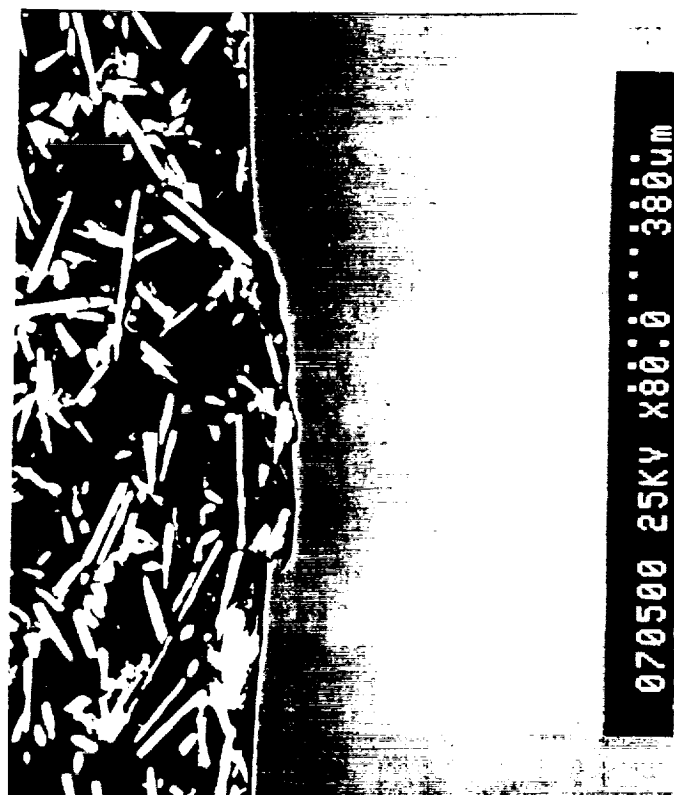
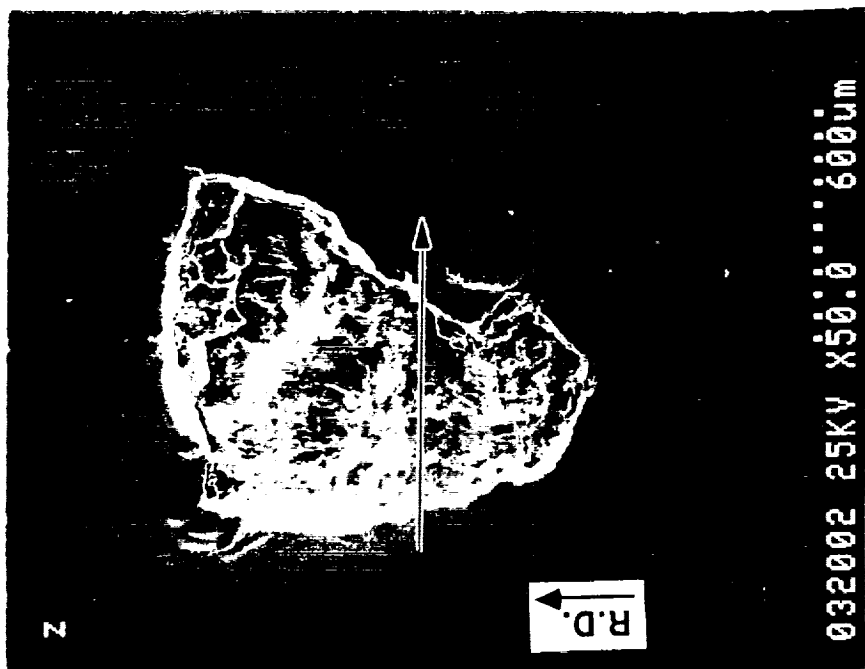


Figure 5.13.b Radial view of spall A7-L5 at 50X, the axial cut is shown at 80X. This experiment was run under a peak pressure of $p_0=5.45$ GPa, with rough balls.

ORIGINAL PAGE IS
OF POOR QUALITY

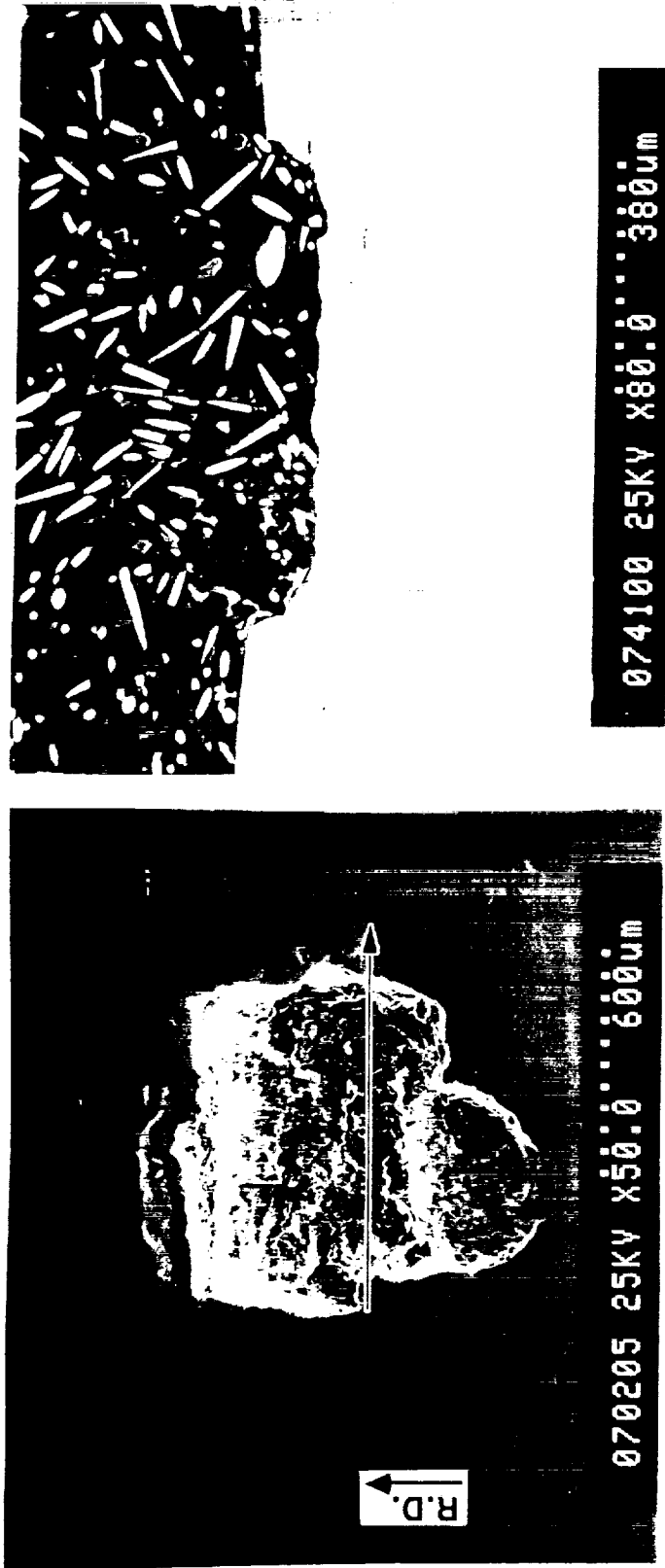


Figure 5.13.c Radial view of spall A7-L4 at 50X, the axial cut is shown at 50X. This experiment was run under a peak pressure of $p_0=5.45$ GPa, with rough balls.

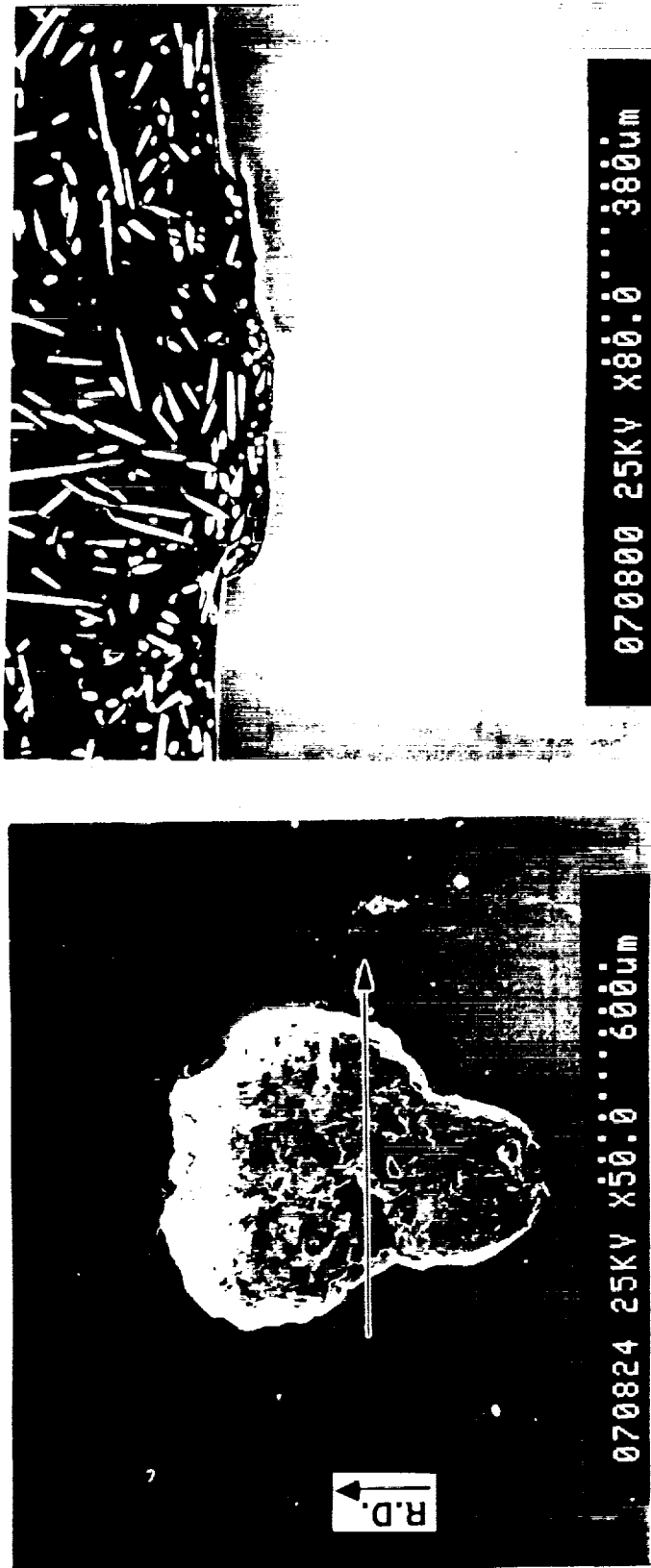


Figure 5.13.d Radial view of spall A7-L8 at 50X, the axial cut is shown at 80X. This experiment was run under a peak pressure of $p_0=5.45$ GPa, with rough balls.

ORIGINAL PAGE IS
OF POOR QUALITY

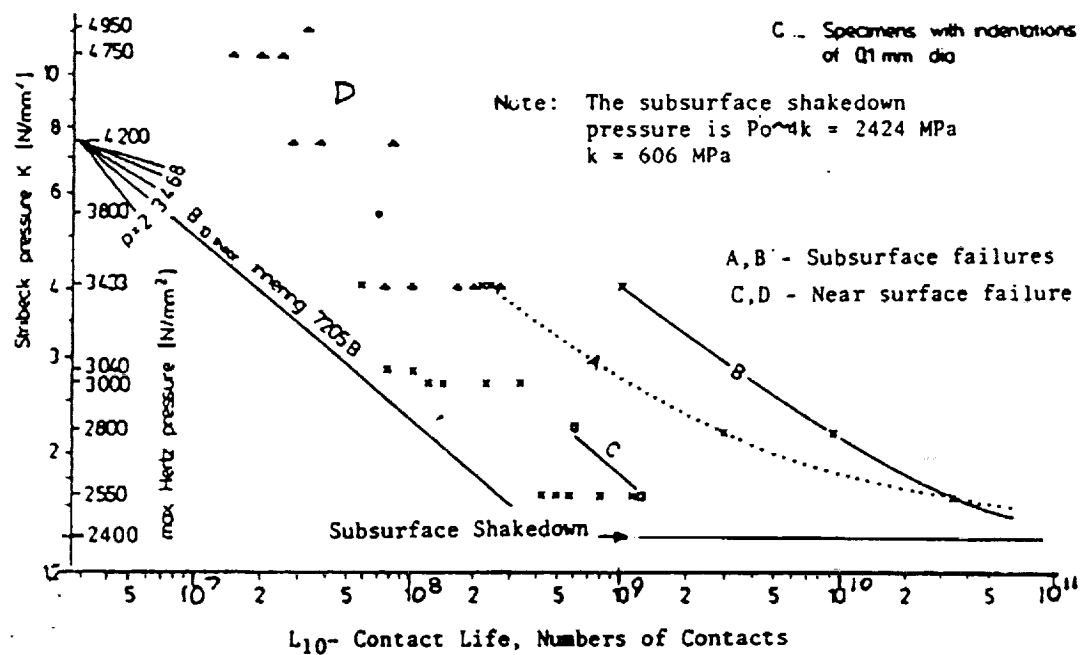


Figure 5.15 Cyclic lives and shakedown pressures for near-surface (C,D) and subsurface rolling contact failures (A,B) in steel 52100 after Lorosch (1987). Results labeled (C) are for 100 μ m surface indents.

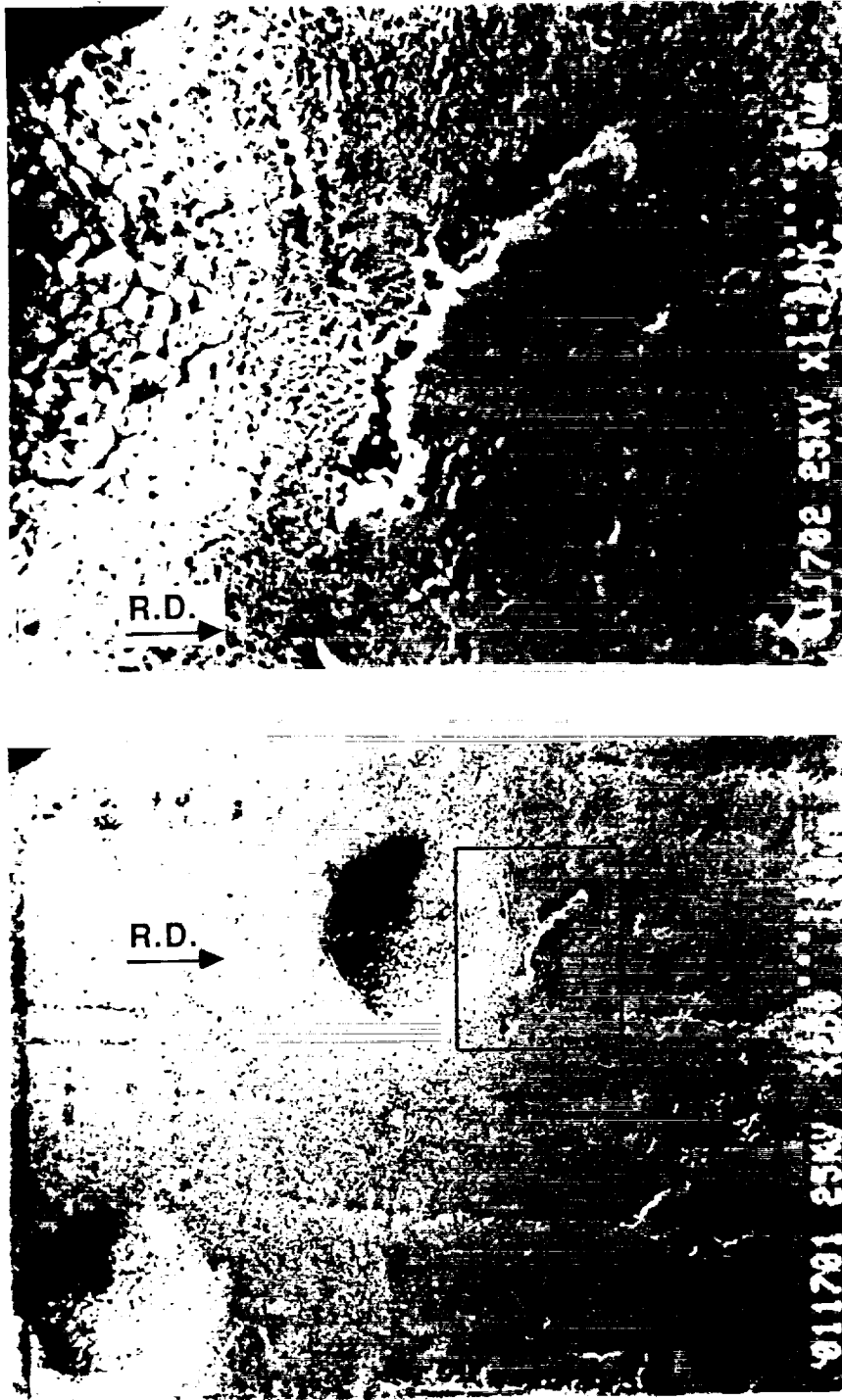


Figure 5.16.a Examples of early stages of spall formation near the hardness indent. The photomicrograph was taken after 4 hours of run time (approx. 2.1 million stress cycles). The boxed region shown in (a) is magnified further in (b).



Figure 5.16.b The location shown in Figure 5.16.a is shown here after 6 hours run time (approx. 3.1 million stress cycles). The boxed region shown in (a) is magnified further in (b).

ORIGINAL PAGE IS
OF POOR QUALITY

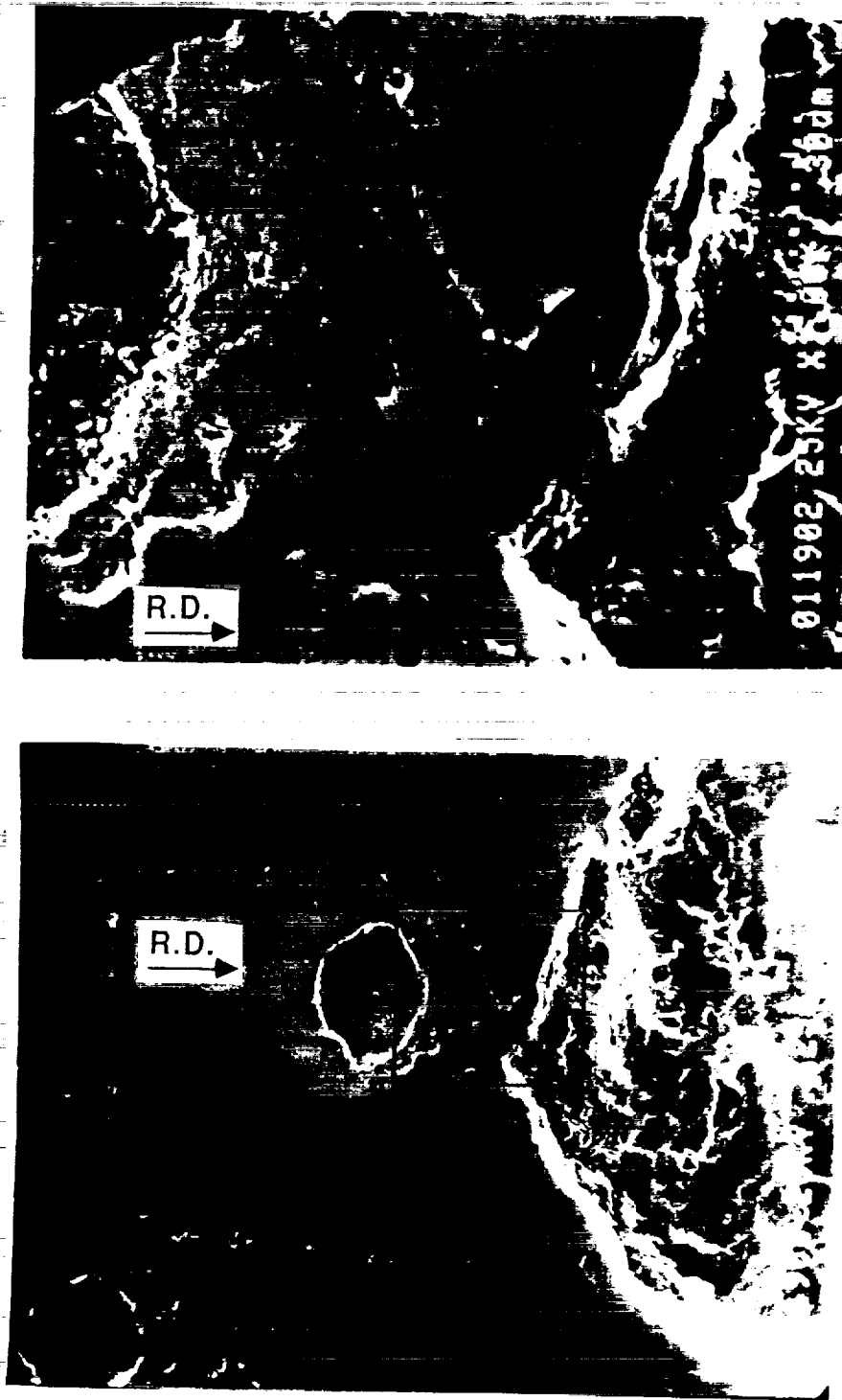


Figure 5.16.c Fully formed spall near the location shown in the previous two figures, after 10.3 hours (approx. 5.3 million stress cycles). The boxed region shown in (a) is magnified further in (b).

The growth life, N_G , is defined as the portion of the total life consumed by the cyclic growth of a $10\text{ }\mu\text{m}$ -surface crack into a full fledged spall, as seen in Figure 5.17. The corresponding initiation life, N_I , is obtained by subtracting N_G from the total life, N , obtained by testing samples without a dent. The studies have shown that the growth life is relatively insensitive to the surface conditions and becomes a smaller fraction of the total as the severity of surface defects is reduced. In the case of the ground 440C steel rods tested at $p_0 = 5.4\text{ GPa}$, $N_G/N = 0.4$ for rough balls and $N_G/N = 0.02$ for smooth balls. The conclusion is that the cyclic growth of the spall can dominate the contact life of the near-surface initiated cracks when the surface is rough or damaged; nucleation of the spall dominates when the surface is smooth and undamaged.

Preliminary studies show that nucleated cracks fail to grow at a contact pressure of $p_0 = 2.4\text{ GPa}$. This result points to the existence of a threshold for growth.

5.5 Surface Roughness

DeMul (1987) and Hamrock (1990), among others, have pointed out the important role played by surface asperities, bumps, grooves and dents in the near-surface failure mode. These defects cause stationary pressure spikes, conditioned by "micro" EHDL effects and produce peak amounts of plasticity at depths corresponding roughly with the surface regularity depth or height (2 to $20\text{ }\mu\text{m}$) below the surface.

Surface roughness features of the specimens and balls are characterized by peaks and valleys caused during the surface preparation. Figure 5.18 shows the running surface on specimen A6-L2: a) after 0.26 million stress cycles, and b) after 2.73 million cycles, c) spall formation after 10.09 million stress cycles. Examination of the running surface on the specimens indicates that small surface roughness features are gradually smoothed out with increasing numbers of stress cycles. However, deeper and more prominent features persist even after 15 million cycles. Similar observations are valid for the case of the roughened balls used in the RCF tests. The prominent peaks and valleys persist for millions of cycles and represent possible crack initiation sites. There is evidence (Figure 5.19) that nearby located microspalls may link together, thus providing the initial site for crack initiation.

5.6 Replication and Metallographic Studies of Spalls in 440C

There is a need for a more detailed description of the 3-dimensional geometry of the spalls, as well as of the different crack propagation mechanisms leading to that geometry. There have been previous three dimensional analyses of cracks under rolling

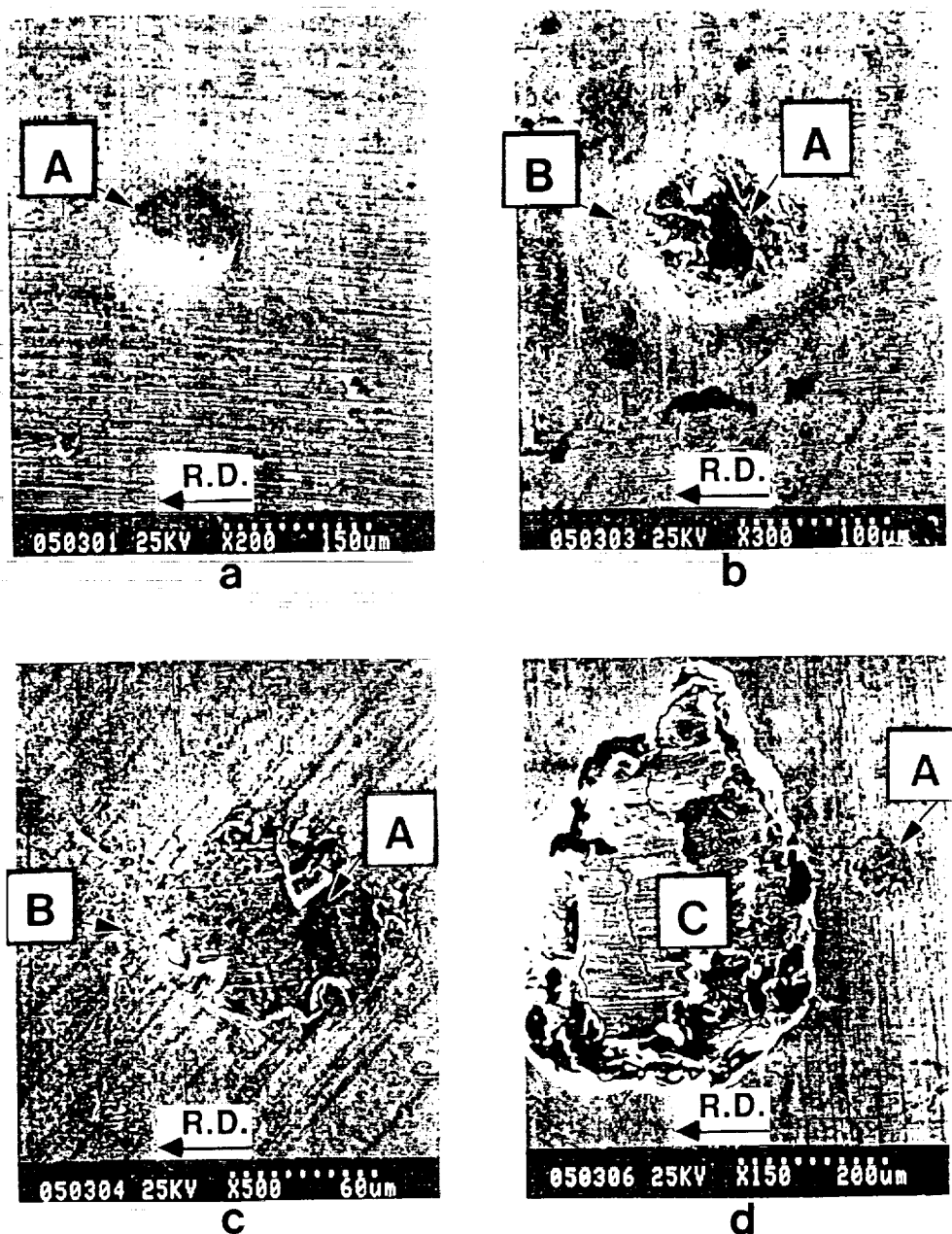
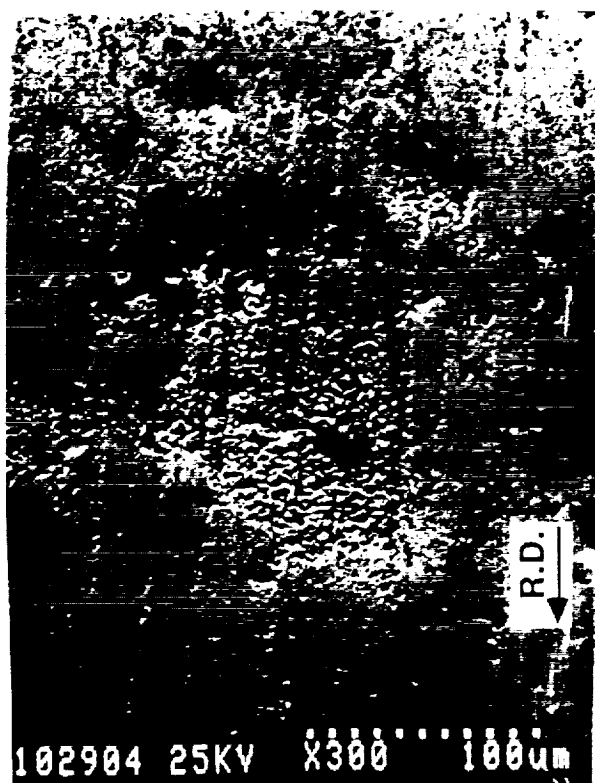


Figure 5.17 Effects of a small, 120 μm dent (A) in the raceway of a bearing steel RCF sample subjected to rolling contact at $p_0/k=8.9$. (a) dent [A] before test, (b) crack nucleus [B] is visible on surface after $N = 0.62 \times 10^6$ contacts, (c) $N = 1.3 \times 10^6$ contacts, and (d) spall [C] forms after $N = 1.5 \times 10^6$ contacts. The rolling direction is also indicated, i.e. R.D.



a



b



ORIGINAL PAGE IS
OF POOR QUALITY

Figure 5.18

Backscattered electron image of the specimen running surface (A6-L2), after (a) 0.26×10^6 cycles, (b) 2.73×10^6 cycles, and (c) lower magnification secondary electron micrograph of the spall formed after 2.73×10^6 cycles. The boxed area shown in (c) is the location chosen for the micrograph in (a) and (b). The rolling direction is also indicated, i.e. R.D.



Figure 5.19

Micrograph of the running surface of the 52100 RCF test balls showing two nearby located microspalls linked together.

ORIGINAL PAGE IS
OF POOR QUALITY

contact by Kaneta and Murakami (1985a, 1985b, 1985c, 1986, 1987). Although these address the problem of the lubricant induced opening mode and crack face friction, they failed to consider the cyclic plasticity induced under rolling contact loading.

The top view and circumferential cuts shown in Figures 5.12.a-d, reveal several important features: a) the cracks seem to have initiated at micro-pits near the tip of the spall (this is provided in the cases of Figures 5.12.b and c by the hardness indentation), b) the crack at the V-apex slightly undercuts the surface, thus indicating a small amount of crack propagation in the reverse direction (more evident in 5.12.a), c) the main cracks propagate at a shallow angle from the surface up to a depth of approximately 60-80 μm (evidence suggests that the crack front is straight along the axial direction and diverges from the initiation point at an angle of $50^\circ - 60^\circ$), d) the cracks then propagate parallel to the surface for 130-200 μm , after which they change direction to an angle of 45° from the surface, e) this process is apparently being repeated cyclicly as evidenced by the unbroken flap still attached at the tip of the spall (clearly seen in 5.12.a).

The micrographs shown in Figures 5.13.a-d present axial cuts of different spalls. These figures suggest that subsurface crack propagation may also take place along the axial direction, as evidenced by the unbroken flap still attached to the surface. The results in Table 5.13 indicate that the maximum spall width is larger than the Hertzian (elastic) contact width, however the spalls were always confined to the wear track. Although some degree of conformity ("sink in") is expected to occur between the rod and ball, due to plastic deformation of the rod, the experimental evidence suggests that the balls are oscillating along the axial direction. This out-of-plane oscillation, and its associated shear tractions, may provide the necessary driving force for the subsurface, axial crack propagation.

This cyclic change in directions would indicate that once the crack has been surface initiated by the micro pressure spikes, its propagation is the result of more than one mechanism. Bower (1988) has indicated that the fluid entrapment mechanism would play an important role in crack propagation. However this mechanism predicts that the crack would turn down, away from the surface, which is not supported by our experiments.

The complicated non-proportional cycle of modes I and II stress intensities at the tip of the crack is more likely to be dictated by a combination of the entrapment mechanism and the resolved cyclic in-plane shear stress. Additionally, the cyclic bending to which the unbroken flap is subjected may favor the formation of cracks connecting the main crack to the surface.

5.7 Rolling Contact of Hardened Aluminum

Rolling tests and finite element calculations using properties of 7075-T6 aluminum have been carried out as part of the present project. Aluminum was chosen primarily because the damage to the microstructure resulting in sub-surface crack formation is easily obtained within a short testing time, $t = 0.5 - 2.0$ hours. In the case of 440C steel, much longer hours of operation are needed to cause crack initiation. Moreover, post-failure electron microscope studies of the spalls would indicate that they are primarily surface initiated cracks.

Additionally, the cyclic stress-strain hysteresis response of 7075-T6 aluminum is qualitatively similar to 440C bearing steels, as indicated in previous sections. Therefore, aluminum proves to be an ideal material to study sub-surface originated failure under rolling contact.

The experiments and calculations performed on this material lead to the following conclusions:

1) The depths at which cracks are observed to form in the RCF test samples are observed to correlate well with the maximum depth at which the maximum cyclic plasticity is calculated, see Figure 3.4.11. Subsurface crack initiation may play a more important role in this material. The accumulation of damage in the plastically strained region extending to a depth of $0.5w$ below the surface as shown in Figure 3.4.10, concurrent with a smoothing out of surface defects²⁸, leads to the translating Hertzian pressure dominated failure.

2) The region where the largest number of cracks is observed is the region where the residual stresses are not compressive and there is still some cyclic plasticity, see Figure 3.4.12. Compressive stresses inhibit cyclic crack growth by enhancing the frictional dissipation between the faces of the crack.

5.8 Conclusions

No connection was found between the amount of retained austenite and the life of the rolling element. More testing may be required before any conclusions may be drawn.

The cyclic growth of the spall dominates the total life of the elements with surface initiated cracks, when the surface is rough or damaged. Nucleation is the controlling event in those samples with smooth and undamaged surfaces.

Surface asperities, grooves, dents and bumps introduced

²⁸ This material shows strong evidence of lateral flow, i.e. ploughing, due to the rolling loading.

during manufacturing of the sample, play an important role in the near-surface failure mode. Prominent features are not smeared out even after several million cycles, thus providing sites for the highly localized, cyclic pressure spikes responsible for failure.

The 3-dimensional features displayed by the spalls would indicate that the surface initiated cracks would propagate driven by several mechanisms. The individual contribution of the complicated, non-proportional cycle of Modes I, II and III, remains to be determined, and it certainly warrants further research in this area.

6. GENERAL DISCUSSION

6.1 Finite Element Calculations of Contact Plasticity

The contact plasticity has 2 components: (i) the transient part which is responsible for the radial displacements and residual stresses and (ii) the steady state or continuing plasticity which leads to damage accumulation and crack nucleation. There is evidence that the ELKP-model, which confines the transient to the first contact cycle, does not describe the transient adequately. The residual stresses for 2-dimensional, line contact derived from finite element calculations with ELKP-properties understate the peak residual stresses by a factor of ≈ 3 and place the peak at a relative depth of $z/w = 1.3$ instead of at $z/w = 0.8$, where it is observed (Hahn et al., 1987). Recently, the authors have treated the 2-dimensional contact with the more sophisticated, non-linear, Mroz-type, 2-surface representation devised by McDowell (McDowell, 1985, Howell, 1991). In this case the transient extends over 15 and possibly more contacts, and while the residual stresses peak at the correct depth, the extrapolated values of the residual stresses are ≈ 3 times larger than the actual values. The steady state cyclic plasticity obtained with the non-linear model agrees with the results obtained with ELKP-behavior. It should also be noted that the 3-dimensional contact plastic zone observed in the aluminum samples in Section 3.4 is in good accord with the ELKP-calculations. These findings support the view that the descriptions of the continuing cyclic plasticity derived from the finite element calculations with ELKP-properties are reliable. However, the cyclic constitutive relations require more work to provide reliable descriptions of the transient and the residual stresses.

While a single set of ELKP-properties has been used so far to characterized hardened steel, it must be noted that the kinematic yield strength, σ_K , is sensitive to microstructure. An ongoing study by the authors shows that σ_K decreases by about 45% at room temperature as the amount of retained austenite increases from 16% to 46%. The loss of cyclic strength is accompanied by a more than 10-fold increase in the cyclic life and both of these changes occur even though the retained austenite is transformed by the cyclic deformation. While increases in the rolling contact life with retained austenite have been reported for 52100 steel, these could not be demonstrated in the present work on 440C steel.

As demonstrated by the 3 dimensional finite element calculations, the addition of a sliding component with heating, results in the introduction of tensile surface residual stresses. The peak value of cyclic plasticity takes place at approximately the same depth as for 3-dimensional pure rolling, i.e. $z/w_1 =$

0.3^{29} , with approximately the same magnitude. However, the sliding component causes a non-zero cyclic plastic component at the surface. The combined effect of the tensile residual stresses and the cyclic plasticity may lead to an exhaustion of ductility, i.e. damage accumulation, thus giving support to the concept of surface originated spall failure (see Section 6.2).

6.2 Spall Nucleation

The present study demonstrates that the spall nucleation component dominates the rolling contact life when the contact surfaces are smooth, defect free and well lubricated. The work also shows, in agreement with previous studies, that modest changes in the surface roughness of the counterface alter the contact life by ≈ 10 -fold. The relatively large indents affect a ≈ 60 -fold reduction in the contact life. These findings are consistent with recent analyses of the effects of surface irregularities, which show that submicron-size grooves or asperities can produce large stationary pressure spikes near the defect (Goglia et al., 1984; de Mul et al., 1987; Hamrock, 1990). Rolling-plus-sliding, with attending frictional tractions, also produces more plasticity closer to or at the surface. As illustrated in Section 3.5, even larger amounts of near-surface plasticity that compete with the peak subsurface values are generated when the sliding is accompanied by intense frictional heating. Either individually or in combination, surface irregularities, sliding and frictional heating can shift the region of peak plasticity and damage from the subsurface to the near-surface, thereby altering the mode of spall failure. Work must be done to treat the plasticity arising from surface irregularities so that this major contribution can be factored into the analysis of nucleation.

The large reduction in the contact life produced by small indents may provide a means for accelerating contact testing. Service life is frequently limited by indents from debris or tramp abrasive particles and natural asperities. Consequently, rolling contact tests might prove more meaningful, and be of shorter duration, if the test samples were fitted at the start with well designed and pedigreed surface defects. This concept is exploited in the 3-ball-rod test which is designed to be conducted with artificially roughened balls. To provide a further test of this idea, the correlation of the nucleation lives obtained with and without defects should be examined. The contribution of inclusion particles may be a complicating factor here. This is because the cyclically deformed volume produced by a small, isolated, surface irregularity is so small that the

²⁹ Where w_1 is the semi-major half-contact width; this is equivalent to $z/w_2 = 0.53$, in terms of the semi-minor half-contact width.

likelihood of an interaction with an inclusion particle is greatly reduced.

In order to perform quantitative treatments of the spall nucleation life, the accumulated damage produced by the continuing cyclic plasticity and the conditions for crack nucleation must be treated. The studies performed on aluminum samples illustrate the complicated nature of the subsurface nucleation process. The results indicate that neither the rates of nucleation nor the rate of crack growth correlate with the amounts of cyclic plasticity. The findings suggest that residual stresses may be playing an important role. The reasons for the $\approx 10^4$ -fold shorter crack nucleation lives at the same relative contact pressure displayed by the hardened aluminum compared with steel are not clear. It is possible that the higher homologous temperature of the aluminum tests and resulting greater atom mobility may facilitate microstructural changes leading to crack nucleation. Since microstructural changes also play a role in the nucleation of failure in steel (Swahn et al., 1976), the stability of specific microstructural elements may affect nucleation.

6.3 Growth and Spalling

The present study shows that the spall growth life is in the range $N = 10^6$ to 10^7 contacts, and is relatively insensitive to the condition of the surface. Similar results have been reported by Shao et al. (1987) for carburized steel. The implication is that the spall growth component is a large fraction of the total life when nucleation is "easy" and the total life is short, e.g. $N < 10^7$ contacts, and a tiny fraction of the total life when nucleation is difficult and the total life is long, e.g., $N \approx 10^{10}$ contacts. The tests also offer evidence of a threshold for crack growth, i.e., crack nuclei about $10 \mu\text{m}$ -long on the surface failed to grow at a contact pressure $p_0 = 2.4 \text{ GPa}$.

The fracture mechanics analyses examined in Section 4 reveal that the Hertzian stresses, centrifugal stresses, thermal stresses and the pressure of fluid in the crack cavity all contribute to a complex superposition of Mode I, Mode II and Mode III crack driving forces. However, the largest contribution appears to be the Mode I driving force resulting from the fluid pressure. Further, it appears that 2-dimensional models of the 3-dimensional crack overstate the driving force.

To critically test these findings, fracture mechanics calculations of the spall growth life were carried out for the conditions in the 3-ball-rod testing machine, and compared with the

measurements of the 440C growth life³⁰. The results are presented in Figure 6.2. They show that the fracture calculations predict both the spall growth lives, at least within an order of magnitude. They also predict the existence of a threshold at roughly the observed contact pressure. Considerable uncertainty is involved in the calculations since the da/dN characteristics of the 440C steel were not known and the details of the dimensional growth were not considered. Further, the Mode II driving force was neglected. Consistent with this, the calculated lives are longer than the measured ones.

The metallographic observations of a step-wise growth suggest that the spall advances into the surface with the lateral sides of the spall attached. At a later stage the lateral sides rupture converting the spall into a loose flap. After propagating parallel to the surface for a short distance, the spall branches away from the surface. Simultaneously, a crack seems to initiate from the surface attending to the cyclic tensile stresses due to the bending of the loose flap (Figure 5.12a). This sets the stage for the formation of the first spall fragment. With the lateral portions of the remaining branch still intact, this branch resumes growth into the material until the lateral connections again break to produce a flap. One important difference is that large, rising and falling pressure spikes are expected to form around the cavity left by the first spall fragment. These pressure spikes will contribute to the crack driving force and accelerate the pace of spall growth.

6.4 Conclusions

(i) The findings reported here, taken together with other recent work, support the view that the descriptions of continuing cyclic plasticity derived from finite element calculations with ELKP-properties are reliable. However, the treatment of the cyclic constitutive relations must be improved to obtain reliable descriptions of the transient and the residual stresses.

³⁰ The total number of stress cycles was calculated by introducing the Mode I crack driving force derived in Section 4.4 (Equation 4.1) into a Paris' type equation, i.e. $da/dN = A(\Delta K)^n$. The constants A and n fit the stage II portion of the results obtained by Bamberger et al. (1982), for different bearing steels (refer to Figure 6.1 and Table 6.1). Numerical integration was carried out assuming an initial crack nucleus of, $a_0 = 10 \mu\text{m}$, and a final crack length of, $a_f = 240 \mu\text{m}$. Small departures from the linear, stage II, portion of the resistance curve lead to a large (3 - 4 orders of magnitude) increase in total number of stress cycles. This can be related to the presence of an effective threshold to crack propagation.

(ii) Either individually or in combination, surface irregularities, rolling-plus sliding and frictional heating can shift the region of peak plasticity and damage from the subsurface to the near-surface, thereby promoting near-surface spall failure.

(iii) The spall nucleation component dominates the rolling contact life of 440C steel when the contact surfaces are smooth, defect free and well lubricated. Small surface irregularities reduce the nucleation life drastically.

(iv) The possibility of accelerating rolling contact testing by fitting samples at the start with well designed and pedigreed surface defects deserves further study.

(v) Studies using hardened aluminum as a model material suggest that residual stresses, atom mobility and the stability of microstructural elements affect the nucleation life.

(vi) The spall growth component is a large fraction of the contact life when nucleation is "easy" and the total life is short, e.g. $N < 10^7$ contacts, and it is a tiny fraction of the total life when nucleation is difficult and the total life is long, e.g. $N \approx 10^{10}$ contacts.

(vii) The experiments provide evidence of a threshold for crack growth.

(viii) The measurements of the spall growth life are in reasonable accord with fracture mechanics predictions based on the Mode I component of the crack driving force generated by 3-dimensional cracks with fluid pressure in the crack cavity. The calculations predict both the growth lives within an order of magnitude and the existence of a threshold close to the observed contact pressure.

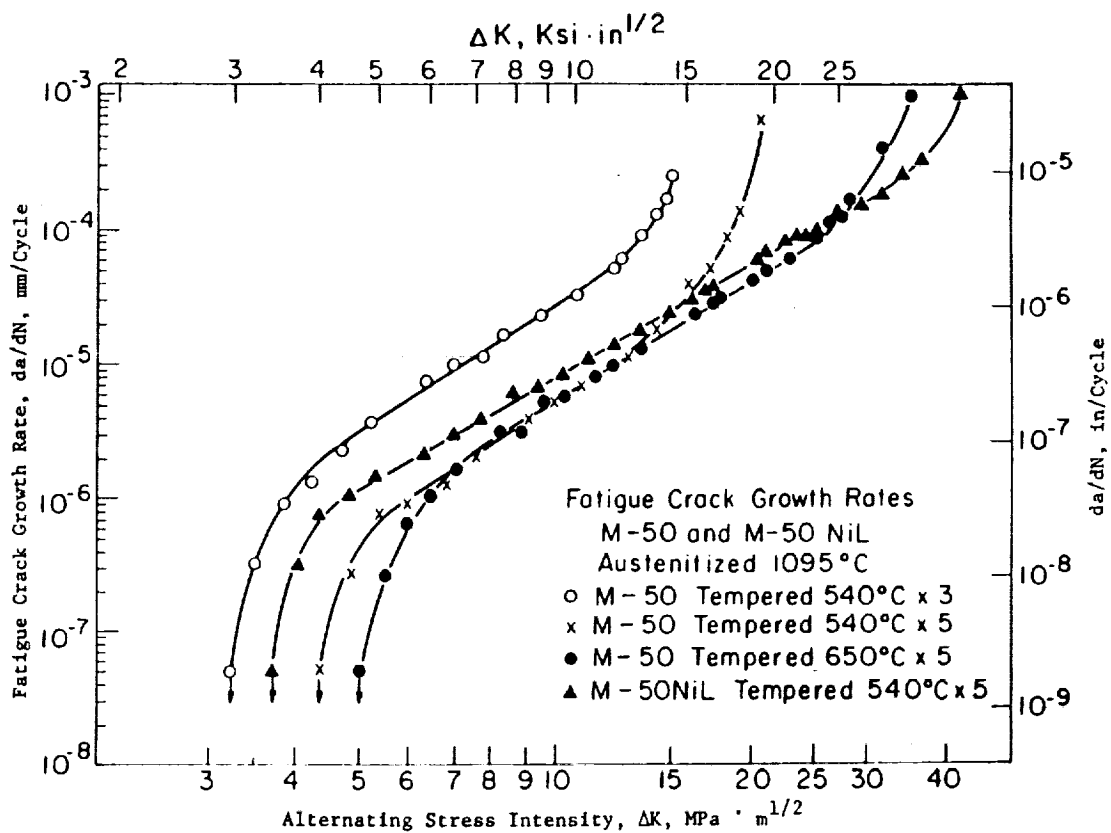


Figure 6.1

Resistance curves for different bearing steels, after Bamberger et al. (1982). Additional information is presente in Table 6.1.

Table 6.1 Heat Treatments and Fracture Toughness
Data for Bearing Steels, after
Bamberger et al. (1982).

Steel	Heat Treatment	Hardness Rc	ΔK_{th} (MPa. \sqrt{m})	K_{Ic} (MPa. \sqrt{m})
M50	A	63	3.1	17.7
M50	B	61	4.2	23.0
M50	C	43	5.0	48.0
M50	D	44	3.8	51.0

Heat Treatment

- A Austenitized at 1095 °C
Tempered at 540 °C, 3 times.
- B Austenitized at 1095 °C
Tempered at 540 °C, 5 times.
- C Austenitized at 1095 °C
Tempered at 650 °C, 5 times.
- D Austenitized at 1095 °C
Cooled at -85 °C
Tempered at 540 °C, 3 times.

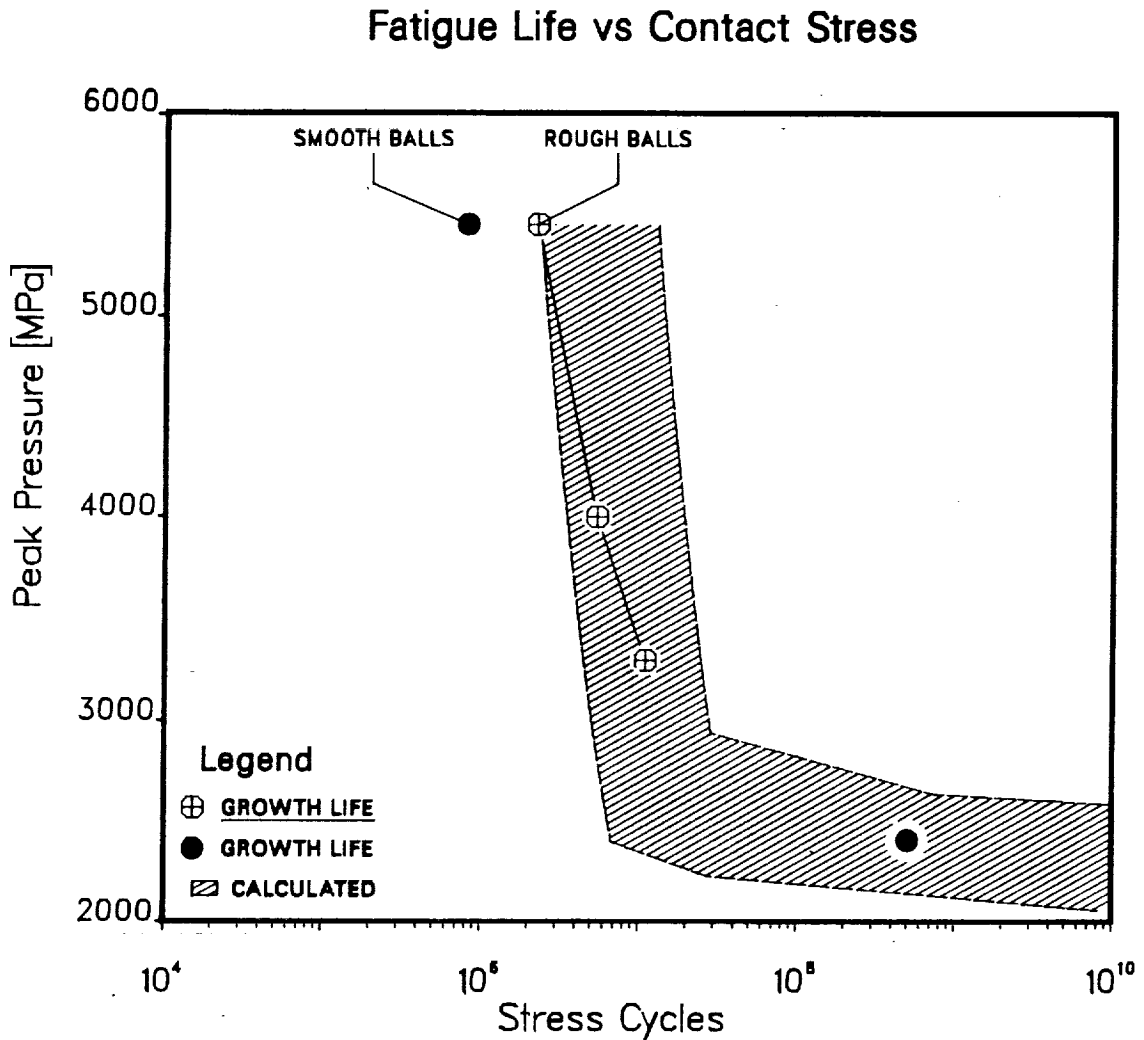


Figure 6.2

Fatigue Life (number of stress cycles to failure) versus the Contact Stress (peak Hertzian pressure) for bearing steel 440C. The figure indicates the experimentally obtained growth lives obtained for tests run with rough and smooth balls. The band represents the upper and lower limits for the total number of cycles calculated using the results from Section 4.4, and the data from Figure 6.1 and Table 6.1.

7. CONCLUSIONS

The following general conclusions can be drawn from the work performed for the present contract:

The ELKP-parameters derived from the hysteresis loops of the 440C steel are similar to those previously reported for hardened AISI 1070 and 52100 bearing steels. After correction for strain rate effects, $\sigma_k = 1050$ MPa and $M = 188$ GPa.

The resistance of aluminum 7075-T6 under cyclic torsion is $1/3$ to $1/2$ of that displayed by 440C steel. However the hysteresis loops reveal a kinematic behavior analogous to the 440C.

Hardened aluminum proves to be a reasonably good model material. Cyclic plasticity can be revealed metallographically, subsurface failure takes place after a moderate number of stress cycles, even at low contact pressures. These qualities may provide opportunities for: i) studying the effects of residual stresses, ii) verification of constitutive formulations, iii) testing fracture mechanics approaches to spall growth analyses.

Three dimensional finite element calculations of repeated frictionless rolling contact have been carried out for ELKP properties of an AISI 440C bearing steel, at relative Hertzian pressures of $p_0/k_k \approx 4.0, 6.6$ and 8.9 , using the geometry of the three ball/rod contact fatigue testing machine. The subsurface stresses, plastic strains, residual stresses and plastic work done are evaluated. Equivalent stresses above the kinematic yield strength extend to the surface only for the highest load level. The peak equivalent plastic strain occurs at approximately $0.25w_1$ ($w_1/w_2 = 1.77$) for all load cases; the values of these strains are 4.4×10^{-4} , 2.33×10^{-3} , and 4.0×10^{-3} , for the low, medium and high loads, respectively.

Three dimensional finite element calculations of repeated frictionless rolling contact have been carried out for ELKP properties of the 7075-T6 aluminum alloy, at a relative Hertzian pressure of $p_0/k_k \approx 5.7$, using the geometry of the three ball/rod contact fatigue testing machine. The subsurface stresses, plastic strains, and residual stresses are evaluated. The peak plastic strain amplitude, $\Delta \epsilon^p_{\max}/2 = 1.6 \times 10^{-3}$, occurs at a relative depth of $z/w = 0.4$ below the surface. Peak residual stresses obtained are $\sigma^r_x(\max) = 26.4$ MPa, and $\sigma^r_y(\max) = 39.7$ MPa, occurring at a relative depth of $z/w = 0.9$.

Two dimensional finite element calculations of repeated rolling-plus-sliding contact have been carried out for ELKP properties of an AISI 440C bearing steel, at relative Hertzian pressures of $p_0/k_k = 5.0$. Plastic strains, residual stresses and temperature distributions are presented. Plastic strains are

shown to be considerable lower for ELKP properties than they for an elastic-perfectly-plastic material (Kulkarni et al., 1989). Steep temperature gradients close to the surface produce high compressive stresses; the ensuing cooling causes residual tensile stresses, a possible mechanism for thermo-cracking. Thermo-mechanical behavior is highly dependent on the material properties, which also may be temperature dependent. A more precise definition of these properties, especially the thermal film coefficient, is recommended.

Efforts have been made to extend the Bower treatment of 2-dimensional, surface breaking cracks with fluid in the crack cavity to smaller relative crack lengths but the Bower algorithm proved unstable for $a/w < 0.5$. In the range $0.5 < a/w < 1.5$, the values of the normalized driving force, $K/p_0/a$, decrease with the relative crack length, a/w , for lubricated contact, but increase for dry contact.

A compilation of ΔK -driving force values of surface breaking cracks has been assembled. This reveals that fluid in the crack cavity, centrifugal stresses, and thermal stresses add significantly to the crack driving force, particularly for relatively short cracks, $a/w < 0.1$. Fluid in the crack cavity is especially potent, producing relatively large Mode I driving force values. The driving forces generated by 3-dimensional cracks are ~20% of the values calculated for 2-dimensional cracks.

As a result of the modest driving force generated by small, 3-dimensional cracks, surface cracks as large as a $\sim 10 \mu\text{m}$ would not be expected to grow in idealized smooth, well lubricated bearings with a Mode I, $\Delta K_{\text{THRESH}} = 5 \text{ MPa}$ subjected to a Hertzian Pressure, $p_0 = 2.4 \text{ GPa}$. This is consistent with experimental results described in Section 5.4.

No connection was found between the amount of retained austenite and the life of the rolling element. More testing may be required before any conclusions may be drawn.

The cyclic growth of the spall dominates the total life of the elements with surface initiated cracks, when the surface is rough or damaged. Nucleation is the controlling event in those samples with smooth and undamaged surfaces.

Surface asperities, grooves, dents and bumps introduced during manufacturing of the sample play an important role in the near-surface failure mode. Prominent features are not smeared out even after several million cycles, thus providing sites for the highly localized, cyclic pressure spikes responsible for failure.

The 3-dimensional features displayed by the spalls would indicate that the surface initiated cracks would propagate

driven by several mechanisms. The individual contribution of the complicated, non-proportional cycle of Modes I, II and III, remains to be determined, and it certainly warrants further research in this area.

The findings reported here taken together with other recent work support the view that the descriptions of continuing cyclic plasticity derived from finite element calculations with ELKP-properties are reliable. However, the treatment of the cyclic constitutive relations must be improved to obtain reliable descriptions of the transient and residual stresses.

Either individually or in combination, surface irregularities, rolling-plus sliding and frictional heating can shift the region of peak plasticity and damage from the subsurface to the near-surface, thereby promoting near-surface spall failure.

The spall nucleation component dominates the rolling contact life of 440C steel when the contact surfaces are smooth, defect free and well lubricated. Small surface irregularities reduce the nucleation life drastically.

The possibility of accelerating rolling contact testing by fitting samples at the start with well designed and pedigreed surface defects deserves further study.

Studies using hardened aluminum as a model material suggest that residual stresses, atom mobility and the stability of microstructural elements affect the nucleation life.

The spall growth component is a large fraction of the contact life when nucleation is "easy" and the total life is short, e.g. $N < 10^7$ contacts, and it is a tiny fraction of the total life when nucleation is difficult and the total life is long, e.g. $N \approx 10^{10}$ contacts.

The experiments provide evidence of a threshold for crack growth.

The measurements of the spall growth life are in reasonable accord with fracture mechanics predictions based on the Mode I component of the crack driving force generated by 3-dimensional cracks with fluid pressure in the crack cavity. The calculations predict both the growth lives within an order of magnitude and the existence of a threshold close to the observed contact pressure.

8. ACKNOWLEDGMENTS

The authors wish to thank Hibbitt, Karlsson and Sorensen, Inc., for allowing the use of their finite element code ABAQUS. Thanks are due to Mr. Paul Leung and Mr. Jeff Koplik, from HKS, for their assistance with the use of the code. The three dimensional finite element calculations were performed on a Cray X-MP/48 and a Cray Y-MP8/648, at the San Diego Supercomputer Center. The help of Mr. Charles Charmman, from SDSC, is deeply appreciated. The rolling experiments were performed in a 3-ball-rod testing machine provided by NTN-Bower Corp. The advice and support of Mrs. Mary-Jo Liston, and Mr. James D. Fidler, from NTN-Bower, are appreciated. Part of the 2- dimensional finite element calculations were performed with support provided by the National Science Foundation under grant number DMR-8721915.

References

- ABAQUS, 1989, "User's Manual - Version 4.8", Hibbitt, Karlsson and Sorensen, Inc, Providence, R.I.
- Archard, J.F., 1959, "The Temperature of Rubbing Surfaces", Wear, Vol. 2, pp. 438-455.
- Bamberger, E.N., Averbach, B.L., and Pearson, P.K., 1982, "Improved Fracture Toughness Bearings", Interim Report, AFWAL-TR-83-2022, AFWAL/POSL, WPAFB, Ohio.
- Barber, J.R., 1967, "The Influence of Thermal Expansion on the Friction and Wear Process", Wear, Vol. 10, pp. 155-159.
- Barber, J.R., 1968, "Thermal Effects in Friction and Wear", Dissertation, Cambridge University.
- Barber, J.R., 1969, "Thermoelastic Instabilities in the Sliding of Conforming Solids", Proc. Roy. Soc., Series A, Vol. 312, pp. 381-394.
- Barber, J.R., 1971a, "The Solution of Heated Punch Problems by Point Source Methods", Int. J. Eng. Sci. Vol. 9. pp. 1165-1170.
- Barber, J.R., 1971b, "The Effects of Thermal Distortion on Constriction Resistance", Int. J. Heat Mass Transfer, Vol. 14, pp. 377-393.
- Barber, J.R., 1972, "Distortion of the Semi-infinite Solid due to Transient Surface Heating", Int. Jou. Mech. Sci., Vol. 14, pp. 377-393.
- Barber, J.R., 1973a, "Indentation of the Semi-infinite Elastic Solid by a Hot Sphere", Int. J. Mech. Sci., Vol. 15., pp. 813-819.
- Barber, J.R., 1973b, "Letter to the Editor", Wear, Vol. 26, pp. 425-427.
- Barber, J.R., 1976, "Some Thermoelastic Contact Problems Involving Frictional Heating", The Quarterly Journal of Mechanics and Applied Mathematics, Vol. 29, pp. 9.
- Barber, J.R., 1980a, "Some Implications of Dundurs' Theorem for Thermoelastic Contact and Crack Problems", Journal of Mechanical Engineering Science, Vol 22., No. 5, pp. 229.
- Barber, J.R., 1980b, "The Transient Thermoelastic Contact of a Sphere Sliding on a Plane", Wear, Vol. 59, pp. 21-29.

- Barber, J.R., and Martin-Moran, C.J., 1982, "Green's Functions for Transient Thermoelastic Contact Problems for the Half-plane", *Thermomechanical Effects in Wear*, pp. 11-19.
- Bastias, P.C., Hahn, G.T., and Rubin, C.A., 1989, "Finite Element Modelling of Subsurface, Mode II Cracks Under Contact Loads", *Eng. Fracture Mechanics*, Vol. 33. pp. 143-152.
- Bastias, P.C., 1990, "Analysis of Cyclic Crack Growth Under Rolling Contact Loading Conditions", Ph.D. Dissertation, Vanderbilt University.
- Bhargava, V., Hahn, G.T., and Rubin, C.A., 1985a, "An Elastic-Plastic Finite Element Model of Rolling Contact. Part 1: Analysis of Single Contacts", *ASME Journal of Applied Mechanics*, Vol. 52, No. 1, pp. 67-74.
- Bhargava, V., Hahn, G.T., and Rubin, C.A., 1985b, "An Elastic-Plastic Finite Element Model of Rolling Contact. Part 2: Analysis of Repeated Contacts", *ASME Journal of Applied Mechanics*, Vol. 52, No. 2, pp. 75-82.
- Bhargava, V., Hahn, G.T., Ham, G., Kulkarni, S.M., and Rubin, C.A., 1986, "Influence of Kinematic Hardening on Rolling Contact Deformation", *Proc. 2nd. Int. Symp. on Contact Mechanics and Rail/Wheel Systems*, Kingston, R.I.
- Bhargava, V., Hahn, G.T., and Rubin, C.A., 1988a, "Analysis of Rolling Contact with Kinematic Hardening for Rail Steel Properties", *Wear*, Vol. 122, pp. 267-283.
- Bhargava, V., Hahn, G.T., and Rubin, C.A., 1990, "Rolling Contact Deformation, Etching Effects and Failure of High Strength Bearing Steels", *Met. Trans. A.*, Vol. 21A, pp. 1921-1931.
- Bhat, B.N., and Dolan, F.J., 1982, "Past Performance Analysis of HPOTP Bearings", NASA TM-82470.
- Bhat, B.N., and Dolan, F.J., 1983, "Analysis of Cryogenic Turbopump Bearing Service Life", 24th Structures, Structural Dynamics and Materials Conference, Lake Tahoe, Nevada.
- Blok, H., 1937, "Theoretical Study of Temperature Rise at Surface of Actual Contact Under Oiliness Lubricant Conditions", *General Discussion on Lubrication*, *Inst. Mech. Eng.*, Vol. 2, pp. 222-235.
- Blok, H., 1963, "The Flash Temperature Concept", *Wear*, Vol. 6, pp. 483-494.

- Bower, A.P., 1988, "The Influence of Crack Face Friction and Trapped Fluid on Surface Initiated Rolling Contact Fatigue Cracks", ASME J. of Tribology, Vol. 110, 1988, pp. 704-711.
- Bower, A.P., Johnson, K.L., and Kalousek, 1986, "A Ratcheting Limit for Plastic Deformation of a Quarter Space under Rolling Contact Loads", 2nd. Int. Symposium on Contact Mechanics and Rail/Wheel Systems, Kingston, R.I.
- Bower, A.P., and Cheesewright, P.R., "Measurement of Residual Shear Stresses near the Surface of a Rail head".
- Burton, R.A., Nerlikar, V., and Kilaparti, S.R., 1973, "Thermoelastic Instability in a Seal-like Configuration", Wear, Vol. 24, pp. 177-188.
- Carslaw, H.S., and Jaeger, J.C., 1959, "The Conduction of Heat in Solids", Oxford University Press, London.
- Cheng, Q., Hahn, G.T., Rubin, C.A., and Bhargava, V., 1988, "The Influence of Residual Stresses on Rolling Contact Mode II Driving Force in Bearing Raceways", Wear, Vol. 126, pp. 17-30.
- Chiu, Y.P., and Hartnett, M.J., 1983, "A Numerical Solution for Layered Solid Contact Problems with Application to Bearings", Journal of Lubrication Technology, Vol. 195, pp. 585-590.
- Clark, J.C., 1985, "Fracture of Bearings for High Stress Applications", Proc. AIAA/SAE/ASME/ASEE 21st Joint Propulsion Conference.
- Clayton and Hill, 1961.
- Comninou, M., and Dundurs, J., 1979, "On the Barber Boundary Condition for Thermoelastic Contact", J. of App. Mech., Vol. 46, pp. 849.
- Comninou, M., Dundurs, J., and Barber, J.R., 1981, "Planar Hertz Contact with Heat Conduction", J. of Appl. Mech., Vol. 48, pp. 549.
- deMul, J.M., Vree, J.M., and Kuypers, J.C., 1987, "The Influence of Certain Raceway Dent Geometries (3-D) on Contact Stresses and Rating Fatigue Life of Rolling Bearings", J. Tribology, 109, 452-461.
- Dawson, P.H., 1962, "Effect of Metallic Contact on the Pitting of Lubricated Rolling Surfaces", J. Mech. Eng. Sci., Vol. 3, pp. 16-21.

- Dow, T.A., 1972, "Thermoelastic Instabilities in Sliding Contact", Dissertation, Northwestern University.
- Dow, T.A., and Burton, R.A., 1972, "Thermoelastic Instability of Sliding Contact in the Absence of Wear", *Wear*, Vol. 19., pp. 315-328.
- Dow, T.A., and Burton, R.A., 1973, "The Role of Wear in the Initiation of Thermoelastic Instabilities of Rubbing Contact", *ASME Journal of Lubrication Technology*, Vol. 95., pp. 71-75.
- Dow, T.A., and Stockwell, R.D., 1977, "Experimental Verification of Thermoelastic Instabilities in Sliding Contact", *ASME Journal of Lubrication Technology*, Vol. 99, pp. 359-364.
- Du, J., Bastias, P.C., Hahn, G.T., and Rubin, C.A., "Three-Dimensional Finite Element Analysis of Repeated Rolling-Sliding Contacts in Bearing Steels", To be Submitted to *Wear*.
- Durkee, D.B., 1978, "Mechanical Aspects of Scuffing Failure of Concentrated Simple Sliding Contacts", Dissertation, Northwestern University.
- Durkee, D.B., and Cheng, H.S., 1979, "Initial Scuffing Damage in Simple Sliding Contacts", *Proc. Int. Conf. on Wear of Materials*, St. Louis, MO, 1979, American Society of Mechanical Engineers, New York, pp. 81-88.
- Elsharkawy, A.A., and Hamrock, B.J., 1991, "Subsurface Stresses in Micro-EHL Line Contacts", *J. Tribology* (To be published).
- Fujita, 1984.
- Fujita, K., and Yoshida, A., 1986, *Wear*, Vol. 51, pp. 365-374.
- Ghonem, H., and Kamath, S., 1984, "Experimental Study of Cyclic Ratcheting Damage in Pearlite Rail Steel", *Proc. Pressure Vessel Conf.*, San Antonio, TX.
- Glover, D., 1982, "A Ball-Rod Rolling Contact Fatigue Tester", *ASTM STP 771*, J.J.C. Hoo, Ed., p. 107-124.
- Goglia, P.R., Conry, T.F., and Cusano, C., 1984, "The Effects of Surface Irregularities on the Elastohydrodynamic Lubrication of Sliding Line Contacts, Part 1 - Single Irregularities and Part 2 - Wavy Surfaces", *J. Tribology*, Vol. 106, pp. 104-119.
- Goshima, T., and Keer, L.M., 1990, "Thermoelastic Contact Between a Rolling Rigid Indenter and a Damaged Elastic Body", *J.*

Tribology, Vol. 112, pp. 382-391.

- Groom, J.J., 1983, "Determination of Residual Stresses in Rails", Final Report to U.S. Dept. of Transportation, Contract DOT-TSC-1426.
- Hahn, G.T., Bhargava, V., Rubin, C.A., Chen, Q., and Kim, K.Y., 1987, "Analysis of Rolling Contact Residual Stresses and Cyclic Plastic Deformation of SAE 52100 Steel Ball Bearings", J. Tribology, Vol. 109, pp. 618-627.
- Hahn, G.T., Bhargava, V., and Chen, Q., 1990, "The Cyclic Stress Strain Properties, Hysteresis Loop Shape and Kinematic Hardening of Two High Strength Bearing Steels", Met. Trans. A, Vol. 21A, pp. 653-665, 1990.
- Hahn, G.T., and Rubin, C.A., "Elastoplastic Analysis of Repeated Rolling and Sliding Contact", Proc. Int. Symp. on Industrial Tribology, Evanston, IL, 1990.
- Ham, G.L., Rubin, C.A., Hahn, G.T., and Bhargava, V., 1988, "Elasto-Plastic Finite Element Analysis of Repeated, Two-Dimensional Rolling Sliding Contacts", Journal of Tribology, Vol. 110, pp. 44-49.
- Hamilton, G.M., and Goodman, L.E., 1966, "The Stress Field Created by a Circular Sliding Contact", Journal of Applied Mechanics, pp. 371-376.
- Hamrock, B.J., 1990, "Recent Developments in Elastohydrodynamic and Micro-elastohydrodynamic Lubrication", Proceedings International Symposium on Industrial Tribology, August, Evanston, IL.
- Hanson, M.T., and Keer, L.M., 1990, "An Analytical Life Prediction Model for the Crack Propagation Occurring in Contact Fatigue Failure", STLE Trans. (To be published).
- Hardy, C., Baronet, C.N., and Tordion, G.V., 1971, "The Elasto-Plastic Indentation of a Half-Space by a Rigid Sphere", Int. Journal of Num. Methods in Engineering, Vol. 3, pp. 451-462.
- Hellier, A.K., Corderoy, D.J.H., and McGirr, M.B., 1986, "A Study of Subsurface Rail/Wheel Contact Stresses with Application to Modelling Rail Fatigue", Proc. 2nd. Int. Symp. on Contact Mechanics and Rail/Wheel Systems, Kinston, R.I.
- Hills, D.A., and Ashelby, D.A., 1982, "The Influence of Residual Stresses on Contact Load Bearing Capacity", Wear, Vol. 75, pp. 221-240.

- Hills, D.A., and Sackfield, A., 1983a, "Some Useful Results in the Classical Hertz Contact Problem", *Journal of Strain Analysis*, Vol. 18, No. 2, pp. 101-105.
- Hills, D.A., and Sackfield, A., 1983b, "Some Useful Results in the Tangentially Loaded Hertz Contact Problem", *Journal of Strain Analysis*, Vol. 18, No. 2.
- Hills, D.A., and Sackfield, A., 1984, "Yield and Shakedown States in the Contact of Generally Curved Bodies", *Journal of Strain Analysis*, Vol. 19, No. 1, pp. 9-14.
- Hills, D.A., and Barber, J.R., 1986, "Steady Sliding of a Circular Cylinder over a Dissimilar Thermally Conducting Half-Plane", *Int. J. Mech. Sci.*, Vol. 28, No. 9, pp. 613-622.
- Hills, D.A., and Sackfield, A., 1986, "The Stress Field Induced by a Twisting Sphere", *ASME Journal of Applied Mechanics*, Vol. 53, pp. 372-378.
- Holm, R., 1948, "Calculation of the Temperature Development in a Contact Heated in the Contact Surface and Application to the Problem of the Temperature Rise in a Sliding Contact", *Journal of Physics*, Vol. 19, pp. 361-366.
- Johns, T.G., and Davies, K.B., 1976, "A Preliminary Description of Stresses in Railroad Rail", Interim Report to U.S. Dept. of Transportation, Contract DOT-TSC-1038.
- Johnson, K.L., and Jefferis, J.A., 1963, "Plastic Flow and Residual Stresses in Rolling and Sliding Contact", *Proc. Inst. Mech. Eng.*, London, Vol. 177, pp. 54-65.
- Johnson, K.L., 1986, "Plastic Flow, Residual Stresses and Shakedown in Rolling Contact", 2nd. Int. Symposium on Contact Mechanics and Rail/Wheel Systems, Kingston, R.I.
- Johnson, R.R., Dow, T.A., and Zhang, Y.Y., 1988, "Thermoelastic Instabilities in Elliptic Contact Between Two Sliding Surfaces", *Transactions of the ASME, J. of Tribology*, Vol. 110, pp. 80-86.
- Kalker, J.J., 1979, "The Computation of Three-Dimensional Rolling Contact with Dry Friction", *Int. Journal of Num. Methods in Engineering*, Vol. 14, pp. 1293-1307.
- Kaneta, M., Murakami, Y. and Yatsuzaka, H., 1985a, "Mechanism of Crack Growth in Lubricated Rolling Contact", *ASLE Trans.*, Vol. 28, pp. 407-414.
- Kaneta, M., Murakami, Y., and Yatsuzaka, H., 1985b, "Propagation

- of Surface Crack in Rolling Contact", Proc. JSLE Int. Tribology Conf., pp. 911-916.
- Kaneta, M., Murakami, Y., and Okazaki, T., 1985c, "Mechanism of Opening/Closure of a Subsurface Crack Due to a Moving Hertzian Loading", Proc. of the 12th Leeds-Lyon Symp. on Tribology, pp. 29-38.
- Kaneta, M., Suetsugu, M., and Murakami, Y., 1986, "Mechanisms of Surface Crack Growth in Lubricated Rolling/Sliding Spherical Contact", ASME Journal of Applied Mechanics, Vol. 53, pp. 354-360.
- Kaneta, M., and Murakami, Y., 1987, "Effects of Oil Hydraulic Pressure on Surface Crack Growth in Rolling/Sliding Contact", Tribology Int., Vol. 20, pp. 210-217.
- Kaneta, M., and Murakami, Y., 1990, "Propagation of Semi-Elliptical Surface Cracks in Lubricated Rolling/Sliding Elliptical Contacts", J. Tribology (To be published).
- Keer, L.M., and Bryant, M.D., 1983, "A Pitting Model for Rolling Contact Fatigue", ASME J. of Lubrication Technology, Vol. 105, pp. 198-205.
- Keer, L.M., Farris, T.N., and Steele, R., 1986, "On some aspects of Fatigue Crack Growth in Rails induced by Wheel/Rail Contact Loading", Proc. 2nd. Int. Symp. on Contact Mechanics and Rail/Wheel Systems, Kingston, R.I.
- Kennedy, F.E., and Karpe, S.A., 1982, "Thermocracking of a mechanical face seal", Thermomechanical Effects in Wear, pp. 21-36.
- Korovchinski, M.V., 1965, "Plane-Contact Problem of Thermoelasticity During Quasi-Stationary Heat Generation on the Contact Surfaces", J. of Basic Engineering, pp. 811.
- Kuhlmann-Wilsdorf, D., 1985, "Flash Temperatures due to Friction and Joule Heat at Asperity Contacts", Wear, Vol. 105, pp. 187-198.
- Kulkarni, S.M., Rubin, C.A., and Hahn, G.T., 1988, "An Elasto-Plastic Coupled Temperature Displacement Finite Element Analysis of Rolling-Sliding Contact", Engineering Science Preprints of the 25th Annual Technical Meeting, Society of Engineering Science, University of California at Berkeley.
- Kulkarni, S.M., Hahn, G.T., Rubin, C.A., and Bhargava, V., 1990a, "Elasto-Plastic Finite Element Analysis of Three-Dimensional Pure Rolling Contact at the Shakedown Limit", Journal Appl. Mechanics.

- Kulkarni, S.M., Hahn, G.T., Rubin, C.A., and Bhargava, V., 1990b, "Elasto-Plastic Finite Element Analysis of Three-Dimensional Pure Rolling Contact above the Shakedown Limit", Submitted to the Journal of Appl. Mechanics.
- Kulkarni, S.M., Hahn, G.T., Rubin, C.A., and Bhargava, V., 1990c, "Elasto-Plastic Finite Element Analysis of Repeated Three-Dimensional, Elliptical Rolling Contact with Rail Steel", Submitted to the Journal of Applied Mechanics.
- Kumar, A.M., Kulkarni, S.M., Bhargava, V., Hahn, G.T., and Rubin, C.A., 1987, "Mechanisms of Rolling Contact Spalling", Final Report submitted to NASA/MSFC, NAS8-36651.
- Ling, F.F., and Mow, V.C., 1965, "Surface Displacement of a Convecting Elastic Half-Space Under an Arbitrarily Distributed Fast-Moving Heat Source", J. of Basic Engineering, pp. 729.
- Lorosch, H.K., 1982, "Influence of Load on the Magnitude of the Life Exponent for Rolling Bearings", ASTM STP 771, J.C. Hoo, Ed., pp 275-292.
- McDowell, D.L., and Moyer, G.J., "A more realistic model of Nonlinear Material Response: Application to Elasto-Plastic Rolling Contact", Proc. 2nd. Int. Symp. on Contact Mechanics and Rail/Wheel Systems, Kingston, R.I.
- Martin, G.C., and Hay, W.W., 1972, "The Influence of Wheel-Rail Contact Forces on the Formation of Rail shells", Paper 72-WA/RT-8, ASME.
- Maurer, R.E., and Pallini, R.A., 1985, "Computer Aided Selection of Materials for Cryogenic Turbopump Bearings", 40th A.S.L.E. Annual Meeting, Las Vegas.
- Mendelson, A., and Ghosn, L.J., 1986, "Analysis of Mixed Mode Crack Propagation Using Boundary Integral Method", NASA Report 179518.
- Merwin, J.E., and Johnson, K.L., 1963, "An Analysis of Plastic Deformation in Rolling Contact", Proc. Inst. Mech. Eng., London, Vol. 177, pp. 676-690.
- Mikic, B.B., 1974, "The Solution of Heated Punch Problems by Point Source Methods", Int. J. Heat Mass Transfer, Vol. 17, pp. 205-214.
- Mow, V.C., and Cheng, H.S., 1967, "Thermal Stress in an Elastic Half-Space Associated with an Arbitrarily Distributed Moving Heat Source", ZAMP, Vol. 18, pp. 501.

- Nagaraj, H.S., Sanborn, D.M., and Winer, W.O., 1978, "Direct Surface Temperature Measurement by Infrared Radiation in Elastohydrodynamic Contacts and the Correlation with the Blok Flash Temperature Theory", *Wear*, Vol. 49, pp. 43-59.
- Nakajima, A., Ichimaru, K., Hirano, F., and Nishimura, M., 1983, "Effects of Combination of Rolling Direction and Sliding Direction on Pitting of Rollers", *JSLE Int.*, Vol. 4, pp. 94-98.
- Newman, S.Z., 1986, "FEM Model of 3-D Transient Temperature and Stress Fields in Welded Plates", Ph.D. Dissertation, Carnegie-Mellon University.
- O'Reagan, S.D., Hahn, G.T., and Rubin, C.A., 1985, "The Driving Force for Mode II Crack Growth Under Rolling Contact", *Wear*, Vol. 101, pp. 333-346.
- Orkisz, J., Perlman, A.B., Harris, A., and Orringer, O., 1986, "Recent progress in the development of a Rail Residual Stress Calculation Method", *Proc. 2nd. Int. Symp. on Contact Mechanics and Rail/Wheel Systems*, Kingston, R.I.
- Panek, C., and Dundurs, J., 1979, "Thermoelastic Contact Between Bodies with Wavy Surfaces", *Transactions of the ASME*, Vol. 46, pp. 854.
- Ponter, A.R.S., Hearle, A.D. and Johnson, K.L., 1985, "Application of the Kinematical Shakedown Theorem to Rolling and Sliding Point Contacts", *J. Mech. and Physics of Solids*.
- Rydholm, G., and Fredriksson, B., 1981, "Shakedown Analysis of Three-Dimensional Rolling Contact Problems", *Linkoping Studies in Science and Technology, Dissertations*, No. 61.
- Shao, E., Huang, X., Wang, C., and Cheng, Q., 1987, "A Method of Detecting Rolling Contact Initiation and the Establishment of Crack Propagation Curves", *ASLE Reprint 87-AM-4E*.
- Soda, N., and Yamamoto, T, 1982, "Effect of Tangential Traction and Roughness on Crack Initiation/Propagation During Rolling Contact", *ASLE Transactions*, Vol. 25, No. 2, pp. 198-206.
- Sovak, S.J., and Cheng, H.S., 1982, "Effect of Contact Geometry on Initial Scuffing Damage in Simple-Sliding Elastohydrodynamics Lubrication Contacts", *Thermomechanical Effects in Wear*, pp. 145-160.
- Tseng, M.L., and Burton, R.A., 1982, "Thermal Stress in a Two-dimensional (plane stress) Half Space for a Moving Heat Input", *Thermomechanical Effects in Wear*, pp. 1-9.

- Way, S., 1935, "Pitting Due to Rolling Contact", ASME J. of Applied Mechanics, Vol. 2, pp. A49-A58.
- Winer, W.O., and Cheng, H.S., 1980, "Film Thickness, Contact Stress and Surface Temperatures", in Wear Control Handbook, Peterson, M.B., and Winer, W.O., Eds., ASME, New York, pp. 81-141.
- Xiao, H., Cheng, Q., Shao, E., Wu, D., Chen, Z., Wang, Z., and Changchun, C., 1990, "The Effect of Shot Peening on Rolling Contact Fatigue Behavior and Its Crack Initiation and Propagation in Carburized Steel", J. Tribology (To be published)
- Zumgahr, K., 1987, "Microstructure and Wear of Materials, Elsevier, Holland.

APPENDIX 1

3-D DISPLACEMENT BOUNDARY CONDITIONS

Frictionless 3-D contact is simulated by translating a Hertzian pressure distribution across the surface of a semi-infinite body. This semi-infinite body is represented by a 3-D finite element mesh with appropriate displacement boundary conditions on the non-surface sides of the mesh. The boundary nodes are elastically displaced for each translating increment using the Boussinesq's solution to the problem of a concentrated force acting on the surface of a semi-infinite body. For this purpose, the Hertzian pressure distribution is discretized into numerous concentrated forces. The boundary displacements due to each concentrated force are calculated and superposed for each increment. This appendix presents the detailed derivation of the Boussinesq's solution for the case of the concentrated normal force, and then is extended for the case of the normal plus the tangential forces acting on the half-space.

There are two ways of solving problems in elasticity. The first way is to find a set of stresses and strains which satisfy certain equations. This is the First Boundary Value Problem of Elasticity. The stresses must satisfy the equilibrium equations and the boundary conditions. The strains must satisfy the compatibility equations and the stresses must be related to the strains through appropriate stress-strain relations [See Appendix 2]. Alternately, as for Boussinesq's solution, it is possible to reduce the above set of equations to three equations, the Navier equations, involving only the displacements, u_i . The problem is then known as the Second Boundary-Value Problem of Elasticity. The Navier equations in tensor notation are

$$\mu \nabla^2 u_i + (\lambda + \mu) v_{,i} = -F_{,i} \quad (1)$$

for simply connected domains bounded by a smooth surface, τ where ∇^2 is the Laplacian operator, λ and μ or G are Lamé's constants, and v is the invariant defined as, $v = u_{i,i}$. The solution of the Navier equations appropriate to the deformation of an elastic body by the concentrated force, F_i^0 , applied at some point, ξ_i , can be deduced from the particular integral due to Lord Kelvin,

$$u_i(x) = A \int_{\tau} \left[B \frac{F_i(\xi)}{r} - \left(\frac{1}{r} \right)_{,i} (x_j - \xi_j) F_j(\xi) \right] d\tau \quad (2)$$

where

$$A = \frac{\lambda + \mu}{8\pi\mu(\lambda + 2\mu)},$$

$$B = \frac{\lambda + 3\mu}{\lambda + \mu},$$

$$\left(\frac{1}{r} \right)_{,i} = \frac{\partial}{\partial x_i} \left(\frac{1}{r} \right)$$

and

$$r = [(x_i - \xi_i) \cdot (x_i - \xi_i)]^{1/2}$$

is the distance from the field point, x_i , to the variable point, ξ_i in τ . It is supposed that the body forces F_i are distributed over some subregion, τ_1 of τ , including the point, ξ_i , and vanish over the rest of the region. The resultant of the body forces acting on τ_1 is

$$F_i^0 = \int_{\tau_1} F_i d\tau$$

Let F_i increase in such a way that this integral has a finite limit, F_i^0 as τ_1 ap-

proaches 0, to arrive at the notion of the concentrated force, F_i^0 acting at the point, ξ_i . Therefore, the displacements, $u_i(x)$, produced at the point $x_i \neq \xi_i$, are

$$u_i(x) = \frac{\lambda+3\mu}{8\pi\mu(\lambda+2\mu)} \frac{F_i^0}{r} + \frac{\lambda+\mu}{8\pi\mu(\lambda+2\mu)} \frac{(x_i-\xi_i)(x_j-\xi_j)}{r^3} F_j^0 \quad (3)$$

These expressions satisfy the homogeneous Navier equations at all points of the region except at the point of application of the force, $x_i = \xi_i$. But if this point is deleted from the region by enclosing it in a sphere S of small radius a , the above solution in the remaining region corresponds to the deformation present in a body, τ , with a cavity, S , subjected to the action of forces with the resultant, F_i^0 . For the case considered, let F_i^0 act at the origin, $\xi_i=0$ and $F_1^0=F_2^0=0$, and $F_3^0=P$, to get

$$u_\alpha = C \frac{x_\alpha x_3}{r^3}, \alpha=1,2 \quad (4)$$

and

$$u_3 = C \left(\frac{\lambda+3\mu}{(\lambda+\mu)r} + \frac{x_3^2}{r^3} \right) \quad (5)$$

where $C = \frac{\lambda+\mu}{8\pi\mu(\lambda+2\mu)}$ and $r^2 = x_i x_i$. The stresses can be calculated by

$$\tau_{ij} = \lambda u_{k,k} \delta_{ij} + \mu (u_{i,j} + u_{j,i})$$

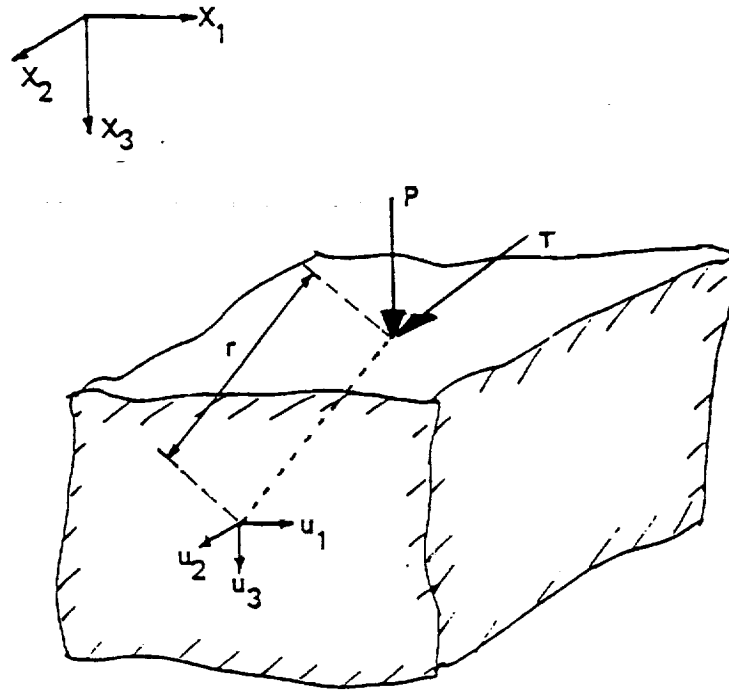


Figure A.1.1 A concentrated vertical force, P , and a tangential force, T , acting on the surface of a half space.

The tractions produced by these stresses over the sphere S of radius $r=a$, are determined from

$$T_i = \tau_{ij} \nu_j$$

where $\nu_j = x_j/a$. Integrating these tractions over the surface of the sphere, $r=a$, we obtain the components of the resultant force exerted on S by matter exterior to S . To solve the problem of deformation of the elastic half-space bounded by a plane subjected to the action of a concentrated force, it is necessary to account for the singularity at $x_i = \xi_i$. Boussinesq combined the earlier derived equations (11) and (12) with certain other singular solutions of Navier's equations to get the dilationless ($v=0$) solution of Navier's equations, so long as $r \neq 0$, namely

$$u_\alpha = \frac{D x_\alpha}{r(r+x_3)} \quad (6)$$

and

$$u_3 = \frac{D}{r} \quad (7)$$

where $r^2 = x_i x_i$, and $D = \text{constant}$.

Now let us calculate the deformation of an elastic half space, $x_3 \geq 0$, due to a concentrated force, P , applied at the origin, acting in the positive direction of the x_3 -axis (see Fig. A.2.1) Since the point of application of the load is a singular point in the solution of Navier's equations, delete it from $x_3 \geq 0$ by

describing a hemisphere of small radius 'a/a' and consider the semi-infinite region bounded by the hemisphere and the x_1x_2 -plane. Construct a solution such that the resultant of all external stresses acting on the hemisphere is P, and $\tau_{i3} = 0$, over the rest of the boundary. Adding equations (11) to (13), and (12) to (14) and applying appropriate boundary conditions, we get equations (15) and (16),

$$u_{\alpha} = \frac{P}{4\pi\mu} \left(\frac{x_3 x_{\alpha}}{r^3} - \frac{\mu}{\lambda + \mu} \frac{x_{\alpha}}{r(x_3 + r)} \right), \alpha = 1, 2 \quad (8)$$

and

$$u_3 = \frac{P}{4\pi\mu} \left(\frac{x_3^2}{r^3} + \frac{\lambda + 2\mu}{\lambda + \mu} \frac{1}{r} \right) \quad (9)$$

Rewriting these equations using

$$\mu = \frac{E}{2(1+\nu)}$$

and

$$\lambda = \frac{E\nu}{(1+\nu)(1-2\nu)}$$

where E is the Young's modulus and ν is the Poisson's ratio, we get

$$u_{\alpha} = \frac{(1+\nu)P}{2\pi E} \left(\frac{x_3 x_{\alpha}}{r^3} - (1-2\nu) \frac{x_{\alpha}}{r(x_3 + r)} \right), \alpha = 1, 2 \quad (10)$$

and

$$u_3 = \frac{(1+\nu)P}{2\pi E} \left(\frac{x_3^2}{r^3} + 2(1-\nu) \frac{1}{r} \right) \quad (11)$$

The same line of reasoning could be used to derive the appropriate boundary displacements for the case where the half-space is acted upon by a tangential force, T^1 .

$$u_x = \frac{(1+\nu)T}{2\pi E} \left[\frac{xy}{r^3} - (1-2\nu) \frac{xy}{r(r+z)^2} \right] + \frac{(1+\nu)P}{2\pi E} \left[\frac{xz}{r^3} - (1-2\nu) \frac{x}{r(r+z)} \right] \quad (12)$$

$$u_y = \frac{(1+\nu)T}{2\pi E} \left[\frac{1}{r} + \frac{y^2}{r^3} + (1-2\nu) \left(\frac{1}{r+z} - \frac{y^2}{r(r+z)^2} \right) \right] + \frac{(1+\nu)P}{2\pi E} \left[\frac{yz}{r^3} - (1-2\nu) \frac{y}{r(r+z)} \right] \quad (13)$$

$$u_z = \frac{(1+\nu)T}{2\pi E} \left[\frac{yz}{r^3} + (1-2\nu) \frac{y}{r(r+z)} \right] + \frac{(1+\nu)P}{2\pi E} \left[2(1-\nu) \frac{1}{r} + \frac{z^2}{r^3} \right] \quad (14)$$

The SUBROUTINE DISP in ABAQUS uses the last three equations to prescribe the elastic displacements on the non-surface boundary nodes for each translating increment.

³¹ T is related to the normal force P through the friction coefficient μ .

APPENDIX 2

BOUNDARY CONDITIONS FOR 2-D FRICTIONAL CONTACT

Frictional 2-D rolling contact is simulated by translating a Hertzian thermo-mechanical load across the surface of a semi-infinite body. The thermo-mechanical load consists of three parts -

1. normal mechanical pressure, $p(x) = p_o \left(1 - \frac{x^2}{w^2}\right)^{1/2}$,
2. tangential surface traction, due to friction, $t(x) = \mu p(x)$ and
3. thermal load, due to the friction, $q(x) = v t(x)$

The semi-infinite body is represented by a 2-D plane strain finite element mesh with appropriate boundaries. Describing the boundary conditions at the non-surface boundary nodes, consists of two problems,

1. Prescribing the boundary temperatures due to the translating thermal load and
2. Prescribing the boundary displacements due to the translating thermo-mechanical load.

Boundary Temperatures

Physical visualization of the problem, in conjunction with the work of Carslaw and Jaeger (1959), implies that the temperature gradients, which give rise to thermal stresses and distortions, are large only in the vicinity of the contact, extending to depth of a maximum of $0.5w$. Hence, the temperatures at the bottom of the mesh could be fixed at the ambient temperature. In this part of the appendix, mathematical equations have been developed to reach the above conclusion, which extend the work of Carslaw and Jaeger, to predict temperatures in a half space due to a translating non-uniform heat source. Carslaw and Jaeger derived the solution, for the temperature distribution in an infinite solid, due to

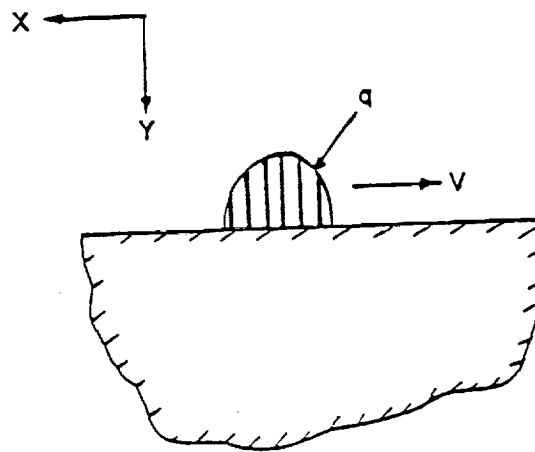


Figure A.2.1 The thermal load, $q(x)$, translating across the surface of the half-space at a velocity, V .

'Q' units of heat/unit length liberated along the z-axis (See Fig. A.2.1), at the point $(x',0,y')$.

The temperature, $T = \theta - \theta_o$, at a point $(x,0,y)$ at time 't' is

$$T = \frac{Q}{4\pi Kt} \exp\left[-\frac{(x-x')^2 + (y-y')^2}{4\kappa t}\right]$$

where, θ_o = ambient temperature, K = thermal conductivity, κ = thermal diffusivity = $K/\rho C$, ρ = density and C = specific heat capacity. The result needed, for a half-space, can be obtained by appropriately choosing the heat source, Q , and integrating the above equation. The variation of the non-uniform translating heat source, distributed over a width $2w$, is given by

$$q(x) = \mu p_o V \left(1 - \frac{x^2}{w^2}\right)^{1/2} \quad (15)$$

and hence the limits of integration are from $-w$ to w . Also, for temperatures at the current state, we have the heat source that has been moving for an infinite time at a velocity 'v' across the half-space. Hence, the limits for the integration with respect to time are from 0 to ∞ , with the present time being ∞ . At an earlier time 't', the center of the heat source was located at $-Vt$. Now, the heat source 'Q' is $2qdx'dt$ heat units/unit length (to account for the semi-infinite solid) through the point $(x'-Vt,0,0)$. The temperature T' is now given by

$$T' = \frac{qdx'dt}{2\pi Kt} \exp\left[-\frac{(x-x'+Vt)^2 + y^2}{4\kappa t}\right] \quad (16)$$

The required result is obtained by integrating the above equation, using equation (20) with respect to 'x' over the limits -w to w and with respect to time 't' from 0 to ∞ . Hence,

$$T = \int \int T' = \frac{q_o}{2\pi K} \int_{-w}^w \left(1 - \frac{x'^2}{w^2}\right)^{1/2} dx' \int_0^\infty \frac{dt'}{t} \exp\left[-\frac{(x - x' + Vt)^2 + y^2}{4\kappa t}\right]$$

Evaluating the time integral, the above equation becomes

$$T = \frac{q_o}{2\pi K} \int_{-w}^w e^{\frac{-V(x - x')}{2\kappa}} K_o\left\{\frac{V}{2\kappa}[(x - x')^2 + y^2]^{1/2}\right\} \left(1 - \frac{x'^2}{w^2}\right)^{1/2} dx' \quad (17)$$

where $K_o(x)$ is the modified Bessel function of the second kind of order zero. To enable Gaussian integration the limits of the integral need to be changed to -1 to 1.

$$T = \frac{q_o}{2\pi K} \int_{-1}^1 e^{\frac{-v(x - wu)}{2\kappa}} K_o\left\{\frac{v}{2\kappa}[(x - wu)^2 + y^2]^{1/2}\right\} (1 - u^2)^{1/2} w du \quad (18)$$

For the calculations, $v = 0.9$ m/s, $\kappa = 1.4E-5$ m²/s and the smallest value of the argument of K_o comes out to be 192.0 and its value tends to zero and θ tends to θ_o . Hence, the temperatures on the bottom of the mesh are fixed to ambient values and the effect of these temperatures in calculating the boundary displacements is neglected.

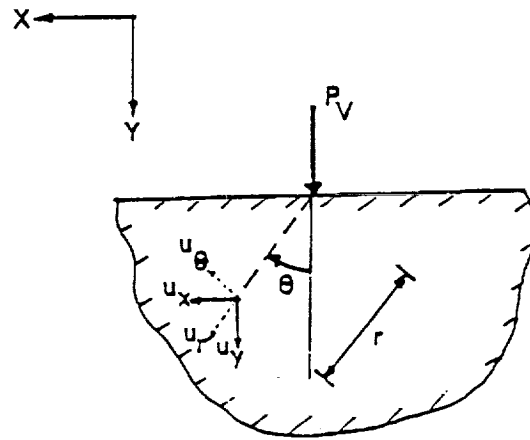


Figure A.2.2 A concentrated vertical force, P_V , acting on the surface of a half-plane.

Boundary Displacements

In Appendix B, two methods of solving problems in elasticity were mentioned and the second method, namely, the Second Boundary Value Problem of Elasticity, was used to derive the solution to Boussinesq's problem. Here, for the 2-D plane strain problem, the first method, namely, the First Boundary Value Problem of Elasticity will be used, in polar coordinates. The stresses must satisfy the equilibrium equations as well as the boundary conditions, the strains must satisfy the compatibility equations and the stresses must be related to the strains, by Hooke's law. A suitable Airy Stress Function can be found to satisfy the equilibrium equations, the boundary conditions and the compatibility equations. From the Airy Stress Function, the stresses are calculated, then strains are found using Hooke's law and the displacements are obtained from the strain-displacement relations and the boundary conditions. The derivations of the displacement equations due to a concentrated vertical and horizontal line load indenting a half-space are presented in this section.

a) Vertical or Normal line load at the surface of a half-plane : (see Fig. A.2.2).

The appropriate Airy Stress Function is

$$U = -\frac{P}{\pi} r\theta \sin \theta$$

1) The stresses are given by

$$\sigma_{rr} = \frac{1}{r} \frac{\partial U}{\partial r} + \frac{1}{r^2} \frac{\partial^2 U}{\partial \theta^2} = -\frac{2P \cos \theta}{\pi r}$$

$$\sigma_{r\theta} = -\frac{\partial}{\partial r} \left(\frac{1}{r} \frac{\partial U}{\partial \theta} \right) = 0$$

$$\sigma_{\theta\theta} = \frac{\partial^2 U}{\partial r^2} = 0$$

Then, using Hooke's law, the strains are given by

$$2G\epsilon_{rr} = \sigma_{rr} - \frac{3-\kappa}{4}(\sigma_{rr} + \sigma_{\theta\theta}) = -\frac{P(1+\kappa)\cos\theta}{2\pi r} \quad (19)$$

$$2G\epsilon_{r\theta} = \sigma_{r\theta} = 0 \quad (20)$$

$$2G\epsilon_{\theta\theta} = \sigma_{\theta\theta} - \frac{3-\kappa}{4}(\sigma_{rr} + \sigma_{\theta\theta}) = \frac{P(3-\kappa)\cos\theta}{2\pi r} \quad (21)$$

But the strains are related to the displacements by the strain-displacement equations, given by

$$2G\epsilon_{rr} = 2G \frac{\partial u_r}{\partial r} \quad (22)$$

$$2G\epsilon_{r\theta} = 2G \left[\frac{1}{r} \left(r \frac{\partial}{\partial r} \left(\frac{u_\theta}{r} \right) + \frac{1}{r} \frac{\partial u_r}{\partial \theta} \right) \right] \quad (23)$$

$$2G\epsilon_{\theta\theta} = 2G \left[\frac{1}{r} \left(\frac{\partial u_\theta}{\partial \theta} + u_r \right) \right] \quad (24)$$

Using equations (23) and (26) and integrating, we get

$$2G u_r = -\frac{P}{2\pi} (1+\kappa) \cos\theta \ln r + F(\theta) \quad (25)$$

Along the same lines, using equations (25) and (28), we get

$$2G u_\theta = \frac{P}{2\pi} (1+\kappa) \sin\theta \ln r - F(\theta) + g(r) + \frac{P}{2\pi} (3-\kappa) \sin\theta \quad (26)$$

Now, using equations (24), (27), (29) and (30), we get

$$F(\theta) + F''(\theta) + \frac{P}{\pi} (\kappa-1) \sin\theta + r^2 \frac{\partial}{\partial r} \left(\frac{g(r)}{r} \right) = 0 \quad (27)$$

Let,

$$A = F(\theta) + F''(\theta) + \frac{P}{\pi} (\kappa-1) \sin\theta \quad (28)$$

then

$$-A = r^2 \frac{\partial}{\partial r} \left(\frac{g(r)}{r} \right) \quad (29)$$

The solution of the ordinary differential equation given by Eqn. (32) is

$$F(\theta) = C_1' \cos \theta + C_2' \sin \theta + A + \frac{P}{2\pi} (\kappa - 1) \theta \sin \theta$$

and the solution of the ordinary differential equation given by Eqn. (33) is

$$g(r) = A + B'r,$$

where A, B', C₁' and C₂' are constants. The displacements are found to be

$$2G u_r = -\frac{P}{2\pi} [(1+\kappa) \cos \theta \ln r - (\kappa-1) \cos \theta + (\kappa-1) \theta \sin \theta] - C_1' \sin \theta + C_2' \cos \theta$$

and

$$2G u_\theta = \frac{P}{2\pi} [(1+\kappa) \sin \theta \ln r - (\kappa-1) \theta \cos \theta + (3-\kappa) \sin \theta] - C_1' \cos \theta - C_2' \sin \theta + B'r$$

For plane strain, $2G = \frac{E}{1+\nu}$, $\kappa = 3-4\nu$ and hence we have

$$u_r = \frac{P(1+\nu)}{2\pi E} [4(\nu-1) \cos \theta \ln r + 2(1-2\nu)(\cos \theta - \theta \sin \theta)] + C_1 \sin \theta + C_2 \cos \theta \quad (30)$$

and

$$u_\theta = \frac{P(1+\nu)}{2\pi E} [4(1-\nu) \sin \theta \ln r - 2(1-2\nu) \theta \cos \theta + 4\nu \sin \theta] + C_1 \cos \theta - C_2 \sin \theta + Br \quad (31)$$

The constants C₁, C₂ and B are calculated using the following boundary conditions - a) Points on the vertical axis have no lateral displacement, i.e. u_θ = 0 for θ = 0. From Eqn. (34)

$$C_1 + Br = 0 \text{ i.e. } C_1 = B = 0$$

b) For θ = 0 and r = d, there is no vertical displacement.

$$\text{i.e. } (u_r)_{\theta=0, r=d} = 0$$

From Eqn. (34), we have

$$(u_r)_{\theta=0} = \frac{P(1+\nu)}{2\pi E} [4(\nu-1) \ln r + 2(1-2\nu)] + C_2$$

Hence,

$$C_2 = -\frac{P(1+\nu)}{2\pi E} [4(\nu-1) \ln r + 2(1-2\nu)]$$

and we get

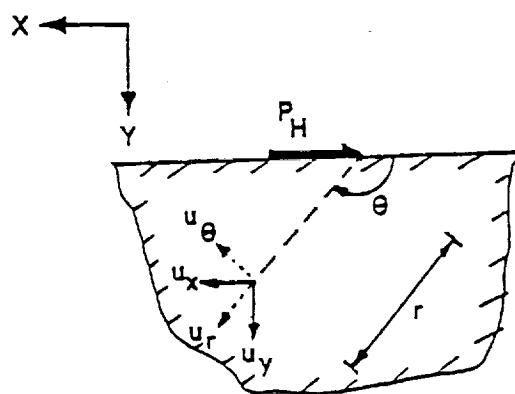


Figure A.2.3 A concentrated horizontal force, P_H , acting on the surface of a half-plane.

$$u_r = \frac{P(1+\nu)}{2\pi E} [4(\nu-1)\cos\theta \ln(r/d) - 2(1-2\nu)\theta \sin\theta]$$

and

$$u_\theta = \frac{P(1+\nu)}{2\pi E} [4(1-\nu)\sin\theta \ln(r/d) - 2(1-2\nu)\theta \cos\theta + 2\sin\theta]$$

With Poisson's ratio, $\nu = 0.3$, Young's modulus, $E = 207E9$ Pa and

$$\frac{(1+\nu)}{2\pi E} = 9.9E-13$$

$$u_r = P_V \times 9.9E-13 [-2.8 \cos\theta \ln(r/d) - 0.8 \theta \sin\theta] \quad (32)$$

and

$$u_\theta = P_V \times 9.9E-13 [2.8 \sin\theta \ln(r/d) - 0.8 \theta \cos\theta + 2\sin\theta] \quad (33)$$

These are the equations used in the SUBROUTINE DISP to prescribe the boundary displacements due to the vertical or normal force, P_V , by transforming these equations from polar to cartesian coordinate system, namely,

$$u_x = u_r \sin\theta + u_\theta \cos\theta$$

and

$$u_y = u_r \cos\theta - u_\theta \sin\theta$$

b) Horizontal force at the surface of the half plane : (see Fig. A.2.3) For

this case the appropriate Airy Stress Function is also

$$U = -\frac{P}{\pi} r\theta \sin\theta,$$

but the definition of θ is different and from the earlier discussion we get the same equations (34) and (35). The constants C_1 , C_2 and B are different and come out to be : a) For $\theta = \pi/2$ and $r = d$, there is no vertical displacement, i.e.

$(u_r)_{\theta=\pi/2, r=d} = 0$. We have,

$$C_1 = \pi(1-2\nu)$$

b) Also, for $\theta = \pi/2$ and $r = d$, there is no lateral displacement i.e.

$$(u_\theta)_{\theta=\pi/2, r=d} = 0.$$

We have,

$$4(1-\nu)\ln d + 4\nu - C_2 + Bd = 0$$

c) And, for $\theta = \pi/2$ and $r = d$, $(\frac{\partial u_r}{\partial \theta})_{\theta=\pi/2, r=d} = 0$. So,

$$-4(\nu-1)\ln d - 4(1-2\nu) - C_2 = 0$$

Solving these simultaneously,

$$C_2 = -4(\nu-1)\ln d - 4(1-2\nu)$$

and

$$B = \frac{1}{d}[4(\nu-1)]$$

The equations now are

$$u_r = \frac{P(1+\nu)}{2\pi E} [4(\nu-1)\cos \theta \ln(r/d) - 2(1-2\nu)(\cos \theta + \theta \sin \theta) + \pi(1-2\nu)\sin \theta]$$

and

$$u_\theta = \frac{P(1+\nu)}{2\pi E} [4(1-\nu)\sin \theta \ln(r/d) - 2(1-2\nu)\theta \cos \theta + 4(1-\nu)\sin \theta + \pi(1-2\nu)\cos \theta + \frac{4r}{d}(\nu-1)]$$

Once again, $\frac{(1+\nu)}{2\pi E} = 9.995E-13$ And,

$$u_r = P_H \times 9.9E-13 [-2.8\cos \theta \ln(r/d) - 0.8(\cos \theta + \theta \sin \theta) + 1.256\sin \theta] \quad (34)$$

and

$$u_\theta = P_H \times 9.9E-13 [2.8\sin \theta \ln(r/d) - 0.8\theta \cos \theta + 2.8\sin \theta + 1.256\cos \theta - \frac{2.8r}{d}] \quad (35)$$

These equations are used in the SUBROUTINE DISP to prescribe the boundary displacements due to the horizontal force, P_H , by transforming these equations from polar to cartesian coordinate system, namely,

$$u_x = u_\theta \sin \theta - u_r \cos \theta$$

and

$$u_y = u_r \sin \theta + u_\theta \cos \theta$$

APPENDIX 3

STRESS-STRAIN CONTOURS FOR 3-D ROLLING CONTACT IN AL

Some of the stress-strain contours calculated from the three dimensional finite element analyses of rolling contact in aluminum alloys are presented here. Figure A.3.1 through A.3.6 show the six components of stress when the contact pressure distribution is in the center of the mesh. Figures A.3.7 through A.3.16 illustrate the residual stress components and the residual plastic strain components after one contact sequence. The miniature schematic drawing by the side of each figure represents the sectional planes of the mesh on which the corresponding contours are calculated.

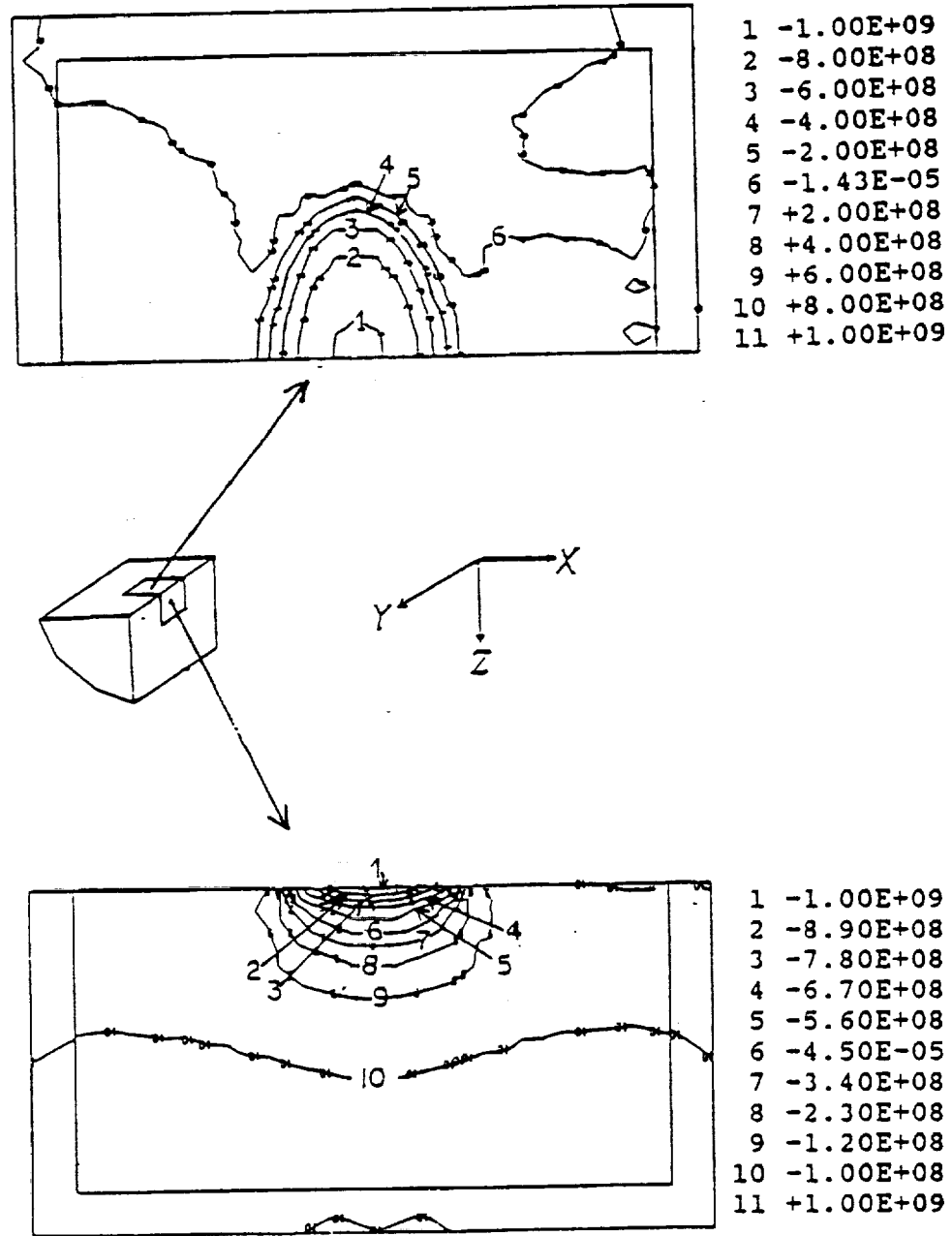


Figure A.3.1 Axial stress (σ_x) contours when the load is in the center of the mesh.

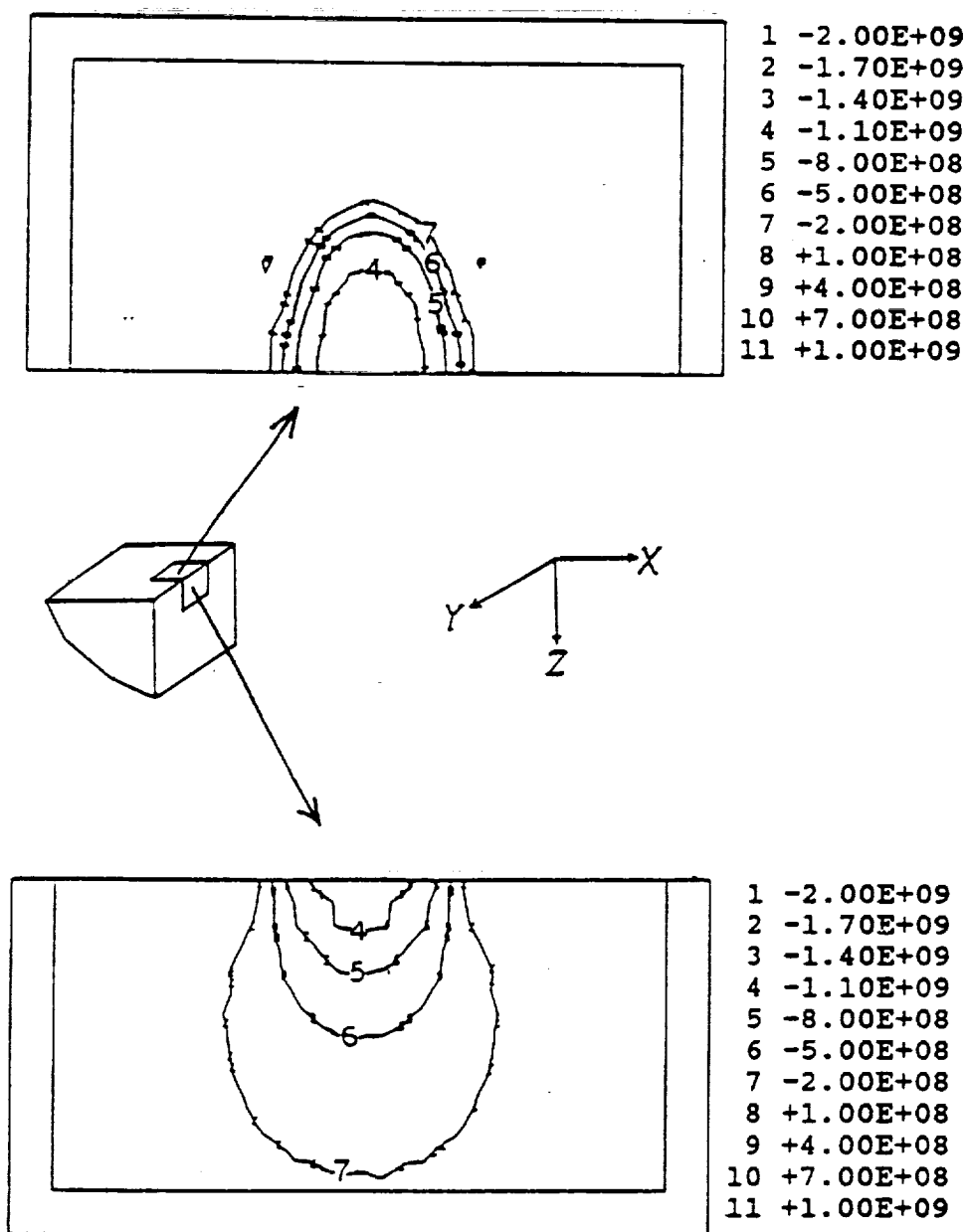


Figure A.3.2 Circumferential stress (σ_y) contours when the load is in the center of the mesh.

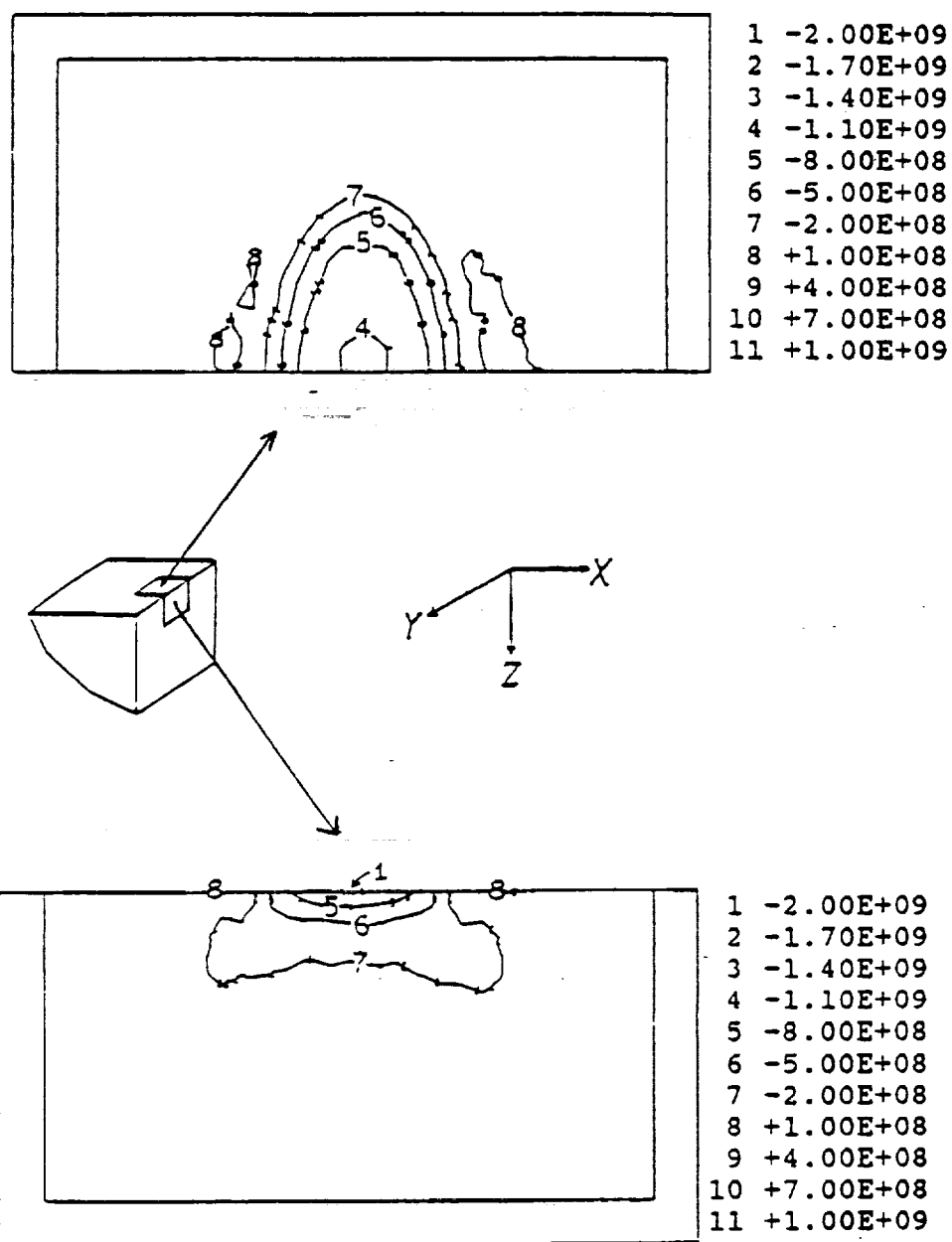


Figure A.3.3 Radial stress (σ_z) contours when the load is in the center of the mesh.

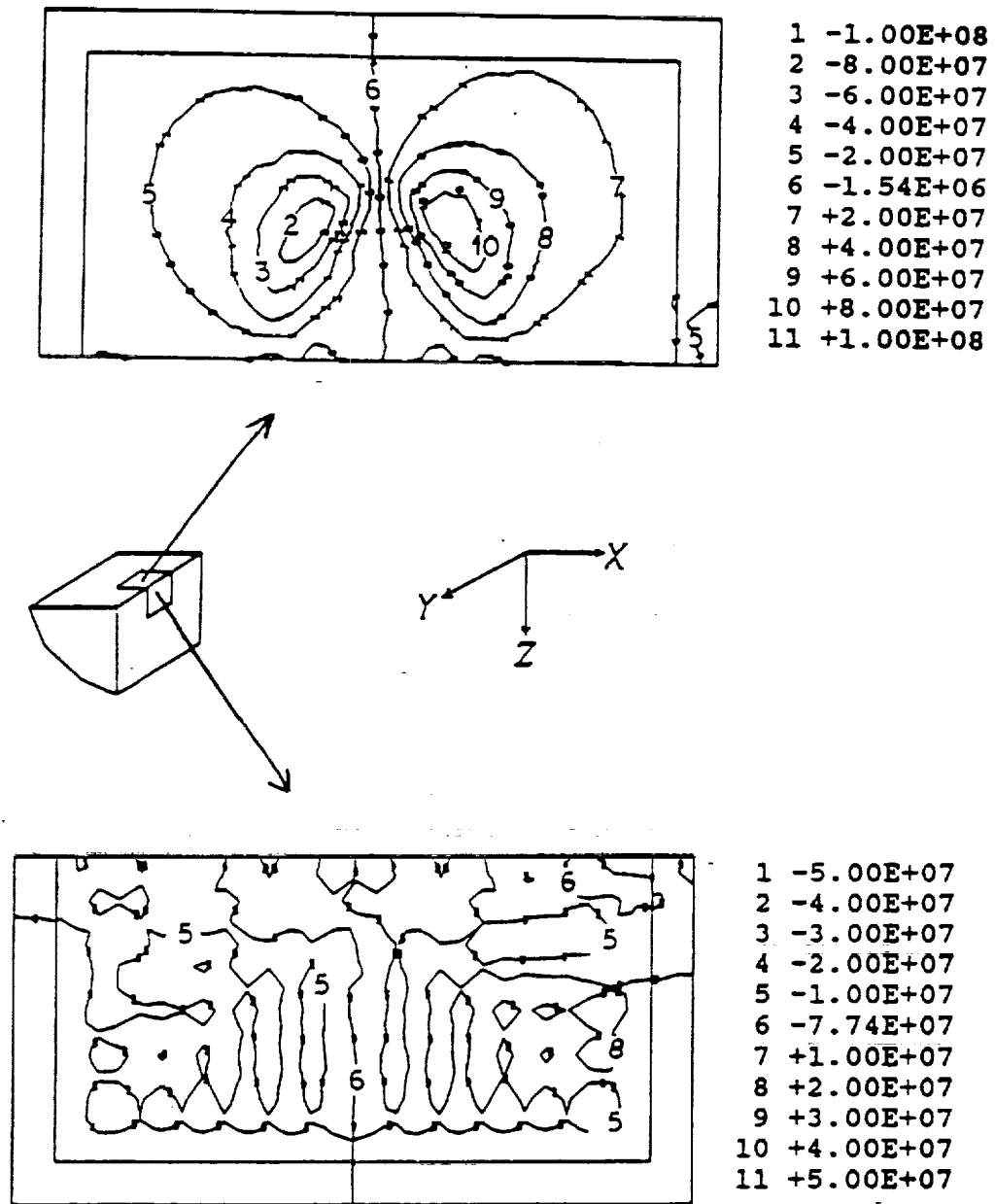


Figure A.3.4 Shear stress (σ_{xy}) contours when the load is in the center of the mesh.

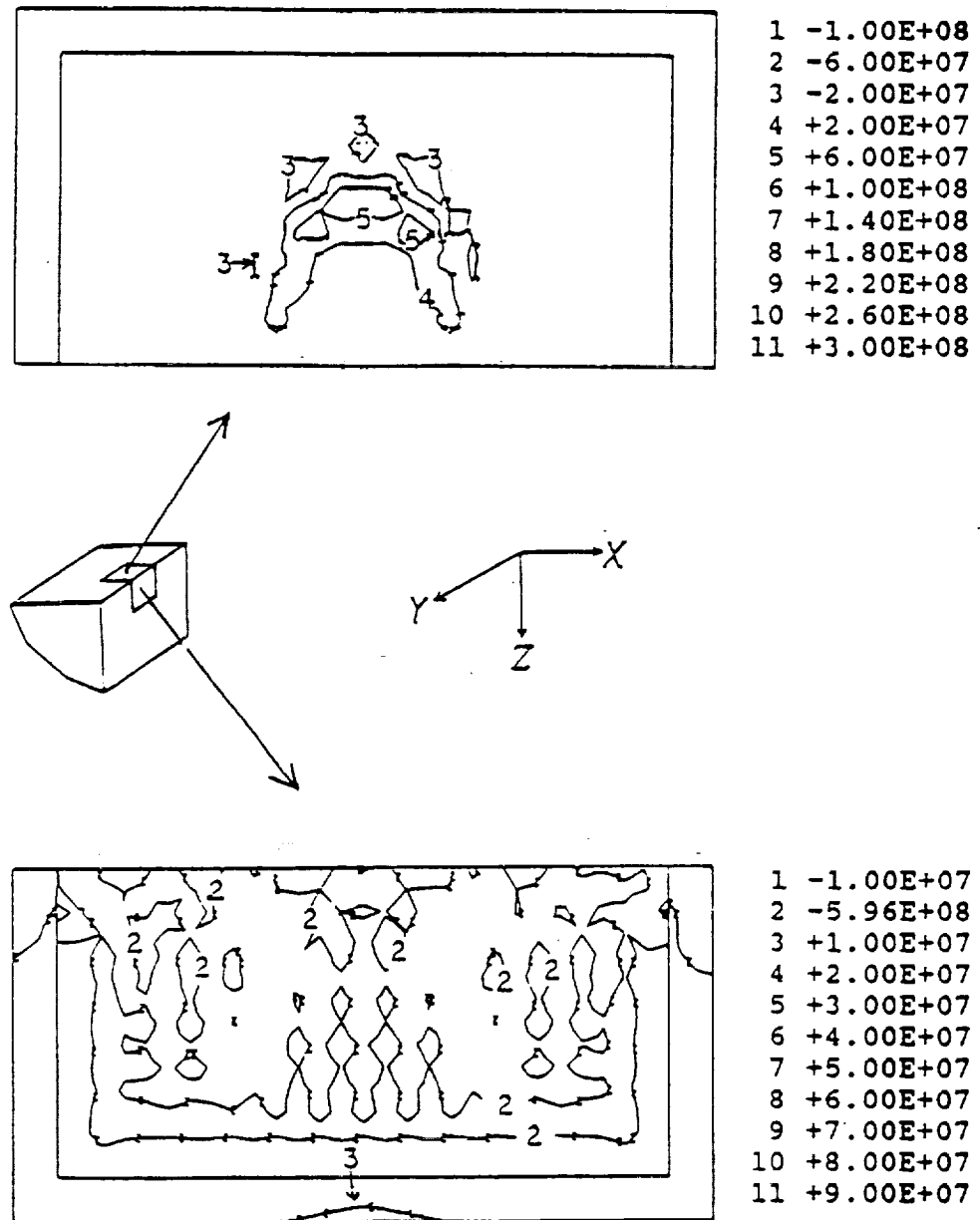


Figure A.3.5 Shear stress (σ_{yz}) contours when the load is in the center of the mesh.

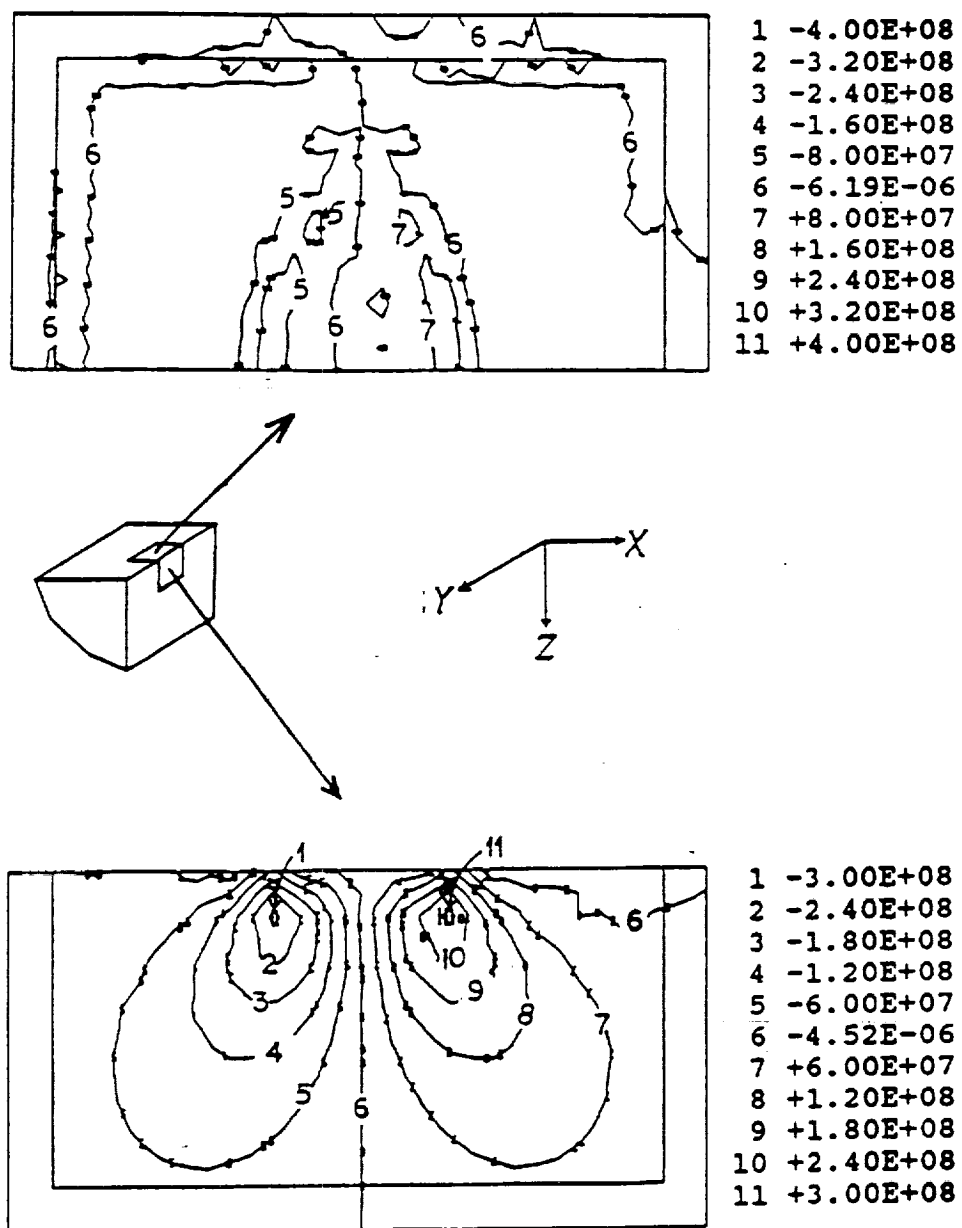


Figure A.3.6 Shear stress (σ_{xz}) contours when the load is in the center of the mesh.

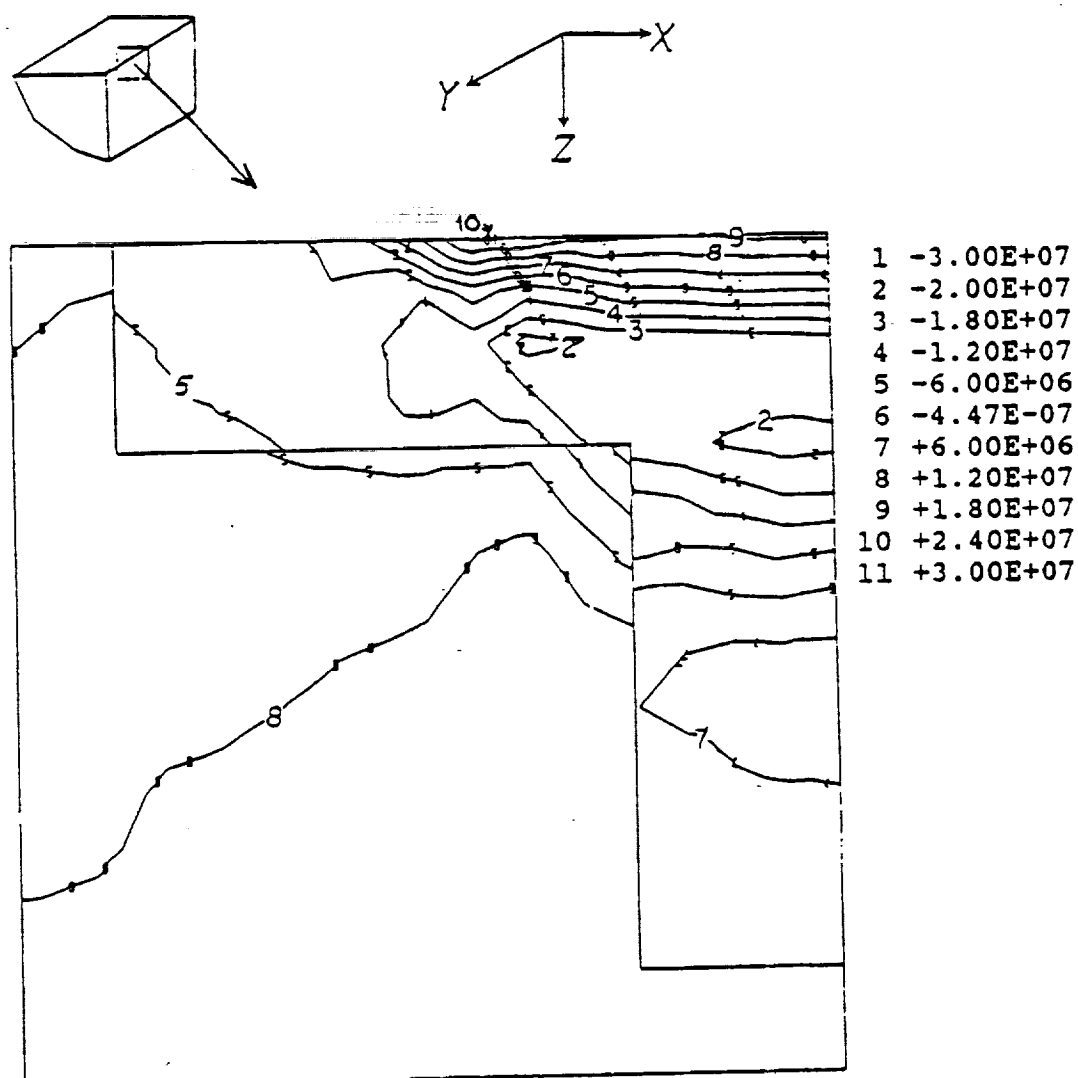


Figure A.3.7 Axial residual stress (σ_x) contours.

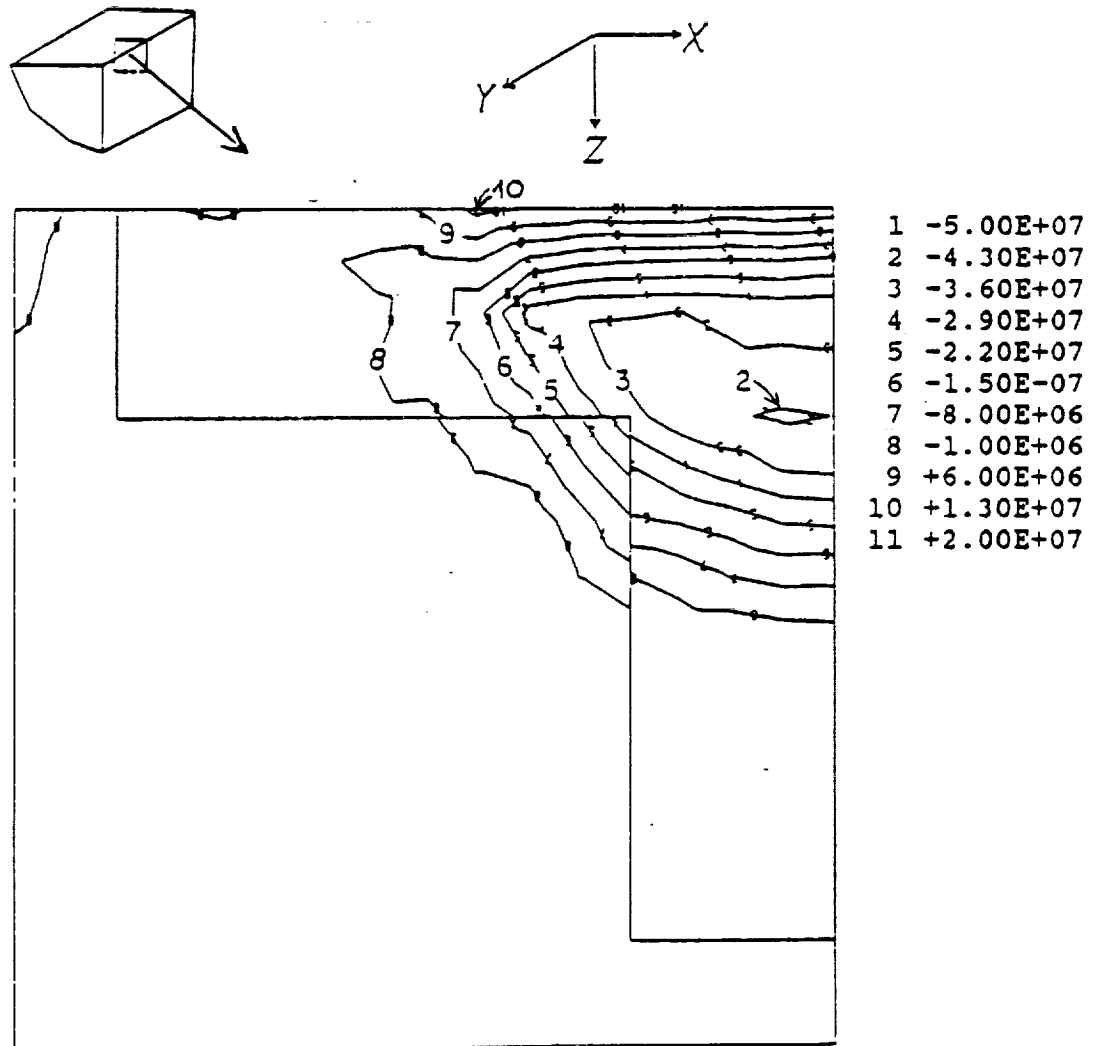


Figure A.3.8 Circumferential residual stress (σ_{ry}^r) contours.

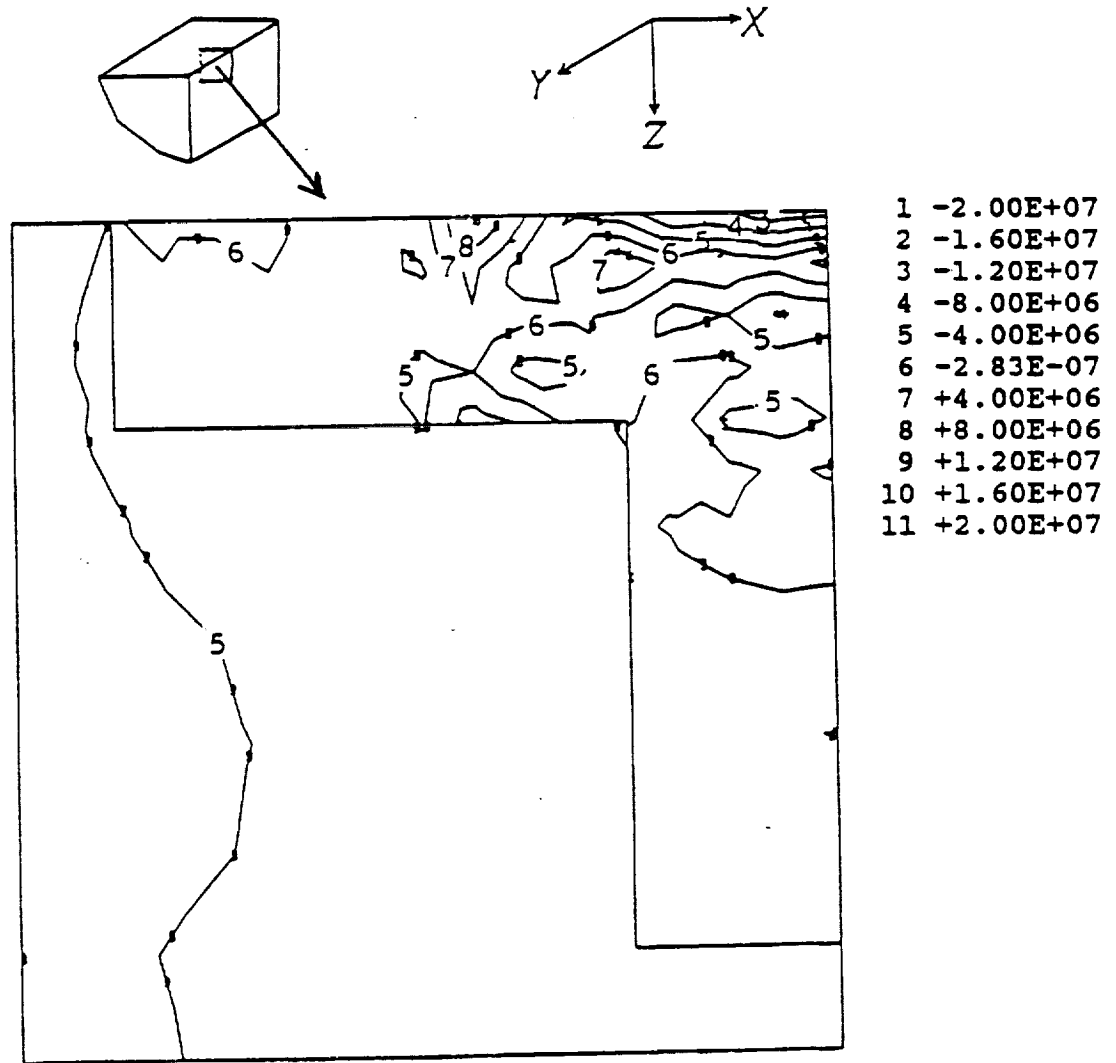


Figure A.3.9 Radial residual stress (σ^r_z) contours.

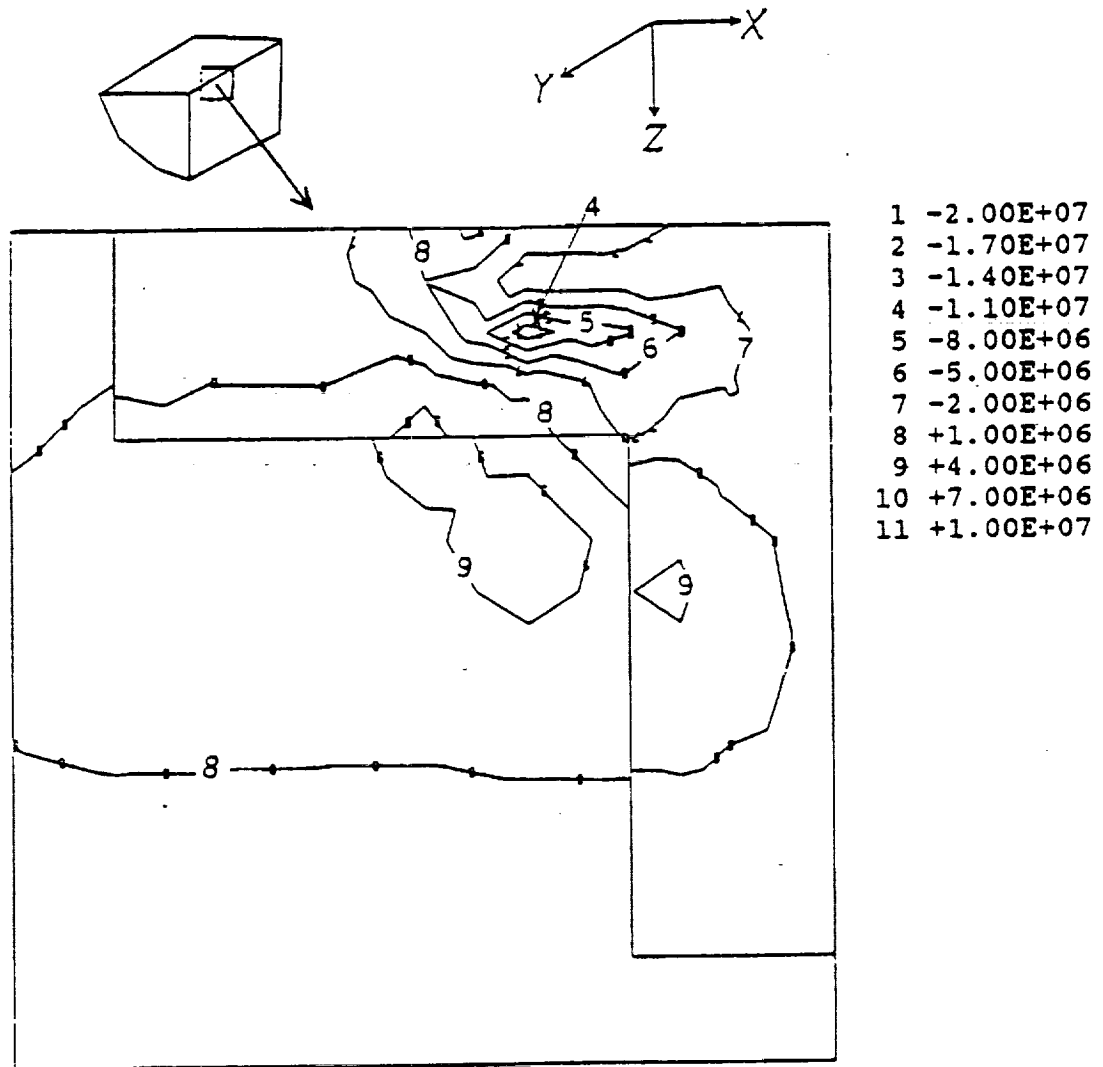


Figure A.3.10 Residual shear stress (σ^r_{yz}) contours.

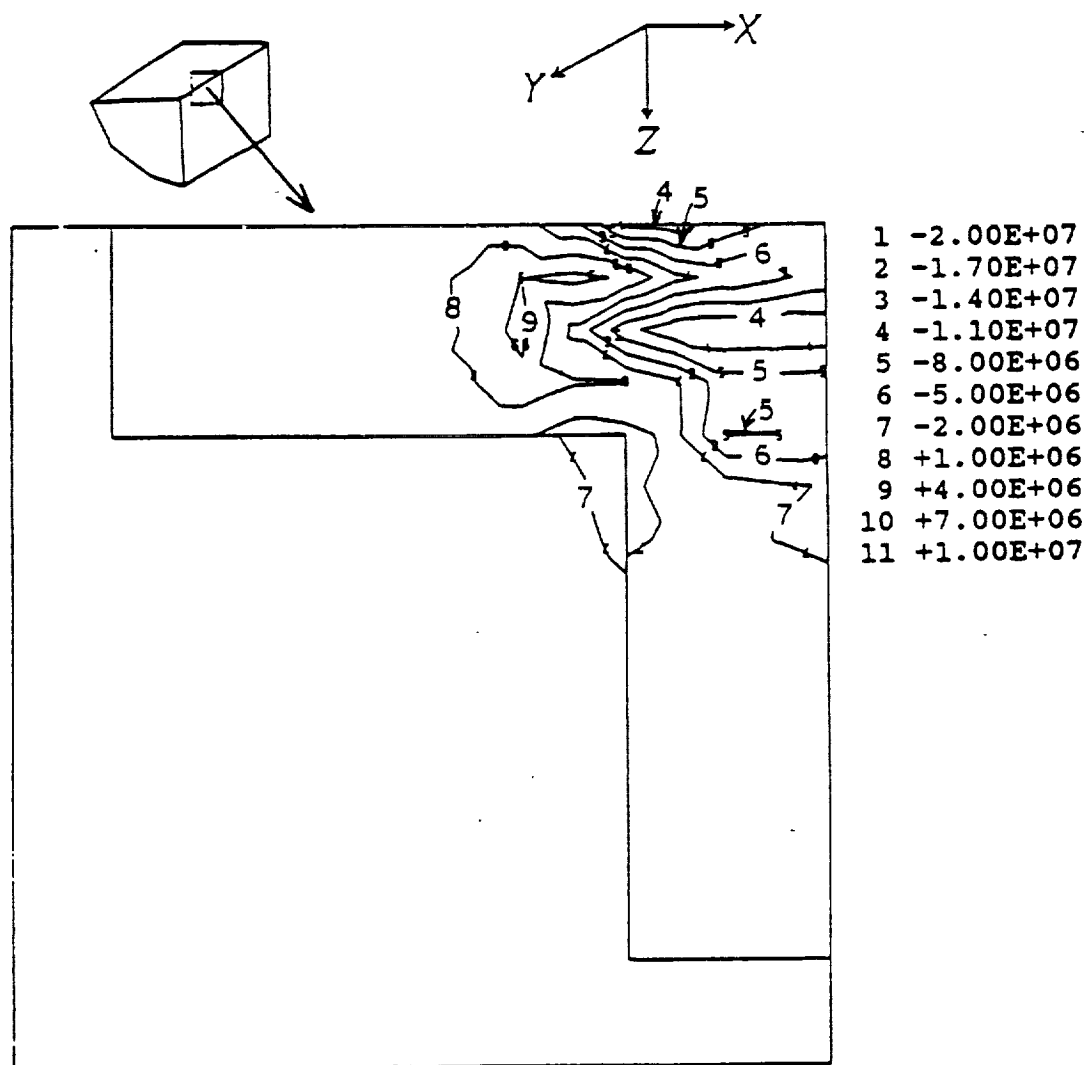


Figure A.3.11 Residual shear stress (σ^r_{xz}) contours

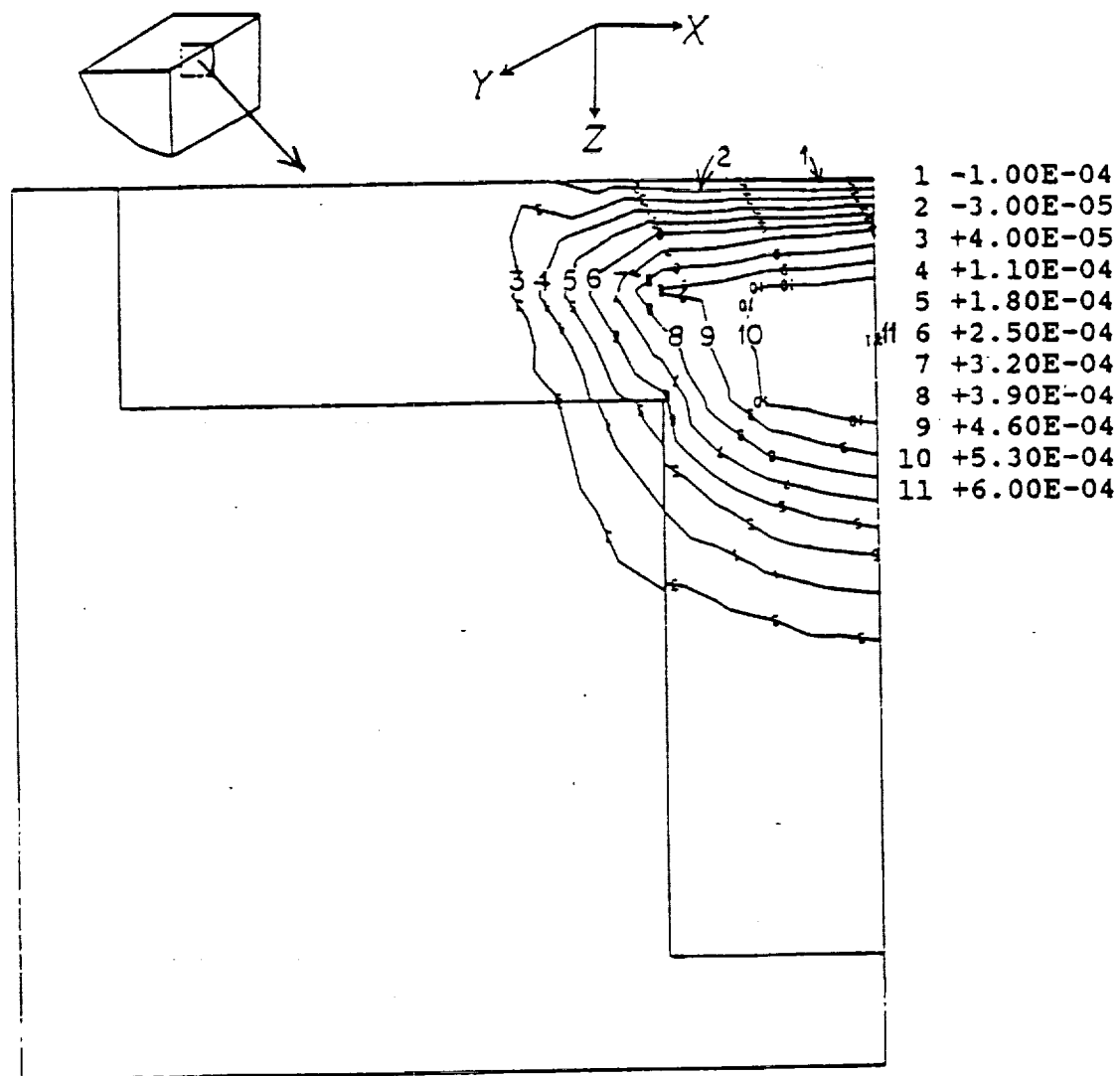


Figure A.3.12 Axial residual plastic strain (ϵ^{pr}_x) contours.

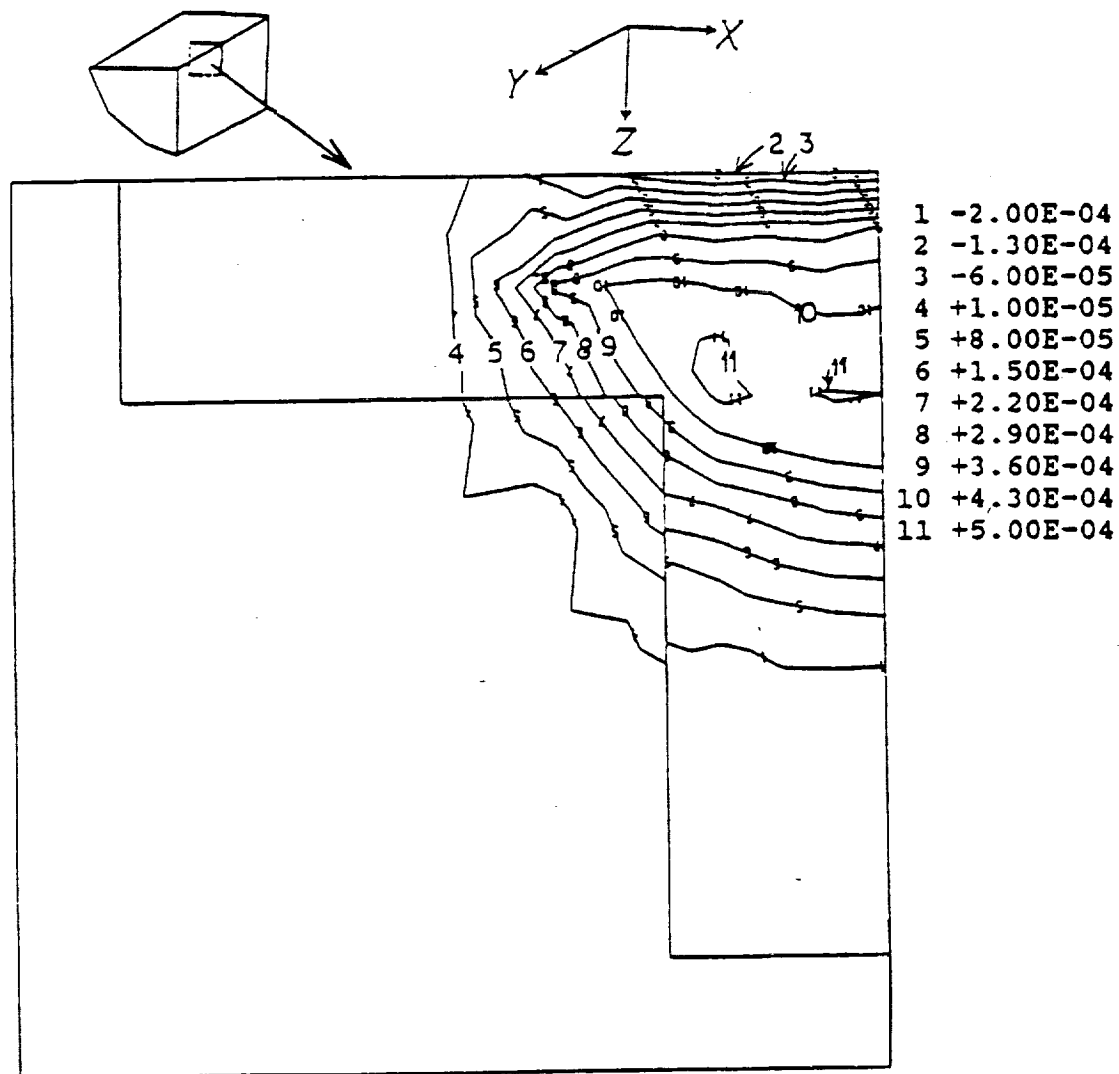


Figure A.3.13 Circumferential residual plastic strain (ϵ^{pr}_y) contours.

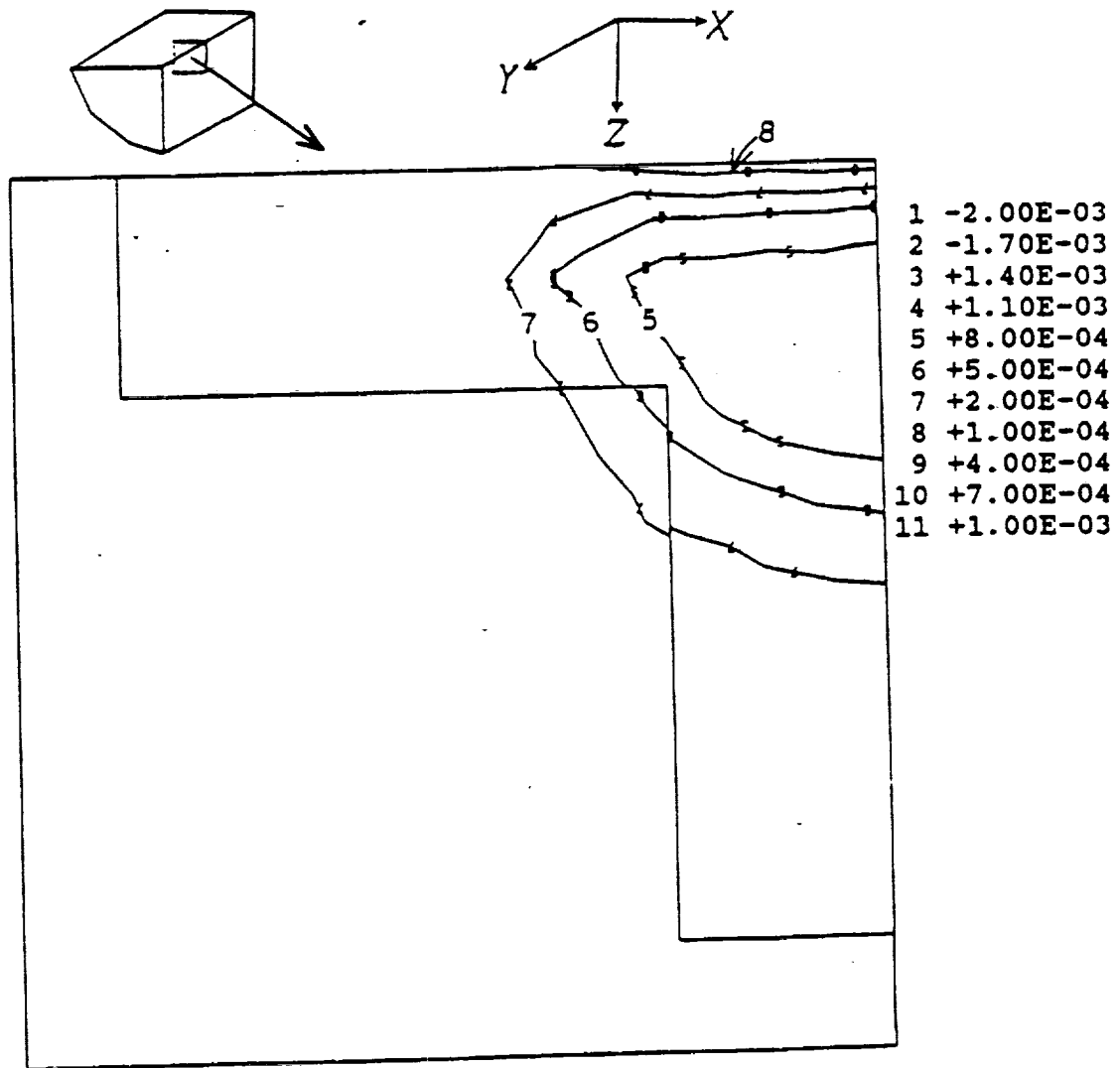


Figure A.3.14 Radial residual plastic strain (ϵ^{pr}_z) contours.

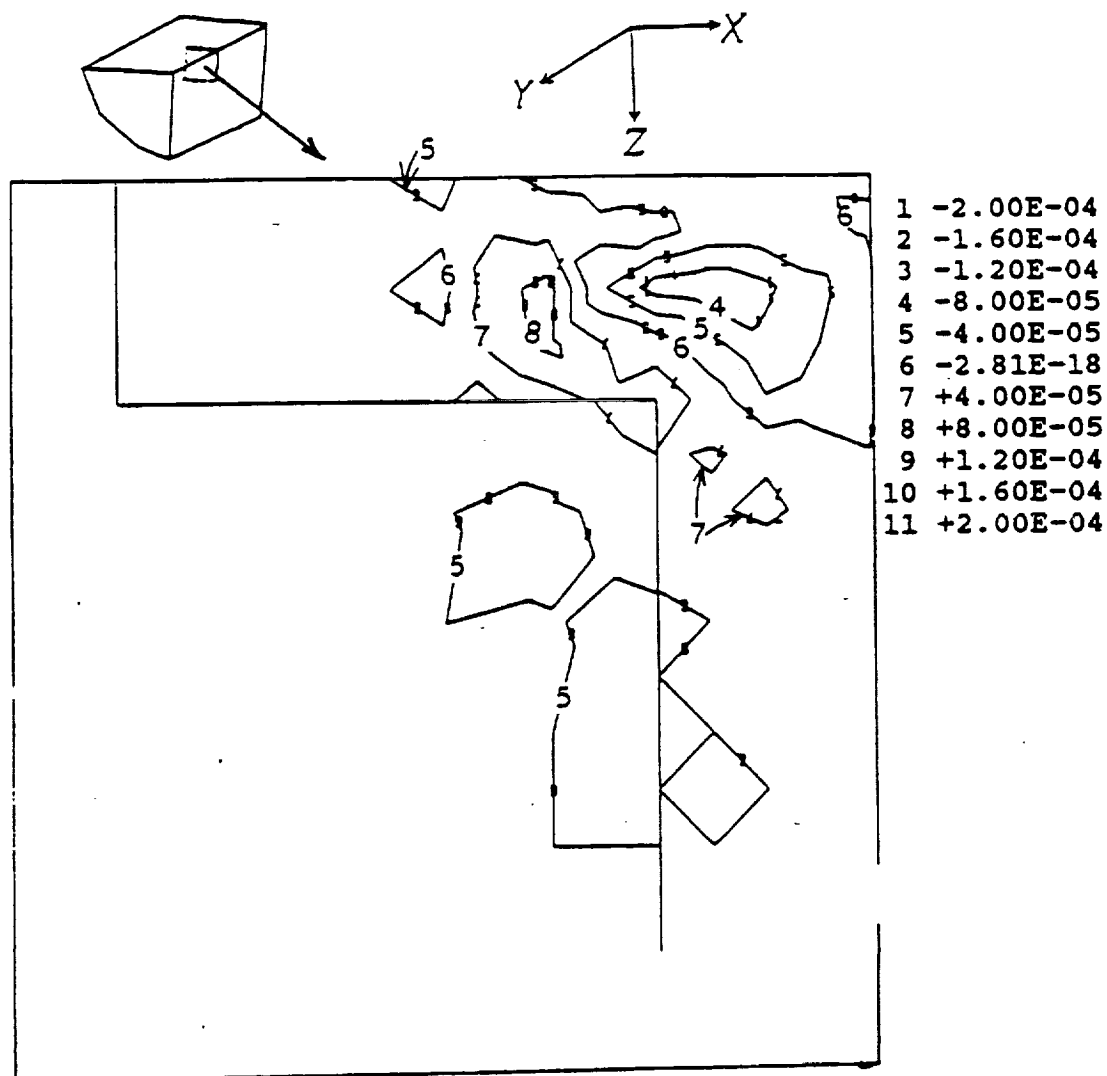


Figure A.3.15 Residual shear plastic strain (γ^{pr}_{xy}) contours.

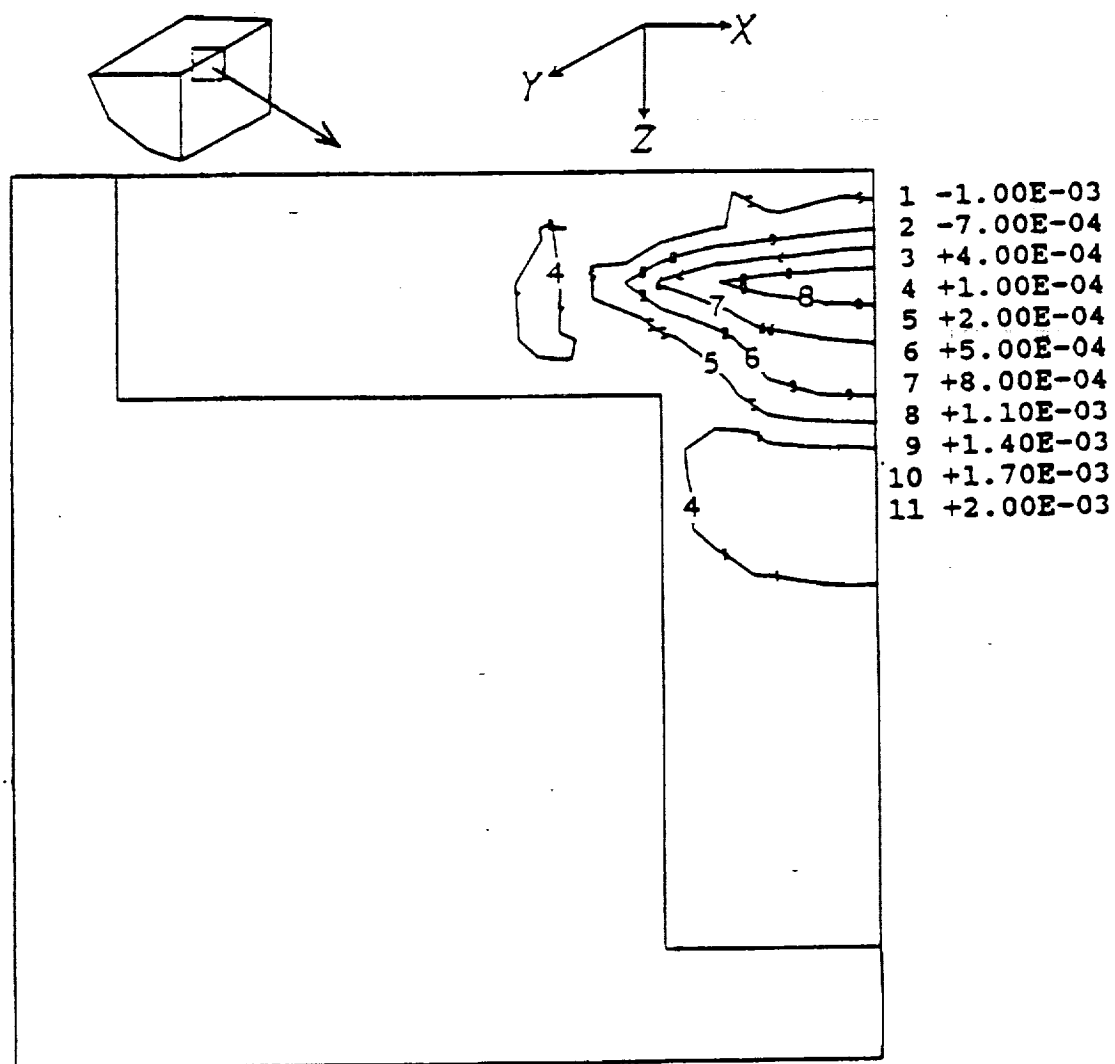


Figure A.3.16 Residual shear plastic strain (γ^{pr}_{xz}) contours.